

Multimode microwave circuit optomechanics as a platform to study coupled quantum harmonic oscillators

Thèse N° 9217

Présentée le 30 janvier 2019

à la Faculté des sciences de base

Laboratoire de photonique et mesures quantiques (SB/STI)

Programme doctoral en physique

pour l'obtention du grade de Docteur ès Sciences

par

NATHAN RAFAËL BERNIER

Acceptée sur proposition du jury

Prof. H. M. Rønnow, président du jury

Prof. T. Kippenberg, Dr O. Feofanov, directeurs de thèse

Prof. K. Hammerer, rapporteur

Prof. M. Sillanpää, rapporteur

Prof. C. Galland, rapporteur

2019

Acknowledgements

The journey of a doctoral student is a long and winding road, and I was fortunate to be well surrounded by colleagues and have more than a little help from my friends and family. I thank Tobias who initially gave me this opportunity to partake in scientific research at such a high level, trusting me who had only done theory before to learn how to deal with the realities of experimental work, and for his continuous interest and enthusiasm for the project, always finding time in his busy schedule. I thank Alexey for always being available to share his plentiful experience (even while travelling abroad, in a few emergencies), all the while trusting me to work independently, and for staying dedicated to help with my thesis beyond his official presence at EPFL. I cannot forget the unsung heroes who keep the complicated machinery of a large research group ticking day after day. H el ene, Antonella and Kathleen tolerated my inquiries and helped me many times along the years not only with great patience but a guarantee to raise a smile.

A large research group means a large number of colleagues whom I was glad to share this time with. In particular, I am very grateful to Daniel, who had the patience to work in very close collaboration with me for many years, enduring my constant blabber and occasional singing. The two of us share many happy memories in and outside the lab and I hope the road that we will share stretches long out ahead. Thanks to Philippe, who unsuccessfully tried to escape me after our common Bachelor's and Master's, for always keeping me updated with every significant cultural event of the Lemanic region and for giving me practice as an amateur psychoanalyst by regularly dropping by my office to unload his mind. I had the chance to engage in illuminating exchanges of ideas with many colleagues over the years, both of a scientific and non-scientific nature, which provided necessary breaks from the routine of daily work and stimulation for creativity. Without going

through an exhaustive list, let me briefly mention lively debates with Nico and Victor, forays in the esoteric aspects of optomechanics theory with Vivishek, swapping cultural references with Miles, and the generosity of Itay in sharing his positive outlook on life and general good humor. I'm glad that I could share my passion for whisky and beer with many and in particular with fellow taste snobs Philippe, Daniel and Nils. Outside of EPFL, I was blessed to have the opportunity to collaborate with Andreas Nunnenkamp and Daniel Malz. I thank Daniel for his relentless energy that he put in our theoretical collaboration, as well as for sharing an apartment and his flu in Trieste with me. Finally I am in tremendous debt to Amir and Nick, who picked up the microwave optomechanics project to carry it into the future, infusing it with new ideas and improvements despite my grumblings.

I am very grateful to my family, and especially to my sister, father and mother, who were there for me in the good and the less good times, and supported me through all those years, even tolerating most of my jokes. Thanks to my friends for helping me balance my private and professional life and for joining me to the many films, theater plays and concerts that I invited them to attend through the years. Finally thanks to my soon-to-be wife Ada, for constantly radiating positive energy and making my life an exciting adventure full of possibilities.

Résumé

Les oscillateurs harmoniques font partie des objets les plus fondamentaux décrits par la physique, mais restent malgré tout un sujet de recherche actuel. Les propriétés topologiques associées aux points exceptionnels qui peuvent apparaître lorsque deux modes interagissent ont suscité un grand intérêt récemment. Les oscillateurs harmoniques sont au coeur de nouvelles technologies quantiques : la longue durée de vie de résonateurs à haut facteur Q en fait d'excellentes mémoires quantiques ; ils sont aussi employés pour traiter des signaux quantiques de faible bande passante, par exemple dans les amplificateurs paramétriques Josephson.

Le but de cette thèse est d'explorer différents régimes fondamentaux de deux oscillateurs harmoniques couplés en utilisant l'optomécanique comme support expérimental. Suite au progrès constant dans leurs facteurs de qualité, les résonateurs mécaniques et électromagnétiques réalisent des oscillateurs harmoniques quasi-idéaux. Avec une modulation paramétrique du couplage optomécanique non-linéaire qui les lie, on peut réaliser un couplage linéaire dont la force et la fréquence relative des deux modes peuvent être contrôlés. Ainsi, l'optomécanique constitue une plateforme qui permet d'étudier un système de deux oscillateurs couplés, en réglant précisément leurs paramètres. Les systèmes optomécaniques que nous utilisons sont des circuits supraconducteurs dans lesquels la plaque supérieure d'un condensateur vibre et sert d'élément mécanique. Des circuits multimodes sont réalisés, dans lesquels deux modes micro-ondes interagissent avec un ou deux modes mécaniques. Les modes supplémentaires servent soit d'intermédiaires dans la relation des deux modes principaux, soit d'auxiliaires pour le contrôle d'un paramètre du système.

Trois résultats expérimentaux principaux sont obtenus. Premièrement, un mode micro-onde auxiliaire permet de contrôler le taux de dissipation effec-

tif d'un oscillateur mécanique. Ce dernier joue alors le rôle d'un réservoir thermodynamique pour le mode micro-onde principale avec lequel il interagit. La susceptibilité du mode micro-onde peut être modifiée, ce qui résulte en une instabilité analogue à celle du maser et à l'amplification résonante des signaux micro ondes incidents avec un bruit proche du minimum quantique. Deuxièmement, nous étudions les conditions dans lesquelles la relation entre deux modes micro-ondes devient non-réciproque, telle que l'information est transmise dans une direction mais pas dans l'autre. Les deux modes interagissent par le biais de deux oscillateurs mécaniques, ce qui permet une conversion en fréquence entre les deux cavités micro-ondes. La dissipation des modes mécaniques est essentielle pour deux raisons : elle permet une phase réciproque nécessaire à l'interférence et permet d'éliminer les signaux indésirables. Troisièmement, nous réalisons une attraction de niveaux entre un mode micro-onde et un mode mécanique, dans laquelle les fréquences propres du système se rapprochent à cause de l'interaction, au lieu de s'éloigner comme dans le cas plus usuel de répulsion de niveaux. Le phénomène est relié de manière théorique aux points exceptionnels, ce qui permet une classification générale des différents régimes d'interactions entre deux modes harmoniques, dont la répulsion et l'attraction de niveaux constituent deux exemples.

Mots-clés : optomécanique, circuits supraconducteurs micro-ondes, réservoirs quantiques, amplification à la limite quantique, non-réciprocité, attraction de niveaux

Abstract

Harmonic oscillators might be one of the most fundamental entities described by physics. Yet they stay relevant in recent research. The topological properties associated with exceptional points that can occur when two modes interact have generated much interest in recent years. Harmonic oscillators are also at the heart of new quantum technological applications: the long lifetime of high- Q resonators make them advantageous as quantum memories, and they are employed for narrowband processing of quantum signals, as in Josephson parametric amplifiers.

The goal of this thesis is to explore different fundamental regimes of two coupled harmonic oscillators using cavity optomechanics as the experimental platform. With consistent progress in attaining ever increasing Q factors, mechanical and electromagnetic resonators realize near-ideal harmonic oscillators. By parametrically modulating the nonlinear optomechanical interaction between them, an effective linear coupling is achieved, which is tunable in strength and in the relative frequencies of the two modes. Thus cavity optomechanics provides a framework with excellent control over system parameters for the study of two coupled harmonic modes. The specific optomechanical implementation employed are superconducting circuits with the vibrating top plate of a capacitor as the mechanical element. Multimode optomechanical circuits are realized, with two microwave modes interacting with one or two mechanical oscillators. The supplementary modes serve either as intermediaries in the relation of the two modes of interest, or as auxiliaries used to control a parameter of the system.

Three main experimental results are achieved. First, an auxiliary microwave mode allows the engineering of the effective dissipation rate of a mechanical oscillator. The latter then acts as a reservoir for the main microwave mode with which it interacts. The microwave mode susceptibility

can be tuned, resulting in an instability akin to that of a maser and in resonant amplification of incoming microwave signals with an added noise close to the quantum minimum. Second, we study the conditions for a nonreciprocal interaction between two microwave modes, when the information flows in one direction but not in the other. The two modes interact through two mechanical oscillators, leading to frequency conversion between the two cavities. Dissipation in the mechanical modes is essential to the scheme in two ways: it provides a reciprocal phase necessary for the interference and eliminates the unwanted signals. Third, level attraction between a microwave and a mechanical mode is demonstrated, where the eigenfrequencies of the system are drawn closer as the result of interaction, rather distancing themselves as in the more usual case of level repulsion. The phenomenon is theoretically connected to exceptional points, and a general classification of the possible regimes of interaction between two harmonic modes is exposed, including level repulsion and attraction as special cases.

Keywords: cavity optomechanics, superconducting microwave circuits, quantum reservoirs, quantum-limited amplification, nonreciprocity, level attraction

List of publications

- C. Javerzac-Galy, K. Plekhanov, **N. R. Bernier**, L. D. Tóth, A. K. Feofanov and T. J. Kippenberg: On-chip microwave-to-optical quantum coherent converter based on a superconducting resonator coupled to an electro-optic microresonator. *Physical Review A* **94**, 053815 (2016). Arxiv: <https://arxiv.org/abs/1512.06442>
- L. D. Tóth¹, **N. R. Bernier**¹, A. Nunnenkamp, A. K. Feofanov and T. J. Kippenberg: A dissipative quantum reservoir for microwave light using a mechanical oscillator. *Nature Physics* **13**, 787-793 (2017). Arxiv: <https://arxiv.org/abs/1602.05180>
- **N. R. Bernier**¹, L. D. Tóth¹, A. Koottandavida, M. A. Ioannou, D. Malz, A. Nunnenkamp, A. K. Feofanov and T. J. Kippenberg: Non-reciprocal reconfigurable microwave optomechanical circuit. *Nature Communications* **8**, 604 (2017). Arxiv: <https://arxiv.org/abs/1612.08223>
- L. D. Tóth¹, **N. R. Bernier**¹, A. K. Feofanov and T. J. Kippenberg: A maser based on dynamical backaction on microwave light. *Physics Letters A* **382**, 2233 (2018). Arxiv: <https://arxiv.org/abs/1705.06422>
- D. Malz, L. D. Tóth, **N. R. Bernier**, A. K. Feofanov, T. J. Kippenberg and A. Nunnenkamp: Quantum-limited directional amplifiers with optomechanics. *Physical Review Letters* **120**, 023601 (2018). Arxiv: <https://arxiv.org/abs/1705.00436>
- **N. R. Bernier**, L. D. Tóth, A. K. Feofanov and T. J. Kippenberg: Nonreciprocity in microwave optomechanical circuits. Special issue “Magnet-less Nonreciprocity in Electromagnetics” in IEEE Antennas

¹ Equally contributing authors.

and *Wireless Propagation Letters*, **17**, 1983–1987 (2018).

Arxiv: <https://arxiv.org/abs/1804.09599>

- **N. R. Bernier**, L. D. Tóth, A. K. Feofanov and T. J. Kippenberg: Level attraction in a microwave optomechanical circuit. *Physical Review A*, **98**, 023841 (2018).

Arxiv: <https://arxiv.org/abs/1709.02220>

Contents

Acknowledgements	iii
Résumé	v
Abstract	vii
List of publications	ix
Contents	xi
List of Figures	xv
List of Symbols	xix
1 Introduction	1
2 Theoretical background	7
2.1 A short review of cavity optomechanics	7
2.1.1 The optomechanical interaction	8
2.1.2 The Langevin formalism	9
2.1.3 Linearization in the Langevin picture	11
2.1.4 Linearization in the Hamiltonian picture	14
2.1.5 Optomechanical damping and amplification	15
2.2 Quantum noise and amplification	19
2.2.1 Input and output modes	19
2.2.2 The Wiener-Khinchin theorem and the spectral density	21
2.2.3 The linear amplifier and its quantum limits	24
2.3 Optomechanical microwave circuits	27

2.3.1	Optomechanics with LC circuits	27
2.3.2	Transmission line theory	30
2.3.3	Input and output relations for an inductively coupled LC circuit	34
2.3.4	Quantization of the microwave and mechanical modes	38
3	Design and measurement of optomechanical microwave cir- cuits	43
3.1	Fabrication of the devices	43
3.2	Simulation tools as aides for design and characterization	46
3.2.1	Sonnet software	48
3.3	Experimental setup	51
3.3.1	Sample holder	51
3.3.2	Mounting and bonding the chip	53
3.3.3	Inside the dilution refrigerator	55
3.3.4	Room-temperature equipment	59
3.4	Noise calibrations	63
3.4.1	Phase and amplitude noise of the sources	63
3.4.2	Calibration of the HEMT	65
3.5	Characterization of the chip	68
3.5.1	Fitting microwave resonances with circles	69
3.5.2	Measurement of g_0	77
3.6	Routine optomechanical measurements	81
3.6.1	Sideband cooling	81
3.6.2	Optomechanically induced transparency and absorption	83
4	A dissipative quantum reservoir for microwaves using a me- chanical oscillator	87
4.1	Introduction	88
4.2	Dark and bright modes	89
4.3	Realization of a mechanical reservoir	93
4.4	Tuning a mode using a reservoir	95
4.5	Interpretation as dynamical backaction	95
4.5.1	Origin of the concept of dynamical backaction	95
4.5.2	Modeling dynamical backaction	98
4.6	Controllable microwave susceptibility	100
4.7	Maser action and amplification	102
4.8	Near-quantum-limited amplification	106
4.9	Injection locking of the maser tone	109
4.10	Conclusions	111

5	Nonreciprocity in microwave optomechanical circuits	113
5.1	Introduction	113
5.2	Gyrators and nonreciprocity	115
5.2.1	The gyrator-based isolator	115
5.2.2	Nonreciprocity in optomechanical systems	117
5.3	Optomechanical isolator	121
5.3.1	Theoretical model	121
5.4	Experimental results	125
5.4.1	Transmission measurements	127
5.4.2	Noise measurements	131
5.5	Optomechanical circulator	133
5.6	Outlook	135
6	Level attraction in a microwave optomechanical circuit	137
6.1	Introduction	137
6.2	Theoretical exposition of level attraction	140
6.2.1	Symmetry of level repulsion and attraction	143
6.2.2	Classification of exceptional points	145
6.3	Optomechanical level attraction	148
6.3.1	Experimental results	149
6.4	Outlook	153
7	Outlook on high-efficiency optomechanical measurements with a traveling-wave parametric amplifier	155
7.1	Introduction	155
7.2	Installing and operating the TWPA	156
7.3	Detailed balance in sideband cooling	158
7.3.1	Theoretical model	159
7.3.2	Preliminary experimental results	160
7.4	Precise noise calibration	162
8	Conclusions and outlook	167
8.1	Summary of the results	167
8.2	Outstanding challenges and outlook	168
A	The rotating wave approximation	171
B	Heterodyne detection as amplification	175
B.1	Quantum measurements and spectral densities	176
B.2	Direct photodetection	177
B.3	Optical heterodyne detection	179

B.4 Comparison between heterodyne detection and phase-preserving amplification	181
C Samples used in the experiment	183
Bibliography	189
Curriculum Vitae	203

List of Figures

1.1	The circular motion of a harmonic oscillator	3
2.1	Archetypical optomechanical system.	8
2.2	Schematic representation of a linear scattering amplifier	25
2.3	Ideal LC circuit with an inductor in series with a capacitor. .	28
2.4	Lumped-element model of the transmission line.	32
2.5	Different loads on the line for which the reflection coefficient are computed.	33
2.6	Lumped-element model of the resonator coupled to the line. .	36
3.1	Photograph and scanning-electron micrograph of the optome- chanical circuit	44
3.2	Schematic of the main steps of fabrication of the chips.	46
3.3	Example of Sonnet simulation	48
3.4	Microwave resonances simulated with Sonnet for the sample HYB-20150924-4-24	50
3.5	Photographs of the sample holder.	52
3.6	Schematics of the setup inside the dilution refrigerator.	57
3.7	Room-temperature equipment.	60
3.8	Filter cavity photograph and response	62
3.9	Measured phase and amplitude noise of Rohde & Schwartz SMF 100A	65
3.10	Scheme for the calibration of the HEMT amplifiers	66
3.11	Example measurement for the calibration of the HEMT	69
3.12	Example of fitting a circle to the complex response S_{11}	71
3.13	Model for impedance mismatch	74
3.14	Calibration of g_0	80
3.15	Sideband cooling of the mechanical mode	82

3.16	Measurement of OMIT/OMIA with a red-detuned pump tone	84
3.17	OMIT power sweep to the onset of strong coupling	85
4.1	Realization of a mechanical reservoir for a microwave cavity in circuit optomechanics.	90
4.2	Unsuccessful design to obtain asymmetrically coupled microwave modes	92
4.3	Device, experimental setup, and characterization of the elec- tromechanical circuit	94
4.4	The role of dissipation in dynamical backaction.	97
4.5	Dynamical backaction on the microwave mode using an engi- neered mechanical reservoir.	101
4.6	Amplified vacuum fluctuations and parametric instability of the microwave mode (masing).	103
4.7	Interaction between modes of positive and negative energy as population inversion	105
4.8	Near-quantum-limited phase-preserving amplification.	107
4.9	Injection locking of a maser based on dynamical backaction . .	110
5.1	Gyrator and optomechanical coupling.	116
5.2	Gyrator-cased isolator compared to optomechanical multimode schemes.	118
5.3	Scheme for a multimode optomechanical isolator	122
5.4	Implementation of a superconducting microwave circuit op- tomechanical device for nonreciprocity.	126
5.5	Diagram of the measurement chain for frequency conversion .	128
5.6	Experimental demonstration of nonreciprocity.	130
5.7	Asymmetric noise emission of the nonreciprocal circuit.	132
5.8	Proposal for a microwave optomechanical circulator.	134
5.9	Schemes for directional amplification with an optomechanical circuit	136
6.1	Level repulsion and attraction.	139
6.2	The effect of dissipation on level attraction.	141
6.3	Systematic comparison of level repulsion and attraction. . . .	146
6.4	Engineering dissipation in a multimode optomechanical circuit.	150
6.5	Experimental demonstration of level repulsion and attraction in a microwave optomechanical circuit.	152
6.6	Amplitude and complex responses for level repulsion and at- traction	154
7.1	Setup for the TWPA	157

7.2	Scheme for tone cancellation	158
7.3	Sideband asymmetry experiment with the TWPA	161
7.4	Comparison of the sideband measurement with the TWPA turned on and off	163
7.5	Setup for the calibration of the TWPA	164
8.1	Proposal for a new geometry for the capacitor	170
A.1	Comparison of cases when the RWA is valid or not.	172
B.1	Scheme for heterodyne detection.	181

List of Symbols

G	Position-dependent optomechanical coupling constant; definition p. 8, expression for the capacitor p. 30.
g_0	Vacuum optomechanical coupling strength; definition p. 9, expression for the capacitor p. 41.
κ_{ex}	External coupling rate of the electromagnetic cavity; definition p. 10, expressions for an LC resonator in reflection p. 35 and in transmission p. 37, expressions in the presence of an impedance mismatch p. 73 in transmission and p. 76 in reflection.
κ_0	Internal dissipation rate of the electromagnetic cavity; definition p. 10, expression for an <i>LC</i> resonator p. 35.
Γ_{m}	Mechanical dissipation rate; definition p. 10.
ω_c	Cavity resonance frequency: definition p. 10, expression for an <i>LC</i> resonator p. 28, expressions in the presence of an impedance mismatch p. 73 in transmission and p. 76 in reflection.
κ	Electromagnetic dissipation rate; definition p. 10.
Ω_{m}	Mechanical resonance frequency; definition p. 10.
\bar{n}_c	Mean intracavity photon number due to a driving tone; definition p. 12.

Δ	Pump tone frequency detuning; definition p. 13.
g	Linearized field-enhanced optomechanical coupling strength definition p. 13.
Γ_{eff}	Effective mechanical dissipation rate; definition p. 17.
\mathcal{C}	Optomechanical cooperativity; definition p. 17.
$\bar{n}_{\text{m,th}}$	Mean mechanical number occupancy at thermal equilibrium; definition p. 17.
\bar{n}_{m}	Mean mechanical number occupancy; definition p. 18.
\bar{n}_{th}	Mean thermal occupancy for a travelling electromagnetic wave; definition p. 20.
\mathcal{S}	Spectral density; classical definition p. 21, quantum definition p. 23.
$\bar{\mathcal{S}}$	Symmetrized spectral density; definition p. 23.
\mathcal{G}	Amplifier gain; definition p. 24.
\mathcal{N}	Added noise of an amplifier (in quanta); definition p. 26.
m_{eff}	Effective mass of the mechanical oscillator; definition p. 39.

Introduction

Motion in a circle has exerted a strong fascination on the human mind through the ages. It is most evident in cosmology and the “changing vision of the universe” (Koestler, 1959). The idea of heavenly bodies that rotate in circles around a spherical earth can be traced back to the school of Pythagoras in the 6th century BCE. Their global vision of sciences, imbued with mysticism, encompassed mathematics, medicine and the arts. The musical notes produced by the rotation of each cosmic body at various speeds composed a harmony of the spheres that supposedly only Pythagoras himself could hear.

Plato, in the 4th century BCE, confirmed the Pythagorean intuition by a priori reasoning concluding that the universe should have the perfect shape of a sphere and the perfect motion of a circular trajectory at uniform speed. Subsequently, his contemporary Aristotle formalized this notion into a dogma of circular motion that humanity only abandoned two thousand years later. The spherical earth, immobile in the center of the universe belongs to the sublunar realm of change and decay. It is surrounded by nine concentric spheres, increasing in purity and holiness with radius, all moving in circles around their center. The relative motion of spheres rotating with respect to each other uniformly (54 spheres in total in the complete Aristotelian model that result in convoluted trajectories for the nine spheres that carry celestial objects) could only very roughly account for the actual apparent movements in the sky. Ptolemy, in 2nd century BCE, discarded the spheres and only kept the rule of circular motion at the letter. His planets move uniformly in circles around points that themselves follow a circular orbit around the earth

(or rather a point slightly away from the earth, named the eccentric). By varying the radii and relative velocity of those circular motions, complicated noncircular trajectories on the epicycles can be constructed from circles only. Through that technique, the strange wandering of the planets could be approximately accounted for, at least well enough for the needs of time keeping and navigation at the time. Copernicus in the 16th century, unsatisfied with the status quo, attempted a new model that placed the sun in the center of the orbits of all planets (as Philolaus, Heraclides and Aristarchus had done long before). That model simplified things slightly, but could not escape the curse of the circular dogma, filled as the Ptolemaic system with complicated epicycles.

The holiness of circular motion was so well entrenched that it took until the 17th century for Kepler to finally renounce it and introduce elliptic orbits instead. Motivated by a mystical urge to decrypt the universe with the language of mathematics, he took the very modern step of comparing a model to precise data. The inevitable conclusion came at great pains to Kepler who despaired that giving up on the circles and epicycles that had cluttered astronomy for millenia left him with “only a single cart-full of dung”¹, the ellipse. Such was the strength of the delusion that Galileo, a contemporary who had access to Kepler’s results but believed firmly in Copernicus’s epicycles, held that matter, left to its own device, would naturally move in circles. Finally, Descartes found soon afterwards the correct law of inertia, pronouncing the infinite line as the natural trajectory of matter.

I will argue that the obsession with circular motion was only misdirected when applied to astronomy. A circular orbit is indeed only possible for a body whose initial velocity and distance from the sun are such that the gravitational force precisely corresponds to the centripetal force required to bend the trajectory into a circle. Any other initial conditions and the orbit forms an ellipse. There is however an entity that always travels on a circle at uniform velocity: the harmonic oscillator in phase space.

The harmonic oscillator is a physical abstraction that represents an ideal periodic motion in a quadratic potential. Its archetype is a mass bouncing on a linear spring, as shown in fig. 1.1a. When the mass m departs its equilibrium position, a recoil force $F(x) = -kx$ (with k the spring constant) pulls it back. The resulting motion is periodic, with $x(t) = x_0 \sin(\omega_0 t + \phi)$, where the amplitude x_0 and phase ϕ are determined by the initial condition, and $\omega_0 = \sqrt{k/m}$ is the oscillation frequency (fig. 1.1b). The velocity oscillates out of phase with the position as $v(t) = \omega_0 x_0 \cos(\omega_0 t + \phi)$ (fig. 1.1b). Rep-

¹ Letter to Longomontanus, 1605, as quoted by Koestler (1959).

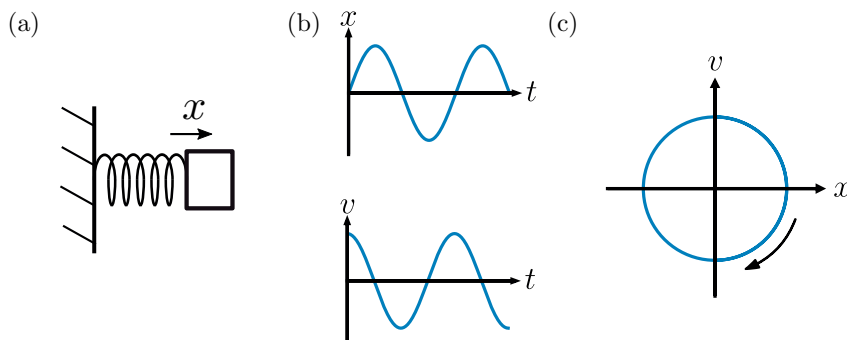


Figure 1.1: The circular motion of a harmonic oscillator. (a) Archetypical harmonic oscillator formed by a mass on a spring. (b) Periodic oscillations of the position x and velocity v of the oscillator. (c) Phase space representation of the circular trajectory on the plane formed by x and v .

resented in the phase space in fig. 1.1c, with x the horizontal axis and v the vertical one, it follows a circular trajectory at uniform speed. The periodic oscillation can be interpreted as stemming from a competition between the kinetic energy $\frac{1}{2}mv^2$ and the potential spring energy $\frac{1}{2}kx^2$, with an increase in velocity when the distance reduces and a decrease in velocity when the distance increases. Written in terms of the normalized position $q = \sqrt{k/\omega_0} x$ and momentum $p = \sqrt{m/\omega_0} v$, the total energy $E = \frac{1}{2}\omega_0(q^2 + p^2)$ describes geometrically a circle on the plane formed by q and p (with a radius of $\sqrt{2E/\omega_0}$). The quadratic form of the potential is essential to this property. It is a posteriori clear how doomed the ancient astronomers were, who wrestled unknowingly with a gravitational potential of the form $-GM/r$, failing to fit circles in the resulting motion.

The harmonic oscillator is perhaps the most fundamental object described by physics. Beyond mechanical resonators, it models the periodic changes of any degree of freedom in a quadratic potential: electromagnetic radiation bouncing back and forth in optical cavities, sound waves resonating as a note in a musical instrument, or the vibrations of fundamental quantum fields that constitute the particles of the standard model. Despite its simplicity (or perhaps because of it), the realization of an actual near-ideal harmonic oscillator is technically challenging and an engineering goal to this day.

Two practical constraints prevent the implementation of an ideal oscillator a priori: deviations from the quadratic harmonic potential and damping of the oscillations due to the environment. The former, known as anharmonicities, can be easily remedied. By reducing the oscillation amplitude,

any higher-order component of the potential beyond the quadratic eventually becomes negligible. For instance the pendulum, whose nonlinear recoil force is $F(\theta) = -mg \sin \theta$, is a harmonic oscillator for small angles θ for which the force is approximately linear, with $F(\theta) \approx -mg\theta$. In fact, the principal deviation of practical oscillators from the ideal originate from their interaction with the environment. Through friction, a pendulum loses momentum oscillation after oscillation and the amplitude of motion continuously reduces until the pendulum eventually reaches a stop. This loss of energy can be quantified and defined to occur at a rate κ called the energy dissipation rate, such that after a time Δt the energy is reduced by a factor $e^{-\kappa \Delta t}$. The quality factor $Q = \omega_0/\kappa$ is a measure of how close to the ideal the oscillator is: it counts the number of free oscillations before the energy decays to $e^{-2\pi}$ of its initial value, a number that tends to infinity for the perfect harmonic oscillator.

The last decades have seen a substantial rise in the Q factors of both mechanical and electromagnetic resonators. The natural decoupling of mechanical elements to their environment makes them technologically appealing as narrowband oscillators, with quartz oscillators ubiquitous in applications of timekeeping and MEMS devices used for narrowband filtering in telecommunication (Lam, 2008). Recently, through new techniques such as soft clamping and strain engineering, nanomechanical oscillators have been realized with Q factors of up to nearly 10^9 (Tsaturyan et al., 2017; Ghadimi et al., 2018). In parallel, tremendous progress has also been achieved in electromagnetic resonators. Optical cavities such as Fabry-Perot etalons are used as frequency references (Kruk et al., 2005) and to form lasers (Bromberg, 2008). The nonlinear medium of certain high- Q microresonators can spawn optical frequency combs of regularly spaced emission (Kippenberg, Holzwarth, and Diddams, 2011). In the microwave range, superconducting resonators formed by 3D cavities or circuits have been realized with high Q factors (Megrant et al., 2012; Bruno et al., 2015; Romanenko and Schuster, 2017). Both optical (Walther et al., 2006) and microwave (Devoret and Schoelkopf, 2013) cavities have been exploited to interact with natural and artificial atoms at the quantum level.

A single harmonic oscillator, while useful as a timekeeper or filter, predictably beats at the same frequency and lacks interesting dynamics. Two coupled oscillators however offer a much more colorful panel of associated phenomena. Cavity optomechanics (Aspelmeyer, Kippenberg, and Marquardt, 2014), or the study of interaction between a mechanical oscillator and an electromagnetic cavity, realizes a coupling between two near-ideal harmonic oscillators. Through the optomechanical interaction, mechanical

oscillators have been cooled close to their ground state (Teufel, Donner, et al., 2011), squeezed light has been produced (Purdy et al., 2013), and the mechanical motion measured by evading the backaction usually imposed by quantum mechanics (Møller et al., 2017), among many other demonstrations. It also sets fundamental limits on the sensitivity of gravitational-wave detectors (Evans et al., 2015).

The nonlinear optomechanical interaction can be linearized through parametric modulation by applying an electromagnetic driving tone to the system. The resulting linear coupling is tunable in strength and the relative frequencies of the two harmonic modes (in a rotating frame) can be varied as well. Thus, optomechanical systems are highly controllable platforms for the exploration of the fundamental properties of linearly interacting harmonic oscillators.

That constitutes the thread of Ariadne that binds together the results of this thesis. An optomechanical system allows us to explore the wealth of phenomena arising from a linear coupling between two harmonic modes. The specific implementation is a microwave optomechanical circuit (Teufel, D. Li, et al., 2011), where the electromagnetic mode is a superconducting LC resonator and the mechanical element is the vibrating top plate of the capacitor. More specifically, the possibilities of multimode optomechanical systems are explored, where two microwave modes interact with one or two mechanical modes. When considering the interplay between two given oscillators, the supplementary modes act either as intermediaries in the relation or auxiliary degrees of freedom that permit the tuning of a system parameter.

In summary, the present thesis is structured as follows. In chapter 2, a quick overview of the necessary theoretical models is attempted. In chapter 3, the main features of the experiments are exposed, including short summaries of the nanofabrication of the devices and the numerical simulation tools used. In chapter 4, the first main experimental result is presented, concerning the realization of a reservoir for a microwave cavity using an auxiliary microwave mode to engineer the dissipation of a mechanical oscillator. In chapter 5, the second result is discussed, about the possibility to construct a nonreciprocal pathway between two microwave modes with two mechanical modes serving as intermediaries. In chapter 6, the third main result is introduced: we describe theoretically the classes of interaction between two harmonic modes and demonstrate experimentally level attraction between a microwave and a mechanical mode. In chapter 7, recent progress is reported on the implementation of a new experimental tool to achieve higher quantum efficiency in measurements. In chapter 8, we finally conclude and provide an outlook for future possible extensions of the work.

Supporting data and code to the results of this thesis are available online (Bernier, 2018). This includes the files of the design of custom components fabricated for the experiment, code used to produce the figures contained in this thesis, and the measurement scripts used to acquire the experimental data.

Theoretical background

In this chapter, we present the different theoretical models that constitute the backbone of the phenomena studied in this thesis. In section 2.1, we present a theoretical background for general cavity optomechanics. In section 2.2, the notion of quantum noise as it applies to amplification and our system is developed. Finally, in section 2.3, we introduce our specific implementation of an optomechanical system using superconducting LC circuits. The aim is not to provide an exhaustive review of cavity optomechanics, but only the fundamental theoretical tools required to present the results of this thesis. We refer the reader interested in a more thorough presentation to the existing literature (Aspelmeyer, Kippenberg, and Marquardt, 2014; Bowen and G. J. Milburn, 2015).

2.1 A short review of cavity optomechanics

Here we expose rapidly the fundamental ideas of cavity optomechanics. In section 2.1.1, the optomechanical interaction is introduced, leading to the quantum optomechanical Hamiltonian in eq. (2.2). In section 2.1.2, the Langevin equation for a quantum mode (2.4) is introduced that accounts for the dissipation in the open system. In sections 2.1.3 and 2.1.4, the non-linear optomechanical interaction is linearized in the presence of a driving tone, first in the Langevin formalism, then at the level of the Hamiltonian. In section 2.1.5, the immediate consequences of the linearized optomechanical interaction are presented, in the form of a shift in the mechanical frequency

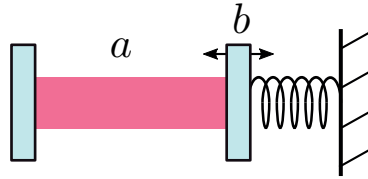


Figure 2.1: Archetypical optomechanical system. A Fabry-Perot cavity with an optical mode a has one mirror that is mounted on a spring. Its mechanical motion, the mode b , modulates the resonance frequency of mode a and in turn the light in the mode a exerts a force on the oscillator b due to radiation pressure.

and dissipation rate.

2.1.1 The optomechanical interaction

The defining feature of cavity optomechanics is a specific form for the interaction between two harmonic oscillators. Independently of the nature of the two modes, the coupling will determine the dynamics and associated phenomena, whichever system is used for its realization.

Consider two harmonic oscillators with quadratures x_1, p_1 and x_2, p_2 , and frequencies ω_1 and ω_2 . We define the optomechanical interaction as the coupling that results from the linear dependence of the frequency of the first mode on a quadrature of the second mode, such that

$$\omega_1(x_2) = \omega_{1,0} + Gx_2. \quad (2.1)$$

The coupling constant G depends on the choice of normalization for the quadrature x_2 and is in general not always clearly defined.

The archetypal example of optomechanical interaction, shown in fig. 2.1 is an optical Fabry-Perot cavity formed by two parallel mirrors, one of which is attached to a spring and constitutes a mechanical harmonic oscillator. The displacement of the mirror changes the length of the optical cavity and thus its frequency. For small enough oscillation amplitudes, the dependence in position can be linearized such that eq. (2.1) is obtained. There is however nothing requiring the first mode to be optical and the second to be mechanical in nature. Only the structure of the Hamiltonian (as well as the interaction with the environment in the form of the dissipation rate, as explained in section 2.1.5) determine the dynamics of the system.

We note that other types of optomechanical couplings have been studied as well. In particular, the quadratic optomechanical interaction $\omega_1(x_2) = \omega_{1,0} + G_2 x_2^2$ has been experimentally achieved with membrane-in-the-middle experiments (Jayich et al., 2008; Thompson et al., 2008; Sankey et al., 2010) and photonic crystals (Paraïso et al., 2015). Within this thesis, we are only concerned with the linear kind and we will always mean a coupling of the form eq. (2.1) by “optomechanical interaction”.

In the language of quantum mechanics, which we will use throughout this thesis, the two modes are described by the annihilation operators \hat{a} , \hat{b} , such that the quadratures of the two modes (now promoted to operators) take the form $x_1 \propto \hat{a} + \hat{a}^\dagger$, $p_1 \propto i(\hat{a}^\dagger - \hat{a})$, $x_2 \propto \hat{b} + \hat{b}^\dagger$, $p_2 \propto i(\hat{b}^\dagger - \hat{b})$. They obey the bosonic canonical commutation relations $[\hat{a}, \hat{a}^\dagger] = 1$ and $[\hat{b}, \hat{b}^\dagger] = 1$. In that language, the Hamiltonian for the system is expressed as

$$H = \hbar\omega_1(x_2)\hat{a}^\dagger\hat{a} + \hbar\omega_2\hat{b}^\dagger\hat{b} = \hbar\omega_{1,0}\hat{a}^\dagger\hat{a} + \hbar\omega_2\hat{b}^\dagger\hat{b} + \hbar g_0(\hat{b} + \hat{b}^\dagger)\hat{a}^\dagger\hat{a}, \quad (2.2)$$

where g_0 is called the vacuum optomechanical coupling strength and corresponds to G when the second mode quadrature has the dimensionless normalization $x_2 = \hat{b} + \hat{b}^\dagger$. We will refer to the last term of eq. (2.2) as the optomechanical coupling term.

2.1.2 The Langevin formalism

A capital aspect that is not taken into account in the Hamiltonian formalism is the interaction with the environment. This is not merely a non-ideal feature of the system implying dissipation and loss, but an essential one. One of the two modes at least must be accessible through a channel in order to transfer information to and from the system for any measurement to take place. We use the quantum Langevin formalism to account for the role of the environment, and briefly review it here. A thorough exposition can be found in the appendix E.2 of the review on quantum noise by Clerk et al. (2010).

The mode of interest, which we will denote by the annihilation operator \hat{a} , is assumed to interact with a number of bath modes, of annihilation operators \hat{c}_q , through the coupling Hamiltonian

$$H_{\text{bath}} = -i\hbar \sum_q [\lambda\hat{a}^\dagger\hat{c}_q - \lambda^*\hat{c}_q^\dagger\hat{a}], \quad (2.3)$$

with λ an (a priori complex) coupling strength. In the case of the interaction with a waveguide channel, the bath modes are standing modes of the waveguide (determined by the boundary conditions, including the cavity itself).

In the case of internal loss mechanisms, the bath modes are any external degrees of freedom coupled to the mode of interest that are not described by the model (such as power radiating away from the cavity).

The equation of motion for each bath mode is first solved exactly, and the result, that depends both on the initial conditions $\hat{c}_q(t=0)$ and on the state of the mode $\hat{a}(t)$, is inserted in the equations of motion for $\hat{a}(t)$. This results in

$$\dot{\hat{a}}(t) = -i\omega_{1,0}\hat{a}(t) - \frac{\kappa}{2}\hat{a}(t) + \sqrt{\kappa}\hat{a}_{\text{in}}(t), \quad (2.4)$$

where the dissipation rate

$$\kappa = 2\pi|\lambda|^2\rho \quad (2.5)$$

depends on the density of states by frequency unit ρ of the bath modes. The input mode is identified as the operator

$$\hat{a}_{\text{in}}(t) = \frac{1}{\sqrt{2\pi\rho}} \sum_q e^{-i\omega_q t} \hat{c}_q(0), \quad (2.6)$$

where ω_q is the resonance frequency of the mode \hat{c}_q . The input mode is a linear combination of the reservoir modes that can be interpreted as representing the incoming flux of quanta arriving at the mode \hat{a} through the channel. Note that since ρ has units of ω^{-1} , \hat{a}_{in} has units of $\sqrt{\omega}$ (such that $\hat{a}_{\text{in}}^\dagger(t)\hat{a}_{\text{in}}(t)$ gives a number of quanta per unit time). Equation (2.4) is called a quantum Langevin equation.

The procedure can be done independently for each bath. In particular for the mode \hat{a} , which we will identify as the electromagnetic one, a distinction should be made between the coupling to the waveguide used to probe the cavity, of rate κ_{ex} , and all other degrees of freedom that interact with the cavity, of rate κ_0 (representing internal losses). For the mode \hat{b} , identified with the mechanical motion, no communication exists (in our system), only losses, at a rate Γ_m . The full equations of motion, taking into account both the interaction of eq. (2.2) and the loss terms from the Langevin treatment, are

$$\dot{\hat{a}} = -(i\omega_c + \frac{\kappa}{2})\hat{a} - ig_0(\hat{b} + \hat{b}^\dagger)\hat{a} + \sqrt{\kappa_{\text{ex}}}\hat{a}_{\text{in}}(t) + \sqrt{\kappa_0}\hat{a}_0(t), \quad (2.7)$$

$$\dot{\hat{b}} = -(i\Omega_m + \frac{\Gamma_m}{2})\hat{b} - ig_0\hat{a}^\dagger\hat{a} + \sqrt{\Gamma_m}\hat{b}_0(t), \quad (2.8)$$

where $\kappa = \kappa_{\text{ex}} + \kappa_0$ and we use the new notation $\omega_c = \omega_{1,0}$ and $\Omega_m = \omega_2$.

Two assumptions used in the derivation of the Langevin equation eq. (2.4) are worth mentioning. First, a major assumption is that the reservoir modes can be approximated by an infinite continuum of modes. This is required

for the reservoir to be Markovian in the sense that it instantly forgets all information about the mode \hat{a} . If only a finite number of modes existed, the information dissipated from \hat{a} would bounce between them and eventually be fed back into \hat{a} . Then the past state of the mode could affect its current state. In a realistic system, the bath modes (although maybe not infinite) are themselves interacting with many other degrees of freedom such that all information about \hat{a} is diluted and lost, making in practice the continuum of modes a valid hypothesis.

A second assumption is that all reservoir modes are coupled to the mode \hat{a} with the same coupling strength λ . This can be justified in a self-consistent manner. There might be differences between the bath modes, such that the coupling strength λ_q effectively has a dependence on the frequency ω . However, we find retrospectively that the mode \hat{a} is only sensitive to perturbation in a finite bandwidth κ . The assumption is then only that the mode bandwidth κ (itself due to interaction with the reservoir) is narrow compared to any variation as a function of frequency of the coupling to the bath modes.

Finally, the quantum Langevin equation eq. (2.4) can be understood as an example of the fluctuation-dissipation theorem (Callen and Welton, 1951). Interacting with its reservoir, the mode \hat{a} is damped. This cannot happen without fluctuations from the modes of the reservoir in turn driving the system through the input mode $\hat{a}_{\text{in}}(t)$. As we will show in section 2.2.2, the fluctuations have an effective temperature to which the mode \hat{a} will equilibrate.

2.1.3 Linearization in the Langevin picture

The optomechanical interaction (eq. (2.2)) is a nonlinear three-wave-mixing coupling that is rather weak for most systems. The coupling strength g_0 is usually much smaller than most other rates in the system (except Γ_{m} typically). In order to effectively amplify this interaction, an electromagnetic drive is applied to the cavity \hat{a} . We outline here how this drive linearizes the coupling with a much increased coupling strength.

Through the input channel of mode \hat{a} is introduced a driving tone at the frequency ω_{d} . The input operator can be decomposed as

$$\hat{a}_{\text{in}}(t) = \sqrt{n_{\text{in}}}e^{-i\phi}e^{-i\omega_{\text{d}}t} + \delta\hat{a}_{\text{in}}(t), \quad (2.9)$$

where the first term represent a classical flux of n_{in} quanta per unit time and the second term $\delta\hat{a}$ contains the leftover quantum fluctuations. The phase ϕ of the coherent field is left arbitrary. No approximation is made in eq. (2.9);

the creation operator is just displaced by a term proportional to the identity operator.

The coherent drive induces coherent oscillations in \hat{a} and the resulting field intensity displaces the equilibrium position of the mechanical oscillator with a radiation-pressure force. The operators for the two modes can be rewritten with the ansatz solutions

$$\hat{a} = \sqrt{\bar{n}_c} e^{-i\omega_d t} + \delta\hat{a}, \quad (2.10)$$

$$\hat{b} = b_{\text{shift}} + \delta\hat{b}, \quad (2.11)$$

where \bar{n}_c is the squared amplitude of coherent oscillations of the cavity field due to the drive (in units of quanta) and b_{shift} is the new rest position of the mechanical mode.

We insert eqs. (2.10) and (2.11) in the Langevin eqs. (2.7) and (2.8) and solve order by order in the powers of the quantum fluctuations $\delta\hat{a}$, $\delta\hat{b}$.

At zeroth order, the purely classical response of the system to the drive gives

$$-i\omega_d \sqrt{\bar{n}_c} = -\left(i\omega_c + \frac{\kappa}{2}\right) \sqrt{\bar{n}_c} - ig_0 (b_{\text{shift}} + b_{\text{shift}}^*) \sqrt{\bar{n}_c} + \sqrt{\kappa_{\text{ex}}} \sqrt{n_{\text{in}}} e^{-i\phi}, \quad (2.12)$$

$$0 = -\left(i\Omega_m + \frac{\Gamma_m}{2}\right) b_{\text{shift}} - ig_0 \bar{n}_c \quad (2.13)$$

The coupling term in eq. (2.12) makes the equation nonlinear and in general complicated to solve. It can however usually be neglected, since the field amplitude is small, such that $\bar{n}_c g_0^2 / \sqrt{\Omega_m^2 + \Gamma_m^2/4} \ll \sqrt{(\omega_d - \omega_c)^2 + \kappa^2/4}$. In that case, the equations are solved by

$$\sqrt{\bar{n}_c} = \frac{\sqrt{\kappa_{\text{ex}}} e^{-i\phi} \sqrt{n_{\text{in}}}}{-i(\omega_d - \omega_c) + \kappa/2}, \quad (2.14)$$

$$b_{\text{shift}} = \frac{-ig_0 \bar{n}_c}{i\Omega_m + \Gamma_m/2}. \quad (2.15)$$

Note that taking the nonlinearity of the equations into account results only in a small renormalization of those results, except for very large amplitudes, for which it is possible that the system has multiple stable solutions (Marquardt, Harris, and Girvin, 2006). For convenience of notation, we can assume ϕ such that \bar{n}_c is real, as a shift in the phase is simply equivalent to a change in the origin of time.

At the first order in $\delta\hat{a}$, $\delta\hat{b}$, the linear equations of motion for the fields are

$$\dot{\delta\hat{a}} = -\left(i\omega_c' + \frac{\kappa}{2}\right)\delta\hat{a} - ig_0\sqrt{\bar{n}_c}e^{-i\omega_a t}(\delta\hat{b} + \delta\hat{b}^\dagger) + \sqrt{\kappa_{\text{ex}}}\delta\hat{a}_{\text{in}} + \sqrt{\kappa_0}\hat{a}_0, \quad (2.16)$$

$$\dot{\delta\hat{b}} = -\left(i\Omega_m + \frac{\Gamma_m}{2}\right)\delta\hat{b} - ig_0\sqrt{\bar{n}_c}(e^{-i\omega_a t}\delta\hat{a}^\dagger + e^{i\omega_a t}\delta\hat{a}) + \sqrt{\Gamma_m}\hat{b}_0. \quad (2.17)$$

The static displacement of the mechanical oscillator results in a small shift in the cavity resonance frequency $\omega_c' = \omega_c + g_0(b_{\text{shift}} + b_{\text{shift}}^*)$.

We arrive at the first important approximation, which is to neglect higher-order terms in $\delta\hat{a}$, $\delta\hat{b}$ and only consider the linear equations of motion. This is justified when the coherent amplitude \bar{n}_c is large and dominates over any other signals in $\delta\hat{a}$, whether quantum fluctuations or any other classical signal or noise.

The time-dependence of eqs. (2.16) and (2.17) is removed by going to a rotating frame. A change of variable is done for the cavity $\delta\hat{a}$, with the new operators given by $\delta\hat{a}' = \delta\hat{a}e^{i\omega_a t}$, $\delta\hat{a}'_{\text{in}} = \delta\hat{a}_{\text{in}}e^{i\omega_a t}$, $\hat{a}'_0 = \hat{a}_0e^{i\omega_a t}$. The new equations of motion become (removing an overall factor $e^{-i\omega_a t}$ from the first equation)

$$\dot{\delta\hat{a}'} = \left(i\Delta - \frac{\kappa}{2}\right)\delta\hat{a}' - ig(\delta\hat{b} + \delta\hat{b}^\dagger) + \sqrt{\kappa_{\text{ex}}}\delta\hat{a}'_{\text{in}} + \sqrt{\kappa_0}\hat{a}'_0, \quad (2.18)$$

$$\dot{\delta\hat{b}} = -\left(i\Omega_m + \frac{\Gamma_m}{2}\right)\delta\hat{b} - ig(\delta\hat{a}'^\dagger + \delta\hat{a}') + \sqrt{\Gamma_m}\hat{b}_0. \quad (2.19)$$

We have defined the detuning $\Delta = \omega_d - \omega_c'$ and the linear field-enhanced optomechanical coupling strength $g = g_0\sqrt{\bar{n}_c}$.

The equations eqs. (2.18) and (2.19) involve both creation and annihilation operators. They belong to a set of 4 linear equations, including the equations of motion for $\delta\hat{a}'^\dagger$, $\delta\hat{b}^\dagger$. Together, they can be solved by inverting a matrix to obtain the response of the system $\delta\hat{a}'$, $\delta\hat{b}$ for a certain input $\delta\hat{a}'_{\text{in}}$, \hat{a}'_0 , \hat{b}_0 . Under certain conditions, a rotating-wave approximation (RWA) can be made to keep only two equations. The detailed conditions for the RWA are discussed in appendix A, and we discuss only briefly the approximation in the following. If a red detuning $\Delta < 0$ is chosen such that the effective frequency of the cavity $\delta\hat{a}'$ in the rotating frame is close to the mechanical frequency ($\Delta \approx -\Omega_m$), the free oscillations of the two modes (when $g = 0$) are at a similar frequency with $\delta\hat{a}'(t) = e^{i\Delta t}\delta\hat{a}'(0)$, $\delta\hat{b}(t) = e^{-i\Omega_m t}\delta\hat{b}$. For small enough coupling strengths g , the frequencies will not be modified. As a result, the term of eq. (2.18) in $\delta\hat{b}^\dagger$ and the one in eq. (2.19) in $\delta\hat{a}'^\dagger$ are counter-rotating, with a relative frequency of $2\Omega_m$ with respect to the other terms. They can be neglected, since they oscillate very fast and cancel out on average. In

the related case of a blue detuning, with $\Delta \approx \Omega_m$, the opposite terms can be neglected such that $\delta\hat{a}'$ couples only to $\delta\hat{b}^\dagger$. In that case, the cavity $\delta\hat{a}'$ effectively has a negative frequency in the rotating frame, as it oscillates at a slower rate compared with the drive frequency ω_d in the laboratory frame. The effective negative frequency is key for the phenomenon of level attraction discussed in section 6.3.

2.1.4 Linearization in the Hamiltonian picture

Alternatively, it is instructive to study the linearization of the optomechanical coupling at the level of the Hamiltonian. The ansatz solutions of eqs. (2.10) and (2.11) are inserted in the Hamiltonian eq. (2.2), which can then be expanded in powers of $\delta\hat{a}$, $\delta\hat{b}$, order by order.

At zeroth order, there is a constant shift in energy, with no influence on the dynamics, that can be ignored. At first order, we get the expression

$$H_{1st} = \hbar\omega_c(\sqrt{\bar{n}_c}e^{-i\omega_d t}\delta\hat{a}^\dagger + \sqrt{\bar{n}_c}e^{i\omega_d t}\delta\hat{a}) + \hbar\Omega_m(b_{\text{shift}}^*\delta\hat{b} + b_{\text{shift}}\delta\hat{b}^\dagger) + \hbar g_0\bar{n}_c(\delta\hat{b} + \delta\hat{b}^\dagger) + \hbar g_0(b_{\text{shift}} + b_{\text{shift}}^*)(\sqrt{\bar{n}_c}e^{-i\omega_d t}\delta\hat{a}^\dagger + \sqrt{\bar{n}_c}e^{i\omega_d t}\delta\hat{a}). \quad (2.20)$$

The equations of motion deriving from eq. (2.20) result in eqs. (2.12) and (2.13) when the dissipation and input terms are added. Their solution are the mean-field responses for $\sqrt{\bar{n}_c}$ and b_{shift} introduced above.

At second order, we find a time-dependent bilinear coupling with

$$H_{2nd} = \hbar\omega_c'\delta\hat{a}^\dagger\delta\hat{a} + \hbar\Omega_m\delta\hat{b}^\dagger\delta\hat{b} + \hbar g(\delta\hat{b} + \delta\hat{b}^\dagger)(e^{-i\omega_d t}\delta\hat{a}^\dagger + e^{i\omega_d t}\delta\hat{a}). \quad (2.21)$$

Once again, as a first approximation we neglect higher-order terms. This Hamiltonian can be made time-independent by rotating the reference frame, using the interaction picture with respect to the reference Hamiltonian $H_0 = \hbar\omega_d\delta\hat{a}^\dagger\delta\hat{a}$. All operators \hat{O} then evolve as $\hat{O}_I(t) = e^{iH_0 t/\hbar}\hat{O}(0)e^{-iH_0 t/\hbar}$ with the effective Hamiltonian $H_I = e^{iH_0 t/\hbar}(H - H_0)e^{-iH_0 t/\hbar}$, here given by

$$H_{2nd,I} = -\hbar\Delta\delta\hat{a}^\dagger\delta\hat{a} + \hbar\Omega_m\delta\hat{b}^\dagger\delta\hat{b} + \hbar g(\delta\hat{b} + \delta\hat{b}^\dagger)(\delta\hat{a} + \delta\hat{a}^\dagger). \quad (2.22)$$

The RWA here consists in neglecting terms that do not conserve the number of excitations resulting in

$$H_{2nd,I} \approx -\hbar\Delta\delta\hat{a}^\dagger\delta\hat{a} + \hbar\Omega_m\delta\hat{b}^\dagger\delta\hat{b} + \hbar g(\delta\hat{a}\delta\hat{b}^\dagger + \delta\hat{a}^\dagger\delta\hat{b}), \quad \text{for } \Delta \approx -\Omega_m, \quad (2.23)$$

$$H_{2nd,I} \approx -\hbar\Delta\delta\hat{a}^\dagger\delta\hat{a} + \hbar\Omega_m\delta\hat{b}^\dagger\delta\hat{b} + \hbar g(\delta\hat{a}\delta\hat{b} + \delta\hat{a}^\dagger\delta\hat{b}^\dagger), \quad \text{for } \Delta \approx \Omega_m. \quad (2.24)$$

The conditions of validity of the RWA are derived in details in appendix A and are $\kappa \ll 4\Omega_m$, $|\Delta - \Omega_m| \ll 2\Omega_m$, and $g \ll 2\Omega_m$.

The linearized optomechanical interaction is an example of parametric interaction (Mumford, 1960; Bertet, Harmans, and Mooij, 2006; Tian, Allman, and Simmonds, 2008), where a parameter of the system is modulated externally in a way that affects two subsystems and thus couple them together. In this case, the electromagnetic drive modulates the cavity field. This affects the mechanical mode, as the field intensity applies a force to the oscillator, and the cavity as well, since a mechanical displacement changes the cavity resonance frequency. The pump tone effectively linearizes the coupling by bridging the gap in frequency between the electromagnetic and mechanical harmonic modes.

The linearized system offers an ideal playground to study the interaction between two harmonic oscillators. Their linear coupling strength can be adjusted by varying the intensity of the driving field. The effective relative frequency of the modes (in the rotating picture) can also be tuned, with the pump detuning. Even effectively negative frequencies can be achieved for one of the oscillator. Overall, almost all the parameters in the Hamiltonian for linearly coupled harmonic oscillators can be tuned experimentally and chosen at will. In the Langevin picture, the interaction with the environment and the dissipation rates appear fixed to their original values. As detailed in the following section 2.1.5, the linear coupling in fact results in a change of the effective dissipation rate for one of the two modes. Generalizing this notion, a significant result of this thesis, detailed in chapter 4, is an experimental technique to independently tune the dissipation rate of one of the two oscillator in an independent way. Thus we gain control over almost all the parameters that determine the dynamics of this two-mode system and can study the interaction of the two modes in all possible regimes, as explained in chapter 6.

2.1.5 Optomechanical damping and amplification

The linearized Hamiltonian eq. (2.22) is symmetric for the modes $\delta\hat{a}$ and $\delta\hat{b}$. The drive tone even bridges the frequencies such that the two modes, with frequency scales orders of magnitude apart in the laboratory frame, have similar frequencies in the rotating frame Hamiltonian. It is therefore natural to expect a symmetric effect for both modes. That is not the case however. The dissipation rates κ and Γ_m enforce a strong hierarchy of time scales, with $\kappa \gg \Gamma_m$ for most systems (since the electromagnetic mode frequency is usually much greater than the mechanical one). The way that the mechanical and electromagnetic modes are affected by the coupling is therefore quite different. The cavity mode can be interpreted as constituting a reservoir

mode for the mechanical oscillator, altering the effective dissipation rate and resonance frequency of the latter. In chapter 4, we will see how those two roles can be reversed.

We first consider the linearized interaction in the Langevin picture of eqs. (2.18) and (2.19), for a detuning nearly resonant with the red mechanical sideband $\Delta \approx -\Omega_m$. We consider how the response of the modes to their inputs $\delta\hat{a}_{\text{in}}$ and \hat{b}_0 is affected by the interaction. To solve the equations of motion, which are invariant under time translations, we use the Fourier transform, defined as

$$\hat{O}[\omega] = \int_{-\infty}^{+\infty} dt e^{i\omega t} \hat{O}(t). \quad (2.25)$$

In section 2.2, where we define the power spectra of the input and output modes, the use of the Fourier transform is made more precise. Here, the definition above is sufficient to study the response of the modes as a function of frequency.

Note that since we consider the mode $\delta\hat{a}$ in the rotating frame, the frequency ω is the relative frequency with respect to the pump frequency ω_d when considering the cavity mode $\delta\hat{a}$. For the mechanical mode, ω is the real frequency in the laboratory frame. The frequencies are bridged by the drive field, that upconverts the mechanical signal to electromagnetic frequencies and downconverts electromagnetic signals to mechanical frequencies. This means that from the point of view of the mechanical mode, there is a copy of the cavity mode with which it interacts at a nearby frequency, and reciprocally the cavity mode sees a copy of the mechanical mode as well.

In Fourier frequency and using the RWA in the case $\Delta \approx -\Omega_m$, we rewrite eqs. (2.18) and (2.19) as

$$\left(-i(\omega + \Delta) + \frac{\kappa}{2}\right) \delta\hat{a}[\omega] = -ig\delta\hat{b}[\omega] + \sqrt{\kappa_{\text{ex}}}\delta\hat{a}_{\text{in}}[\omega], \quad (2.26)$$

$$\left(-i(\omega - \Omega_m) + \frac{\Gamma_m}{2}\right) \delta\hat{b}[\omega] = -ig\delta\hat{a}[\omega] + \sqrt{\Gamma_m}\delta\hat{b}_0[\omega], \quad (2.27)$$

where the electromagnetic input noise \hat{a}_0 is neglected. In the absence of an optomechanical coupling g , the two modes have the responses

$$\delta\hat{a}[\omega] = \frac{\sqrt{\kappa_{\text{ex}}}}{-i(\omega + \Delta) + \kappa/2} \delta\hat{a}_{\text{in}}[\omega] = \chi_c[\omega] \delta\hat{a}_{\text{in}}[\omega], \quad (2.28)$$

$$\delta\hat{b}[\omega] = \frac{\sqrt{\Gamma_m}}{-i(\omega - \Omega_m) + \Gamma_m/2} \delta\hat{b}_0[\omega] = \chi_m[\omega] \delta\hat{b}_0[\omega] \quad (2.29)$$

to the external perturbation $\delta\hat{a}_{\text{in}}[\omega]$ and $\hat{b}_0[\omega]$, where we have defined the respective susceptibilities χ_c and χ_m for each mode. In amplitude, the susceptibilities $|\chi_c|^2$, $|\chi_m|^2$ correspond to Lorentzians of respective widths κ and Γ_m . Since in general $\kappa \gg \Gamma_m$, the mechanical mode is sensitive to stimuli in a much narrower bandwidth than the electromagnetic mode. In comparison, the cavity response looks flat in frequency from the point of view of the mechanical oscillator and equivalent to a continuum of bath modes.

To see the change in the mechanical response due to the optomechanical interaction, we solve eq. (2.26) with respect to $\delta\hat{a}[\omega]$ (neglecting the input $\delta\hat{a}_{\text{in}}[\omega]$) and insert it in eq. (2.27) to obtain

$$\left(-i(\omega - \Omega_m) + \frac{\Gamma_m}{2} + \frac{g^2}{-i(\omega + \Delta) + \kappa/2} \right) \delta\hat{b}[\omega] = \sqrt{\Gamma_m} \hat{b}_0[\omega]. \quad (2.30)$$

The supplementary third term in the parentheses is proportional the cavity susceptibility and varies very slowly compared to the bare mechanical response. It can be approximated by its value at the mechanical resonance $\omega = \Omega_m$. The modified mechanical response becomes

$$\delta\hat{b}[\omega] = \frac{\sqrt{\Gamma_m}}{-i(\omega - \Omega_m') + \Gamma_{\text{eff}}/2} \hat{b}_0[\omega] \quad (2.31)$$

with a modified frequency $\Omega_m' = \Omega_m + \text{Im}(g^2/(-i(\Omega_m + \Delta) + \kappa/2))$ and a modified effective dissipation rate $\Gamma_{\text{eff}} = \Gamma_m + \text{Re}(2g^2/(-i(\Omega_m + \Delta) + \kappa/2))$. The first effect is called the optical spring effect and is an effective modification of the mechanical spring constant due to the optomechanical coupling. The second effect is the optomechanical damping. The effective dissipation rate is always increased with respect to the bare rate when $\Delta \approx -\Omega_m$. The cavity acts as a supplementary reservoir that damps the mechanical motion. On resonance $\Delta = -\Omega_m$, the expression becomes

$$\Gamma_{\text{eff}} = \Gamma_m + 4g^2/\kappa = \Gamma_m(1 + \mathcal{C}) \quad (2.32)$$

where we have defined the optomechanical cooperativity as $\mathcal{C} = 4g^2/(\kappa\Gamma_m)$.

Since the frequency of the cavity is much larger than the mechanical frequency, its thermal occupancy in terms of quanta is much lower (as explained in section 2.2). As a result, the mechanical mode sees two thermal baths at two very different effective temperatures and settles to some average of the two, in this case to a lower temperature than in the absence of the optomechanical coupling. If the mechanical oscillator is initially at thermal equilibrium, with an occupancy given by the Bose-Einstein statistics

$$\bar{n}_{\text{m,th}} = \frac{1}{e^{\hbar\Omega_m/k_B T} - 1}, \quad (2.33)$$

in sideband cooling it reduces to (Aspelmeyer, Kippenberg, and Marquardt, 2014, section VII.A)

$$\bar{n}_m = \frac{\Gamma_{\text{om}} n_{\text{min}} + \Gamma_m \bar{n}_{m,\text{th}}}{\Gamma_m + \Gamma_{\text{om}}} \quad (2.34)$$

where $\Gamma_{\text{om}} = \mathcal{C}\Gamma_m$ and n_{min} represents the lowest achievable mechanical occupancy. This is why driving an optomechanical with a tone detuned close to the red mechanical sideband ($\Delta \approx -\Omega_m$) is referred to as the sideband cooling of the mechanical oscillator. In section 3.6.1, we demonstrate such a measurement.

Similarly, we can compute the effect of the mechanical mode for the cavity response. We find

$$\left(-i(\omega + \Delta) + \frac{\kappa}{2} + \frac{g^2}{-i(\omega - \Omega_m) + \Gamma_m/2} \right) \delta\hat{a}[\omega] = \sqrt{\kappa_{\text{ex}}}\delta\hat{a}_{\text{in}}[\omega]. \quad (2.35)$$

Here the supplementary term is fast compared to the bare cavity response. It acts as a resonance within the resonance. The phenomenon is named optomechanically induced transparency (OMIT) or absorption (OMIA), depending whether it locally increases or decreases the amplitude response of the cavity mode.

The procedure can be repeated for a blue-detuned pump, with $\Delta \approx \Omega_m$. In that case, the equations of motion in Fourier frequency can be written as¹

$$\left(-i(\omega - \Delta) + \frac{\kappa}{2} \right) \delta\hat{a}^\dagger[\omega] = ig\delta\hat{b}[\omega] + \sqrt{\kappa_{\text{ex}}}\delta\hat{a}_{\text{in}}^\dagger[\omega], \quad (2.36)$$

$$\left(-i(\omega - \Omega_m) + \frac{\Gamma_m}{2} \right) \delta\hat{b}[\omega] = -ig\delta\hat{a}^\dagger[\omega] + \sqrt{\Gamma_m}\hat{b}_0[\omega]. \quad (2.37)$$

Here $\delta\hat{a}$ has a negative frequency and $\delta\hat{b}$ couples to $\delta\hat{a}^\dagger$. Because of the sign change in the coupling term, the mechanical response is now

$$\left(-i(\omega - \Omega_m) + \frac{\Gamma_m}{2} - \frac{g^2}{-i(\omega - \Delta) + \kappa/2} \right) \delta\hat{b}[\omega] = \sqrt{\Gamma_m}\hat{b}_0[\omega]. \quad (2.38)$$

The optical spring effect is $\Omega_m' - \Omega_m = -\text{Im}\{g^2/(-i(\Omega_m - \Delta) + \kappa/2)\}$. More importantly, the optomechanical damping becomes negative (or anti-damping) with $\Gamma_{\text{eff}} - \Gamma_m = -\text{Re}\{2g^2/(-i(\Omega_m - \Delta) + \kappa/2)\}$. The effective dissipation rate is reduced, corresponding to amplification of the mechanical

¹ Note the notation subtlety between $\delta\hat{a}^\dagger[\omega] = \int dt e^{i\omega t}\delta\hat{a}^\dagger(t)$ and $[\delta\hat{a}[\omega]]^\dagger = \int dt e^{-i\omega t}\delta\hat{a}^\dagger(t) = \delta\hat{a}^\dagger[-\omega]$.

mode by the cavity. For a critical coupling strength, the mechanical linewidth reaches $\Gamma_{\text{eff}} = 0$. This is called the optomechanical parametric instability. Mechanical oscillations are no longer damped and grow until they are stopped by higher-order nonlinear terms.

2.2 Quantum noise and amplification

The issue of quantum noise, or how to characterize power spectra according to quantum mechanics, is central to our study of an optomechanical system. Since in most cases only linear coupling terms dominate, the system is linear and the equations of motion (2.18) and (2.19) do not differ between the classical and quantum cases. The only quantum characteristics are due to the nature of the noise coming from the input operators $\delta\hat{a}_{\text{in}}$, \hat{a}_0 and \hat{b}_0 . Only when they have quantum attributes, such as limitations due to the vacuum fluctuations or quantum squeezed quadratures, can the state of the optomechanical system not be described classically.

We provide here an overview of the indispensable notions of quantum noise required to understand the results of this thesis. The much more thorough review by Clerk et al. (2010) might be useful for the reader to dig deeper in the subject, and was used as the main reference. In particular, their appendix E analyzes quantum noise for the Langevin equations for a harmonic mode.

First, in section 2.2.1, we elaborate on the quantum properties of the input mode defined in section 2.1.3 and introduce the output mode. In section 2.2.2, the capital notion of spectral densities is introduced, for both classical and quantum signals, using the Wiener-Khinchin theorem. Finally, in section 2.2.3, the linear amplifier is exposed and its quantum limits discussed.

2.2.1 Input and output modes

We recall the definition of the input mode in eq. (2.6) from the treatment of the Langevin equation for a general mode \hat{a} of section 2.1.2,

$$\hat{a}_{\text{in}}(t) = \frac{1}{\sqrt{2\pi\rho}} \sum_q e^{-i\omega_q t} \hat{c}_q(0). \quad (2.39)$$

Note that the density of states in frequency ρ allows the switch from discrete modes to a continuum with $\sum_q \dots \rightarrow \int \rho \dots d\omega$, for the Markovian approximation taken in the following. Similarly, an output operator can be defined

as

$$\hat{a}_{\text{out}}(t) = \frac{1}{\sqrt{2\pi\rho}} \sum_q e^{-i\omega_q(t-t_1)} \hat{c}_q(t_1) \quad (2.40)$$

where t_1 is a time long compared to all the timescales in the system. The operator \hat{a}_{out} represents the field in the waveguide travelling away from the mode after interacting with it. It can be shown that the fields obey the input-output relation (Gardiner and Collett, 1985)

$$\hat{a}_{\text{out}}(t) = \hat{a}_{\text{in}}(t) - \sqrt{\kappa_{\text{ex}}}\hat{a}(t). \quad (2.41)$$

This relation can also be obtained independently from the Langevin treatment, through considerations of power conservation and time-reversal symmetry (Haus, 1983, Chapter 7).

The operators \hat{a}_{in} and \hat{a}_{out} represent travelling modes and as such differ from standard harmonic-oscillators operators. While the reservoir modes \hat{c}_q obey the canonical commutation relations

$$\left[\hat{c}_q, \hat{c}_{q'}^\dagger \right] = \delta_{q,q'} \text{ and } \left[\hat{c}_q, \hat{c}_{q'} \right] = 0, \quad (2.42)$$

the travelling mode operators obey the different commutation relations

$$\left[\hat{a}_{\text{in}}(t), \hat{a}_{\text{in}}^\dagger(t') \right] = \delta(t-t'), \quad (2.43)$$

$$\left[\hat{a}_{\text{out}}(t), \hat{a}_{\text{out}}^\dagger(t') \right] = \delta(t-t'). \quad (2.44)$$

They represent fluxes of quanta and have units of rates. Thanks to the Markovian approximation of a continuum of bath modes, they have no memory and commute for different times. The quantum noise has a vanishingly short correlation time and, as we will see next in section 2.2.2, a white spectrum as a result.

We now want to study the noise characteristics of the travelling field for a given thermal occupancy of the reservoir modes. In the case of the electromagnetic cavity, the driving field is subtracted from the input mode to only consider the spectrum due to the bath $\delta\hat{a}_{\text{in}}$. If the reservoir modes are in thermal equilibrium at temperature T , they have the average number of quanta

$$\langle \hat{c}_q^\dagger(0) \hat{c}_q(0) \rangle = \bar{n}_{\text{th}} = \frac{1}{e^{\hbar\omega_q/k_{\text{B}}T} - 1} \quad (2.45)$$

that obeys Bose-Einstein statistics. The corresponding thermal ‘‘occupancy’’ for the travelling input mode is

$$\langle \delta\hat{a}_{\text{in}}^\dagger(t) \delta\hat{a}_{\text{in}}(t') \rangle = \bar{n}_{\text{th}}\delta(t-t'), \quad (2.46)$$

$$\langle \delta\hat{a}_{\text{in}}(t) \delta\hat{a}_{\text{in}}^\dagger(t') \rangle = (\bar{n}_{\text{th}} + 1)\delta(t-t'). \quad (2.47)$$

The input operators \hat{a}_0 and \hat{b}_0 have spectra of an effective noise temperature as well and obey similar expressions.

The conditions for the Markovian approximation that implies vanishing correlation time and a white noise spectrum for the input travelling modes are not very stringent. The modes \hat{a} and \hat{b} are only sensitive to noise in the narrow bandwidth corresponding to their dissipation rates. Even when the input modes cannot be said to be in thermal equilibrium and emit colored noise, an effective noise temperature can still be defined at the resonance frequency. The only requirement is for the noise to be “flat enough” at the scale of the mode linewidth.

The Markovian approximation and the continuum of modes imply that the instantaneous rate of photos $\langle \delta \hat{a}_{\text{in}}^\dagger(t) \delta \hat{a}_{\text{in}}(t) \rangle = \delta(0)$ formally diverges. All white noises have this property; since they have constant power for all frequencies, that implies an infinite power overall through a type of ultraviolet catastrophe. Some kind of regularization with a cutoff frequency must be done in order to deal with the infinity. One can assume that the infinitely narrow correlation functions (2.46), (2.47) are only an approximation. In practice, the correlation time just has to be narrow compared to the bandwidth of the detector. The real instantaneous power has a finite value.

2.2.2 The Wiener-Khinchin theorem and the spectral density

An indispensable quantity in the study of random signals, whether classical or quantum, is that of the spectral density. It is a measure of the “intensity” (or power) of the signal at a given frequency ω . The Wiener-Khinchin theorem allows its definition purely in terms of the auto-correlation function of the signal. This circumvents all issues of convergence that arise for Fourier transforms of infinite-time functions and gives a tidy prescription of how to compute spectral densities in practice.

We want to define the spectral density for the random signal $V(t)$, assumed to be stationary and to have zero average ($\langle V(t) \rangle = 0$) (Clerk et al., 2010, Appendix A). With this aim, we define the windowed Fourier transform

$$V_T[\omega] = \frac{1}{\sqrt{T}} \int_{-T/2}^{T/2} dt e^{i\omega t} V(t). \quad (2.48)$$

The spectral density is then defined as

$$\mathcal{S}_{VV}[\omega] = \lim_{T \rightarrow \infty} \langle |V_T[\omega]|^2 \rangle \quad (2.49)$$

where the average is taken over the ensemble of the random process. The normalization by $1/\sqrt{T}$ is important for convergence. Since the signal $V(t)$ has in general non-zero fluctuations for an infinite time (as it is stationary), it in effect contains infinite “energy” and its Fourier transform is not necessarily well-defined. The only assumption here is for $V(t)$ to have a finite correlation time τ . Then the integral in eq. (2.48) can be roughly split in segments of τ that each gives an independent random variable. For a stationary process, the result is a sum of $\sim T/\tau$ identical uncorrelated random variables. By the central limit theorem, the variance of the sum scales with $\sqrt{T/\tau}$. The normalization then ensures that $\langle |V_T[\omega]|^2 \rangle$ converges to a finite value for $T \rightarrow \infty$.

By construction, the power spectral density is designed such that it gives the average “power” P in the signal, when integrated over all frequencies

$$P = \int_{-\infty}^{\infty} \mathcal{S}_{VV}[\omega] \frac{d\omega}{2\pi} \quad (2.50)$$

with P defined by

$$P = \lim_{T \rightarrow \infty} \frac{1}{T} \int_{-T/2}^{T/2} dt |V(t)|^2. \quad (2.51)$$

The normalization of the Fourier transform means that the spectral density can be interpreted as a density in frequency f rather than in pulsation ω . For a constant spectral density \mathcal{S}_{VV} , the power in a bandwidth B (in frequency units) is given by $\mathcal{S}_{VV}B$. Note also that the spectral density is defined for positive and negative frequencies. In certain contexts and depending on the convention, a factor 2 must be used to sum over positive and negative frequencies in a certain bandwidth (the so-called one-sided spectral density).

The Wiener-Khinchin theorem states that the spectral density corresponds to the Fourier transform of the correlation function, as

$$\mathcal{S}_{VV}[\omega] = \int_{-\infty}^{\infty} dt e^{i\omega t} \langle V(t)V(0) \rangle. \quad (2.52)$$

Note that since the process is stationary, its correlation function is independent of time: $\langle V(t)V(0) \rangle = \langle V(t_0+t)V(t_0) \rangle \forall t_0$. In fact, for all intents and purposes, the Wiener-Khinchin result of eq. (2.52) can be taken as the definition of the spectral density for $V(t)$. As an added advantage compared to the more physical definition of eq. (2.49), the convergence of the regular Fourier transform is guaranteed if $V(t)$ has a finite correlation time and $\langle V(t)V(0) \rangle$ decays sufficiently fast for large t . For practical purposes, a supplementary benefit is that the signal needs only to be recorded for a time comparable

to the correlation time τ , even if in reality the signal is recorded for much longer in order to use a time average to approximate the ensemble average.

While $V(t)$ is classical, we have assumed very little in our definitions. The only difference between the classical and the quantum cases is that when $\hat{V}(t)$ is promoted to a quantum operator, it might no longer commute with itself when evaluated at different times. For a classical signal, $\langle V(t)V(0) \rangle = \langle V(0)V(t) \rangle = \langle V(-t)V(0) \rangle$ implies that the spectral density is symmetric in frequency, with $\mathcal{S}_{VV}^{\text{cl}}[\omega] = \mathcal{S}_{VV}^{\text{cl}}[-\omega]$. This does not have to be the case in the quantum world.

In general, for a non-Hermitian operator \hat{A} , the spectral density can be defined as

$$\mathcal{S}_{\hat{A}^\dagger \hat{A}}[\omega] = \int_{-\infty}^{\infty} dt e^{i\omega t} \langle \hat{A}^\dagger(t) \hat{A}(0) \rangle. \quad (2.53)$$

A symmetrized spectral density, that mimics the classical case can be defined as

$$\bar{\mathcal{S}}_{\hat{A}^\dagger \hat{A}}[\omega] = \frac{1}{2} \int_{-\infty}^{\infty} dt e^{i\omega t} \left(\langle \hat{A}^\dagger(t) \hat{A}(0) \rangle + \langle \hat{A}(0) \hat{A}^\dagger(t) \rangle \right). \quad (2.54)$$

In what exact sense it resembles the classical case is not evident in the case of non-Hermitian operator, where the definition does not in fact guarantee a symmetric spectral density $\bar{\mathcal{S}}_{\hat{A}^\dagger \hat{A}}[\omega] = \bar{\mathcal{S}}_{\hat{A}^\dagger \hat{A}}[-\omega]$ in general. For the symmetrized spectral density to be symmetric in frequency, the correlation function should be even with $\langle \hat{A}^\dagger(t) \hat{A}(0) \rangle = \langle \hat{A}^\dagger(-t) \hat{A}(0) \rangle$, in which case the unsymmetrized spectral density function $\mathcal{S}_{\hat{A}^\dagger \hat{A}}[\omega]$ is symmetric as well. As emphasized in appendix B where the case of heterodyne detection is detailed, the details of the quantum measurement must be taken into account in order to use the correct definition of the quantum spectral density.

For the travelling-wave signal $\delta \hat{a}_{\text{in}}(t)$, with correlation functions given in eqs. (2.46) and (2.47), the spectral densities are

$$\mathcal{S}_{\delta \hat{a}^\dagger \delta \hat{a}}^{\text{in}}[\omega] = \int_{-\infty}^{\infty} dt e^{i\omega t} \langle \delta \hat{a}_{\text{in}}^\dagger(t) \delta \hat{a}_{\text{in}}(0) \rangle = \bar{n}_{\text{th}}, \quad (2.55)$$

$$\mathcal{S}_{\delta \hat{a} \delta \hat{a}^\dagger}^{\text{in}}[\omega] = \int_{-\infty}^{\infty} dt e^{i\omega t} \langle \delta \hat{a}_{\text{in}}(0) \delta \hat{a}_{\text{in}}^\dagger(t) \rangle = \bar{n}_{\text{th}} + 1, \quad (2.56)$$

$$\begin{aligned} \bar{\mathcal{S}}_{\delta \hat{a}^\dagger \delta \hat{a}}^{\text{in}}[\omega] &= \frac{1}{2} \int_{-\infty}^{\infty} dt e^{i\omega t} \left(\langle \delta \hat{a}_{\text{in}}^\dagger(t) \delta \hat{a}_{\text{in}}(0) \rangle + \langle \delta \hat{a}_{\text{in}}(0) \delta \hat{a}_{\text{in}}^\dagger(t) \rangle \right) \\ &= \frac{1}{2} (\mathcal{S}_{\delta \hat{a}^\dagger \delta \hat{a}}^{\text{in}}[\omega] + \mathcal{S}_{\delta \hat{a} \delta \hat{a}^\dagger}^{\text{in}}[\omega]) = \bar{n}_{\text{th}} + \frac{1}{2}. \end{aligned} \quad (2.57)$$

The noise is white with a flat spectrum independent of frequency. All three spectral densities are thus symmetric in frequency, if not classical. While

the spectral densities seem dimensionless, there is in fact an implicit unit. They are densities in frequencies of the “power” as defined by $\delta\hat{a}_{\text{in}}^\dagger\delta\hat{a}_{\text{in}}$, which has units of a flux of quanta per second. As a result, the number \bar{n}_{th} gives the number of photons per second in a bandwidth of 1 Hz and the spectral density has the units of quanta \times s⁻¹Hz⁻¹.

Even for a noise that is not flat in frequency, an effective temperature can be defined from the imbalance between $\mathcal{S}_{\delta\hat{a}^\dagger\delta\hat{a}}^{\text{in}}[\omega]$ and $\mathcal{S}_{\delta\hat{a}\delta\hat{a}^\dagger}^{\text{in}}[\omega]$. Because of the commutation relation (2.43), the relation

$$\mathcal{S}_{\delta\hat{a}^\dagger\delta\hat{a}}^{\text{in}}[\omega] - \mathcal{S}_{\delta\hat{a}\delta\hat{a}^\dagger}^{\text{in}}[\omega] = 1 \quad (2.58)$$

always holds. The effective temperature corresponding to given level of noise at the frequency ω is

$$T_{\text{eff}} = \frac{\hbar\omega/k_{\text{B}}}{\ln \mathcal{S}_{\delta\hat{a}\delta\hat{a}^\dagger}^{\text{in}}[\omega] - \ln \mathcal{S}_{\delta\hat{a}^\dagger\delta\hat{a}}^{\text{in}}[\omega]}. \quad (2.59)$$

2.2.3 The linear amplifier and its quantum limits

Linear amplifiers play a central role in the experimental results of this thesis. Firstly, they are the only available practical tool to perform quantum measurements at microwave frequencies. The weak signals carrying quantum information (or at least close to having only vacuum fluctuations as the background noise) must be first amplified with minimal added noise before they are analyzed using standard microwave equipment. Precise calibration of the added noise of the measurement chain (mostly due to the first amplifier) is required in order to have an absolute power reference for the signals before they are amplified. Secondly, part of the results of this thesis, detailed in section 4.8, is to build and characterize a microwave amplifier that functions close to the quantum limit of added noise using an optomechanical system. We therefore expose here the fundamental quantum limits for a linear amplifier (Caves, 1982) and how it can be interpreted as performing a quantum measurement.

We consider a scattering linear amplifier that is phase-preserving, represented schematically in fig. 2.2. For an input travelling-wave mode \hat{d}_{in} , the output field \hat{d}_{out} is an outgoing wave, proportional to the input with an amplification factor $\sqrt{\mathcal{G}}$. The relation between input and output is given by

$$\hat{d}_{\text{out}}(t) = \sqrt{\mathcal{G}}\hat{d}_{\text{in}}(t) + \hat{F}(t). \quad (2.60)$$

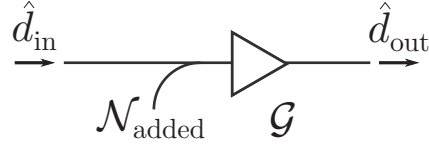


Figure 2.2: Schematic representation of a linear scattering amplifier. The amplification of power gain \mathcal{G} , adds a noise $\mathcal{N}_{\text{added}}$ to the signal.

The fluctuations \hat{F} must be added to the signal for both input and output operators to obey the canonical commutation relations

$$\left[\hat{d}_{\text{in}}(t), \hat{d}_{\text{in}}^\dagger(t') \right] = \delta(t - t') \quad \text{and} \quad \left[\hat{d}_{\text{out}}(t), \hat{d}_{\text{out}}^\dagger(t') \right] = \delta(t - t'). \quad (2.61)$$

This implies that the fluctuation operator must obey

$$\left[\hat{F}(t), \hat{F}^\dagger(t') \right] = (1 - \mathcal{G})\delta(t - t'). \quad (2.62)$$

The simplest way to satisfy this requirement is for the fluctuations to come from an idler mode \hat{d}_{fluct} with

$$\hat{F}(t) = \sqrt{\mathcal{G} - 1} \hat{d}_{\text{fluct}}^\dagger(t) \quad \text{and} \quad \left[\hat{d}_{\text{fluct}}(t), \hat{d}_{\text{fluct}}^\dagger(t') \right] = \delta(t - t'). \quad (2.63)$$

From this we can derive some constraints on the minimal noise that can be added during amplification. The fluctuation mode \hat{d}_{fluct} is assumed to contain thermal noise and obey

$$\langle \hat{d}_{\text{fluct}}^\dagger(t) \hat{d}_{\text{fluct}}(t') \rangle = \bar{n}_{\text{fluct}} \delta(t - t') \quad (2.64)$$

where \bar{n}_{fluct} is the occupancy of the mode. The output field \hat{d}_{out} combines the noise of both the input and the fluctuations with

$$\langle \hat{d}_{\text{out}}^\dagger(t) \hat{d}_{\text{out}}(t') \rangle = \mathcal{G} \langle \hat{d}_{\text{in}}^\dagger(t) \hat{d}_{\text{out}}(t') \rangle + (\mathcal{G} - 1) \langle \hat{d}_{\text{fluct}}^\dagger(t) \hat{d}_{\text{fluct}}(t') \rangle, \quad (2.65)$$

$$\langle \hat{d}_{\text{out}}(t) \hat{d}_{\text{out}}^\dagger(t') \rangle = \mathcal{G} \langle \hat{d}_{\text{in}}(t) \hat{d}_{\text{out}}^\dagger(t') \rangle + (\mathcal{G} - 1) \langle \hat{d}_{\text{fluct}}(t) \hat{d}_{\text{fluct}}^\dagger(t') \rangle. \quad (2.66)$$

The amplifier can be characterized by how it modifies the spectral density of its output with respect to its input. For the comparison to be on equal footing, the spectral density of the output field is divided by the power gain \mathcal{G} to get the equivalent signal at the input of the amplifier. It is however not a priori evident which definition of the spectral density is relevant and the

exercise is done for the three kinds defined in eqs. (2.55) to (2.57), resulting in

$$\frac{\mathcal{S}_{\hat{d}^\dagger \hat{d}}^{\text{out}}[\omega]}{\mathcal{G}} = \mathcal{S}_{\hat{d}^\dagger \hat{d}}^{\text{in}}[\omega] + \frac{\mathcal{G} - 1}{\mathcal{G}} \bar{n}_{\text{fluct}} + 1 - \frac{1}{\mathcal{G}} \approx \mathcal{S}_{\hat{d}^\dagger \hat{d}}^{\text{in}}[\omega] + \bar{n}_{\text{fluct}} + 1, \quad (2.67)$$

$$\frac{\mathcal{S}_{\hat{d} \hat{d}^\dagger}^{\text{out}}[\omega]}{\mathcal{G}} = \mathcal{S}_{\hat{d} \hat{d}^\dagger}^{\text{in}}[\omega] + \frac{\mathcal{G} - 1}{\mathcal{G}} \bar{n}_{\text{fluct}} \approx \mathcal{S}_{\hat{d} \hat{d}^\dagger}^{\text{in}}[\omega] + \bar{n}_{\text{fluct}}, \quad (2.68)$$

$$\frac{\bar{\mathcal{S}}_{\hat{d}^\dagger \hat{d}}^{\text{out}}[\omega]}{\mathcal{G}} = \bar{\mathcal{S}}_{\hat{d}^\dagger \hat{d}}^{\text{in}}[\omega] + \frac{\mathcal{G} - 1}{\mathcal{G}} \bar{n}_{\text{fluct}} + \frac{1}{2} - \frac{1}{2\mathcal{G}} \approx \bar{\mathcal{S}}_{\hat{d}^\dagger \hat{d}}^{\text{in}}[\omega] + \bar{n}_{\text{fluct}} + \frac{1}{2}. \quad (2.69)$$

The approximation are for the case of large gain $\mathcal{G} \gg 1$ that is of interest.

The added noise of the amplifier is often defined with the symmetrized output spectral density (2.69). It is the excess noise compared to the amplified signal in the output, referred to the input, $\mathcal{N}_{\text{added}} = \bar{\mathcal{S}}_{\hat{d}^\dagger \hat{d}}^{\text{out}}[\omega]/\mathcal{G} - \bar{\mathcal{S}}_{\hat{d}^\dagger \hat{d}}^{\text{in}}[\omega]$. The added noise is here

$$\mathcal{N}_{\text{added}} = \bar{n}_{\text{fluct}} + 1/2. \quad (2.70)$$

The limit of 1/2 for the lowest possible added noise even in the absence of any thermal excitation in the fluctuations \hat{d}_{fluct} is a fundamental quantum limit for a linear phase-preserving amplifier². It can be directly traced to the commutation relations (2.62) that the fluctuations \hat{F} must satisfy. In some sense, $\mathcal{S}_{\hat{d}^\dagger \hat{d}}^{\text{out}}[\omega]$ has an added noise of $\bar{n}_{\text{fluct}} + 1$ and $\mathcal{S}_{\hat{d} \hat{d}^\dagger}^{\text{out}}[\omega]$ an added noise of \bar{n}_{fluct} only, averaging to $\bar{n}_{\text{fluct}} + 1/2$ for the symmetrized spectrum.

By comparing the spectral density of the output to the input, the definition of added noise is hypothetical. It is assumed that a measurement of the output field is performed such that the unsymmetrized spectral density corresponds to the outcome of the measurement. This is compared to the gedanken experiment of performing the exact same measurement on the input signal when the amplifier is removed. When the amplifier is used and the signal amplified, the spectral density of the input is not experimentally accessible.

Examining the non-symmetrized output spectral densities in eqs. (2.55) and (2.56), we find that the spectral density is in effect symmetric. Using the relation (2.58), we have that

$$\frac{\mathcal{S}_{\hat{d}^\dagger \hat{d}}^{\text{out}}[\omega]}{\mathcal{G}} = \mathcal{S}_{\hat{d}^\dagger \hat{d}}^{\text{in}}[\omega] + \bar{n}_{\text{fluct}} + 1 = \frac{\mathcal{S}_{\hat{d} \hat{d}^\dagger}^{\text{out}}[\omega]}{\mathcal{G}} \quad (2.71)$$

² Phase-sensitive amplifiers that amplify only one quadrature from the signal can reach an arbitrarily low added noise. The cost is for extra noise in the other quadrature.

in the approximation of large \mathcal{G} . The only asymmetry is due to the vacuum fluctuations of the outgoing field \hat{d}_{out} (from its commutation relations (2.61)) that give the term $1/\mathcal{G}$ in eq. (2.67). It becomes negligible compared to other sources of noise that have been amplified greatly. The vacuum fluctuations of \hat{d}_{fluct} are amplified and imprinted on $\mathcal{S}_{\hat{d}^\dagger \hat{d}}^{\text{out}}[\omega]$. They match exactly the amplified vacuum fluctuations due to the input mode \hat{d}_{in} in $\mathcal{S}_{\hat{d}^\dagger \hat{d}}^{\text{out}}[\omega]$. In effect, the vacuum fluctuations from the input have become classical in the output, as they were amplified greatly. For a classical signal, the order of the operator does not matter and the spectral density must be independent of the ordering.

2.3 Optomechanical microwave circuits

The implementation of cavity optomechanics used for the work of this thesis is through superconducting microwave LC circuits with vibrating capacitors. In the following, we present the concepts that are characteristic of this specific implementation. A few necessary elements of microwave engineering will be introduced as needed. The textbook of Pozar (2011) serves as a main reference for the microwave engineering aspects.

In section 2.3.1, we start by introducing LC resonators and how they become optomechanical if the capacitance is modulated by a mechanical oscillator. In section 2.3.2, the model of the transmission line is developed, that allows the description of the interaction of incoming microwave signals with the circuit. In section 2.3.3, the interaction of the optomechanical circuit and the transmission line is described. Finally, in section 2.3.4, the model for the optomechanical circuit is quantized and the vacuum optomechanical coupling strength g_0 is defined for our system.

2.3.1 Optomechanics with LC circuits

We start by introducing the relevant circuit on its own, illustrated in fig. 2.3. We first describe the microwave mode, and then the mechanical oscillations of the capacitor plate.

The microwave cavity that serves as the electromagnetic degree of freedom in the optomechanical system is an LC resonator. In its ideal realization, a capacitor of capacitance C is in series with an inductor of inductance L . The dynamical equation for the voltage of the capacitor ($\dot{U} = \frac{1}{C}I$) and for

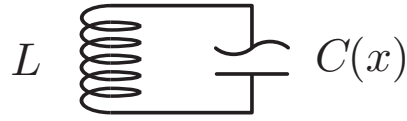


Figure 2.3: Ideal LC circuit with an inductor in series with a capacitor. The latter's capacitance C is modulated by the displacement x of a mechanical oscillator.

the voltage of the inductor³ ($U = -L\dot{I}$) are combined to obtain

$$\ddot{U} = -\frac{1}{LC}U, \quad (2.72)$$

an equation for harmonic oscillations at a resonance frequency $\omega_c = 1/\sqrt{LC}$. Alternatively, the resonance frequency can also be defined as the frequency at which the equivalent impedance of the circuit⁴

$$Z_{LC} = i \left(\frac{1}{\omega C} - \omega L \right) \quad (2.73)$$

vanishes (or has a minimum in the presence of resistance).

The second main role is played by the motional degree of freedom of the capacitor. The simplest model is to represent one electrode of a parallel-plate capacitor as a mass m on a spring of constant k , with the equation of motion

$$\ddot{x} = -\frac{k}{m}x \quad (2.74)$$

where the position of the plate is taken to be $x = 0$ at rest. That is precisely the definition of a harmonic oscillator of resonance frequency $\Omega_m = \sqrt{k/m}$.

Bringing the two elements together, the motion of the plate modulates the capacitance that in turn modulates the cavity resonance frequency. The capacitance becomes position-dependent, with

$$C(x) = \epsilon \frac{A}{d+x} \quad (2.75)$$

where ϵ is the (average) dielectric constant between the plates, A their surface and d their distance when the mechanical oscillator is at rest. For oscillations of small amplitude, the linear expansion approximation $C(x) \approx C_0(1 - x/d)$

³ Note the minus sign because of the opposite direction for the current in the inductor.

⁴The sum of the impedances of a capacitor $i/(\omega C)$ and an inductor $-i\omega L$, since the two elements are in series in the resonator.

can be taken. In turn, the change in capacitance implies a modulation in frequency of the microwave cavity as

$$\omega_c(x) = \frac{1}{\sqrt{LC(x)}} \approx \omega_{c,0} + Gx \quad (2.76)$$

with the linear constant $G = \omega_{c,0}/(2d)$ and the rest cavity frequency $\omega_{c,0} = 1/\sqrt{LC_0}$.

That such a simplistic model captures the dynamics of a realistic system warrants some justifications and caveats. In the physical capacitor that we use, the plate does not move rigidly constrained by an external linear spring force. Rather, it deforms into a complicated shape and is subjected to internal forces from its elastic properties, that can in general be nonlinear.

The first major assumption is that for small enough deformation, the linear elastic terms dominate. A displacement field $\mathbf{u}(\mathbf{r}, t)$ can be defined to describe how each point in the solid goes from its rest position at \mathbf{r} to a deformed position $\mathbf{r} + \mathbf{u}(\mathbf{r}, t)$. If only the linear order is kept for the elastic-strain properties, the field obeys a quadratic field equation (Sudhir, 2018). Subject to boundary conditions, this equations has eigensolutions of the form

$$\mathbf{u}(\mathbf{r}, t) = x(t)\mathbf{u}_n(\mathbf{r}) \text{ with } \ddot{x} = -\omega_n x \quad (2.77)$$

that are the normal modes of the structure. For a given mode labeled by n , the motion is decomposed into a certain fixed deformation $\mathbf{u}_n(\mathbf{r})$ and a time-dependent amplitude $x(t)$ that obeys the equation of motion of a harmonic oscillator. Note that the units of x and \mathbf{u}_n are arbitrary. For instance, $x(t)$ can be taken to be the position of the highest amplitude point or the average displacement of the plate, and the deformation $\mathbf{u}_n(\mathbf{r})$ would be unitless. In those cases, the motion $x(t)$ maps precisely to the motion of an ideal mass on a spring examined above.

The next question is how to account for the change in capacitance due to a specific vibrational mode of a plate of an arbitrary deformation shape. If the plate is thin and taken to be deformed along the vertical axis only, such that $\mathbf{u}(\mathbf{r}) = u_z(x, y)\hat{z}$, the resulting capacitance can be computed as an integral over the surface of the plate as

$$C(x) = \epsilon \int \frac{dxdy}{d + u_{n,z}(x, y)} \approx C \left(1 - \frac{x}{d} \frac{\int u_{n,z}(x, y) dxdy}{A} \right), \quad (2.78)$$

valid for small amplitude of the mode. The same linear expansion can be done for each eigenmode. Expanding the resonance frequency similarly, the

expression of eq. (2.76) is recovered, with x now standing for the amplitude of motion of a given mode, and a generalized coupling constant given by

$$G = \frac{\omega_{c,0}}{2d} \frac{A_{\text{eff}}}{A} \quad (2.79)$$

where $A_{\text{eff}} = \int u_{n,z}(x, y) dx dy$ is the effective area of the capacitor that is modified by the motion of the mode. The arbitrariness of the definition of the coupling constant G becomes clear, as it depends on the choice of normalization of the decomposition into x and \mathbf{u}_n for each eigenmode, with no unique objective way to do it. The right way to uniquely characterize the coupling between the motional and microwave modes is through the quantum coupling strength g_0 , introduced in section 2.3.4 where the degrees of freedom are quantized.

For small enough mode amplitudes $x(t)$, the linear expansion, neglecting higher-order terms, is in general valid. The only requirement is that the linear coupling term of mode n , proportional to $\int u_{n,z} dx dy$, does not vanish. This could be the case for higher-order modes with nodes such that the average displacement is zero. In conclusion, it is an important feature of cavity optomechanics, not unique to this implementation, that under broadly valid assumptions even complicated realistic systems behave close to the canonical example of the mass on a spring modulating the cavity resonance frequency linearly. The small lengthscale of displacement guarantees the validity of the model.

2.3.2 Transmission line theory

At microwave frequencies, the wavelength of electromagnetic waves is small compared to the length of cables where the signals propagate, and comparable to the size of circuits. A proper account of wave propagation is therefore capital. Input signals interrogating the circuit and output signals carrying the outcome of measurement take a finite time to travel. They can reflect on certain microwave elements and interfere with themselves.

The waveguide that is used in our case is a microwave transmission line, composed of two conductors that are laid out parallel to each other. This can for instance be a coaxial cable or a microstrip line on the chip. They all follow the same general theory, that we will briefly outline here. For a more in-depth and exhaustive exposition, the reader is referred to Pozar (2011).

Lumped elements can be used to model the transmission line. The microwave properties of the line are assumed to be locally equivalent to the effect of combined individual ideal microwave elements. A small section of

length Δx is shown in fig. 2.4. The voltage $V(x)$ and current $I(x)$ are compared before and after that section. The length of line is supposed to have some inductance and resistance, as well as a capacitance with respect to the second conductor. They are assumed to be proportional to the length, with an inductance $l\Delta x$, a resistance $r\Delta x$ and a capacitance $c\Delta x$. The changes in voltage and current are given by

$$V(x + \Delta x) = V(x) - r\Delta x I(x) - l\Delta x \frac{\partial I}{\partial t}(x), \quad (2.80)$$

$$I(x + \Delta x) = I(x) - c\Delta x \frac{\partial V}{\partial t}(x + \Delta x). \quad (2.81)$$

Taking the limit of infinitesimal length $\Delta x \rightarrow 0$, we get continuous partial differential equations linking voltage and current as

$$\frac{\partial V}{\partial x} = -rI - l \frac{\partial I}{\partial t}, \quad (2.82)$$

$$\frac{\partial I}{\partial x} = -c \frac{\partial V}{\partial t}. \quad (2.83)$$

They can be combined to obtain a wave equation for the voltage

$$\frac{\partial^2 V}{\partial x^2} - rc \frac{\partial V}{\partial t} - lc \frac{\partial^2 V}{\partial t^2}. \quad (2.84)$$

It is solved by the ansatz solutions

$$V(x, t) = V_0^+ e^{i(kx - \omega t)} + V_0^- e^{i(-kx - \omega t)}, \quad (2.85)$$

$$I(x, t) = I_0^+ e^{i(kx - \omega t)} + I_0^- e^{i(-kx - \omega t)}, \quad (2.86)$$

with forward and backward travelling waves. Inserting this expression in eq. (2.84), we get the complex dispersion relation

$$k^2 = lc\omega^2 + irc\omega. \quad (2.87)$$

In the lossless case $r = 0$, this gives a phase velocity $v_p = \omega/k = \sqrt{lc}$ for the waves. The amplitudes of the voltage to current for the travelling waves are constrained to follow

$$\frac{V_0^+}{I_0^+} = -\frac{V_0^-}{I_0^-} = Z_0 \quad (2.88)$$

where $Z_0 = \sqrt{l/c}$ is called the characteristic impedance of the line. The transmission line can be characterized by its phase velocity v_p and its characteristic impedance Z_0 , alternatively to the lumped-element parameters l and c .

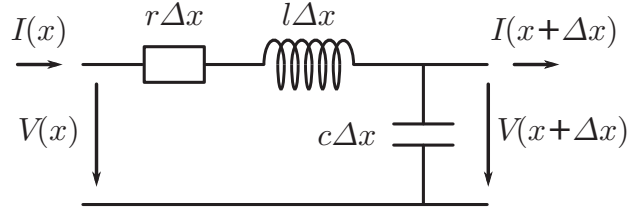


Figure 2.4: Lumped-element model of the transmission line. A short segment of length Δx is modeled as a resistance and inductance along the line and a capacitance between the two conductors, all proportional to the length.

On an infinite transmission line with constant impedance Z_0 , waves keep travelling indefinitely. Boundary conditions, involving changes of impedance, cause reflections of the waves. We analyze a few such cases in the following.

First, the simple case of a transmission line of impedance Z_0 terminated by a load Z , shown in fig. 2.5a, is analyzed. This boundary condition implies a certain relation between the incoming wave amplitude V_0^+ and the reflected outgoing wave amplitude V_0^- . By definition, the impedance of the load is the ratio of the total voltage V to total current I given by

$$Z = \frac{V}{I} = \frac{V_0^+ + V_0^-}{I_0^+ + I_0^-} = Z_0 \frac{V_0^+ + V_0^-}{V_0^+ - V_0^-} \quad (2.89)$$

where the phases of the waves (kx and $-kx$) are set to be zero at the load. The reflection coefficient is then

$$\frac{V_0^-}{V_0^+} = \frac{Z - Z_0}{Z + Z_0}. \quad (2.90)$$

If $Z = Z_0$, the load is said to be matched to the line. There are no reflections and the wave is perfectly absorbed by the load. The situation is indistinguishable from an infinitely long transmission line from the point of view of the incoming wave. For an open circuit, $Z \rightarrow \infty$, the total current must be zero $I = I_0^+ + I_0^- = 0$ implying $V_0^- = V_0^+$. The wave is perfectly reflected with the same phase. For a short circuit, $Z = 0$, the total voltage is zero with $V_0^- = -V_0^+$. The wave is perfectly reflected, with a phase-shift of π .

Second, we consider how the situation is changed if we set the reference plane of zero phase a length L of line before the load Z , as shown in fig. 2.5b. The voltage and current at the load now follow

$$Z = \frac{V}{I} = Z_0 \frac{V_0^+ e^{ikL} + V_0^- e^{-ikL}}{V_0^+ e^{ikL} - V_0^- e^{-ikL}}. \quad (2.91)$$

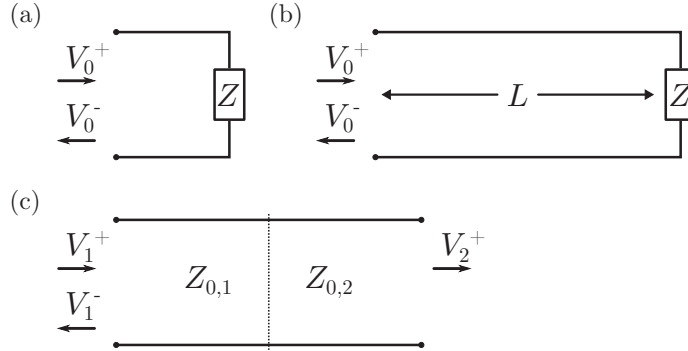


Figure 2.5: Different loads on the line for which the reflection coefficient are computed. (a) Case of a simple load of impedance Z . (b) Same but preceded by a length L of transmission line. (c) Impedance mismatch between two transmission lines of characteristic impedances $Z_{0,1}$ and $Z_{0,2}$.

The reflection coefficient becomes

$$\frac{V_0^-}{V_0^+} = e^{-2ikL} \frac{Z - Z_0}{Z + Z_0} = \frac{Z_{\text{eq}} - Z_0}{Z_{\text{eq}} + Z_0} \quad (2.92)$$

where the equivalent impedance at the reference plane Z_{eq} was defined, given by

$$Z_{\text{eq}} = Z_0 \frac{Z + iZ_0 \tan kL}{Z_0 + iZ \tan kL}. \quad (2.93)$$

The length of line L in general modifies the apparent impedance of the load. The equivalent impedance rotates on the complex plane, from the bare load Z when $kL = n\pi$ to the inverse load Z_0^2/Z when $kL = \frac{\pi}{2} + n\pi$. For instance, a length $L = \frac{\pi}{2k}$ transforms an open circuit boundary condition to a short circuit, and conversely. Only the matched load $Z = Z_0$ stays unchanged, with $Z_{\text{eq}} = Z_0$ no matter the length L .

Finally, the case of the junction between two transmission lines is considered, shown in fig. 2.5c. An incoming wave of amplitude V_1^+ on a line of impedance $Z_{0,1}$ arrives at the boundary and is split between a reflected component of amplitude V_1^- and a transmitted component of amplitude V_2^+ on the second line of impedance $Z_{0,2}$. By continuity, the voltages and currents on the left and right must be the same, with

$$V_1^+ + V_1^- = V_2^+, \quad (2.94)$$

$$\frac{1}{Z_{0,1}} (V_1^+ - V_1^-) = \frac{1}{Z_{0,2}} V_2^+. \quad (2.95)$$

From this we deduce the transmission and reflected components

$$\frac{V_2^+}{V_1^+} = \frac{2Z_{0,2}}{Z_{0,1} + Z_{0,2}}, \quad (2.96)$$

$$\frac{V_1^-}{V_1^+} = \frac{Z_{0,2} - Z_{0,1}}{Z_{0,1} + Z_{0,2}}. \quad (2.97)$$

If another wave impinges on the junction from the right, it must obey similar equations for its own reflection and transmission to the left. The two solutions can be added together by linearity. Note the strong similarities between eq. (2.97) and eq. (2.90). They are not accidental. In fact, since we consider only right-travelling waves, the same result could have been obtained by assuming the second line terminated by a matched load $Z = Z_{0,2}$. As explained above, the length of line of impedance $Z_{0,2}$ before the load is irrelevant for the circuit properties, and can be taken to be zero. The same reflected wave, given by eq. (2.90) would occur. The transmitted wave can be extracted from this simplified model as well, as the voltage dissipated at the load, given by $V_1^+ + V_1^-$.

2.3.3 Input and output relations for an inductively coupled LC circuit

We are now equipped to model the interaction with our LC cavity with incoming signals propagating on a transmission line which are inductively coupled. Before the full problem is tackled, the cavity on its own is once more considered, with a resistor added to model losses. This allows us to connect with the language that was used in section 2.1.2 and section 2.2.1 to describe a generic electromagnetic cavity in the Langevin picture.

In a RLC resonator, a resistor, inductor and capacitor are in series, obeying their respective constitutive equations $V_R = RI$, $V_L = L\dot{I}$, $\dot{V}_C = I/C$. They can be combined together, using the the fact that the total voltage in the loop must be zero $V_R + V_L + V_C = 0$ to obtain the differential equation for the current

$$\ddot{I} + \frac{R}{L}\dot{I} + \frac{1}{LC}I = 0. \quad (2.98)$$

It can be solved with the ansatz $I(t) = I_0 e^{\alpha t}$, giving a quadratic equation for α , solved by

$$\alpha_{1,2} = -\frac{R}{2L} \pm \sqrt{\left(\frac{R}{2L}\right)^2 - \frac{1}{LC}} \approx -\frac{R}{2L} \pm i\frac{1}{\sqrt{LC}} \quad (2.99)$$

where the approximation can be made if $R \ll \sqrt{L/C}$, valid when the quality factor of the resonator is large. On top of the previously identified resonance frequency $\omega_c = 1/\sqrt{LC}$ at which the resonator oscillates, there is an exponential decay of the current, as $e^{-\frac{1}{2}(R/L)t}$. The energy, which is proportional to the square of the current, decays at double the rate $\kappa_0 = R/L$, which we identify to the internal energy decay rate introduced in section 2.1.2.

In the experiment, the RLC circuit couples to the line via a mutual inductance M (as illustrated in fig. 2.6a). Two situations were realized: one where the line extends beyond the resonator in the so-called “notch configuration”; the other where the line is short-circuited after the cavity and the resonance can only be probed in reflection. We model both cases in the following.

First, we analyze the situation of the cavity measured in reflection. We start by studying how the coupling affects the dynamics of the RLC circuit itself. If the resonator is excited with some energy then let to decay, there will be only outgoing waves on the line. The line can in this case be replaced by a matched impedance Z_0 that effectively dissipates the signals (see fig. 2.6d). The goal is then to model the effect of the line as an effective impedance Z_{coup} added to the RLC circuit, as shown in fig. 2.6b. The voltage and current on the line obey

$$V_{M,2} = -Z_0 I_2 = -i\omega M I_1 \quad (2.100)$$

where the second equality is the constituting equation of the mutual inductance. By expressing I_2 in terms of I_1 and inserting the expression of the induced voltage in the resonator, we find

$$Z_{\text{coup}} = \frac{V_{M,1}}{I_1} = -i\omega M \frac{I_2}{I_1} = \frac{\omega^2 M^2}{Z_0} \approx \frac{\omega_c^2 M^2}{Z_0}. \quad (2.101)$$

The interaction to the line results in an increase of the effective resistance in the RLC resonator. The extra dissipation corresponds precisely to the external dissipation rate as

$$\kappa_{\text{ex}} = \frac{\omega_c^2 M^2}{L Z_0} \quad (2.102)$$

in analogy with the argument above. The approximation of evaluating the impedance at resonance ($\omega \rightarrow \omega_c$) is valid if $\kappa_{\text{ex}} \ll \omega_c$, equivalent to requiring a large quality factor for the external coupling as well for internal losses. Note that an advantage of inductive coupling is that it exclusively adds resistance to the circuit and does not change the resonance frequency at all, unlike coupling the circuit capacitively for instance.

The next step towards the reflection coefficient is to compute the effective impedance Z_{eq} of the circuit for the transmission line (see fig. 2.6d). The

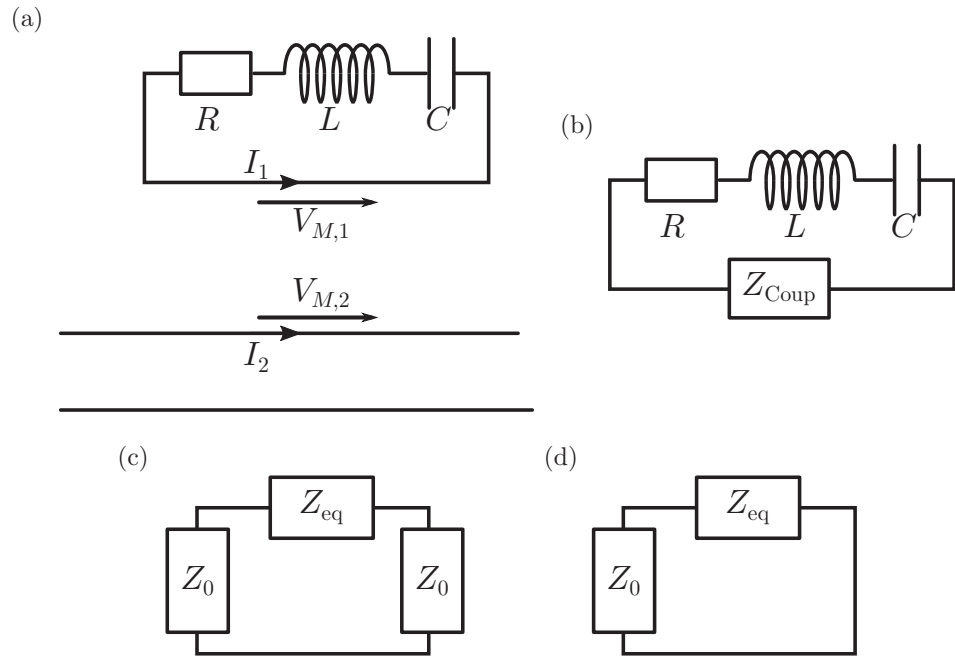


Figure 2.6: Lumped-element model of the resonator coupled to the line. (a) Model for the resonator coupled to the line. The coupling, through mutual inductance, implies that a current on the line I_2 creates a voltage in the circuit $V_{M,1}$ and reciprocally a current in the circuit I_1 creates a voltage on the line $V_{M,2}$. (b) The coupling to the line is modeled as the equivalent impedance Z_{coup} (or Z_{coup}^n for the two-sided cavity). (c,d) The resonator can be modeled as contributing an equivalent impedance Z_{eq} on the transmission line. The transmission line are modeled by their characteristic impedance Z_0 , sufficient to take into account outgoing signals. The circuit is shown both for the two-sided cavity (c) and for the one-sided cavity when one end of the transmission line is shorted.

inverse procedure is done compared to computing Z_{coup} above. First, the current in the RLC resonator I_1 due to the induced voltage $V_{M,1}$ is found to be

$$V_{M,1} = - \left(R - i\omega L + \frac{i}{\omega C} \right) I_1 = -i\omega M I_2. \quad (2.103)$$

The effective impedance is given by

$$Z_{\text{eq}} = \frac{V_{M,2}}{I_2} = \frac{\omega^2 M^2}{R + i(\frac{1}{\omega C} - \omega L)} \approx \frac{\omega_c^2 M^2 / (2L)}{\frac{R}{2L} - i(\omega - \omega_c)} = Z_0 \frac{\frac{1}{2}\kappa_{\text{ex}}}{\frac{1}{2}\kappa_0 - i(\omega - \omega_c)}. \quad (2.104)$$

In the short-circuited case, this equivalent impedance is the load on the line. The reflection coefficient is given by

$$\frac{V_0^-}{V_0^+} = \frac{Z_{\text{eq}} - Z_0}{Z_{\text{eq}} + Z_0} = - \frac{\frac{1}{2}(\kappa_0 - \kappa_{\text{ex}}) - i(\omega - \omega_c)}{\frac{1}{2}(\kappa_0 + \kappa_{\text{ex}}) - i(\omega - \omega_c)}. \quad (2.105)$$

Up to an overall minus sign, this is exactly what is expected from the generic treatment of a mode with Langevin equation (2.4) and input-output relation (2.41). The phaseshift of π comes from the short-circuit. The input-output relation should here be $\hat{a}_{\text{out}} = -\hat{a}_{\text{in}} + \sqrt{\kappa_{\text{ex}}}\hat{a}$ rather than eq. (2.41) to reflect the correct boundary condition.

We now analyze the situation where the line continues after interacting with the cavity (two-sided cavity). When considering the decay of the signal in the cavity, outgoing waves propagate in both direction. Both lines can be modeled by matched loads Z_0 , with total load given by the two in series as $2Z_0$ (see fig. 2.6c). The equivalent impedance in the circuit is here

$$Z_{\text{coup}}^{\text{n}} \approx \frac{\omega_c^2 M^2}{2Z_0}, \quad (2.106)$$

twice as small as for a cavity in reflection. Keeping all parameters the same, the total external dissipation rate $\kappa_{\text{ex}}^{\text{n,tot.}} = Z_{\text{coup}}^{\text{n}}/L$ is half what it is in the case of a short-circuited line. Moreover, this is the sum of the coupling rate for the transmission line in each direction. The individual channel coupling rate is $\kappa_{\text{ex}}^{\text{n}} = \kappa_{\text{ex}}^{\text{n,tot.}}/2$.

To find the reflection coefficient, the line on the right, carrying the transmitted wave can be replaced by a matched load Z_0 . We find

$$\frac{V_0^-}{V_0^+} = \frac{(Z_{\text{eq}} + Z_0) - Z_0}{(Z_{\text{eq}} + Z_0) + Z_0} = \frac{\frac{1}{2}\kappa_{\text{ex}}^{\text{n}}}{\frac{1}{2}(\kappa_0 + \kappa_{\text{ex}}^{\text{n}}) - i(\omega - \omega_c)}. \quad (2.107)$$

For the transmitted wave, the voltage amplitude of the outgoing wave is equivalent to the voltage that dissipates in the load Z_0 . The transmission coefficient is given by

$$\frac{V_1^+}{V_0^+} = \frac{1}{V_0^+} \frac{Z_0}{Z_0 + Z_{\text{eq}}} (V_0^+ + V_0^-) = \frac{2Z_0}{Z_{\text{eq}} + Z_0} = \frac{1}{1 + \frac{\kappa_{\text{ex}}^2}{\kappa_0 - i2(\omega - \omega_c)}}. \quad (2.108)$$

2.3.4 Quantization of the microwave and mechanical modes

So far, we gave a classical analysis of the LC resonator and how it interacts with the motion of the capacitor plate. In order to recover the results of the general analysis of sections 2.1 and 2.2 and consider the quantum implications, the two modes should be quantized. A standard quantization procedure is done (Le Bellac, 2012), through the definition of a generalized coordinate and its conjugated momentum for each mode in a classical Hamiltonian formalism, which are then promoted to quantum operators satisfying the canonical commutation relations. First the microwave resonator is analyzed, then the mechanical oscillator and finally the resulting quantum interaction.

We start with the quantization of the current and charge in the LC resonator. The classical Hamiltonian of the system corresponds to the total energy, that sums the energy in the capacitor and in the inductor as

$$H_{LC}^{\text{cl}} = \frac{1}{2} \frac{1}{C} Q^2 + \frac{1}{2} LI^2. \quad (2.109)$$

It should result in the dynamical equation (2.72) that can be expressed as $L\dot{I} = -\frac{1}{C}Q$, with $I = \dot{Q}$. If we take the charge to be the generalized coordinate of the system, then its conjugated momentum must be $P = LI$. This produces the correct Hamiltonian equations of motion

$$\dot{Q} = \frac{\partial H}{\partial P} = I, \quad (2.110)$$

$$\dot{P} = -\frac{\partial H}{\partial Q} = -\frac{1}{C}Q. \quad (2.111)$$

The quantization procedure amounts simply to promote Q and P to operators that satisfy the canonical commutation relation

$$[\hat{Q}, \hat{P}] = i\hbar. \quad (2.112)$$

Renormalized conjugated operators can be defined as $\hat{Q}' = \sqrt[4]{L/\hbar^2 C} \hat{Q}$ and $\hat{P}' = \sqrt[4]{C/\hbar^2 L} \hat{P}$, such that the Hamiltonian can be written in the symmetric form

$$\hat{H}_{LC} = \frac{1}{2} \frac{1}{C} \hat{Q}'^2 + \frac{1}{2} \frac{1}{L} \hat{P}'^2 = \frac{1}{2} \hbar \omega_c (\hat{Q}'^2 + \hat{P}'^2). \quad (2.113)$$

Finally, the annihilation operator \hat{a} can be defined from the unitless conjugated operators as $\hat{a} = \frac{1}{\sqrt{2}}(\hat{Q}' + i\hat{P}')$. By design, it obeys the commutation relation $[\hat{a}, \hat{a}^\dagger] = 1$. The Hamiltonian takes its recognizable form

$$\hat{H}_{LC} = \hbar \omega_c (\hat{a}^\dagger \hat{a} + \frac{1}{2}) \quad (2.114)$$

introduced in section 2.1. The term $\frac{1}{2} \hbar \omega_c$ is the energy of the vacuum state and can in general be omitted as it has no effect on the dynamics.

We now proceed to quantize the mechanical degree of freedom. In section 2.3.1, it was shown that quite generally the motion of the capacitor plate can be decomposed into normal modes with displacement fields $\mathbf{u}(\mathbf{r}, t) = x(t) \mathbf{u}_n(\mathbf{r})$ (where n labels the mode). The coordinate $x(t)$ describes the collective motion of the deformed plate, following the equation of motion $\ddot{x} = -\Omega_m^2 x$. The same equations of motion can be derived from the classical Hamiltonian of a harmonic oscillator

$$H_m^{\text{cl}} = \frac{1}{2} m_{\text{eff}} \dot{x}^2 + \frac{1}{2} m_{\text{eff}} \Omega_m^2 x^2. \quad (2.115)$$

Note that the equations of motion are independent of the effective mass m_{eff} . In order for the Hamiltonian H_m^{cl} to correspond to the energy of the oscillator, the effective mass should be such that the first term gives the kinetic energy of the deformed plate

$$U_K = \int d^3r \frac{1}{2} \rho |\dot{x} \mathbf{u}_n(\mathbf{r})|^2 = \frac{1}{2} \dot{x}^2 \rho \int d^3r |\mathbf{u}_n(\mathbf{r})|^2 \quad (2.116)$$

where ρ is the mass density of the material. The effective mass is identified as

$$m_{\text{eff}} = \rho \int d^3r |\mathbf{u}_n(\mathbf{r})|^2. \quad (2.117)$$

The arbitrariness in the definitions of the relative scales of $x(t)$ and $\mathbf{u}_n(\mathbf{r})$ (as discussed in section 2.3.1) in turn makes the definition of the effective mass arbitrary. In particular, it does not have to correspond to the mass of the oscillating plate or any other physical mass. Rather, it is the mass density ρ multiplied by an effective volume, that is weighted by the deformation profile of the mode \mathbf{u}_n .

Conjugated coordinate q and momentum p are defined as $q = x$, $p = m_{\text{eff}}\dot{x}$ in order to reproduce the equations of motion

$$\dot{q} = \frac{\partial H_{\text{m}}^{\text{cl}}}{\partial p} = \frac{p}{m_{\text{eff}}}, \quad (2.118)$$

$$\dot{p} = -\frac{\partial H_{\text{m}}^{\text{cl}}}{\partial q} = -m_{\text{eff}}\Omega_{\text{m}}^2 q. \quad (2.119)$$

Quantized versions of the coordinate and momentum, \hat{q} and \hat{p} , are defined as obeying the commutation relation

$$[\hat{q}, \hat{p}] = i\hbar \quad (2.120)$$

as for the microwave mode. The renormalized unitless operators are defined to be $\hat{q}' = \hat{q}\sqrt{m\Omega_{\text{m}}/\hbar}$ and $\hat{p}' = \hat{p}/\sqrt{m\Omega_{\text{m}}\hbar}$. Finally, the annihilation operator of the mechanical mode \hat{b} is defined as $\hat{b} = (\hat{q}' + i\hat{p}')/\sqrt{2}$. The quantum Hamiltonian is then

$$\hat{H}_{\text{m}} = \frac{1}{2}\hbar\Omega_{\text{m}}(\hat{q}'^2 + \hat{p}'^2) = \hbar\Omega_{\text{m}}(\hat{b}^\dagger\hat{b} + \frac{1}{2}). \quad (2.121)$$

Of particular interest are the fluctuations in position of the ground state of the mechanical oscillator, the vacuum state $|0\rangle$ that obeys $\hat{b}|0\rangle = 0$. They can be computed as

$$x_{\text{zpf}}^2 = \langle \hat{q}^2 \rangle = \frac{1}{2}\langle 0|(\hat{b} + \hat{b}^\dagger)(\hat{b} + \hat{b}^\dagger)|0\rangle \frac{\hbar}{m_{\text{eff}}\Omega_{\text{m}}} = \frac{\hbar}{2m_{\text{eff}}\Omega_{\text{m}}}. \quad (2.122)$$

They are called the zero-point fluctuations of the oscillator. They depend on the effective mass and therefore on the arbitrary normalization of the motion x .

Finally, the quantum optomechanical interaction can be reconstructed. Classically, eq. (2.76) means that a displacement x induces a change in the cavity frequency of Gx . The corresponding quantum Hamiltonian term is

$$\hat{H}_{\text{OM}} = \hbar G \hat{q} \left(\hat{a}^\dagger \hat{a} + \frac{1}{2} \right). \quad (2.123)$$

The contribution of $1/2$ is similar to a Casimir pressure force, due to the vacuum fluctuations of the LC resonator. It can be absorbed in a renormalization of the mode x with a slightly displaced rest position.

Using the expression for G from eq. (2.79) and $\hat{q} = x_{\text{zpf}}(\hat{b} + \hat{b}^\dagger)$, the optomechanical coupling can be reconstructed as

$$\hat{H}_{\text{OM}} = \hbar g_0 (\hat{b} + \hat{b}^\dagger) \hat{a}^\dagger \hat{a} \quad (2.124)$$

with the vacuum optomechanical coupling strength

$$g_0 = \sqrt{\frac{\hbar}{2m_{\text{eff}}\Omega_m} \frac{\omega_c}{2d} \frac{A_{\text{eff}}}{A}}. \quad (2.125)$$

Note that although both A_{eff} and m_{eff} depend on the arbitrary normalization of $x(t)$ and $u_{n,z}(x, y)$, g_0 does not, as any change of normalization is canceled in the ratio $A_{\text{eff}}/\sqrt{m_{\text{eff}}}$.

For the simple case of a plate that moves uniformly with $u_{n,z} = 1$ (as a rigid object attached to a spring), the expression simplifies to

$$g_0^{\text{rigid}} = \sqrt{\frac{\hbar}{2m\Omega_m} \frac{\omega_c}{2d}} \quad (2.126)$$

where $m = \rho h A$ is the physical mass of the plate. For a more general displacement profile $u_{n,z}(x, y)$, the coupling strength of eq. (2.125) is the simple expression of eq. (2.126) multiplied by the geometrical factor

$$\frac{\int u_{n,z}(x, y) dx dy}{\sqrt{A \int u_{n,z}^2(x, y) dx dy}}. \quad (2.127)$$

If the average of an arbitrary function $f(x, y)$ over the surface of the capacitor is defined as $\langle f \rangle = \frac{1}{A} \int f(x, y) dx dy$, this geometric factor can be rewritten as

$$\left(1 + \frac{\langle (u_{n,z} - \langle u_{n,z} \rangle)^2 \rangle}{\langle u_{n,z} \rangle^2} \right)^{-1/2}. \quad (2.128)$$

The maximum is 1 for a rigid plate where $u_{n,z} = \langle u_{n,z} \rangle$. For any other deformation profile, $u_{n,z}$ differs from the average and the factor is reduced. It can be interpreted as the change in capacitance due to the displacement normalized by the cost in terms of kinetic energy.

Design and measurement of optomechanical microwave circuits

In this chapter, we present the experimental background information required to understand how the results of this thesis were obtained. A generic equipment configuration valid for most measurements is described here. In the following chapters, specific setup requirements and techniques are introduced for the relevant experiments.

In section 3.1, we allude to the fabrication process for the optomechanical circuits. In section 3.2, we explain how simulation has aided the design and characterization of the circuits. In section 3.3, we delve into the different pieces of equipment and components that comprise the experimental setup. In section 3.4, we present the schemes for the noise calibration, both of the emitted noise of the microwave sources and of the added noise of the HEMT amplifiers. In section 3.5, the main characterization procedures for the chip are described. Finally, in section 3.6, we present a few standard measurements for an optomechanical system.

3.1 Fabrication of the devices

The systems at the heart of the experimental results of this thesis are optomechanical microwave circuits, an example of which is illustrated in fig. 3.1. Here we present briefly their general structure, as well as a succinct overview of their fabrication. A much more detailed account of the numerous steps

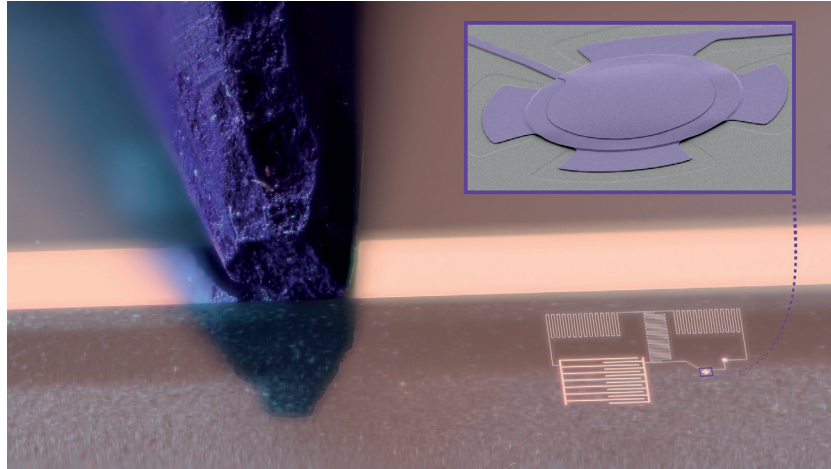


Figure 3.1: Photograph and scanning-electron micrograph of the optomechanical circuit. The circuit, at the bottom right is shown next to the sharpened tip of a pencil for scale. The inset is a scanning-electron micrograph that represents a zoom on the vibrating capacitor.

involved in the nanofabrication of the devices can be found in the doctoral thesis of Tóth (2018), who developed a process for their fabrication at the Center of MicroNanoTechnology at EPFL (CMi), where all the devices for this thesis were realized.

In its simplest realization, the optomechanical microwave circuit implements a single LC resonator with a capacitor whose top plate has a vibrational degree of freedom. On a sapphire rectangular chip of $9.6 \text{ mm} \times 6.5 \text{ mm}$, the circuit is deposited as a thin film of aluminium. A central microstrip constitutes a transmission line matched to 50Ω , on which incoming and outgoing signals can travel. On each side can be placed a number of LC resonators, that couple inductively to the line.

A single LC resonator is constituted by an inductor and capacitor in series, forming a loop. In this work, the inductor is a meandering line of approximately $3 \mu\text{m}$ in width. In other realizations (Teufel, D. Li, et al., 2011; Suh et al., 2014), spiraling inductors were used, necessitating an air bridge to connect the line from the inside to the outside of the spiral.

The most critical and delicate element is the capacitor. Above the bottom electrode that lies on the sapphire substrate like the rest of the circuit, the top plate is suspended, with vacuum between the two. It is attached to the substrate at four clamping points and bends upwards such that the flat central part is free to vibrate (see SEM image in fig. 3.1). The gap between the two electrodes should be as small as possible in order to maximize the

optomechanical coupling strength (see eq. (2.125)). We estimate the gap to be approximately 40 nm for most working devices (the estimation relies on simulations, as detailed in section 3.2).

The fabrication of the capacitor compounds several challenges. For one, a floating structure is especially vulnerable. For instance, the slanted sidewall from the clamping point to the flat electrode can tear, or under some conditions the whole top plate can collapse and stick permanently to the bottom plate. Moreover, the design of the resonance frequency of the microwave circuit depends critically on the rest position of the plate, which is hard to control. Beyond the constraints on the microwave properties, the top plate should also have good mechanical properties, such as a stable resonance frequency and low mechanical losses. The local stress in the aluminium film affects strongly those properties and is hard to be made uniform and reproducible. It depends on the details of the deposition process but can also be modified by heating, for instance by intentionally annealing the sample after fabrication.

A schematic representation of the main steps in the fabrication process is shown in fig. 3.2. The bottom layer of aluminium is first deposited (I) and patterned (II) to form most of the circuit and the bottom plate. Then a layer of amorphous silicon is deposited as a sacrificial layer (III) and itself patterned (IV and V). This forms the protective layer that preserves a gap with the bottom plate when the second aluminium film is deposited to form the top plate (VI) and patterned (VII). Both aluminium films are 100 nm thick. The final crucial step is to etch the sacrificial layer (VIII) that must be removed in order to release the top plate that eventually floats freely above the bottom plate.

This final release is one of the most important as well as delicate steps. This is done with a pulsed vapour XeF_2 etch. Relatively small openings on the sides prevent the etching from being uniform and must progress from the circumference to the center of the electrode. The chemical process is exothermic and care must be taken for it not to be too fast and damage the top film by overheating it, since the heat changes the stress in an undesired way. This might increase the chance for the top plate to collapse or affect the mechanical properties by making the vibrational mode spatially distorted.

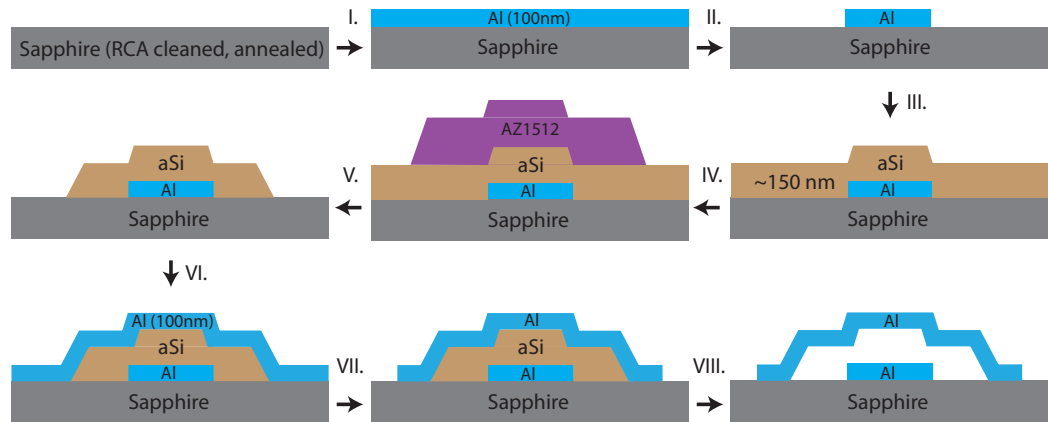


Figure 3.2: Schematic of the main steps of fabrication of the chips. See main text for a description of each step. Figure courtesy of L. D. Tóth, reproduced from Tóth (2018).

3.2 Simulation tools as aides for design and characterization

Since the aim is to construct devices that realize ideal LC resonators, the necessity of simulation tools is not evident and should be motivated. As was shown in sections 2.3.1 and 2.3.3, only a few constants (L , C and the mutual inductance M) are required to know the resonance frequency of the microwave resonator and how it couples to the waveguide. They can in principle be estimated purely based on the geometry. Only the resistance of the circuit R is a priori fabrication-dependent and should be measured.

In fact, the lumped-element model is not always valid for our devices. Their relatively large size, of several millimeters, amounts to a significant fraction of the wavelength of microwaves at the frequency of interest (about 3 cm at a frequency of 5 GHz), due to the finite velocity of electromagnetic waves that travel at around half the vacuum velocity c in microwave circuits. Take for example a loop of wire, which normally has an inductance scaling with the inscribed area. For large frequencies at which the loop length is comparable to the wavelength, the effective inductance is reduced. Not all the wire carries the same current. The changing phase of the travelling wave implies that the current oscillates along the wire and cancels at nodes every half wavelength.

Simulations are thus required for larger circuits that cannot be properly modeled with lumped elements such as individual capacitors and inductors.

The effective role of each element in the circuit depends critically in practice on the boundary conditions and surrounding elements. Two parts of a circuit might behave differently when connected to one another compared to on their own. For this reason, on top of estimations and simulations for the individual components, it is useful to simulate the circuit as a whole in order to verify that the model makes sense.

For the work of this thesis, simulations were used mainly to aid the design of the circuit on the chips. As the nanofabrication of the devices is costly in terms of labor and time, a new design should ideally be well simulated before it is implemented. This is unfortunately not entirely feasible. The actual properties of the circuit depend on details in the fabrication process that cannot be known perfectly a priori. Namely those are the rest position of the capacitor plate after release, when cooled at cryogenic temperatures, and the kinetic inductance of the material.

Superconducting materials have two contributions to their inductance. The first, “geometric” component relates to the potential energy of the magnetic field induced by the currents in the material, which scales with the inscribed area for a loop. On top of that there is a second, kinetic contribution to the inductance (Cardwell and Ginley, 2003). Since resistance is virtually absent from superconductors, the Cooper pairs that carry charges can reach very large velocities to supply a given current. Despite their low masses, this can make their kinetic energy appreciable and comparable to the magnetic energy. The kinetic inductance depends on the number of available charge carriers in the material: the fewer there are, the faster they must travel to achieve a given current and therefore the larger the kinetic energy required. This depends heavily on the fabrication as it depends on the exact cross-section of the material, and the width and thickness of the lines can vary slightly for different fabrication processes.

Simulations cannot then predict measurements ex nihilo. The two must work hand in hand. A typical chronology is the following. A new circuit design is conceived based on approximate estimations of the gap distance and the kinetic inductance based on earlier experiments. The design is fabricated multiple times on the same wafer with a range of variation for the topology of the circuits, with different sizes for the inductors or the capacitors. One of the fabricated devices is measured and its properties are compared to the simulation. This allows the correct gap size and kinetic inductance of the batch to be computed. Finally, the device with the ideal parameters can be selected in the parameter range and measured.

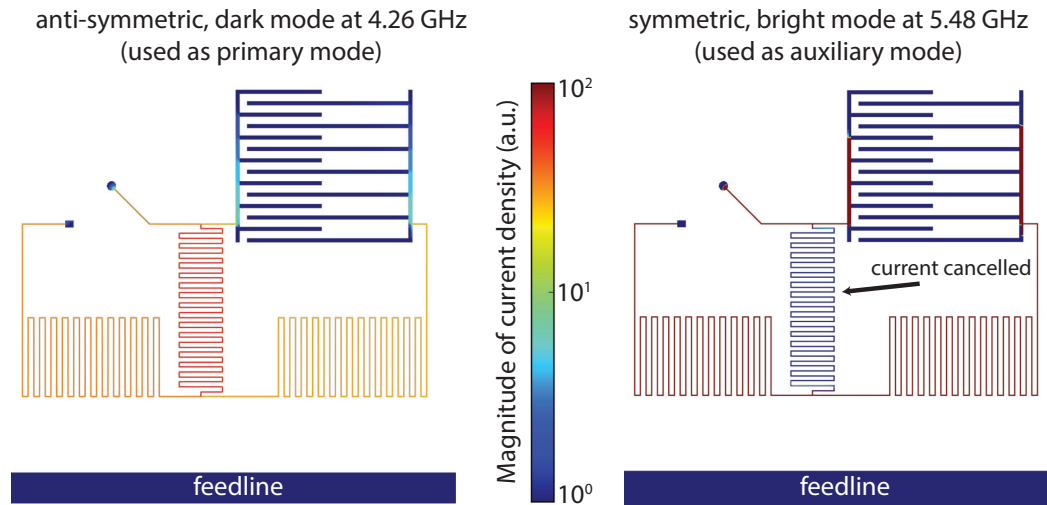


Figure 3.3: Example of a Sonnet simulation. The current density is represented in a simulation of the full circuit, including its coupling to the transmission line (labeled feedline). The circuit in question is the hybrid circuit introduced in section 4.2. Figure reproduced from the supplementary information of Tóth, Bernier, Nunnenkamp, et al. (2017).

3.2.1 Sonnet software

The main simulation tool that we used in the work of this thesis is Sonnet¹. This is a general software to compute the response of microwave circuits with a flat topology (or constituted of several flat parallel layers). As well as simulating individual components to design the inductors and capacitors, it is powerful enough to simulate the circuit in its entirety, even including a transmission line (as illustrated in fig. 3.3). This makes it a very complete tool and extremely useful to test the limits of the lumped-element model.

We review schematically how Sonnet functions in the following. A more thorough exposition of the theory is done in Rautio, J. C. (1986) and Rautio and Harrington (1987). The box that contains the circuit is modeled as a vertical waveguide in which several horizontal planes form boundary conditions between different dielectric layers. Sitting on top of a dielectric that represents the substrate, the circuit is constituted of metal patches on one (or more) such boundary planes. The patches are conceptually split into a number of segments. If a current flows into one of the segments, electromagnetic waves will be emitted in the waveguide, both upwards and downwards, and will reflect on the boundary conditions to form standing waves. The fields

¹ <https://www.sonnetsoftware.com/>

of these standing waves can be computed analytically and depend linearly on the current. The goal of the simulation is to find the right current distribution in the circuit that will satisfy all boundary conditions on the sides of the waveguide. Typically, the whole box is grounded, except for a number of ports where a voltage can be applied to drive the system. The core of the computation is to invert the matrix that gives the boundary fields due to the currents, in order to compute the currents from the boundary conditions. The equations for the electromagnetic field are solved exactly in the waveguide, in contrast to finite-element methods. The approximation comes from the segmentation of the circuit and of the boundary conditions. The finer the meshing, the more accurate the computations will be, but the larger the matrix to invert becomes. Both the response of the circuit and optionally the charge and current distribution can be computed for each segment as a function of the input frequency (as shown in fig. 3.3).

In particular, the resonance frequency ω_c and the external coupling rate κ_{ex} can be simulated. An example is shown in fig. 3.4, where the resonances of the sample HYB-20150924-4-24 are simulated. The gds file that is used in the fabrication of the chip is imported into Sonnet and gives the 2D layout that is simulated. Missing is the third dimension, namely the gap distance between the two plates of the drum capacitor. In fig. 3.4a, the resonances are simulated for various gap distances. Comparing the result with the measured resonances, the gap in the fabricated chip can be estimated to be approximately 35 nm. While simulating for individual frequencies take time, Sonnet offers an option called “adaptive sweep”, where it simulates a few points and interpolates between them, without recomputing the full matrix. This is enough to get an estimate of the resonance frequency, but not to extract precisely the resonance response, needed to obtain the external coupling rate. In fig. 3.4b and c, the response of the circuit is simulated at a few points around the resonance frequency, in the case of the dark mode at 4.3 GHz, for a gap of 35 nm. This takes more time than an adaptive sweep, but gives the exact shape of the resonance. The simulated data are fitted by a circle on the complex plane, as detailed in section 3.5.1, to extract the resonance frequency and linewidth. Note that the simulated resonator is strongly over-coupled. The internal-losses mechanism are difficult to model. To a first approximation, the simulation can only model the external coupling rate κ_{ex} and has a negligible internal decay rate κ_0 . The simulated external coupling, of 60 kHz is comparable to the measured value of 42 kHz. For the design with hybrid modes, described in section 4.2, exact coupling rates are difficult to predict as they depend strongly on the resonance frequencies of the bare modes, and therefore on the exact capacitance of the drum capacitor.

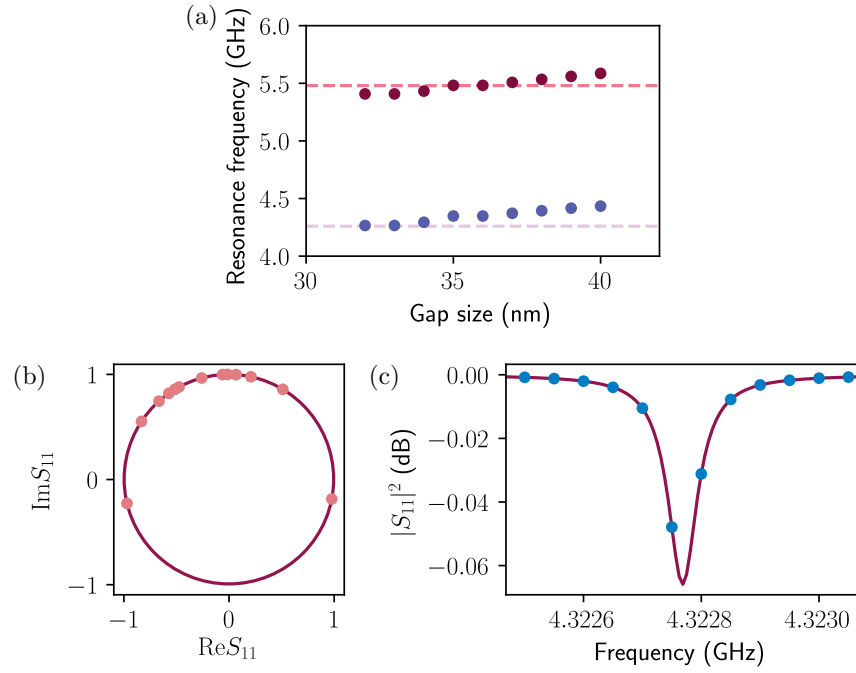


Figure 3.4: Microwave resonances simulated with Sonnet for the sample HYB-20150924-4-24. (a) Approximate resonance frequencies of the two hybrid modes as a function of the capacitor gap size. The horizontal dashed lines give the resonances measured in the experiment, which correspond to a gap of about 35 nm. The adaptive sweep is used in Sonnet to find approximate resonance frequencies. (b,c) Fitted response of the dark mode near 4.3 GHz, to extract the precise resonance frequency and the external coupling rate κ_{ex} , for a simulated gap of 35 nm. The resonance is fitted with a circle on a complex plane, as explained in section 3.5.1.

3.3 Experimental setup

We list in the following the equipment and components that are employed in the experiment. In section 3.3.1, we describe the design and assembly of the sample holder in which fabricated chips are fixed for measurement. In section 3.3.2, the mounting and wire bonding of the chip inside the holder is detailed. In section 3.3.3, the components installed inside the dilution refrigerator are presented. In section 3.3.4, the equipment that stands outside the dilution refrigerator at room temperature is described.

3.3.1 Sample holder

The chips that contain the circuits to be studied are mounted inside a sample holder to perform the measurements. We describe here the design of the sample holders and how it is assembled.

The sample holder fulfills multiple purposes. On a very pragmatic level, it provides a structure with SMA connectors that can easily be connected to the rest of the experimental setup by attaching coaxial cables. Importantly, it constitutes a grounded shielding that protects the circuit from any stray radiation. This both reduces the possibility for microwave noise to couple in the cavities and prevents higher frequency radiation from disturbing the superconductors, for instance by creating quasiparticles (Barends et al., 2011; Córcoles et al., 2011). Finally, it forms a large heat reservoir that should be well thermally coupled to the cryogenic environment such that the circuit is surrounded by a cold environment and cools down properly.

The sample holder design is shown in fig. 3.5 and the files are available online (Bernier, 2018). The central compartment, shaped like an “H” holds the chip. On both sides are rectangular receptacles to place small printed circuit boards (PCB) that serve as intermediary between the chip and the two SMA connectors. The connectors are placed on both ends through cylindrical holes and held in place by screws in threaded holes (M2.5) on the outside. Next to the PCB receptacles are pads where certain parts of the circuits can be grounded directly. A lid is designed to close the box, leaving as little open volume as possible inside. This pushes the resonance frequencies of the 3D cavity modes upwards much beyond the frequencies of the circuit, where they cannot disturb it. Two vertical holes pass through the box and lid, with threading in the box (M3). This serves the double purpose of closing the lid tightly and securely, as well as clamping the sample holder to the breadboard in the the cryostat to ensure good thermalization (see fig. 3.6).

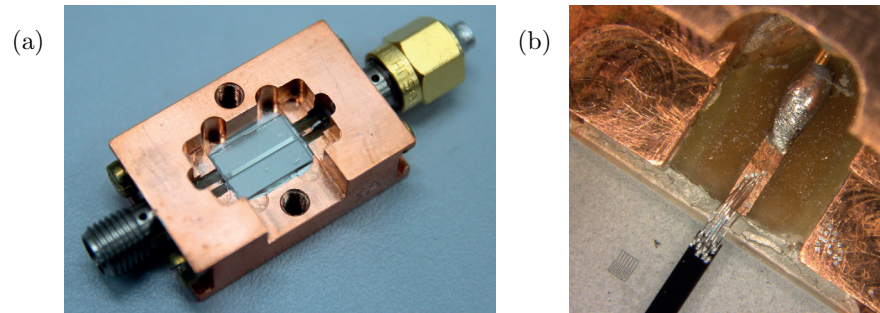


Figure 3.5: Photographs of the sample holder. (a) Photograph of the mounted sample holder with a chip mounted and wire-bonded. A shorted cap is attached to one port to measure in reflection. (b) Photograph taken with a microscope, zooming on the wire bonds between the chip and the PCB transmission line. The soldering of the SMA central pin to the PCB is visible in the top right.

The sample holders are realized out of a single piece of OFHC (oxygen-free high conductivity) copper, at the mechanical workshop of the institute of physics at EPFL². It is important to use OFHC copper for two reasons. First, it has a high thermal conductivity even at cryogenic temperatures. Second, it contains minimal magnetic impurities whose stray magnetic fields can create vortices in the superconductor. The PCBs are fabricated by the electronic workshop (ACI) of the electrical engineering institute of EPFL³. Layers of 18 μm of copper are deposited on both sides of a substrate of 0.3 mm thickness made of FR-4 (a dielectric material that works well at cryogenic temperatures).

To assemble the sample holders, the PCB must be glued in place and the SMA connectors soldered to the PCBs. The conductive epoxy Epo-Tek H20E is used to keep the PCB solidly in place cooldown after cooldown, and connect its ground plane to the sample holder. First, both the sample holder receptacle surface and the ground plane of the PCB are cleaned with a fiber brush to remove the copper oxide layer and guarantee good long-term adhesion. The corners of the PCB can be cut with pliers such that it fits better the receptacle which has rounded edges. After cutting the PCB, the rough edges can be smoothed with sand paper. While we would like the wire bonds between the chip and the PCB to be as short as possible, it is not possible to fabricate the PCB with a copper transmission line until the edge. One can cut the end of the PCB with pliers to have the transmission line as close to

²<https://iphys.epfl.ch/page-139526-en.html>

³<https://sti-ateliers.epfl.ch/page-19942.html>

the edge as possible. The mixed epoxy is applied in small quantity and the pieces assembled. To cure the epoxy, the lowest recommended temperature of 80 °C is used, placing the sample holder on a hot plate for at least 90 mn.

The final step to prepare the sample holder is to solder the SMA connector. We used the model R125.462.001 from Radiall. It is critical to prevent the flux from covering all the surface of the PCB copper plate when soldering. One technique is to protect the half of the copper line that is closest to the chip with a piece of masking tape. The SMA connector is fixed with two screws and the central pin is soldered to the PCB (see the assembled sample holder in fig. 3.5). It is advisable to test the sample holder with a multimeter to check the soldering and ensure that there is no accidental short circuit of the central pin to the ground. One location to be wary of is between the dielectric of the SMA connector and the PCB. There can be a gap, where conductive debris might fall and short the central pin.

With every cooldown of new chips, successive wire bonding to the PCB line degrades the copper surface. At some point, it becomes difficult to wire bond successfully close to the edge and minimize the bond length. The PCB can then be replaced. The connector is unsoldered and removed. Then the PCB is detached using a blade to break the epoxy. The surface of the sample holder is cleaned thoroughly with a fiber brush or a piece of sand paper to remove all traces of the epoxy. Finally a new PCB can be glued in place with the steps outlined above and the sample holder reassembled.

3.3.2 Mounting and bonding the chip

The chips are glued and wire-bonded to the sample holder to be measured at cryogenic temperatures. We describe here this procedure.

First, the sample holder is thoroughly cleaned. Residues of glue in the central compartment are removed with isopropanol and all surfaces to be glued or wire bonded are brushed to remove the oxide layer. Small debris are removed using compressed air. The cleaning should be completed at this stage, since once the chip is glued it is no longer possible to do so in order not to damage the fragile capacitors.

Silver conductive paint is used to attach the chip to the sample holder. It must conduct to connect electrically the backside aluminium layer to the sample holder and form the ground plane. Not too much glue should be used. The excess overflows on the sides when the chip is gently pressed down to ensure good contact on the whole surface. It can short-circuit the central line of the PCB or the chip and accidentally ground them. Before cooling

down the chip, it is useful to verify with a multimeter if the central line is accidentally grounded, either with paint or with a fallen wire bond. The paint used is CMR RS186 (manufactured by RS components). The glue is left to dry for about an hour at least to ensure the chip is firmly fixed before it is wire bonded.

The wire bonding is performed with a TPT HB10 machine from the CMI, with an aluminium wire $33\ \mu\text{m}$ in diameter. Both ends of the central transmission line on the chip are connected to the PCBs with about 10 bonds each. If the device is measured in reflection, it is also possible to bond one end of the line to one ground pad of the sample holder next to the PCB.

The sample holder has two ports such that the chip can be measured both in transmission and in reflection. There are advantages and inconveniences for both cases. As explained in section 3.5.1, measuring the microwave resonances in transmission is required to calibrate out any impedance mismatch on the line and extract precisely the internal and external dissipation rates κ_0 and κ_{ex} . This comes at the cost of a reduced coupling rate compared to a single-sided cavity (see section 2.3.3). More importantly, it also reduces the signal to noise for the emissions from the cavity. Outgoing signals divide into travelling waves in two directions and at best only half of the total signal can be measured in any single direction. For measurements where the signal-to-noise ratio is essential (for emission close to the quantum limit), a one-sided cavity is greatly beneficial and the devices are measured in reflection only.

Altering appropriately the boundary conditions at one end of the central transmission line of the chip reflects incoming signals and allows single-sided measurements. Not all reflecting boundary conditions are equivalent. As shown in section 2.3.2, both open and short-circuited transmission lines are fully reflective. However, the resonators are coupled inductively to the feed-line and the coupling strength depends on the amplitude of current locally on the line. An open boundary condition forms a node in the current which cancels exactly at the boundary point. Near an open boundary, any inductive coupling is strongly reduced up to a distance of a quarter wavelength away where the current has an antinode and the coupling is restored. To achieve sufficient coupling rates, short-circuited boundaries are beneficial since they have a maximum of current instead. The distance on the line between the short circuit and the resonator determines the coupling rate. For consistent coupling rates, the resonators are placed always at the same position on the chip.

A short-circuited cap, shown in fig. 3.5a, is connected to the sample holder to achieve reflective boundary conditions in a non-destructive way. It is constructed by soldering the central pin of an SMA connector to the outer

shield to ground it. Optionally, the line can also be grounded to the sample holder with wire bonds. This gives a shorted boundary condition a few millimeters closer to the chip.

3.3.3 Inside the dilution refrigerator

The devices are mounted inside a BF-LD250 dilution refrigerator from Blue Fors. We describe here what components are installed inside. One set of lines for input and output signals to a sample holder is described. Usually, two similar sets are installed such that two devices can be measured in a given cooldown. We review in the following what a typical setup entails and the rationale behind each component. The actual components used for the experiments of this thesis deviate slightly and the differences are introduced in the respective chapters.

In summary, input and output lines are needed for signals to propagate to and back from the device that is mounted to the plate of the mixing chamber, the coldest point of the dilution refrigerator. Three lines are needed in fact. One carries the input signals to the chip. A second carries away the output signals to be amplified and measured. A third, auxiliary, line can be used to perform tone cancellation if required. In the following, we first describe the input lines and how the signal is attenuated to lower the thermal noise, then how the signals are coupled to the chip at the base plate, finally the output line and how the outgoing signal is amplified.

One key requirement when interfacing microwave signals from room temperature with devices at cryogenic temperatures is to reduce the intrinsic thermal noise of the former as to not disturb the latter. At 300 K, the thermal noise emitted from any load has a symmetrized spectral density of 1250 quanta/s/Hz at 5 GHz (from eq. (2.57)). This corresponds in units of power to -173.8 dBm/Hz. This level of noise provides a thermal bath much larger than the cryogenic temperature and would heat the system, preventing any measurement of weak quantum signals. The noise travelling on the input line must be reduced with attenuators that are thermalized to a lower temperature.

An attenuator can be modeled as a beam-splitter that takes a fraction α of the incoming signal and replaces it with a fraction $1 - \alpha$ of the noise of a matched load. This added noise is necessary for the time-evolution to be unitary and the commutation relations of the travelling mode to be preserved. This implies

$$\bar{S}_{\delta\hat{a}^\dagger\delta\hat{a}}^{\text{out}}[\omega] = \alpha\bar{S}_{\delta\hat{a}^\dagger\delta\hat{a}}^{\text{in}}[\omega] + (1 - \alpha)\bar{S}_{\delta\hat{a}^\dagger\delta\hat{a}}^{\text{load}}[\omega] \quad (3.1)$$

where the spectral density of the load $\mathcal{S}_{\delta\hat{a}^\dagger\delta\hat{a}}^{\text{load}}[\omega]$ depends on the temperature of the attenuator. As explained in section 2.2.3, which definition of the quantum spectral density to use does not matter, since the amplified signals are eventually measured classically. The symmetrized spectral density is used for simplicity.

The aim is to reduce the noise from an equivalent temperature of 300 K to close to a noise temperature of about 10 mK, the operating temperature at the mixing-chamber plate. This necessitates multiple stages of attenuation. In a typical setup, illustrated in fig. 3.6, the input signal is first attenuated by 20 dB at the 3K plate, then another 20 dB are removed by coupling the signal to the sample holder through a directional coupler (Pasternack PE2204-20 or similar). In between, copper nickel cables (Coax Ltd SC-086/50-SCN-CN with a silver-plated center conductor) also have an insertion loss of about 6 dB. Normal conductor cables have been found preferable, since large input power can heat superconducting cables until they become normal, increasing the insertion loss suddenly by more than 10 dB.

We compute how the input noise spectrum is reduced from the explicit attenuation on the line, to provide an upper estimate of the noise reaching the chip. The dissipation in the cables reduces the noise further, but the amount depends on the exact thermalization of the cables, which is difficult to estimate. The first 20-dB attenuator at 3 K decreases the noise to $24 + \frac{1}{2}$ quanta/s/Hz, using eq. (3.1) with $\alpha = 0.01$. The second attenuation, with the directional coupler, mixes the attenuated signal with noise travelling backwards from the isolator (see fig. 3.6), which we assume to be thermalized at the base temperature of 10 mK. A noise spectrum of $0.24 + \frac{1}{2}$ quanta/s/Hz then reaches the chip, equivalent to an effective temperature of 147 mK. Note that the noise can only asymptotically reach the cryogenic temperature when the attenuation tends to infinity. One must compromise between good thermalization and how much power to throw away. We settled here for a comparatively low 40 dB of explicit attenuation, since for most experiments of this thesis, large power is required to reach a sufficient coupling strength g .

The cryogenic attenuator (XMA 2082-6418-20 CRYO) at 3 K must be well thermalized. Otherwise, the load can heat up from absorbing the incoming signal and noise. We used unfluxed copper braiding (Chemtronics 70-3-25) tightly wound around the attenuator to thermalize to the 3-K plate by fixing the other end to it with a screw (see photograph in fig. 3.6).

The question of how to arrange a given amount of attenuation between the different temperature stages to obtain maximally reduced noise is not trivial. A priori, placing all the attenuation at the coldest point should

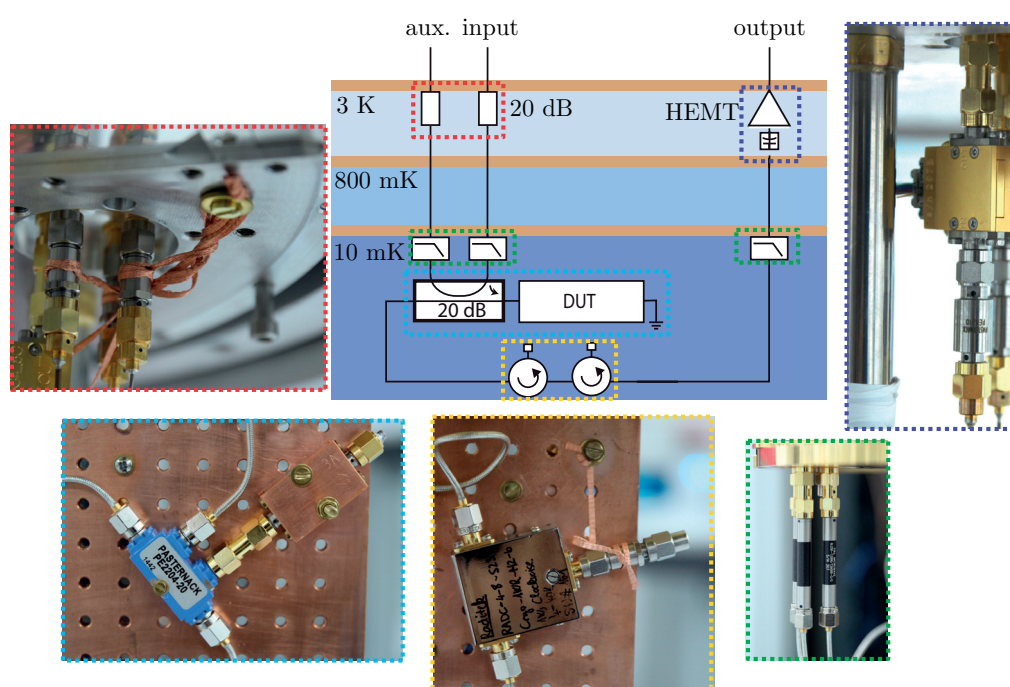


Figure 3.6: Schematics of the setup inside the dilution refrigerator. Illustrative photographs are shown for corresponding key components. In a red frame, the 20-dB attenuators on the the 3-K plate. In a light-blue frame, the chip in the sample holder is interfaced with a directional coupler. In a yellow frame, cryogenic circulators isolate the device from backpropagating noise. In a green frame, low-pass filter shield the superconducting circuit from high frequency radiation. In a purple frame, the HEMT amplifiers are insulated from the line by inner DC blocks.

provide the lowest noise, since the removed noise is replaced by the lowest possible amount. Technical limitations make this solution not ideal. The dilution refrigerator has a finite cooling power at the mixing chamber (of the order of $10 \mu\text{W}$). Dissipating all the power there would heat up the whole plate. The compromise is to remove a large part of the noise at the 3 K plate where the cooling power is larger. One trick to limit the absorption at the base plate is to use a directional coupler instead of an attenuator. Since the four arms of the beam splitters are controlled, this allows the discarded signal and noise to be redirected to higher temperature stages for dissipation, while adding noise that is thermalized at base temperature.

We now describe the components mounted on the base plate. Tubular filters (K&L 6L250-00089 low-pass up to 12 GHz) are used on all lines (see photograph in fig. 3.6) to protect from higher frequency noise that can affect the superconducting circuits by creating quasiparticles. Formable copper cables (Pasternack PE39415) connect the lines to the components placed on the breadboard plate. We removed the paint on the backside of the directional coupler (Pasternack PE2204-20 or similar) with sand paper to have better thermal contact to the copper plate. The sample holder bottom thickness was designed for it to be level with the directional coupler, and connect them with a male-male SMA connector (see photograph in fig. 3.6). Before attaching the sample holder to the breadboard plate, the two surfaces that will become in contact are cleaned with a fiber brush to remove the oxide layer and increase the thermal contact.

The discarded signal from the directional coupler travels upwards on a line identical to the input line. The power dissipates in the cables and at the attenuator at 3 K. This line can also be used for tone cancellation of the microwave pump tones before amplification.

In the output line, cryogenic isolators are used to prevent noise from propagating backwards to the device. Cryogenic circulators (Raditek RADC-4-8-Cryo with a bandwidth 4-8 GHz) are used with one port terminated by a cryogenic 20 dB attenuator and a cryogenic $50\text{-}\Omega$ matched load (XMA 2001-6112-02). The attenuator is redundant but provides a better surface to tighten the copper braiding for thermalization (see photograph in fig. 3.6). Alternatively, cryogenic isolators (Quinstar QCI-075900XM00 with a bandwidth 3-12 GHz) are also used for a larger bandwidth. The sample holder is typically terminated by a shorted cap to measure in reflection.

Finally, we describe the output lines. The signal to be measured travels upwards on niobium titanium superconducting cables (Coax Ltd SC-086/50-NbTi-NbTi) to the 3 K plate where it is amplified with a high-electron-mobility-transistor (HEMT) amplifier. An inner DC block (Paster-

nack PE8210) thermally decouples the amplifier from the superconducting lines and prevents the amplifier heat increasing the temperature of the cables until they are no longer superconducting. Four HEMT models were used all from Low Noise factory: LNF-LNC4-16A with bandwidth 4-16 GHz, two units LNF-LNC1-12A with bandwidth 1-12 GHz, and LNF-LNC4-8C with bandwidth 4-8 GHz with a lower added noise. The amplifiers do dissipate heat, which should be removed. To that end, they are thermally coupled to the 3 K plate with copper braids, attached to the HEMT bodies with screws (see fig. 3.6). The excess length of the DC lines for the power supplies of the amplifiers were attached to the dilution refrigerator posts with PTFE (“teflon”) tape (Klingerflon BS7786) that is compatible with vacuum and cryogenic temperatures. Between the 3 K plate and room temperature, beryllium copper cables (Coax Ltd SC-219/50-B-B) are installed for input and output lines.

3.3.4 Room-temperature equipment

In this section, we review the microwave components outside the dilution refrigerator, for a typical experiment (as schematically represented in fig. 3.7). The two most common measurements are of the linear microwave response of the system, and of the emitted spectrum. They are done while one or multiple microwave tones are applied to the system to alter its state.

Many microwave sources are employed in the experiments of this thesis. They are Rohde & Schwartz SMB 100A, Rohde & Schwartz SMF 100A, Keysight MXG N5183B, and Rohde & Schwartz SGS 100A. For weak tones, the sources can be used interchangeably. Only for the strong microwave pumps needed to attain large coupling strengths g do the noise properties of the source become relevant. Usually, the measured system is only sensitive to noise in a given quadrature (for example phase noise in sideband cooling) and at the specific narrow frequency range that corresponds to the mechanical sideband frequency (offset from the tone by Ω_m). The sources all have various noise emission that depends on the frequency of the source, the frequency of noise with respect to the carrier, and on the power setting. We calibrate the noise level for all the sources (see section 3.4.1) and select the device with the lowest noise in the relevant bandwidth when the noise is critical.

We filter the signal from the sources in multiple stages. Ideally, the noise in the sensitive bandwidth should be reduced to the level of the thermal noise background, although in practice that is not always possible for the strongest pump powers. First, when we work simultaneously with multiple microwave resonances of the optomechanical circuit, the far-detuned noise of

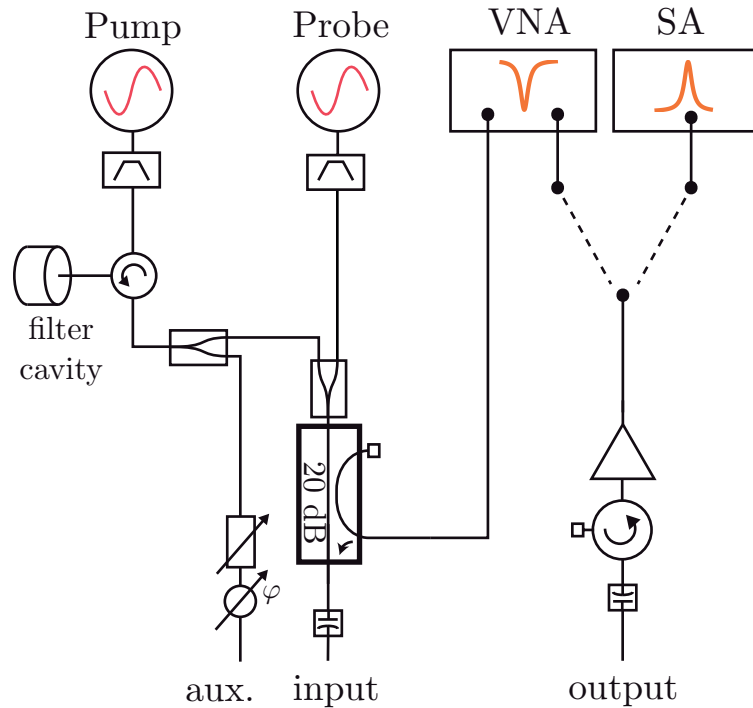


Figure 3.7: Room-temperature equipment that is connected to the ports of the dilution refrigerator (see fig. 3.6). The microwave sources (here labeled Pump and Probe) are filtered by band-pass (or high- and low-pass) filters and combined. For very large pump powers, it is necessary to use a filter cavity to reduce noise in the sensitive bandwidth. The output port of the VNA is combined to the signals with a 20-dB directional coupler, before the signals are sent to the input port. A double DC block prevents ground loops inside the dilution refrigerator. The output signals go through a double DC block and an isolator before being amplified. They are measured either by connecting the line to the input port of the VNA for a response measurement or by connecting the line to the spectrum analyzer (SA). Optionally, part of the strong pump power is split off at the input for tone cancellation. Variable attenuators and phase shifters are used to set its amplitude and phase, in order to cancel the pump tone after it interacts with the chip.

the sources is relevant, since the noise of a pump at one frequency can affect another cavity hundreds of MHz away. Standard filters (such as the band-pass filter Mini-Circuits VBFZ-5500-S+) easily solve the issue by removing the noise far from the carrier.

For the noise close to the tone frequency, custom tunable filter cavities (shown in fig. 3.8) filter out the noise in the critical bandwidth. The cavities, similar in design to those of Lecocq, Teufel, et al. (2015), are fabricated by the mechanical workshop out of two blocks of copper. A threading between the two pieces allows the tuning of the resonance frequency by choosing the length of the inner 3D cylindrical cavity. A threaded ring can block the cavity in a specific setting. A female-female SMA connector serves as an interface to the cavity. Inside, a short length of solder wire (about 2 cm) is inserted in the connector and serves as a formable antenna that can be bent to vary the coupling rate of the cavity to the line. The goal is to reach the critical coupling rate, with equal internal and external dissipation rates. Then the reflection coefficient dips to zero at the resonance frequency. A circulator (Pasternack PE8402) turns the single-sided cavity into a notch filter, which removes noise at the resonance frequency. Varying the length of the cavity allows the tuning of the filtered frequency over about 1 GHz. Multiple cavities of different sizes are needed to cover the range of microwave cavity frequencies in the optomechanical circuits. A cavity linewidth of about 1 MHz close to critical coupling is achieved. A small enough bandwidth is necessary to reduce the noise $\Omega_m/(2\pi) \approx 5 - 10$ MHz away from the tone frequency without absorbing the tone as well.

For a given measurement, the procedure is the following. First the system is measured without the filter cavity. The frequency of the relevant mechanical sideband is measured precisely. Then the filter cavity frequency is tuned and locked to that frequency, while monitoring its response. For fastest measurement, the response of the filter cavity is measured with the VNA. Since the filter cavity can be affected by moving the cables, it is better to do the final tuning when it is connected to the source it should filter. We use the source as a probe tone, and measure the amplitude response with the spectrum analyzer. This allows the precise tuning of the filter cavity in situ, with no need to change the connected cables afterwards. The coupling rate can be adjusted by rotating the SMA connector, to change the orientation of the antenna inside the cavity and its overlap with the mode.

The pump tone can be split in two and one half sent to the auxiliary line for tone cancellation. A variable attenuator (Pasternack PE7065-7) and a variable phase shifter (Pasternack PE8246) are tuned in order for the tone to cancel right after the directional coupler in the dilution refrigerator. Tone

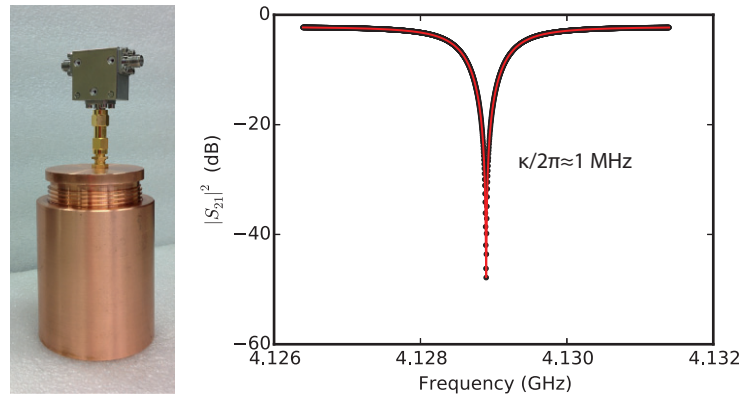


Figure 3.8: Filter cavity photograph and response. The left panel shows a photograph of the filter cavity interfaced with a circulator, to be used as a notch filter. The right panel shows the linear response of the cavity, which removes noise in a bandwidth of about 1 MHz. Figure reproduced from the supplementary information of Tóth, Bernier, Nunnenkamp, et al. (2017).

cancellation is necessary for strong pumps that would otherwise saturate the HEMT partially, causing compression and distortion of the signals. The directional coupler acts as an asymmetric beam-splitter between the tone-cancellation signal and the pump reflected on the chip. If the two signals interfere destructively in the port leaving to the output line, they must interfere constructively in the port travelling backwards on the input line, by conservation of energy. The strong tone backpropagating on the input line causes no harm since it is mostly absorbed at the 3 K attenuator. With this technique, about 30 dB of reduction are achieved for the pump travelling to the HEMT.

The output port of a vector network analyzer (VNA) (Rohde & Schwartz ZNB20) is combined with the microwave-source tones through a directional coupler. This minimizes the insertion loss for the tones, which are sometimes limited in power, at the cost of a large insertion loss for the VNA probe, from which only weak powers are required. Finally, a double DC block (Pasternack PE8212) decouples the lines of the outside and inside of the dilution refrigerator to prevent ground loops.

The output signals from the dilution refrigerator are measured either with the VNA, to extract the linear response of the system, or with a spectrum analyzer (Rohde & Schwartz FSW26), to obtain the spectral density of the signal. Here as well, a double DC block is used. An isolator (Innowave 1060 IQ-2) prevents the noise of the room-temperature active equipment

from travelling back inside the dilution refrigerator. An amplifier (Minicircuits ZVA-183-S+) gives the last stage of gain (26 dB) before the cable is either connected to the VNA or the spectrum analyzer, depending on the measurement. It is important for the added noise of the last amplifier to be small compared to the output noise of the HEMT, to ensure that the whole amplification chain is limited by the HEMT. The cables are room-temperature are Huber Suhner Sucotest 18 cables, as well as formable cables (Pasternack PE39415) for smaller lengths.

All the microwave sources as well as the VNA and the spectrum analyzer are locked to the same reference clock. This ensures that the uncertainty in the relative frequencies of all tones is minimal, and that the relative phases of the microwave sources are fixed. The reference clock from the FSW spectrum analyzer is distributed to all other devices using a low-noise distribution amplifier (Oscilloquartz OSA 5020).

3.4 Noise calibrations

The experiments of this thesis are restricted to linearized interaction between harmonic oscillators. As such, the only quantum aspect resides in the limit of the lowest amount of noise imposed by quantum mechanics. Careful calibration of the noise sources in the experiment is capital, if any statement about quantum noise is to be made. Apart from the thermal noise from room temperature, that need to be dealt with through attenuation at cryogenic temperatures (see section 3.3.3), there are two main sources of noise from active devices in the measurement. The first is the microwave signal generators, whose tones have phase and amplitude noise. The second is the added noise of the HEMT in the amplification process. In the following, we detail how both are calibrated.

3.4.1 Phase and amplitude noise of the sources

The noise of the microwave sources must be taken into account in the experiment. Close to the tone frequency, it can greatly exceed the thermal level and correspond to a very high effective temperature for the incoming microwave field. The optomechanical circuit is however not sensitive at all frequencies. In general, only two frequency ranges are relevant. First are the resonances of the microwave cavities. If there is a large noise within the resonance linewidth, the microwave cavity effectively heats up, as it thermalizes to an average of its internal and external bath temperatures. Second,

if microwave pumps are applied to the optomechanical system, there are frequencies at which the mechanical mode becomes sensitive to incoming microwave signals. Those correspond precisely to the frequencies of the mechanical sidebands of the pump. At those frequencies, the microwave field beats with the strong pump and results in a force unto the mechanical oscillator. Equivalently, the pump can be understood to mediate a frequency conversion pathway between microwave and mechanical frequencies. The noise from the mechanical thermal bath is converted to microwave frequencies (as the mechanical sideband) and reciprocally microwave noise at the same frequency is converted to mechanical motion. In effect, the mechanical mode is sensitive to the effective temperature of the microwave cavity at those particular frequencies. In practice, we are concerned mainly with the noise that reaches the mechanical mode. It is sufficient to have the effective temperature of the microwave cavity low enough locally at the frequency that corresponds to the mechanical resonance.

Phase and amplitude noise measurement are performed by connecting the microwave sources to a signal source analyzer (Rohde & Schwartz FSUP). Alternatively, the spectrum analyzer (Rohde & Schwartz FSW26) can be used, with the software option for the Phase Noise application. In the Phase Noise application, the device locks to the tone of the source. It then measures the noise relative to the carrier frequency and power, in dBc/Hz units (noise density relative to the power of the carrier). The FSW has an option for AM noise rejection, that removes amplitude noise to measure only phase noise. That option is only possible when the device is set to the I/Q sweep mode. Otherwise, it is silently ignored. An estimate of the amplitude noise is obtained by subtracting the phase noise from the total noise.

An example of the noise spectrum of the microwave source Rohde & Schwartz SMF 100A is shown in fig. 3.9. Phase noise dominates over amplitude noise for most frequencies. In fig. 3.9b, there is a sharp increase of the noise when the power increases to 0 dBm. That is related to a change in the internal setting of the device that depends on the exact implementation of the device and is impossible to predict. Amplitude noise increases for larger output powers of the device, until it is commensurate with phase noise at 20 dBm.

In practice, the measurement should be performed at the precise carrier frequency and power needed for the microwave pump in a given experiment, since the relative noise can change for different internal settings of the source. When the noise properties are critical, the microwave source with the lowest noise in the relevant frequency range is picked for that particular experiment. Even the best performing microwave source has a noise exceeding the thermal

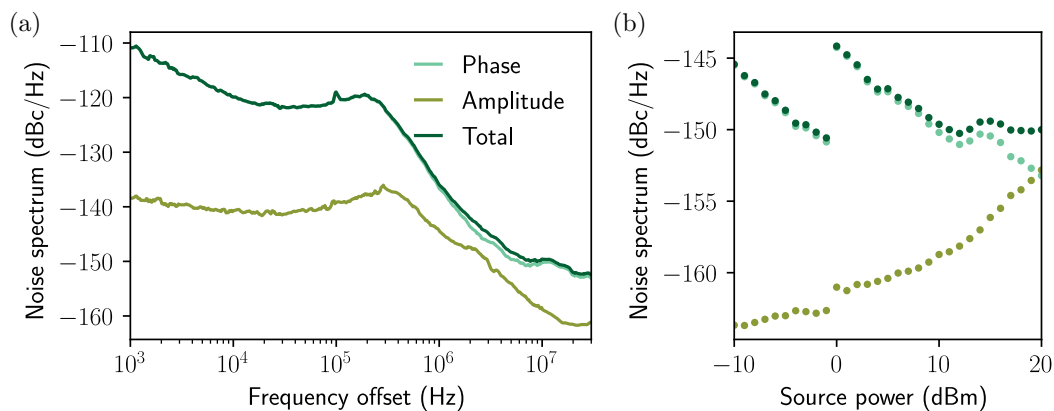


Figure 3.9: Measured phase and amplitude noise of Rohde & Schwartz SMF 100A. (a) Noise spectrum as a function of frequency offset from the carrier set at a frequency of 6 GHz and at a power of 10 dBm. (b) Noise spectrum as a function of the tone power, offset by 10 MHz from the carrier.

level of -174 dBm/Hz at higher powers and a tunable filter is employed to reduce it as much as possible, as detailed in section 3.3.4.

3.4.2 Calibration of the HEMT

The added noise in the amplification chain to the emission spectrum is important to know, since it gives an absolute scale to which to compare the signals. In a microwave measurement setup, the many cables and components prevent from estimating precisely the insertion loss on the line a priori. Even if the characteristics of the individual components are known, their combination can have reflections and standing waves from slight impedance mismatches that modify the insertion loss as a function of frequency in a non-trivial way. Calibrating the added noise of the full chain, as it stands in the experiment, allows the reconstruction of the absolute power of the signal as it was emitted at the beginning of the chain. In the following, we give a model for the gain and added noise in our system, and present the method used to calibrate the added noise of the HEMT in the signal path.

First, we model the measurement chain and what is the added noise, as represented schematically in fig. 3.10b. The signal of interest, of power P_s is emitted from the device in the sample holder. That constitutes the reference point where we want to know the power of the signal. It is then attenuated by a fraction α , due to all the components and cables on its way

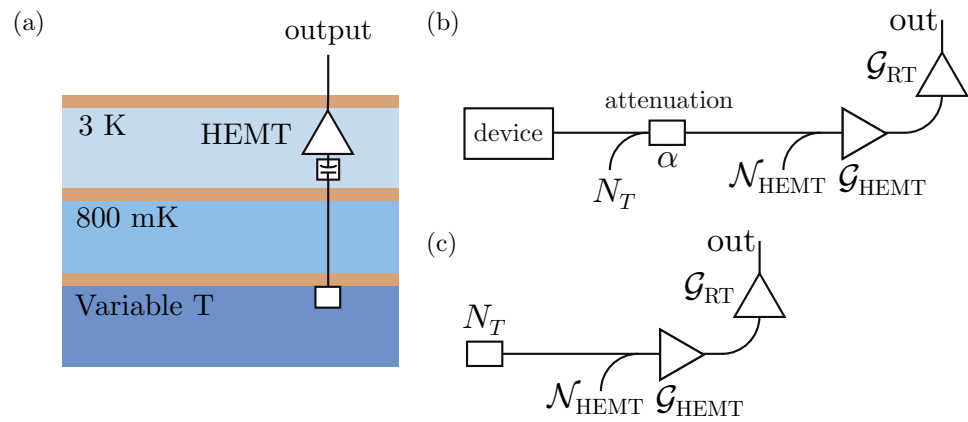


Figure 3.10: Scheme for the calibration of the HEMT amplifiers. (a) Experimental setup to calibrate the HEMT. A cryogenic matched load is attached to the output lines at the base plate. The temperature of the whole plate is tuned to control the temperature of the matched load and inject a known amount of Johnson noise in the HEMT amplifier. (b) Model of the amplification chain in a normal experiment, including the insertion loss α between the device and the HEMT. (c) Model for the calibration method. The insertion loss α is not accounted for with this method and must be estimated independently.

to the HEMT. The HEMT amplifier adds a noise $\mathcal{N}_{\text{HEMT}}$, then amplifies both signal and noise by the power gain $\mathcal{G}_{\text{HEMT}}$. The signal travels finally to the spectrum analyzer where it is measured, with a gain \mathcal{G}_{RT} that includes both room-temperature amplification and all the insertion loss along the line. The measured power is

$$P_{\text{meas}} = \mathcal{G}_{\text{RT}} \mathcal{G}_{\text{HEMT}} (\alpha P_s + (1 - \alpha) N_T + \mathcal{N}_{\text{HEMT}}). \quad (3.2)$$

The insertion loss before the HEMT contributes a noise N_T , due to the effective temperature of the dissipative part of the attenuation. Ideally, the amplification and added noise at room-temperature after the HEMT should add a noise negligible compared to the amplified HEMT noise $\mathcal{G}_{\text{HEMT}} \mathcal{N}_{\text{HEMT}}$. There is no need to suppose this however. Any extra noise can be absorbed in a slightly increased effective $\mathcal{N}_{\text{HEMT}}$, which is taken into account in the calibration. The complete added noise with respect to the reference point at the device is

$$\mathcal{N}_{\text{added}} = \frac{1}{\alpha} \mathcal{N}_{\text{HEMT}} + \frac{1 - \alpha}{\alpha} N_T. \quad (3.3)$$

The first term is the HEMT noise that is effectively increased by the insertion loss, since the signal-to-noise ratio decreases as a result. The second term, the thermal noise due to the temperature of the dissipative component of the attenuation, is normally much smaller than the HEMT noise (with an effective temperature of ~ 100 mK compared to ~ 4 K for the HEMT). While it can usually be neglected, in principle it can also be calibrated as part of the added noise.

Ideally, the full added noise $\mathcal{N}_{\text{added}}$ can be calibrated. A perfect calibration scheme consists in replacing the device by a tunable source of noise N known on an absolute scale. The measured output noise is then

$$P_{\text{meas}}^{\text{ideal cal.}} = \mathcal{G}_{\text{RT}} \mathcal{G}_{\text{HEMT}} \alpha (N + \mathcal{N}_{\text{added}}). \quad (3.4)$$

Two measurements of the output noise for two different known levels of the noise N suffice to calibrate both the added noise and the absolute gain of the full measurement chain $\mathcal{G}_{\text{chain}} = \mathcal{G}_{\text{RT}} \mathcal{G}_{\text{HEMT}} \alpha$. The tunable noise source must affect neither the HEMT performance nor the effective temperature of the attenuation before the HEMT.

We present now the implemented calibration scheme and how it deviates from the ideal case. The setup is illustrated in fig. 3.10a. The noise source is a cryogenic matched load (XMA 2001-6112-02) fixed to the mixing-chamber plate for thermalization. That implies that the insertion loss between the device and the plate is not taken into account in the calibration. Different noise temperatures are reached by stabilizing the base plate temperature

to different levels. The mixture of helium 3 and 4 in the dilution cycle is first collected, then a small proportion is reinjected and circulated to help stabilize the temperature. Using a heater at the base plate, the temperature can be swept from about 0.8 K to 10 K in a controllable manner. As a consequence, the leftover attenuation between the base plate and the HEMT (coming mainly from cable losses) is heated as well as the matched load. One cannot then assume that its temperature is constant. In our model, shown in fig. 3.10c, we neglect this contribution to the insertion loss. That is equivalent to assuming that the dissipative elements in the insertion loss thermalizes to the same temperature as the matched load. The measured noise is

$$P_{\text{meas}}^{\text{cal.}} = \mathcal{G}_{\text{RT}} \mathcal{G}_{\text{HEMT}} (N_T + \mathcal{N}_{\text{HEMT}}) = \mathcal{G}_{\text{RT}} \mathcal{G}_{\text{HEMT}} \lambda (T + T_{\text{HEMT}}). \quad (3.5)$$

The noises N_T and $\mathcal{N}_{\text{HEMT}}$ are large enough to be classical and proportional to a corresponding effective temperature through a proportionality constant λ . For each frequency point, the measured noise can be fitted as a linear function of T (an example is shown in fig. 3.11a). Its intercept with the x -axis corresponds to $-T_{\text{HEMT}}$. In effect, the added noise of the HEMT is compared to the Johnson noise at different temperatures. The calibrated thermometer at the base plate provides the absolute scale that anchors the calibration. An example of the noise temperature as a function of frequency is given for the HEMT amplifier LNF-LNC1-12A in fig. 3.11b.

Since it is not calibrated, the insertion loss α must be independently estimated to properly account for the effective added noise $\mathcal{N}_{\text{added}}$. The main contribution comes from the cables, directional coupler and the cryogenic isolators between the sample holder and the mixing-chamber plate. In the case of two Quinstar isolators, their insertion loss was measured to be 1.6 dB at 77 K. The components were immersed in liquid nitrogen and their insertion loss measured with the VNA. The insertion loss of these components at base temperature should be lower (since the resistivity of normal metals increase with temperature), and this estimate provides an upper-limit for the added noise. However, the relevant attenuation includes the cables and connections between the base plate and the HEMT, that is not completely taken into account in our calibration scheme.

3.5 Characterization of the chip

The first step for a newly cooled device is to subject it to a set of characterization routines and extract important experimental parameters. First, the

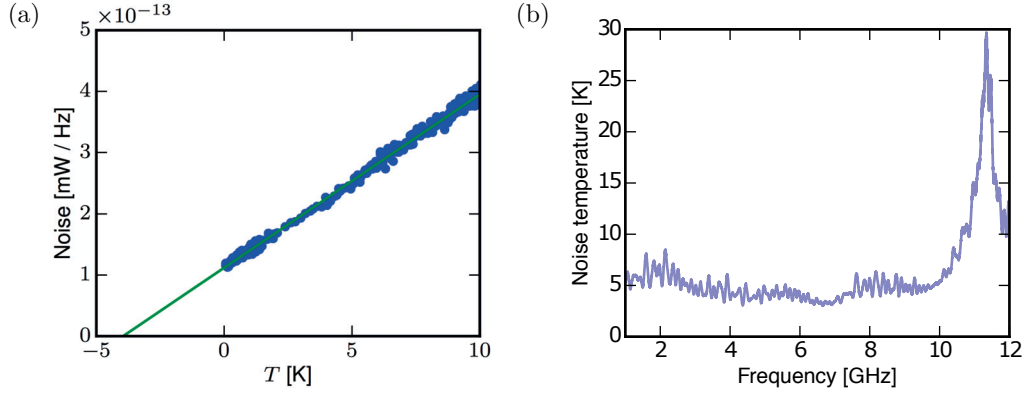


Figure 3.11: Example measurement for the calibration of the HEMT model LNF-LNC1-12A. (a) For each frequency (here 4.13 GHz) the output noise as a function of temperature is fitted, to extract the added noise temperature of the HEMT from the x -axis intercept. (b) Calibrated noise temperature as a function of frequency. Figure adapted from the supplementary information of Tóth, Bernier, Nunnenkamp, et al. (2017).

microwave resonances of the chip are probed and fitted. Then, we look for mechanical modes associated to the various microwave cavities. A few measurements are done on the mechanical oscillator to deduce its resonance frequency, its dissipation rate and the vacuum optomechanical coupling strength g_0 . In the following, we detail the relevant characterization procedures and the theoretical models that support them. In appendix C, the measured parameters of the different samples used for the experimental results of this thesis are listed.

3.5.1 Fitting microwave resonances with circles

When measuring the linear response of the chip with the VNA, the microwave resonances of the circuit are evidenced by sharp dips in amplitude and fast variation in phase. From the response in transmission $S_{21} = V_1^+/V_0^+$ or in reflection $S_{11} = V_0^-/V_0^+$ (see definitions in section 2.3.3), should be extracted the parameters of the cavity: the resonance frequency ω_c , the full dissipation rate κ and the internal and external rates $\kappa_0, \kappa_{\text{ex}}$. The resonance frequency in particular must be known precisely, as it determines the detuning Δ of the microwave pumps applied to the optomechanical system. The dissipation rates are required in the characterization of g_0 (see section 3.5.2).

In the ideal case, the response (given by eq. (2.105) for a one-sided cavity

and by eq. (2.108) for a two-sided cavity in transmission) gives a Lorentzian dip in amplitude, of width κ and centered on the resonance frequency ω_c . From the depth, the ratio $\kappa_0/\kappa_{\text{ex}}$ can be deduced as well. In the actual experiment, the response is altered in two respects. First, attenuation and delay along the line imply that the ideal response is overall multiplied by a complex number of unknown modulus and phase. Renormalizing properly the response solves this issue and it can still be fitted by a Lorentzian. Secondly, there exist in general slight impedance mismatches along the line that cause reflections near the cavity on the transmission line of the chip. These result in interferences which modify the resonance shape into a Fano function (Fano, 1961) rather than a Lorentzian dip in amplitude. Fortunately, the effect of the impedance mismatch can be modeled and the correct parameters still be extracted.

The solution comes from considering both complex components of S_{21} and S_{11} at once rather than fitting individually their amplitude and phase. The response of a harmonic mode forms a circle when represented on the complex plane, as a function of frequency ω . This is one more link between harmonic oscillators and circles. The effect of impedance mismatch amounts to a rotation and a change of diameter of this circle, but the parameters can still be extracted in general (Khalil et al., 2012; Megrant et al., 2012; Deng, Otto, and Lupascu, 2013). An example of how the Fano resonance forms a circle in the complex plane is shown in fig. 3.12. The transmission response of a two-sided cavity (“notch” configuration) is particularly beneficial as it allows the precise characterization of both κ_0 and κ_{ex} as well as κ and ω_c (Probst et al., 2015). For practical reasons, we often measure in reflection only, which makes the parameters harder to estimate (Stevens, 2017). In practice, the complex functions S_{21} and S_{11} are fitted by circles, using code adapted from Probst et al. (2015).

In the following, we give a theoretical description of how resonances form circles on the complex plane. First, the two-sided cavity measured in transmission is analyzed. All the parameters can conveniently be extracted in that case. Second, the one-sided cavity measured in reflection is exposed. While the resonance frequency ω_c and the full dissipation rate κ can still be fitted, it is not clear whether the internal and external dissipation rates can be known in general. In both cases, the ideal case is contrasted with what happens in the presence of impedance mismatch.

Before specific models are explored, we start by analyzing how a circle on the complex plane can be constructed. Consider the function

$$S(x) = \frac{1}{1 + ix} \quad (3.6)$$

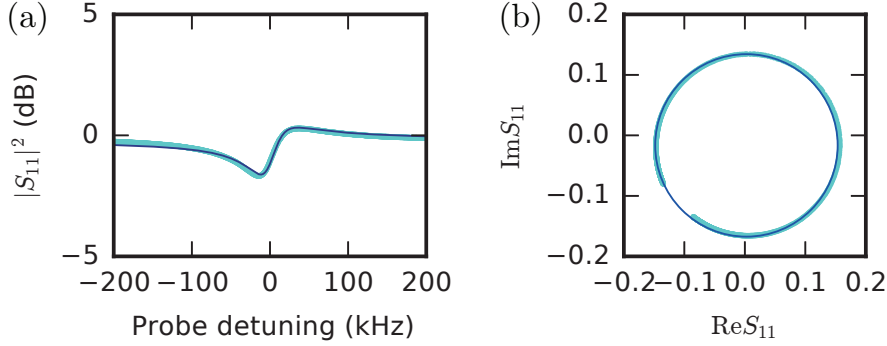


Figure 3.12: Example of fitting a circle to the complex response S_{11} . The very asymmetric Fano response in amplitude (a) corresponds to a perfect circle when both amplitude and phase are considered as a complex response (b). The data corresponds to the matching color curve in fig. 4.5b. Figure reproduced from the supplementary information of Tóth, Bernier, Nunnenkamp, et al. (2017).

with x a real parameter. To understand that this function describes a circle on the complex plane, one can rewrite it as

$$\begin{aligned}
 S(x) &= \frac{1}{2} + \left(\frac{1}{1+ix} - \frac{1}{2} \times \frac{1+ix}{1+ix} \right) = \frac{1}{2} + \frac{1}{2} \times \frac{1-ix}{1+ix} \\
 &= \frac{1}{2} (1 + e^{-i2 \arctan(x)}).
 \end{aligned} \tag{3.7}$$

From this, one deduces that $S(x)$ describes a circle of radius $1/2$ centered on the point $1/2$. Far from resonance ($|x| \gg 1$), $S(x) \approx 0$ and on resonance ($x = 0$), $S(0) = 1$. The aim in the following will be to rewrite the different expressions for the responses in the form of eq. (3.6) in order to identify the circle.

In the fitting algorithm, the position and size of the circle is first determined. Then the function of the angle with respect to the center of the circle $2 \arctan(x)$ is deduced. By fitting this function, one can extract both the angular velocity as a function of the frequency ω , and the frequency that corresponds to $x = 0$, the point at which the angle changes the fastest. The first general gives information about the dissipation rate, and the latter usually corresponds to the resonance frequency.

Two-sided cavities

We start with the ideal case of the two-sided cavity. The expression for S_{21} , already derived in eq. (2.108), can be rearranged as

$$S_{21} = \frac{\frac{1}{2}\kappa_0 - i(\omega - \omega_c)}{\frac{1}{2}\kappa - i(\omega - \omega_c)} = 1 - \frac{\kappa_{\text{ex}}^{\text{n}}}{\kappa} \frac{1}{1 - i2(\omega - \omega_c)/\kappa}. \quad (3.8)$$

It forms a circle of radius $\kappa_{\text{ex}}^{\text{n}}/\kappa$, that starts at $S_{21} = 1$ for $\omega \rightarrow \pm\infty$ and gives $S_{21} = 1 - \kappa_{\text{ex}}^{\text{n}}/\kappa$ at resonance $\omega = \omega_c$. For $\kappa_{\text{ex}}^{\text{n}} = \kappa$, the coupling is critical and the circle crosses the origin. The angular velocity corresponds to the total dissipation rate κ and the fastest point ($x = 0$) to the resonance frequency ω_c .

The inverse of the response function S_{21}^{-1} gives information about the resonance as well. It is expressed as

$$S_{21}^{-1} = 1 + \frac{\kappa_{\text{ex}}^{\text{n}}}{\kappa_0} \frac{1}{1 - i2(\omega - \omega_c)/\kappa_0}. \quad (3.9)$$

The circle also starts at 1 but lies away from the origin. The fastest point is also at resonance, but the angular velocity now corresponds to the internal dissipation rate κ_0 .

An impedance mismatch can be modeled as an additional impedance ΔZ in series with Z_{eq} , the equivalent impedance of the resonator coupled to the line (derived in eq. (2.104)), as shown in fig. 3.13a. Note that in the model it does not matter whether the impedance mismatch physically occurs before or after the resonator, or even spread at different location. It is always equivalent to a modification of the impedance in series with Z_{eq} . We first consider the modification of the dynamics of the resonator due to ΔZ . Following a method similar to what was used in section 2.3.3, we compute the equivalent impedance in the RLC circuit due to the coupling to the transmission line, to be

$$\tilde{Z}_{\text{coup}}^{\text{n}} = \frac{\omega^2 M^2}{2Z_0 + \Delta Z} = \frac{\omega^2 M^2}{|2Z_0 + \Delta Z|} e^{i\phi} \quad (3.10)$$

where ϕ is the complex phase of $1/(2Z_0 + \Delta Z)$. Here $\tilde{Z}_{\text{coup}}^{\text{n}}$ can be complex, since there can in general be a reactance component to ΔZ . In the absence of an impedance mismatch ΔZ , when $Z_{\text{coup}}^{\text{n}}$ is purely real, it increases the bare dissipation rate κ_0 by an amount $\kappa_{\text{ex}}^{\text{n}}$. For a complex $\tilde{Z}_{\text{coup}}^{\text{n}}$, its imaginary component will modify the resonance frequency of the resonator ω_c as well. In the high- Q limit which we consider, the external coupling rate is small compared to the frequency and the change in frequency must be small. We

therefore neglect any higher order nonlinear effect coming from the frequency dependence of eq. (3.10) and substitute $\omega \rightarrow \omega_c$. The total impedance in the *RLC* resonator is given by

$$\begin{aligned} Z_{\text{res}} &= R - iL\omega + \frac{i}{\omega C} + \tilde{Z}_{\text{coup}}^{\text{n}} \\ &\approx L\kappa_0 - iL(\omega - \omega_c) + \tilde{Z}_{\text{coup}}^{\text{n}} \\ &= L(\kappa_0 + \tilde{\kappa}_{\text{ex}}^{\text{n,tot.}}) - iL(\omega - \tilde{\omega}_c^{\text{n}}). \end{aligned} \quad (3.11)$$

The resonance frequency has shifted according to⁴

$$\tilde{\omega}_c^{\text{n}} = \omega_c + \frac{1}{L} \text{Im}\{\tilde{Z}_{\text{coup}}^{\text{n}}\} = \omega_c + \frac{\omega_c^2 M^2}{L|2Z_0 + \Delta Z|} \sin \phi = \omega_c + \kappa_{\text{ex}}^{\text{n,*}} \sin \phi. \quad (3.12)$$

The total external coupling rate is

$$\tilde{\kappa}_{\text{ex}}^{\text{n,tot.}} = \frac{1}{L} \text{Im}\{\tilde{Z}_{\text{coup}}^{\text{n}}\} = \frac{\omega_c^2 M^2}{L|2Z_0 + \Delta Z|} \cos \phi = \kappa_{\text{ex}}^{\text{n,*}} \cos \phi. \quad (3.13)$$

For convenience of notation, we have introduced

$$\kappa_{\text{ex}}^{\text{n,*}} = \frac{\omega_c^2 M^2}{L|2Z_0 + \Delta Z|}. \quad (3.14)$$

The total external coupling rate $\tilde{\kappa}_{\text{ex}}^{\text{n,tot.}}$ includes the power emitted in both transmission lines (dissipated in each Z_0 in the model), as well as what is dissipated in the resistive part of ΔZ (which can be thought of as an extra contribution to the internal losses). The coupling rate for each individual channel is given by

$$\tilde{\kappa}_{\text{ex}}^{\text{n}} = \frac{\omega_c^2 M^2 Z_0}{L|2Z_0 + \Delta Z|^2} = \kappa_{\text{ex}}^{\text{n,*}} \frac{Z_0}{|2Z_0 + \Delta Z|}. \quad (3.15)$$

Note that in the present context, the resonator resonance frequency is defined as the frequency at which the imaginary component of Z_{res} vanishes.

⁴ There is an apparent paradox in this shift of frequency. In eq. (3.11), the expression is expanded around $\omega = \omega_c$ keeping only the first order $\omega - \omega_c$. If the other valid solution $\omega = -\omega_c$ is taken instead, then the change in frequency seems opposite: $\tilde{\omega}_c^{\text{n}} = -\omega_c + \frac{1}{L} \text{Im}\{\tilde{Z}_{\text{coup}}^{\text{n}}\}$ instead of $\tilde{\omega}_c^{\text{n}} = -\omega_c - \frac{1}{L} \text{Im}\{\tilde{Z}_{\text{coup}}^{\text{n}}\}$ to be consistent with the derived expression. One must remember that complex impedances are defined in the Fourier frequency domain. The change of sign in frequency $\omega \rightarrow -\omega$ must be accompanied by a conjugation of the complex phase of all impedances, such that $\phi \rightarrow -\phi$ and $\text{Im}\{\tilde{Z}_{\text{coup}}^{\text{n}}\} \rightarrow -\text{Im}\{\tilde{Z}_{\text{coup}}^{\text{n}}\}$.

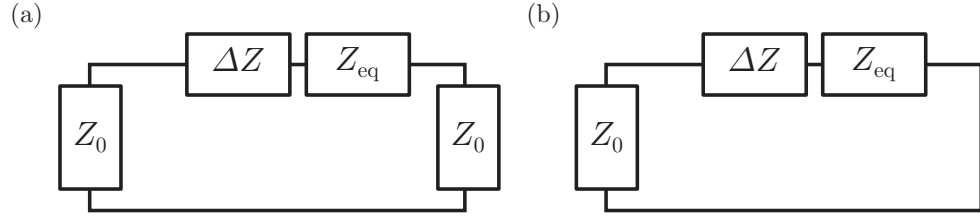


Figure 3.13: Model for impedance mismatch. The impedance mismatch is modeled as adding a potentially complex impedance ΔZ in series with the equivalent impedance of the resonator Z_{eq} to the ideal model shown in fig. 2.6, both in the case of a two-sided cavity (a) and a one-sided cavity (b).

It corresponds to the minimal absolute impedance $|Z_{\text{res}}|$ where an input excitation elicits the largest response. That is the relevant resonance frequency in the optomechanical interaction. The mechanical mode is only “aware” of the actual frequency where the microwave circuit has a resonance $\tilde{\omega}_c^n$, not of the bare frequency ω_c at which the circuit would resonate in the alternative situation where the impedance mismatch is absent.

With the impedance mismatch ΔZ , the response becomes

$$\begin{aligned} \tilde{S}_{21} &= \frac{2Z_0}{2Z_0 + Z_{\text{eq}} + \Delta Z} = \frac{2Z_0}{2Z_0 + \Delta Z} \frac{\kappa_0/2 - i(\omega - \omega_c)}{\frac{1}{2}(\kappa_0 + \kappa_{\text{ex}}^{n,*} e^{i\phi}) - i(\omega - \omega_c)} \\ &= 1 - \frac{\kappa_{\text{ex}}^{n,*} e^{i\phi}}{\kappa_0 + \tilde{\kappa}_{\text{ex}}^n} \frac{1}{1 - i2(\omega - \tilde{\omega}_c^n)/(\kappa_0 + \tilde{\kappa}_{\text{ex}}^n)}. \end{aligned} \quad (3.16)$$

The original circle of eq. (3.8) is transformed. Its diameter is increased and the circle is rotated by an angle ϕ , keeping the point 1 fixed. This rotation is deforming the origin Lorentzian function for the amplitude to an asymmetric Fano function. On the complex plane however, the circle stays a circle. The fastest rotation still occurs at the resonance frequency, now $\tilde{\omega}_c^n$, and the angular velocity gives the total dissipation rate $\tilde{\kappa} = \kappa_0 + \tilde{\kappa}_{\text{ex}}^n$. Conveniently, any overall change of the amplitude and phase in the measurement chain can be normalized away by requiring that $S_{21} \rightarrow 1$ off resonance as $\omega \rightarrow \pm\infty$.

The inverse response is now expressed as

$$\tilde{S}_{21}^{-1} = \left(1 + \frac{\Delta Z}{2Z_0}\right) \left(1 + \frac{\kappa_{\text{ex}}^{n,*} e^{i\phi}}{\kappa_0} \frac{1}{1 - i2(\omega - \omega_c)/\kappa_0}\right). \quad (3.17)$$

Here the apparent resonance frequency when the angle rotates the fastest is the bare one ω_c , not taking into account ΔZ . The angular velocity directly gives the internal dissipation rate κ_0 without any further calculation

required. Fitting this expression is especially useful in the context of optimizing the internal quality factor of the microwave resonator when it should be determined precisely (Probst et al., 2015).

One-sided cavities

We turn to one-sided cavities measured in reflection. The reflection coefficient in the ideal case, already given in eq. (2.105), can be expressed as

$$S_{11} = -1 + \frac{2\kappa_{\text{ex}}}{\kappa} \frac{1}{1 - i2(\omega - \omega_c)/\kappa}. \quad (3.18)$$

Because of the short-circuit boundary condition, the reflection coefficient is -1 away from resonance. The resonance is a circle of radius $2\kappa_{\text{ex}}/\kappa$, going towards the origin. At critical coupling $\kappa_{\text{ex}} = \kappa_0$, the diameter is 1 and the circle crosses the origin. For an overcoupled cavity $\kappa_{\text{ex}} > \kappa_0$, the circle encompasses the origin. The fastest point is at resonance ω_c and the angular velocity gives the total dissipation rate κ .

The inverse response is computed to be

$$S_{11}^{-1} = -1 - \frac{2\kappa_{\text{ex}}}{\kappa_0 - \kappa_{\text{ex}}} \frac{1}{1 - i2(\omega - \omega_c)/(\kappa_0 - \kappa_{\text{ex}})}. \quad (3.19)$$

The circle still starts from -1 , but stands to the left or the right depending on whether the cavity is under- ($\kappa_{\text{ex}} < \kappa_0$) or over-coupled ($\kappa_{\text{ex}} > \kappa_0$). It also rotates one direction or the other, depending on the the case, with a angular velocity that corresponds to $\kappa_0 - \kappa_{\text{ex}}$. In the limit of critical coupling $\kappa_{\text{ex}} = \kappa_0$, the circle asymptotically becomes a vertical line: it starts at -1 for $\omega \rightarrow -\infty$, then goes to $-1 + i\infty$ as $\omega \rightarrow 0^-$; then it jumps to $-1 - i\infty$ for $\omega \rightarrow 0^+$ and finishes back at -1 for $\omega \rightarrow \infty$.

An impedance mismatch is also equivalent to adding ΔZ in series with the resonator equivalent impedance Z_{eq} , as shown in fig. 3.13b. As in the case of the two-sided cavity, it does not matter in the model where the impedance mismatch occurs physically, whether before the cavity or near the short circuit.

We start by analyzing the impact of ΔZ on the dynamics of the *RLC* resonator. The equivalent impedance of the rest of the circuit is

$$\tilde{Z}_{\text{coup}} = \frac{\omega^2 M^2}{Z_0 + \Delta Z} = \frac{\omega^2 M^2}{|Z_0 + \Delta Z|} e^{i\phi} \quad (3.20)$$

where ϕ refers now to the complex phase of $1/(Z_0 + \Delta Z)$. Following the same argument as above, the resonance frequency and the total external

dissipation rate become

$$\tilde{\omega}_c = \omega_c + \kappa_{\text{ex}}^* \sin \phi, \quad (3.21)$$

$$\tilde{\kappa}_{\text{ex}}^{\text{tot.}} = \kappa_{\text{ex}}^* \cos \phi \quad (3.22)$$

with

$$\kappa_{\text{ex}}^* = \frac{\omega_c^2 M^2}{L |Z_0 + \Delta Z|}. \quad (3.23)$$

The coupling rate κ_{ex}^* includes both the power emitted back in the transmission line and what is dissipated in the resistive component of ΔZ . The coupling rate for the transmission line is

$$\tilde{\kappa}_{\text{ex}} = \tilde{\kappa}_{\text{ex}} \frac{Z_0}{|2Z_0 + \Delta Z|}. \quad (3.24)$$

The reflection response with the impedance mismatch is

$$\begin{aligned} \tilde{S}_{11} &= \frac{(Z_{\text{eq}} + \Delta Z) - Z_0}{(Z_{\text{eq}} + \Delta Z) + Z_0} \\ &= -\frac{Z_0 - \Delta Z}{Z_0 + \Delta Z} \left[1 - \frac{2Z_0}{Z_0 - \Delta Z} \frac{\kappa_{\text{ex}}^* e^{i\phi}}{\tilde{\kappa}} \frac{1}{1 - i2(\omega - \tilde{\omega}_c^n)/\tilde{\kappa}} \right] \end{aligned} \quad (3.25)$$

where $\tilde{\kappa} = \kappa_0 + \tilde{\kappa}_{\text{ex}}$ is the total dissipation rate. The overall factor comes from the modification of the reflection boundary condition due to the impedance mismatch ΔZ . As a consequence, the circle is not simply rotated by an angle ϕ as in the case of the two-sided cavity. It becomes more difficult to extract κ_0 and $\tilde{\kappa}_{\text{ex}}$ from the diameter of the circle, as it now depends on ΔZ in a complicated way. Fortunately, the rotation around the circle still gives the correct resonance frequency $\tilde{\omega}_c^n$ and the total dissipation rate $\tilde{\kappa}$.

The inverse response can be expressed as

$$\tilde{S}_{11}^{-1} = -\frac{Z_0 + \Delta Z}{Z_0 - \Delta Z} \left[1 + \frac{2Z_0}{Z_0 - \Delta Z} \frac{\kappa_{\text{ex}}^* e^{i\phi}}{\kappa_0 - \check{\kappa}_{\text{ex}}} \frac{1}{1 - i2(\omega - \check{\omega}_c)/(\kappa_0 - \check{\kappa}_{\text{ex}})} \right]. \quad (3.26)$$

The apparent resonance frequency

$$\check{\omega}_c = \omega_c - \text{Im} \left\{ \frac{\omega_c^2 M^2}{L(Z_0 - \Delta Z)} \right\} \quad (3.27)$$

is shifted in the wrong direction by a different amount compared to the physical resonance frequency $\tilde{\omega}_c^n$. The apparent dissipation rate, deduced from the angular velocity,

$$\kappa_0 - \check{\kappa}_{\text{ex}} = \kappa_0 - \text{Re} \frac{\omega_c^2 M^2}{L(Z_0 - \Delta Z)} \quad (3.28)$$

does not seem to correspond to any physical quantity either.

In conclusion, there is a cost to measuring the chip only in reflection. Not all the parameters can be extracted exactly in the most general case, unlike for transmission in a two-sided cavity. They can only be estimated approximately (Stevens, 2017). Nevertheless, the resonance frequency $\tilde{\omega}_c^n$ and the total dissipation rate $\tilde{\kappa}$ can still be easily extracted from the fitting a circle to \tilde{S}_{11} (similarly to \tilde{S}_{21} for the two-sided cavity). In practice, we only need to estimate $\tilde{\kappa}_{\text{ex}}$ in order to calibrate precisely g_0 and in some cases to fit the model. The most important parameter to know exactly is $\tilde{\omega}_c^n$. It is required to set correctly the detunings of the microwave pumps that determine the linearized optomechanical coupling. As was shown above, that is always possible, regardless of the impedance mismatch.

3.5.2 Measurement of g_0

The vacuum optomechanical coupling strength g_0 (eq. (2.125)) is a measure of how strongly the two quantum harmonic oscillators are coupled together. Unlike the coupling strength G in units of frequency shift per unit length (eq. (2.79)), g_0 is uniquely defined and can be used without ambiguity to compare different systems. In most cases of interest, a good performance indicator is the vacuum cooperativity $\mathcal{C}_0 = 4g_0^2/(\kappa\Gamma_m)$. For given microwave and mechanical quality factors, a higher value for g_0 enables stronger linear coupling strengths g to achieve better quantum control of the system. It is therefore important to correctly calibrate g_0 to be able to gauge the relative strengths of different designs for optomechanical systems.

In the following, we explain our method to calibrate g_0 using the mechanical sideband and a reference calibration tone. The theoretical model is first exposed, including the required assumptions. Then the measurement scheme is presented.

Theoretical model

A relatively weak microwave pump tone is set on resonance ($\Delta = 0$), producing two mechanical sidebands. They are equivalent and we will consider the measurement of the upper sideband ($\omega = \Omega_m$) for the purpose of the calculations. The noise emission in the sidebands corresponds mainly to noise originating from the mechanical thermal bath. If we suppose the mode well thermalized at a given temperature, the absolute scale of this noise as it is emitted is known up to the rate g_0 . With a weak calibration tone that travels

along the pump tone, the unknown attenuation and gain of the measurement chain can be factored out to calibrate g_0 .

The Langevin equations (eqs. (2.18) and (2.18)) with a pump of detuning $\Delta = 0$ in the Fourier domain are

$$\left(-i\omega + \frac{\kappa}{2}\right) \delta\hat{a}[\omega] = -ig \left(\delta\hat{b}[\omega] + \delta\hat{b}^\dagger[\omega]\right), \quad (3.29)$$

$$\left(-i\omega + \frac{\kappa}{2}\right) \delta\hat{a}^\dagger[\omega] = +ig \left(\delta\hat{b}[\omega] + \delta\hat{b}^\dagger[\omega]\right), \quad (3.30)$$

$$\left(-i(\omega - \Omega_m) + \frac{\Gamma_m}{2}\right) \delta\hat{b}[\omega] = -ig (\delta\hat{a}[\omega] + \delta\hat{a}^\dagger[\omega]) + \sqrt{\Gamma_m} \hat{b}_0[\omega], \quad (3.31)$$

$$\left(-i(\omega + \Omega_m) + \frac{\Gamma_m}{2}\right) \delta\hat{b}^\dagger[\omega] = +ig (\delta\hat{a}[\omega] + \delta\hat{a}^\dagger[\omega]) + \sqrt{\Gamma_m} \hat{b}_0^\dagger[\omega]. \quad (3.32)$$

We are interested in the mechanical noise emission, that is dominated by the mechanical bath noise \hat{b}_0 . The microwave thermal baths are assumed to be close to the ground state and negligible compared to the classical mechanical thermal noise. We assume also that the pump power, while relatively weak to disturb the system as little as possible, is still large enough compared to the vacuum fluctuations to linearize the interaction with a linear coupling strength g . For $\Delta = 0$, the two modes have very different frequencies in the rotating frame and it is not possible to take the RWA; the four equations for $\delta\hat{a}[\omega]$, $\delta\hat{a}^\dagger[\omega]$, $\delta\hat{b}[\omega]$ and $\delta\hat{b}^\dagger[\omega]$ must be considered.

In the absence of microwave noise, $\delta\hat{a}[\omega] + \delta\hat{a}^\dagger[\omega] = 0$ (from the sum of eqs. (3.29) and (3.30)) and the mechanical motion is only due to its thermal noise with

$$\delta\hat{b}[\omega] = \frac{\sqrt{\Gamma_m}}{-i(\omega - \Omega_m) + \Gamma_m/2} \hat{b}_0[\omega] \text{ and } \delta\hat{b}^\dagger[\omega] = \frac{\sqrt{\Gamma_m}}{-i(\omega + \Omega_m) + \Gamma_m/2} \hat{b}_0^\dagger[\omega]. \quad (3.33)$$

The output microwave field $\delta\hat{a}_{\text{out}}[\omega] = -\sqrt{\kappa_{\text{ex}}}\delta\hat{a}[\omega]$ carries the mechanical signal as

$$\delta\hat{a}_{\text{out}}[\omega] = \frac{ig\sqrt{\kappa_{\text{ex}}\Gamma_m}}{-i\omega + \kappa/2} \left(\frac{\hat{b}_0[\omega]}{-i(\omega - \Omega_m) + \Gamma_m/2} + \frac{\hat{b}_0^\dagger[\omega]}{-i(\omega + \Omega_m) + \Gamma_m/2} \right). \quad (3.34)$$

The white noise from \hat{b}_0 is filtered by two Lorentzians centered at $\omega = \pm\Omega_m$, resulting in two mechanical sidebands. Considering the upper sideband at $\omega = +\Omega_m$, the \hat{b}_0^\dagger term in eq. (3.34) can be neglected due to the Lorentzian suppression, supposing $\Omega_m \gg \Gamma_m$ (valid for a high mechanical Q factor). The symmetrized output spectrum can then be expressed as

$$\bar{S}_{\delta\hat{a}^\dagger\delta\hat{a}}^{\text{out}}[\omega] = \frac{g^2\kappa_{\text{ex}}\Gamma_m}{\omega^2 + (\kappa/2)^2} \frac{n_m(T)}{(\omega - \Omega_m)^2 + (\Gamma_m/2)^2} \quad (3.35)$$

where we inserted the expression for the thermal noise spectrum $\bar{S}_{\hat{b}^\dagger\hat{b}}^0 = \bar{n}_{\text{m,th}}(T) + 1/2 \approx \bar{n}_{\text{m,th}}(T)$, with $\bar{n}_{\text{m,th}}(T)$ the Bose-Einstein thermal occupancy of the mechanical mode at temperature T . There are two Lorentzian functions with widths of vastly different scales. The narrow mechanical sideband of linewidth Γ_{m} has an amplitude that depends on the state density of the microwave mode at $\omega = \Omega_{\text{m}}$. Since $\kappa \gg \Gamma_{\text{m}}$, we neglect the slow variation of the cavity profile and substitute $\omega \rightarrow \Omega_{\text{m}}$ in the first factor of eq. (3.35) from hereon. The total power in the sideband gives a measure of the rate of the anti-Stokes scattering process

$$\Gamma_{\text{scat}} = \int \frac{d\omega}{2\pi} \bar{S}_{\delta\hat{a}^\dagger\delta\hat{a}}^{\text{out}}[\omega] = \frac{g^2\kappa_{\text{ex}}}{\Omega_{\text{m}}^2 + (\kappa/2)^2} \bar{n}_{\text{m,th}}(T) \quad (3.36)$$

Alternatively, the same expression can be derived using Fermi's golden rule for the scattering rate at first order.

The coupling strength $g = g_0\sqrt{\bar{n}_{\text{c}}}$ depends on the strength of the pump tone, measured in the equivalent mean photon number as

$$\bar{n}_{\text{c}} = \frac{\kappa_{\text{ex}}}{(\kappa/2)^2} \frac{P_{\text{p}}}{\hbar\omega_{\text{c}}} \quad (3.37)$$

for a pump power P_{p} reaching the cavity on resonance. The power in the sideband (in units of W) can be expressed as

$$P_{\text{SB}} = \hbar(\omega_{\text{c}} + \Omega_{\text{m}})\Gamma_{\text{scat}} = 4g_0^2\bar{n}_{\text{m,th}}(T) \frac{(\kappa_{\text{ex}}/\kappa)^2}{\Omega_{\text{m}}^2 + (\kappa/2)^2} \underbrace{\frac{\omega_{\text{c}} + \Omega_{\text{m}}}{\omega_{\text{c}}}}_{\sim 1} P_{\text{p}}. \quad (3.38)$$

The powers P_{p} and P_{SB} are as measured respectively right before and right after interacting with the cavity and are inaccessible in the experiment. The pump power at the microwave source $P_{\text{p}}^{\text{src}}$, is attenuated by an insertion loss α before it reaches the cavity. The sideband emission as measured $P_{\text{SB}}^{\text{meas}}$ is amplified with an overall gain \mathcal{G} . In order to calibrate out these unknown variables, a weak calibration tone is introduced, that follows an identical path as the pump tone. It is tuned near the sideband at $\omega \approx \Omega_{\text{m}}$. We suppose that it is subjected to the same insertion loss α , being only a few MHz away in frequency. The measured sideband and calibration powers are

$$P_{\text{SB}}^{\text{meas}} = \mathcal{G}P_{\text{SB}} = \mathcal{G}\frac{P_{\text{SB}}}{P_{\text{p}}}\alpha P_{\text{p}}^{\text{src}}, \quad (3.39)$$

$$P_{\text{cal.}}^{\text{meas}} = \mathcal{G}\alpha P_{\text{cal.}}^{\text{src}}. \quad (3.40)$$

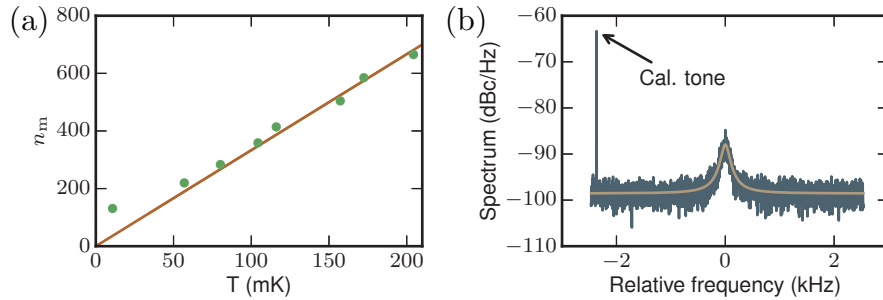


Figure 3.14: Calibration of g_0 . (a) Mechanical sideband power as a function of the temperature of the mixing chamber plate. For large temperature, the mechanical thermal noise is proportional to temperature, implying it is well thermalized. The emitted power is given in units of n_m by using the fit at larger temperatures and assuming thermalization using a classical linear expression for the noise. (b) Measured sideband and calibration tone power for the calibration of g_0 . Figure adapted from the supplementary information of Tóth, Bernier, Nunnenkamp, et al. (2017).

Taking the ratio of eqs. (3.39) and (3.40), α and \mathcal{G} are eliminated and we finally obtain an expression for the vacuum coupling strength

$$g_0^2 = \frac{1}{4\bar{n}_{m,\text{th}}(T)} \frac{\Omega_m^2 + (\kappa/2)^2}{(\kappa_{\text{ex}}/\kappa)^2} \frac{P_{\text{cal.}}^{\text{src}}}{P_{\text{p}}^{\text{src}}} \frac{P_{\text{SB}}^{\text{meas}}}{P_{\text{cal.}}^{\text{meas}}}. \quad (3.41)$$

We have assumed that the calibration tone does not interact with the cavity. That is only valid in the sideband resolved limit $\Omega_m \gg \kappa$. Otherwise, a correction should be included to take into account the fraction of the calibration tone power that is absorbed by the cavity. This fraction is given by the relative amplitude in a linear response measurement of the cavity at the frequency of interest compared to the background level. Note that κ_{ex} in the derivation above refers to the external coupling rate for an individual channel. In the case of a two-sided cavity, it corresponds to half the total external coupling rate $\kappa_{\text{ex}}^{\text{n,tot}}$.

Experiment

An important assumption in the calibration of g_0 is that the mechanical mode is thermalized to a known temperature. That is not the case at base temperature in the dilution refrigerator. We have measured the mode to be at an effective temperature of about 50 mK when the mixing-chamber plate is at the base temperature of 10 mK (see fig. 3.14a) For this reason, the

temperature is elevated to about 200 mK to perform the g_0 measurements, where it is safe to assume the mode to be well thermalized. We are careful to use the same cable type of the same length to connect the microwave sources for the pump and calibration tones to a combiner before the signals are sent into the dilution refrigerator. We present the spectrum from a typical g_0 measurement in fig. 3.14b.

3.6 Routine optomechanical measurements

We describe in the following a few standard measurements that are commonly done on an optomechanical system. In section 3.6.1, sideband damping and cooling of the mechanical mode is demonstrated. In section 3.6.2, the modification of the susceptibility of the microwave mode through the interaction with the mechanical mode is shown, called OMIT or OMIA depending on the parameters.

3.6.1 Sideband cooling

When a driving tone is applied to the red sideband ($\Delta = -\Omega_m$), the mechanical mode is damped and cooled, as explained in section 2.1.5. We measure the spectra of the mechanical sideband on resonance, as a pump tone is swept in power. The resonator with a resonance at 5.3 GHz of the sample HYB-20150924-4-17 was measured. The result is shown in fig. 3.15a. The linewidth of the mechanical sideband, that corresponds to the effective mechanical dissipation rate Γ_{eff} increases linearly with power, as shown in fig. 3.15d. This increase in damping of the mechanical motion results in a reduction of its average energy, since the thermal bath constituted by the microwave mode is effectively at a much lower temperature than the internal thermal mechanical bath. While the mechanical sideband power does not decrease with cooling power, the sideband spectrum normalized by the pump power is proportional to the displacement spectrum and gives a measure of the effective temperature of the mechanical oscillator.

The deduced mechanical mean occupancy n_m is shown in fig. 3.15e. To normalize the data properly, they are anchored to the thermal occupancy of the mechanical oscillator in the absence of cooling, at the effective temperature of 50 mK. This is above the base temperature of the mixing chamber (at about 10 mK), as the mechanical mode is not perfectly thermalized (see fig. 3.14a). The theoretical curve is a fit of the expression in eq. (2.34) to the data. In this example, the mechanical occupancy is reduced to about

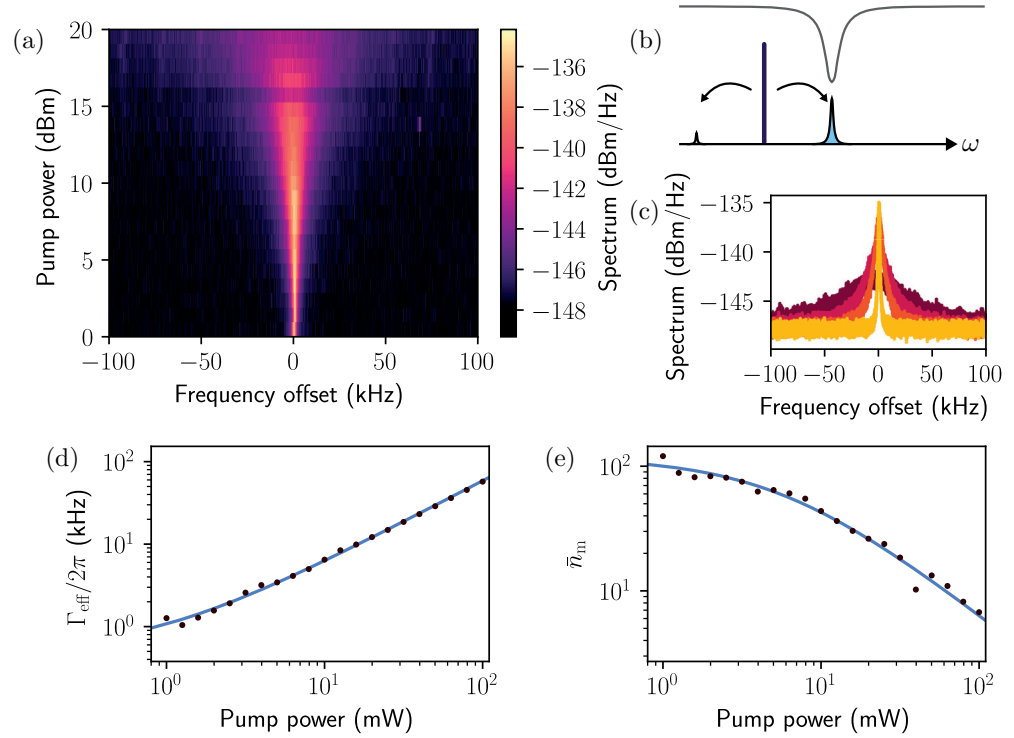


Figure 3.15: Sideband cooling of the mechanical mode. (a) Spectra of the mechanical sideband on resonance for increasing power of a pump tone on the red sideband ($\Delta \approx -\Omega_m$). (b) Scheme for the experiment in the frequency domain. A pump tone is placed red-detuned from the microwave cavity resonance ω_c by the mechanical frequency Ω_m , and its blue modulated sideband is measured on resonance. (c) Individual spectra corresponding to the powers 0, 10, 15, 20 dBm in (a) (increasing powers from yellow to dark red). (d) Fitted linewidth of the Lorentzian sidebands in (a), corresponding to the effective mechanical dissipation rate $\Gamma_{\text{eff}} = \Gamma_m(1 + \mathcal{C})$. (e) Mean mechanical occupancy \bar{n}_m as a function of pump power. The integrated power in the sideband divided by the pump power is proportional to the occupancy. The data is normalized by anchoring the extrapolation at low pump powers to the mechanical thermal occupancy at the estimated equilibrium temperature of 50 mK.

6.7 quanta, corresponding to an effective temperature of 3 mK. The calibration is subject to many systematic issues, which imply potentially large error in the mean occupancy at large cooling rates. Alternative calibration techniques, such as using the added noise of the HEMT as an absolute power reference (see section 4.8) or using sideband asymmetry for thermometry (see section 7.3) can give a more precise estimation of the effective mechanical temperature.

3.6.2 Optomechanically induced transparency and absorption

When a driving tone is applied near the red or blue mechanical sideband of the microwave resonance, the two modes interact, with nearly the same frequency in a rotating frame. The microwave susceptibility is modified according to eq. (2.35) for a red-detuned pump tone. An example measurement is shown in fig. 3.16. The response in amplitude of fig. 3.16a, shows a quick variation in the middle of the cavity resonance. This corresponds to a copy of the mechanical susceptibility, that is translated to microwave frequencies through the parametric interaction. On the complex plane (fig. 3.16b), it corresponds to two circles, one for each resonance. A circle with the angle moving slowly with respect to the frequency describes the microwave resonance (see section 3.5.1). Within this circle, a second circle with an angle changing faster with frequency corresponds to the mechanical resonance. For a pump on the red sideband ($\Delta \approx \Omega_m$), the two circles rotate in the same direction, with the mechanical circle inscribed in the microwave one. In fig. 3.16c, the mechanical feature of OMIT is shown on the complex plane for three different driving tone powers. For low powers, the mechanical-resonance circle starts with a small radius, that increases with the pump power until it reaches the same size as the microwave resonance circle. The speed of the angle around the circle correspond to the effective mechanical dissipation rate Γ_{eff} that also increases with power. The resonator with a resonance at 6.43 GHz of the sample AY_old_moreH-20180516-1-21 was used for the results shown.

In fig. 3.17, OMIT transmission amplitudes are shown for a sweep of the pump power. The effective mechanical dissipation rate Γ_{eff} grows linearly with the power until it reaches a significant fraction of the microwave dissipation rate κ (fig. 3.17b). This corresponds to the onset of the strong-coupling regime (Gröblacher et al., 2009; Teufel, D. Li, et al., 2011; Verhagen et al., 2012). Such a strong damping rate is a necessary condition for the engineering of a mechanical dissipative reservoir, as detailed in chapter 4. The bright resonance at 5.48 GHz of the sample HYB-20150924-4-24 is used for these

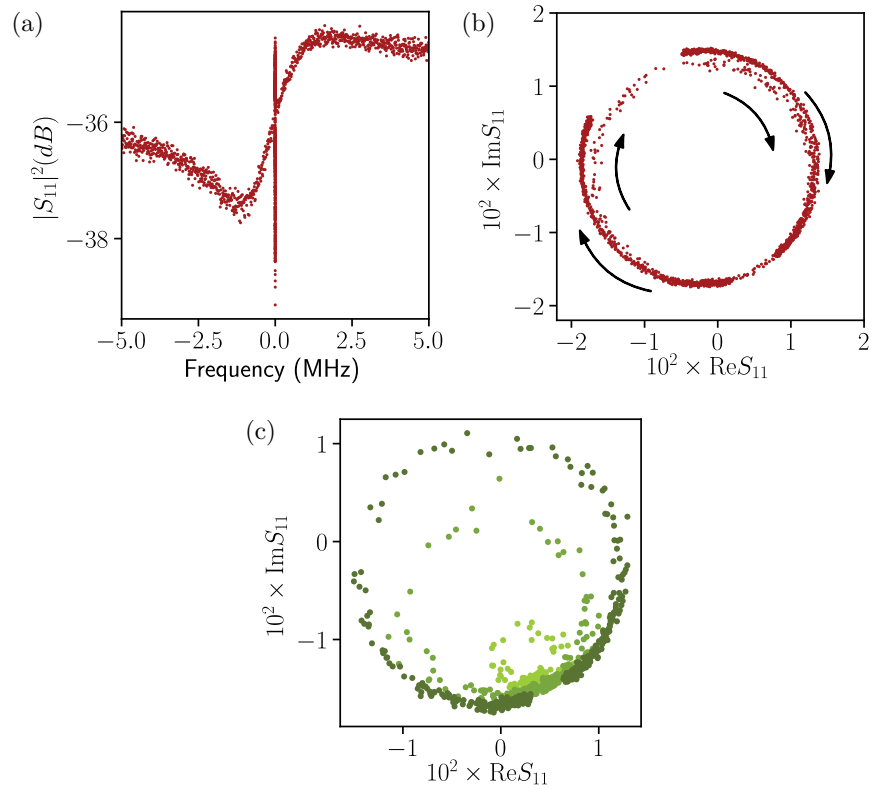


Figure 3.16: Measurement of OMIT/OMIA with a red-detuned pump tone. (a) Response of the microwave cavity in amplitude, with a narrow feature that corresponds to the mechanical resonance. Both the microwave resonance and the narrow mechanical feature have a Fano shape, such that the distinction between OMIT and OMIA (transparency or absorption) has little meaning in this case. (b) Same response shown on the complex plane. The mechanical feature of OMIT/OMIA with a red-detuned pump tone corresponds to a circle within the circle of the mechanical resonance. (c) OMIT/OMIA feature for increasing powers (light to dark green). The circle of the mechanical resonance increases in size with power until it has the same radius as the circle of the microwave resonance.

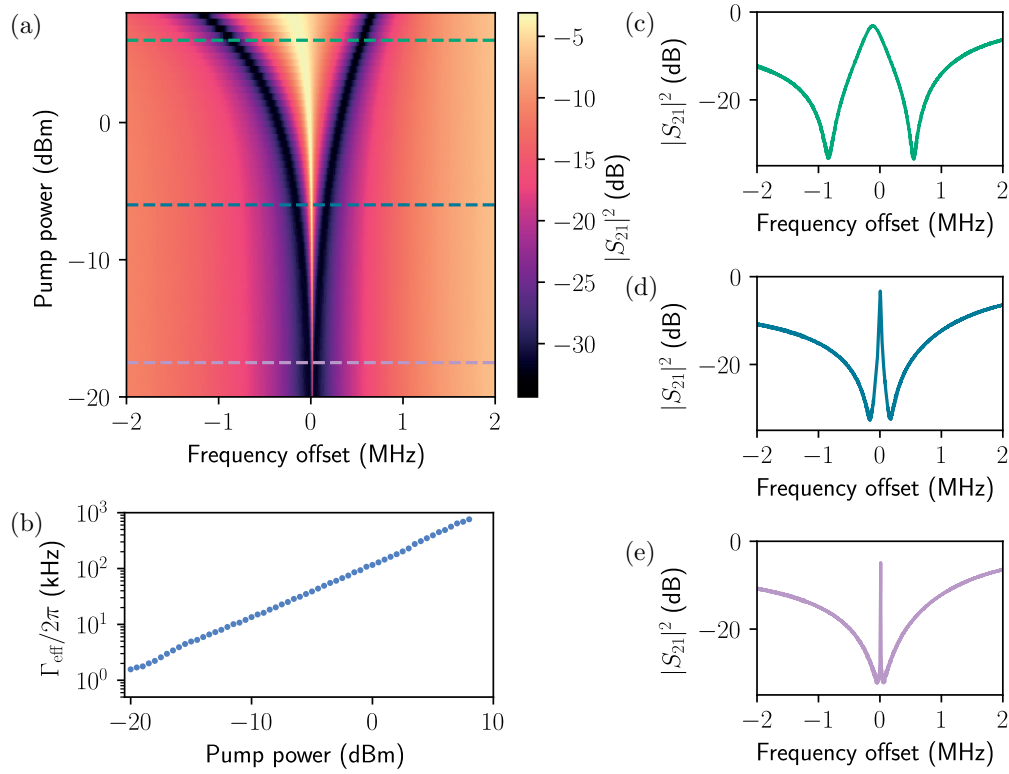


Figure 3.17: OMIT power sweep to the onset of strong coupling. (a) Transmission amplitude of the microwave cavity while a pump tone on the red sideband ($\Delta = -\Omega_m$) is swept in power. (b) Fitted mechanical effective linewidths Γ_{eff} extracted from the traces of the panel (a). (c,d,e) Traces corresponding to the line cuts of matching colors in the panel (a).

data.

A dissipative quantum reservoir for microwaves using a mechanical oscillator

We explain here how a mechanical oscillator can be turned into a dissipative reservoir for a microwave cavity. This chapter is adapted from the text of two previous publications (Tóth, Bernier, Nunnenkamp, et al., 2017; Tóth, Bernier, Feofanov, et al., 2018). In section 4.1, we introduce the experiment. In section 4.2, we explain how the circuit was designed with hybridized microwave modes in order to obtain the required dissipation rates. In section 4.3, we give details on the realization of the circuit. In section 4.4, we show how the interaction with the mechanical reservoir results in a modification of the parameters of the microwave cavity similarly to how the mechanical mode is modified through the usual optomechanical interaction (see section 2.1.5). In section 4.5, we explain the same mechanism in terms of dynamical backaction as originally introduced by Braginsky. In section 4.6, we give the experimental results of the modified microwave susceptibility. In section 4.7, we show how microwave amplification can result from the interaction with the mechanical reservoir, leading to an instability akin to that of a maser. In section 4.8, we measure the performance of the amplifier, which works close to the quantum limit in terms of added noise. In section 4.9, injection locking of the masing tone is demonstrated. Finally, in section 4.10, we conclude.

4.1 Introduction

Dissipation can significantly affect the quantum behavior of a system and even completely suppress it (Caldeira and Leggett, 1981). However, if carefully constructed, dissipation can relax the system of interest to a desired target quantum state. This pioneering insight was originally theoretically conceived and studied in the context of trapped ions (Poyatos, Cirac, and Zoller, 1996), experimentally first realized with trapped atomic ensembles (Krauter et al., 2011) and later with trapped ions (Barreiro et al., 2011; Lin et al., 2013; Kienzler et al., 2015). Moreover, reservoir engineering has recently also been realized in the context of circuit QED (Murch et al., 2012; Shankar et al., 2013; Leghtas et al., 2015). In these experiments the optical or microwave field provides a dissipative reservoir to the quantum systems. In cavity optomechanics (Aspelmeyer, Kippenberg, and Marquardt, 2014), in which a mechanical oscillator and electromagnetic degree of freedom are parametrically coupled, analogous ideas have been developed and reservoir engineering for the preparation of squeezed mechanical states has been theoretically proposed (Kronwald, Marquardt, and Clerk, 2013; Woolley and Clerk, 2014) and recently demonstrated (Wollman et al., 2015; Pirkkalainen, Damskäg, et al., 2015; Lecocq, Clark, et al., 2015). As in the atomic physics case, the electromagnetic field acts as the engineered environment of the quantum system of interest.

In contrast, recent theoretical work (Wang and Clerk, 2013; Metelmann and Clerk, 2014; Nunnenkamp et al., 2014; Kronwald, Marquardt, and Clerk, 2014; Metelmann and Clerk, 2015) has considered the opposite scenario where the mechanical degree of freedom is employed to provide a cold dissipative bath for light. This engineered bath can then be employed to achieve desirable quantum states of light or to modify the optical field properties. For example, such a dissipative reservoir for light can be exploited for amplification (Metelmann and Clerk, 2014; Nunnenkamp et al., 2014), entanglement generation (Wang and Clerk, 2013) or dissipative squeezing of electromagnetic modes (Kronwald, Marquardt, and Clerk, 2014). Moreover, it provides an ingredient to realize nonreciprocal devices (Metelmann and Clerk, 2015) such as isolators, circulators or directional microwave amplifiers. For a sufficiently cold mechanical reservoir, nonreciprocal devices implemented in this manner can operate in the quantum regime, with minimal added noise.

Here we engineer a mechanical oscillator into a quantum reservoir for microwave light. This is achieved in a microwave optomechanical system (Teufel, D. Li, et al., 2011) by engineering the mechanical dissipation rate to exceed that of the electromagnetic mode. This regime allows the demonstration of

dynamical backaction (V. Braginsky and A. Manukin, 1977) on microwave light, and the control of a microwave mode by tuning its coupling to the reservoir. Backaction amplification leads to stimulated emission of microwaves and maser action using the mechanical oscillator as the gain medium. Below the masing threshold, we implement a large-gain phase-preserving amplifier that operates with added noise 0.87 quanta (or a factor 2) above the quantum limit. Critically, this demonstrates that the mechanical reservoir for light can function as a useful quantum resource.

4.2 Dark and bright modes

We utilize a scheme in which two microwave modes are coupled to the same mechanical oscillator (Nunnenkamp et al., 2014). One (auxiliary) electromagnetic mode is used to damp the oscillator via optomechanical sideband cooling (Teufel, Harlow, et al., 2008; Schliesser, Rivière, et al., 2008) and engineer it into a cold bath for the other (primary) electromagnetic mode (fig. 4.1a). A key ingredient for the scheme is an optomechanical cooling rate from the auxiliary mode that greatly exceeds the electromagnetic decay rate of the primary microwave mode, necessitating vastly different decay rates for the employed microwave cavities. This is challenging to achieve with previously realized dual-mode circuits (Lecocq, Clark, et al., 2015), since any parasitic coupling between the two modes opens a decay channel, equilibrating their decay in energy. Here, we address this challenge by engineering hybridized modes with inherently dissimilar decay rates arising from interference in the output channel (cf. fig. 4.1b, c).

Specifically, we design an electromechanical circuit using two LC resonators both coupled inductively to a common feedline, one of which has a mechanically compliant vacuum-gap capacitor (Cicak et al., 2010) coupling mechanical vibrations to the microwave mode. The two resonators are strongly coupled through sharing a common inductor (cf. fig. 4.1b). In terms of the annihilation operators \hat{a}_1 and \hat{a}_2 of the bare modes, the resulting interaction Hamiltonian is given by

$$\hat{H}_{\text{int}} = \hbar J(\hat{a}_1^\dagger \hat{a}_2 + \hat{a}_2^\dagger \hat{a}_1) + \hbar \tilde{g}_0 \hat{a}_1^\dagger \hat{a}_1 (\hat{b} + \hat{b}^\dagger), \quad (4.1)$$

where \hat{b} designates the annihilation operator for the mechanical mode, J the intermode coupling strength, and \tilde{g}_0 the vacuum electromechanical coupling strength to the first mode (\hbar is the reduced Planck's constant). The symmetric and antisymmetric superpositions of the bare modes $\hat{a}_{\text{s,a}} = \frac{1}{\sqrt{2}}(\hat{a}_1 \pm \hat{a}_2)$

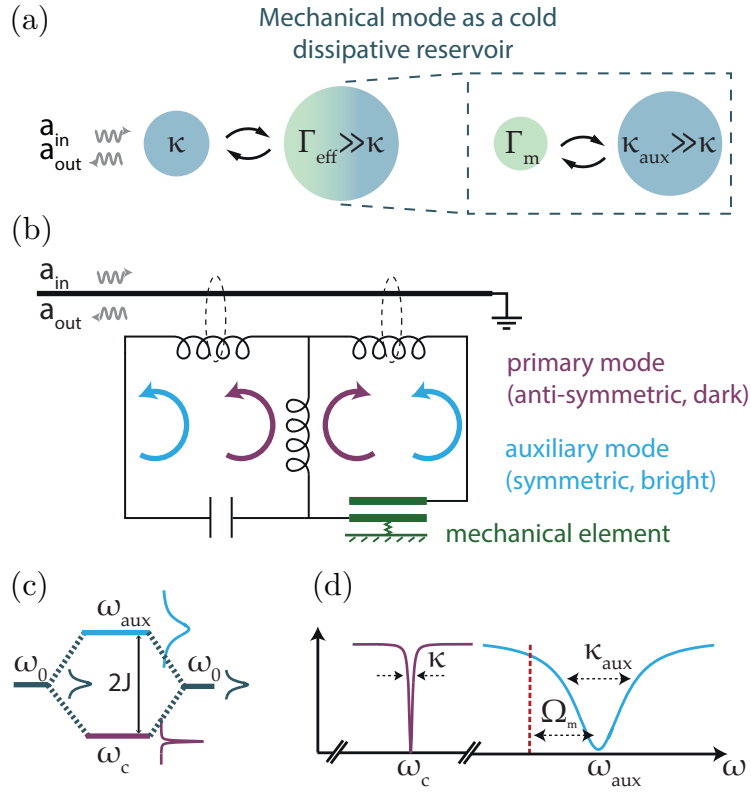


Figure 4.1: Realization of a mechanical reservoir for a microwave cavity in circuit optomechanics. (a) Schematic representation of a multi-mode electromechanical system in which a microwave mode with energy decay rate κ is coupled to an engineered mechanical mode acting as a dissipative reservoir with an effective energy decay rate $\Gamma_{\text{eff}} \gg \kappa$. (b) Circuit realization of the electromechanical system. Two lumped-element LC circuits – one containing a mechanically compliant capacitor – with matching resonance frequencies are inductively coupled and show normal-mode splitting, forming dark and bright modes (respectively used as the primary and auxiliary modes) to achieve $\kappa_{\text{aux}} \gg \kappa$. (c) Visual representation of the mode structure and the resulting asymmetric dissipation rates, originating from the interference in the output coupling. (d) Optomechanical sideband cooling the mechanical mode with the auxiliary, bright mode realizes a cold, dissipative mechanical reservoir for the primary, dark mode. Figure reproduced from Tóth, Bernier, Nunnenkamp, et al. (2017).

diagonalize the Hamiltonian. In terms of these hybridized modes the interaction Hamiltonian is given by

$$\hat{H}_{\text{int}} = \hbar J(\hat{a}_s^\dagger \hat{a}_s - \hat{a}_a^\dagger \hat{a}_a) + \hbar \frac{\tilde{g}_0}{2}(\hat{a}_s^\dagger \hat{a}_s + \hat{a}_a^\dagger \hat{a}_a)(\hat{b} + \hat{b}^\dagger). \quad (4.2)$$

If the bare modes are degenerate, the eigenmodes have an energy difference of $2\hbar J$ (fig. 4.1c) and are now, as a result of the interaction, both coupled to the micromechanical oscillator (Dobrindt, Wilson-Rae, and Kippenberg, 2008) with half the bare vacuum electromechanical coupling strength \tilde{g}_0 . We consider here the limit of a coupling large compared to the mechanical resonance frequency, $J \gg \Omega_m$, implying that we can neglect the cross terms of the form $\hat{a}_s^\dagger \hat{a}_a(\hat{b} + \hat{b}^\dagger)$, which are not resonant.

Critically, the new eigenmodes have dissimilar decay rates and form a bright (strongly coupled) and a dark (weakly coupled) mode resulting from interference of the bare-mode external coupling rates $\kappa_1^{\text{ex}}, \kappa_2^{\text{ex}}$ to the output channel. Physically, one can understand the difference by considering the topology of current flow in the modes (see fig. 4.1b). The symmetric mode has current flowing in the same direction in both resonators, causing their external magnetic flux to create currents that add up, leading to an increased coupling rate to the feedline. The antisymmetric mode has current flowing in opposite directions in the two resonators, causing the external magnetic flux to create currents that cancel out, leading to a suppression in the external coupling to the feedline (see fig. 4.1b, c). The density of current in each mode, computed through simulation, is shown in fig. 3.3.

Since the dissipation rates are proportional to the square of the coupling strength to the transmission-channel modes (see eq. (2.5)), we obtain the following expressions for the dissipation rates. The coupling strength for the symmetric, bright mode interfere constructively, leading to an external energy decay rate to the output feedline of $\kappa_s^{\text{ex}} = \frac{1}{2}(\sqrt{\kappa_1^{\text{ex}}} + \sqrt{\kappa_2^{\text{ex}}})^2$. Whereas, for the antisymmetric, dark mode, the interference is destructive, leading to a decreased external coupling rate $\kappa_a^{\text{ex}} = \frac{1}{2}(\sqrt{\kappa_1^{\text{ex}}} - \sqrt{\kappa_2^{\text{ex}}})^2$. For bare coupling rates similar in magnitude ($\kappa_1^{\text{ex}} \approx \kappa_2^{\text{ex}}$), this enforces the coupling-rate hierarchy $\kappa_a^{\text{ex}} \ll \kappa_s^{\text{ex}}$ necessary to achieve a dissipative mechanical reservoir with the present scheme (Nunnenkamp et al., 2014). In the remaining of the chapter, we refer to the dark mode as the primary mode and the bright mode as the auxiliary mode, with respective resonance frequencies ω_c and ω_{aux} and energy decay rates κ and κ_{aux} (fig. 4.1).

A former, unsuccessful design is illustrated in fig. 4.2. Two independent *LC* circuits interact with the same mechanical oscillator by each sharing one half of the central capacitor, which has a vibrating top plate and a split

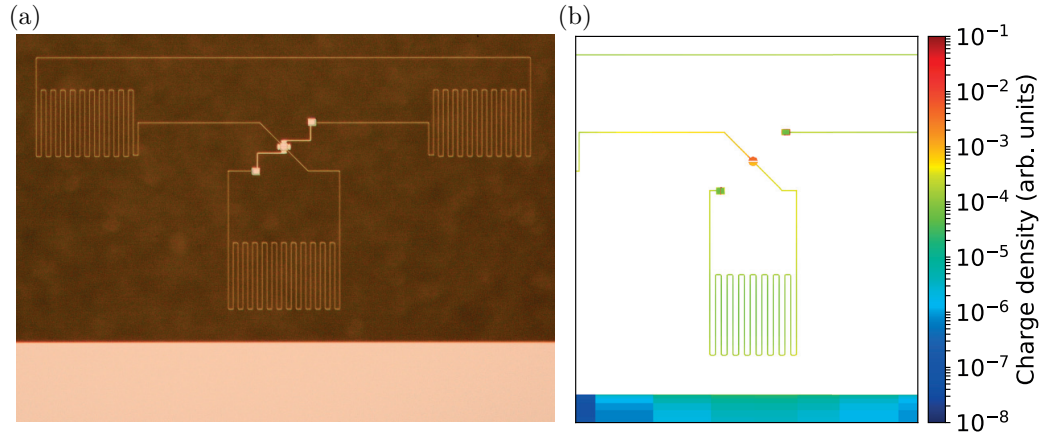


Figure 4.2: Unsuccessful design to obtain asymmetrically coupled microwave modes. (a) Optical microscope image of a fabricated chip. Two LC resonators are coupled to the same mechanical modes by sharing a capacitor with a split bottom plate. By design, the mode that is further from the transmission line is meant to have a lower inductive coupling rate. (b) Simulated charge density at the frequency of resonance of the top mode. The bottom part of the circuit, that is not resonant, acts as a capacitive coupling to the transmission line, increasing the total coupling rate.

bottom plate. An optical micrograph of a fabricated sample is shown in fig. 4.2a. By design, the microwave cavity placed further from the central transmission line should have a lower inductive coupling than the other cavity. In fact, capacitive coupling compensates for the difference in inductive coupling, such that the total external coupling rate of each cavity is similar. Numerical simulation with Sonnet (see section 3.2.1) confirms this. The charge density is computed at the resonance frequency of the top mode and shown in fig. 4.2b. There are significant charge fluctuations in the bottom part of the circuit, which is nonresonant and acts as a capacitive finger to the transmission line. The circuit with dark and bright modes is designed to correct those shortcomings. The hybridized modes have currents flowing in the entire circuit for each resonance, such that there is no idle part of the circuit that can act as a capacitance to the transmission line, leaving only inductive coupling.

4.3 Realization of a mechanical reservoir

We realize the electromechanical circuit experimentally by fabricating two lumped-element LC circuits coupled to each other via a common inductor, made from thin-film aluminium on a sapphire substrate. The sample is HYB-20150924-4-24. The primary and auxiliary modes respectively have resonance frequencies $(\omega_c, \omega_{\text{aux}}) = 2\pi \times (4.26, 5.48)$ GHz and total energy decay rates $(\kappa, \kappa_{\text{aux}}) = 2\pi \times (118, 4478)$ kHz, (thus, $\kappa_{\text{aux}}/\kappa \approx 38$). This clear hierarchy in the energy relaxation rates indeed originates from the vastly dissimilar engineered external coupling to the feedline, with $\kappa_{\text{ex}} = 2\pi \times 42$ kHz $\approx 1\%$ of $\kappa_{\text{aux}}^{\text{ex}}$. The mechanical resonator is a parallel-plate capacitor with a suspended top electrode, having a resonance frequency of the fundamental flexural mode $\Omega_m = 2\pi \times 5.33$ MHz and a decay rate $\Gamma_m = 2\pi \times 30$ Hz. This mechanical mode couples to both the primary and auxiliary modes with a vacuum electromechanical coupling strength $g_0 = \tilde{g}_0/2 = 2\pi \times 60$ Hz. The characterization of the coupling strength g_0 is described in section 3.5.2. Importantly, the resolved sideband regime is still attained for both microwave modes, with $\Omega_m > \kappa_{\text{aux}} \gg \kappa$.

Figure 4.3a, b show respectively an optical image of the fabricated circuit and a scanning electron micrograph of the drum-type capacitor. The simplified measurement setup is shown in fig. 4.3c. In brief, the device is mounted on the base plate of a dilution refrigerator and cooled to a base temperature of ca. 10 mK. The microwave input lines are heavily attenuated to suppress residual thermal noise and, in addition, filter cavities are employed to remove unwanted frequency noise from the applied tones (see section 3.3.4). After amplification with a commercial high-electron-mobility transistor (HEMT) amplifier mounted on the 3 K plate, the signal is measured with a spectrum analyzer or a vector network analyzer.

To prepare a cold, dissipative mechanical bath we follow the approach outlined by Nunnenkamp et al. (2014) and use optomechanical sideband cooling (Teufel, Harlow, et al., 2008; Schliesser, Rivière, et al., 2008) to engineer the dissipation of the mechanical oscillator. We proceed by pumping the auxiliary mode on the lower motional sideband (fig. 4.1d). We strongly damp the mechanical oscillator to an effective energy decay rate $\Gamma_{\text{eff}} \approx 2\pi \times 500$ kHz (corresponding to a mean intra-cavity photon number of $\bar{n}_c^{\text{aux}} \approx 1.5 \times 10^8$), while still remaining in the weak-coupling regime for the auxiliary mode. Examples of OMIT curves taken in such a regime are shown in fig. 3.17. Thereby, we realize a dissipative mechanical reservoir for the primary, high-Q mode, since $\Gamma_{\text{eff}} \gg \kappa$. The effective temperature of this reservoir and its utility as a quantum resource are studied below in the following.

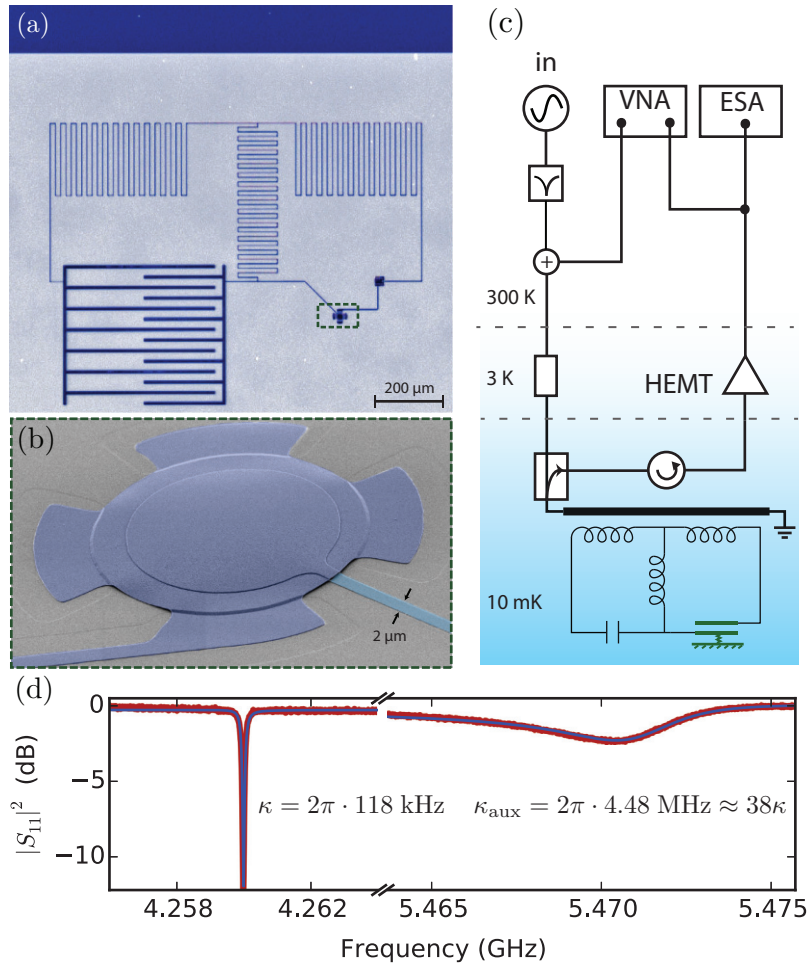


Figure 4.3: Device, experimental setup, and characterization of the electromechanical circuit (a) Inverted-colour optical micrograph of the circuit consisting of two coupled LC resonators, one having a mechanically compliant capacitor. Dark blue regions show aluminium and grey regions that are the exposed sapphire substrate. (b) False-colour scanning electron micrograph of the mechanically compliant drum capacitor. (c) Simplified schematics of the measurement setup with the circuit. The input lines are filtered and attenuated at various stages before reaching the device mounted in a dilution refrigerator. Both the coherent response and the spectral emission can be measured. (d) Linear response measurement of the device revealing the symmetric (bright, used as the auxiliary) and anti-symmetric (dark, used as the primary) microwave modes. Figure reproduced from Tóth, Bernier, Nunnenkamp, et al. (2017).

4.4 Tuning a mode using a reservoir

We first study the modified microwave cavity susceptibility resulting from interaction with the mechanical reservoir. The engineered bath provided by the mechanical resonator modifies the response of the electromagnetic mode when a microwave tone is applied (Nunnenkamp et al., 2014). With a pump detuned by Δ from the primary microwave cavity resonance, the frequency and the decay rate of the mode shift by

$$\delta\omega_{\text{om}} = \text{Re } \Sigma \quad \text{and} \quad \kappa_{\text{om}} = -2\text{Im } \Sigma. \quad (4.3)$$

The self-energy Σ is defined as

$$\Sigma = -ig^2 \left(\frac{1}{\Gamma_{\text{eff}}/2 + i(\Delta + \Omega_{\text{m}})} - \frac{1}{\Gamma_{\text{eff}}/2 + i(\Delta - \Omega_{\text{m}})} \right), \quad (4.4)$$

where $g = g_0\sqrt{\bar{n}_c}$ is the effective electromechanical coupling strength enhanced by the mean intracavity photon number of the primary mode \bar{n}_c . This effect can be viewed as radiation-pressure dynamical backaction (V. Braginsky, A. Manukin, and Tikhonov, 1970; Kippenberg, Rokhsari, et al., 2005; Schliesser, Rivière, et al., 2008) onto the microwave mode, an interpretation further elaborated in section 4.5.

The change in susceptibility leads to a change in the reflection from the microwave cavity (defined as $\hat{a}_{\text{out}}(\omega) = S_{11}(\omega)\hat{a}_{\text{in}}(\omega)$, where $\hat{a}_{\text{in,out}}(\omega)$ are Fourier-domain operators associated with the input and output fields, cf. fig. 4.1b). The response becomes

$$S_{11}(\omega) = \frac{\kappa_0 + \kappa_{\text{om}} - \kappa_{\text{ex}} - i2(\omega - \omega'_c)}{\kappa_0 + \kappa_{\text{om}} + \kappa_{\text{ex}} - i2(\omega - \omega'_c)}, \quad (4.5)$$

where κ_0 is the internal loss of the primary mode and $\omega'_c = \omega_c + \delta\omega_{\text{om}}$ the modified resonance frequency.

4.5 Interpretation as dynamical backaction

In this section, we discuss the interaction between the microwave cavity and its mechanical dissipative reservoir in the framework of dynamical backaction.

4.5.1 Origin of the concept of dynamical backaction

More than 50 years ago, the seminal work of Braginsky (Braginski and A. B. Manukin, 1967; V. Braginsky, A. Manukin, and Tikhonov, 1970) introduced

the notion of radiation pressure dynamical backaction. While a mechanical oscillator coupled parametrically to an electromagnetic mode enables the measurement of mechanical motion with high precision, as required in particular for gravitational wave detectors, radiation pressure poses a limitation. As the cavity field adjusts to the oscillator motion, the radiation pressure force it generates acts as a feedback force which can acquire an out-of-phase component due to the finite cavity delay and modify the mechanical damping rate. This dynamical backaction limits the circulating power in Fabry-Perot interferometers, due the *parametric oscillatory instability*, in which amplification compensates for the intrinsic mechanical losses, leading to regenerative oscillations of the mechanical end mirror.

The radiation-pressure parametric instability, as proposed by Braginsky (V. B. Braginsky, Strigin, and Vyatchanin, 2001) was first observed in toroid microresonators in 2005 (Kippenberg, Rokhsari, et al., 2005), and gives rise to a rich nonlinear dynamics (Marquardt, Harris, and Girvin, 2006). Soon thereafter, dynamical backaction cooling, an effect Braginsky predicted (V. B. Braginsky and Vyatchanin, 2002) to occur for red-detuned laser excitation, was demonstrated (Gigan et al., 2006; Arcizet et al., 2006; Schliesser, Del’Haye, et al., 2006). While the parametric instability was first analyzed for a single electromagnetic mode coupled to a mechanical oscillator, the effect can also occur for multimode systems in which modes are spaced by the mechanical frequencies (Kells and D’Ambrosio, 2002), a scenario in which the parametric oscillator stability in advanced LIGO at the Livingston observatory (Evans et al., 2015) was observed.

Although undesirable in the context of LIGO, the ability to amplify and cool mechanical motion using dynamical backaction is at the heart of the advances in cavity opto- and electromechanics over the past decade (Aspelmeyer, Kippenberg, and Marquardt, 2014) that have enabled mechanical systems to be controlled at the quantum level. Dynamical backaction control over mechanical oscillators has enabled the cooling of micro- and nanomechanical oscillators to unprecedentedly low entropy states (Verhagen et al., 2012; Teufel, Donner, et al., 2011; Chan et al., 2011), and thereby opened a path to study optomechanical quantum effects ranging from optomechanical squeezing, mechanical squeezed states, sideband asymmetry, to entanglement of mechanical motion with microwaves (Safavi-Naeini, Gröblacher, et al., 2013; Purdy et al., 2013; Sudhir et al., 2017; Nielsen et al., 2017; Wollman et al., 2015; Palomaki et al., 2013; Pirkkalainen, Damskäg, et al., 2015; Lecocq, Clark, et al., 2015; Riedinger et al., 2016).

It is interesting to highlight the role of dissipation in dynamical backaction. Indeed dissipation determines the resulting modification of the mechanical

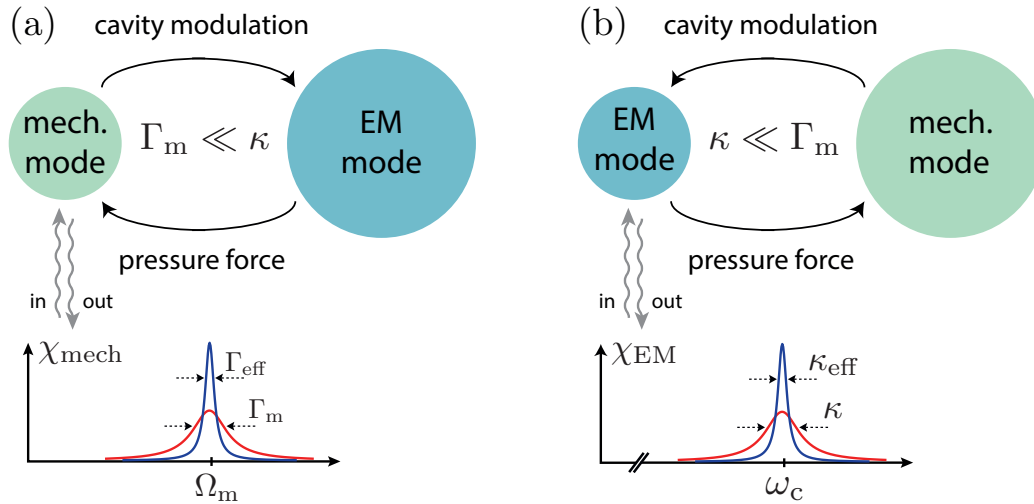


Figure 4.4: The role of dissipation in dynamical backaction. (a) An electromagnetic mode (with resonant frequency ω_c and energy dissipation rate κ) is coupled to a mechanical oscillator (with resonant frequency Ω_m and energy dissipation rate Γ_m) through the optomechanical interaction, in which the former exerts radiation pressure force, while the latter modulates the resonant frequency of the cavity. In standard optomechanical systems, the dissipation rates satisfy the hierarchy $\kappa \gg \Gamma_m$ and this interaction can be viewed as a feedback mechanism acting on the mechanical oscillator. This modifies the oscillator's damping rate, in a process coined as “dynamical backaction” by Braginsky. (b) In the scenario where the optical mode is coupled to a mechanical oscillator whose dissipation rate dominates over that of the optical mode, the role of the modes is reversed. The mechanical mode provides the feedback mechanism (dynamical backaction) for the optical mode, therefore modifying the microwave mode's resonance frequency and damping rate. Figure reproduced from Tóth, Bernier, Feofanov, et al. (2018).

and optical susceptibility due to the optomechanical interaction. In almost all optomechanical systems ranging from gravitational wave observatories to nano-optomechanical systems, the electromagnetic dissipation dominates over the mechanical one, leading to the above mentioned optomechanical phenomena. In contrast, if the mechanical oscillator is more dissipative than the electromagnetic mode, the roles are reversed (Nunnenkamp et al., 2014). In this situation¹, the dynamical backaction that occurs for detuned laser excitation causes a feedback force that is applied to the electromagnetic mode, resulting in amplification or damping. This electromagnetic dynamical backaction leads to a parametric oscillatory instability that corresponds to the action of a maser (the stimulated emission of microwaves).

4.5.2 Modeling dynamical backaction

We start by reformulating Braginsky's original derivation of dynamical backaction (Braginski and A. B. Manukin, 1967; V. B. Braginsky, Strigin, and Vyatchanin, 2001) for the case of a blue-detuned pump, in a way that showcases how the process is reversed in the case of an opposite dissipation hierarchy. Consider an electromagnetic mode with frequency ω_c and energy dissipation rate κ coupled, via the standard optomechanical coupling, to a mechanical mode with resonant frequency Ω_m and energy dissipation rate Γ_m . While Braginsky considered the limit $\Omega_m \leq \kappa$ to derive the delayed feedback force experienced by the mechanical oscillator due to the electromagnetic field, we consider here the sideband-resolved regime, $\Omega_m \gg \kappa$ (Marquardt, J. P. Chen, et al., 2007; Wilson-Rae et al., 2007; Schliesser, Rivière, et al., 2008), relevant to our experiment. We consider the equations of motion parametrically coupling the mechanical oscillator to the electromagnetic cavity. These (for simplicity classical and linearized) equations can be written in a rotating frame for the phasors of the two modes; in the case of a pump driving the system on the upper motional sideband at a detuning $\Delta = \Omega_m$, they are given by the coupled-modes equations

$$\dot{a}^*(t) = -\frac{\kappa}{2}a^*(t) + igb(t) = -\frac{\kappa}{2}a^*(t) - iF_a(t) \quad (4.6)$$

$$\dot{b}(t) = -\frac{\Gamma_m}{2}b(t) - iga^*(t) = -\frac{\Gamma_m}{2}b(t) + iF_b(t), \quad (4.7)$$

where $b(t) = (\sqrt{m\Omega_m}x(t) + i\sqrt{1/m\Omega_m}p(t))/\sqrt{2}$ describes the state of the mechanical mode of mass m , $a(t)$ is the phasor for the electromagnetic mode

¹It is still assumed that the mechanical dissipation occurs on a timescale that is long compared to the mechanical oscillator period, or equivalently that the mechanical quality factor still exceeds unity.

and $g = g_0|\alpha_0|^2$ is the vacuum optomechanical coupling strength g_0 enhanced by the field α_0 of the blue-detuned pump. In the rotating frame, the variables describe the slowly changing amplitude and phase of the rapidly oscillating field and oscillator, at ω_c and Ω_m . Each of the two harmonic oscillators is subject to a “force” (denoted by $F_a(t)$ and $F_b(t)$) proportional to the state of the other harmonic oscillator, establishing a feedback mechanism: cavity intensity fluctuations create a radiation pressure force acting on the mechanical oscillator, while mechanical displacement modulates the cavity resonance frequency. The symmetry of the relationship is broken by the different scales of the dissipation rates.

Braginsky originally considered the case where electromagnetic dissipation dominates ($\kappa \gg \Gamma_m$). This is natural in most systems as the quality factors are commensurate for the electromagnetic and mechanical modes, while there is a large (many orders of magnitude) separation of scales in their respective frequencies. In this limit, the electromagnetic field envelope almost instantly adapts to the mechanical displacement ($\dot{a}^*(t) \approx 0$) and becomes proportional to it such that $a^*(t) = i(2g/\kappa)b(t)$. The field then exerts a force on the mechanical oscillator proportional to the state of the latter, given by $F_b(t) = -i(2g^2/\kappa)b(t)$. Therefore, the interaction can be viewed as a feedback loop. The factor $-i$ represents a delay of a quarter period for the feedback force acting on the mechanical oscillator. This delay means that the force, acting in quadrature, increases the amplitude of the phasor, equivalent to a decrease in mechanical damping or gain. If the pump detuning Δ does not fall exactly on the sideband, the delay is not exactly i and the force has an in-phase component, modifying the frequency of the mechanical oscillator (this effective change of the mechanical spring constant is called the *optical spring* effect). The amplification process can be understood as a positive feedback that measures the state of the mechanical oscillator and returns it with a delay as a force: a dynamical backaction (see fig. 4.4a). For sufficiently high coupling strength g , this leads to a parametric oscillatory instability, that causes regenerative oscillations of the mechanical oscillator, and thus limits the maximal circulating power for a gravitational wave detector (V. B. Braginsky, Strigin, and Vyatchanin, 2001).

Here, we study the converse process, where the mechanical dissipation rate dominates ($\Gamma_m \gg \kappa$). The envelope of mechanical oscillations nearly instantly adjusts to the state of the electromagnetic field ($\dot{b}(t) \approx 0$) and is proportional to it such that $b(t) = -i(2g/\Gamma_m)a^*(t)$. The field is then subject to an in-quadrature “force” proportional to its own state $F_a(t) = i(|\kappa_{\text{DBA}}|/2)a^*(t)$ where $\kappa_{\text{DBA}} = -4g^2/\Gamma_m = -\kappa\mathcal{C}$, introducing the multiphoton cooperativity $\mathcal{C} = 4g^2/(\kappa\Gamma_m)$. Similarly to above, the force has a delay

$+i$ of a quarter period and increases the amplitude of electromagnetic oscillations, compensating for damping by an amount given by κ_{DBA} , such that the effective energy decay rate of the cavity is $\kappa + \kappa_{\text{DBA}}$. A change in detuning Δ would again slightly modify this delay and create components of the in-phase force component, changing the speed of oscillations, and displacing the resonance frequency of the cavity. This is equivalent to a feedback loop for the electromagnetic mode (see fig. 4.4b), and implies that the mechanical oscillator is responsible for dynamical backaction on the microwave cavity. As above, the positive feedback can lead to a parametric instability. For $\kappa_{\text{DBA}} = -\kappa$, the anti-damping caused by this feedback exactly compensates for the losses (both intrinsic and external) of the electromagnetic mode, and the cavity develops self-sustained oscillations: it acts as a maser. The intrinsic optomechanical nonlinearity sets the maximum amplitudes of the oscillations (Nunnenkamp et al., 2014) and the dynamics is no longer captured by the linearized eqs. (4.6) and (4.7).

4.6 Controllable microwave susceptibility

The engineered reservoir therefore supplies a way to tailor the susceptibility of the primary electromagnetic mode, which we can directly probe using a coherent response measurement.

We fix the detuning to either motional sideband of the primary mode ($\Delta = \mp\Omega_{\text{m}}$), and measure $S_{11}(\omega)$ while the power is varied. For this choice of detuning, we have $\delta\omega_{\text{om}} = 0$ (neglecting a term $\propto \Gamma_{\text{eff}}^2/\Omega_{\text{m}}$) and the change in the microwave decay rate simplifies to

$$\kappa_{\text{om}} = \pm\mathcal{C}\kappa, \quad (4.8)$$

directly proportional to the cooperativity $\mathcal{C} = 4g^2/(\kappa\Gamma_{\text{eff}})$. Figure 4.5a, b show the linear response for a tone on the lower and upper sideband for various pump powers. The width of the resonance, corresponding to the effective cavity decay rate, increases (for $\Delta = -\Omega_{\text{m}}$) or decreases (for $\Delta = +\Omega_{\text{m}}$) linearly with \mathcal{C} . The depth of reflection on resonance $|S_{11}(\omega_{\text{c}})|^2$ varies significantly to reflect this change (fig. 4.5c). The effective internal loss of the cavity $\kappa_0 + \kappa_{\text{om}}$ can be tuned on demand by changing the coupling to the dissipative reservoir via the pump tone. While the microwave cavity is initially undercoupled ($\kappa_{\text{ex}} < \kappa_0$), pumping on the upper sideband reduces the effective internal loss and increases the depth on resonance until the cavity becomes critically coupled (the effective internal loss matches the external coupling, $\kappa_0 + \kappa_{\text{om}} = \kappa_{\text{ex}}$). Increasing the power further, the cavity becomes

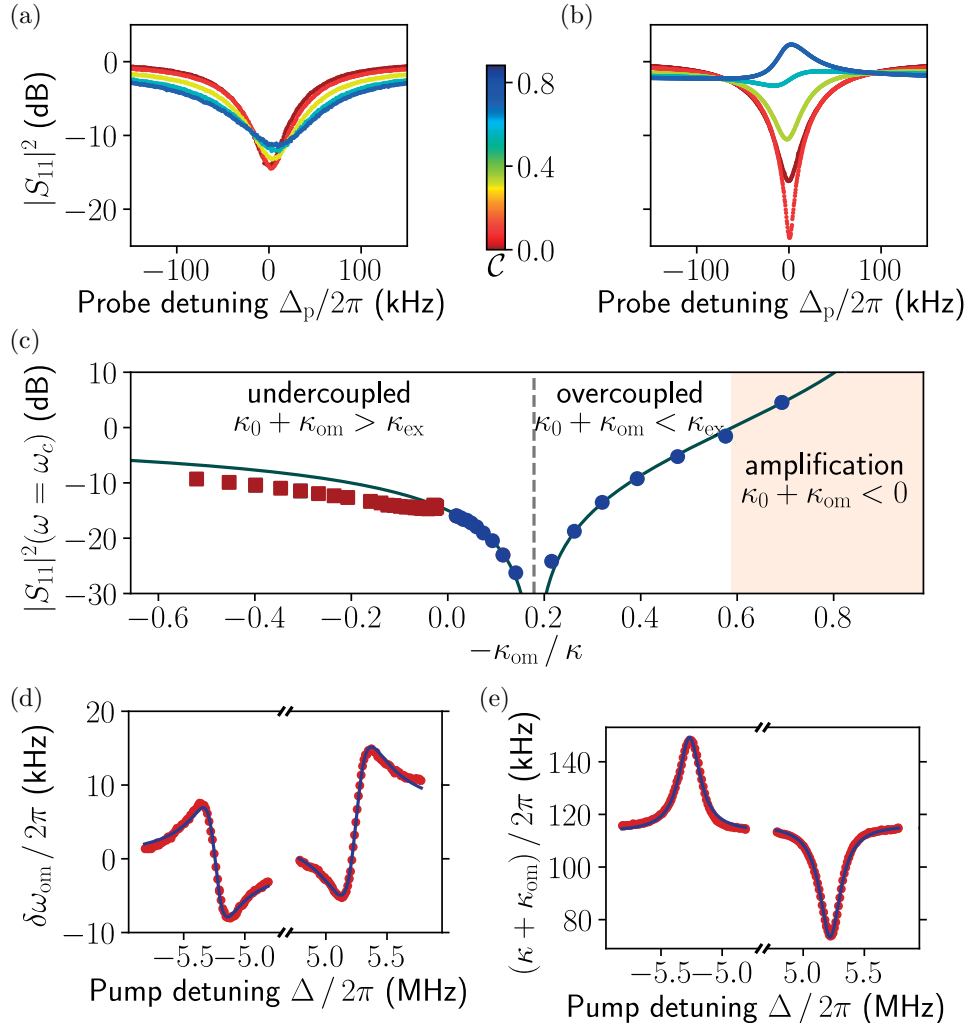


Figure 4.5: Dynamical backaction on the microwave mode using an engineered mechanical reservoir. (a,b) Modification of the susceptibility of the microwave cavity when a pump tone is placed on the lower and upper motional sideband of the primary mode, for various values of the multiphoton cooperativities ($\mathcal{C} = 1$ corresponds to a mean intracavity photon number of $\bar{n}_c \approx 5 \times 10^6$). The slight frequency shift of the peak center is due to the finite sideband resolution parameter of the auxiliary mode (Ω_m/κ_{aux}). (c) Depth of the resonance as a function of the effective internal losses $\kappa_0 + \kappa_{om}$, with a pump tone on the lower ($\Delta = -\Omega_m$, red squares) and upper sideband ($\Delta = +\Omega_m$, blue circles), and a theoretical fit. (d,e) Using a fixed pump power, the detuning Δ of the pump tone is swept and the change in the microwave resonance frequency and decay rate is recorded. The theoretical fit corresponds to eq. (4.3), showing good agreement with the experimental data. Figure adapted from Tóth, Bernier, Nunnenkamp, et al. (2017).

overcoupled ($\kappa_0 + \kappa_{\text{om}} < \kappa_{\text{ex}}$) and resonant reflection increases again. When $\kappa_0 + \kappa_{\text{om}}$ becomes negative, there is a net internal gain: the absorptive feature in the cavity reflection becomes a peak, indicating amplification of the reflected microwave signal. By pumping on the lower sideband ($\Delta = -\Omega_{\text{m}}$), extra damping is introduced and the resonance becomes increasingly undercoupled. The mechanical mode provides a dissipative bath for the microwave resonator, down-converting the cavity photons to the pump. In fig. 4.5c we plot the resonant reflection and observe good agreement with the expected dependence according to eq. (4.5). For the data corresponding to the pump tuned to the lower motional sideband ($\Delta = -\Omega_{\text{m}}$), the depth of the resonance is systematically lower than expected, due to a decrease in the intrinsic microwave cavity loss in the presence of a strong pump (Megrant et al., 2012).

In fig. 4.5d, e, we keep the pump power constant and sweep the detuning Δ to measure the change in the microwave resonance frequency and damping rate. For the frequency shift $\delta\omega_{\text{om}}$, intrinsic non-linearities redshift the resonance frequency in an asymmetric fashion, providing a different background for the red and blue sidebands. The effect agrees well with the prediction from eq. (4.3) when the two sidebands are fitted independently with different constant offsets. We note that the modification of the resonance frequency as a function of detuning has the opposite parity compared to the better known case of the optical spring effect (Aspelmeyer, Kippenberg, and Marquardt, 2014).

4.7 Maser action and amplification

In the following, we demonstrate the cold nature of the dissipative mechanical reservoir by studying the noise properties of the system. To this end, we fix the microwave drive to the upper sideband ($\Delta = +\Omega_{\text{m}}$) and study the regime where the pump introduces net gain in the microwave cavity ($\kappa_0 + \kappa_{\text{om}} < 0$). We use a different device, HYB-20160524-1-12, for this analysis with optimized properties: higher coupling strengths of $g_0 = 2\pi \times (106, 79)$ Hz respectively for the primary and auxiliary modes, and an overcoupled primary mode ($\kappa_{\text{ex}}/\kappa = 0.76$). In fig. 4.6a, the emitted noise spectra of the microwave cavity are shown for different pump powers. The measured power spectrum is rescaled to the symmetrized cavity output field spectrum (Clerk et al., 2010) $\bar{\mathcal{S}}_{aa}(\omega)$ in units of photons per second per unit bandwidth (see definition in section 2.2.2), using the noise temperature of the HEMT as an absolute noise reference (see section 3.4.2). To confirm the calibration, we use the mechanical sideband spectrum obtained from the measurement of

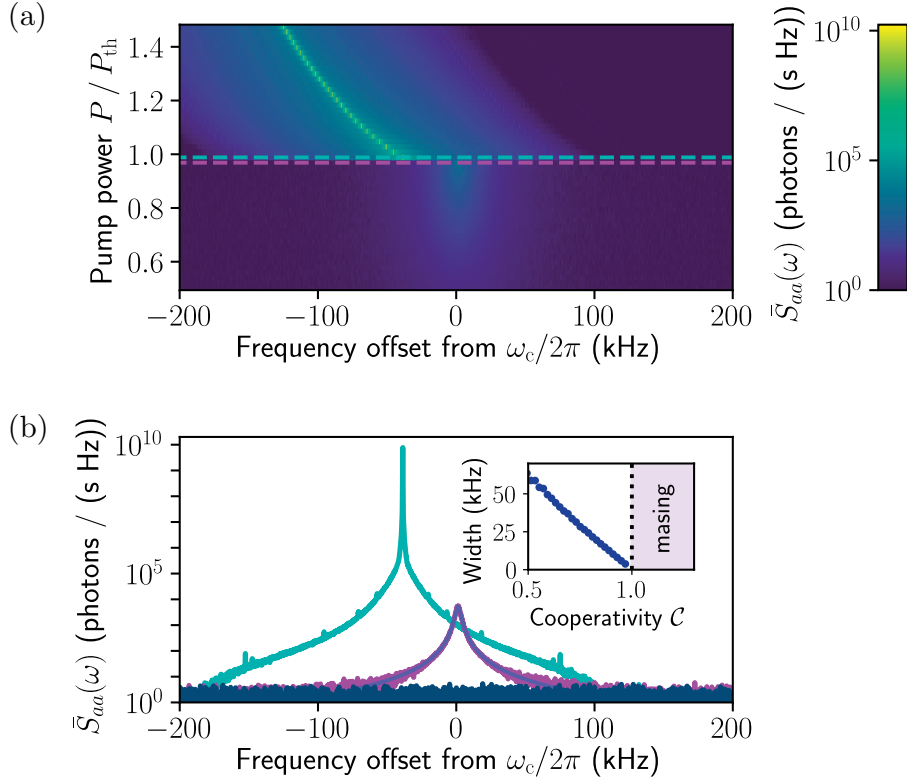


Figure 4.6: Amplified vacuum fluctuations and parametric instability of the microwave mode (masing). (a) Noise spectrum of the cavity emission as a function of the power of a pump on the upper motional sideband. The spectrum is measured in quanta using the HEMT amplifier for calibration. Above a certain threshold power P_{th} , the microwave mode undergoes self-sustained oscillations, characteristic of a maser. The vertical axis is normalized by the pump power at the instability threshold P_{th} , equivalent to the cooperativity $\mathcal{C} = P/P_{th}$ below threshold. (b) Two examples of emission from the microwave mode at the input of the HEMT, below and above threshold (line cuts of (a)), as well as a reference measurement of the background without the pump (dark blue). The inset shows the emission linewidth narrowing below threshold. In this regime, noise emission is composed of amplified vacuum and thermal fluctuations, described by eq. (4.9). Figure adapted from Tóth, Bernier, Nunnenkamp, et al. (2017).

g_0 (see section 3.5.2) to locally compare the known sideband power to the background noise that corresponds to the HEMT added noise. This provides an independent calibration of the HEMT noise, which in this case was found to agree within 1.4 dB.

As the blue-detuned pump compensates for the losses, the width of the emitted noise spectrum, corresponding to the cavity linewidth $\kappa_{\text{eff}} = (1 - \mathcal{C})\kappa$, decreases linearly with the pump power towards zero (at unity cooperativity $\mathcal{C} = 1$), as shown in the inset of fig. 4.6b. In this below-threshold regime, the peak photon flux spectral density emitted from the cavity increases with power, as the vacuum noise and the residual thermal microwave noise (consisting in both a finite residual occupancy \bar{n}_m of the dissipative mechanical reservoir and a finite thermal microwave occupancy of the cavity \bar{n}_{cav}) are amplified according to

$$\bar{\mathcal{S}}_{aa}(\omega) = \kappa_{\text{ex}} \frac{(\kappa_{\text{ex}} - \kappa_{\text{eff}})\frac{1}{2} + \mathcal{C}\kappa(\bar{n}_m + \frac{1}{2}) + \kappa_0(\bar{n}_{\text{cav}} + \frac{1}{2})}{(\frac{\kappa_{\text{eff}}}{2})^2 + (\omega - \omega_c)^2} \quad (4.9)$$

where the thermal input noise is neglected and only the amplified noise is considered. We analyze the noise properties of the device in detail below when considering amplification and added noise. We find the residual thermal occupancy of the dissipative reservoir to be $\bar{n}_m = 0.66$, when neglecting \bar{n}_{cav} . Equation (4.9) then implies that 60% of the emitted noise from the cavity is amplified vacuum fluctuations, when $\mathcal{C} \rightarrow 1$.

For $\mathcal{C} = 1$ and greater pump powers, the microwave mode undergoes self-sustained oscillations. This regime leads to a parametric instability and stimulated emission of microwave photons into the microwave cavity, analog a maser. The salient features of the instability are a transition from sub- to above-threshold masing, as well as linewidth narrowing. These observations are analogues to the radiation-pressure-induced parametric instability of a mechanical mode in the normal optomechanical regime ($\kappa \gg \Gamma_m$) (Kippenberg, Rokhsari, et al., 2005; Marquardt, Harris, and Girvin, 2006; V. Braginsky and A. Manukin, 1977; Grudinin et al., 2010). In the experiments a clear threshold behavior, characteristic of masing, is demonstrated when the emitted noise abruptly increases in strength at $\mathcal{C} = 1$ (fig. 4.6b). Such masing in superconducting circuits has previously been demonstrated using a single artificial atom (Astafiev et al., 2007). Due to the large photon population generated by masing, nonlinearities of the cavities red-shift the frequency of emission. This clearly distinguishes masing from the mechanical parametric instability (also called phonon lasing) (Grudinin et al., 2010) in the normal optomechanical regime. In the latter case, the emission does not follow the cavity but has a constant detuning of $-\Omega_m$ with respect to the

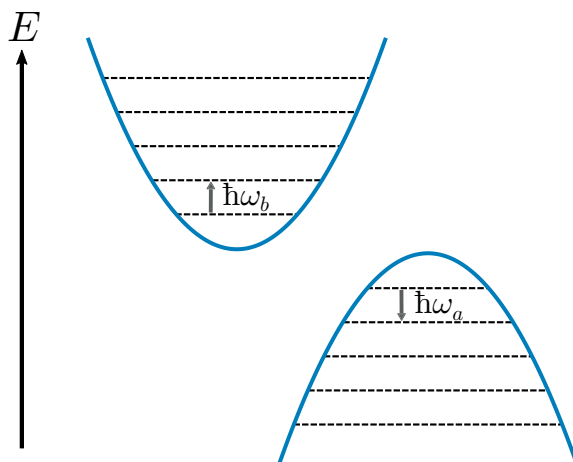


Figure 4.7: Interaction between modes of positive and negative energy as population inversion. In the rotating frame, the microwave and mechanical modes have a negative and a positive energy, and their energy levels can be represented on two inverted parabolas. Through the interaction, the two modes can exchange an excitation that moves the state up the energy ladder on the left and down the energy ladder on the right. This process can be repeated infinitely, leading to amplification and the masing instability.

pump.

In a usual maser, the microwave mode is amplified by interacting with a two-level system in a state of population inversion. The amplification mechanism here can be interpreted similarly. When a blue-detuned drive is applied to the system, the microwave mode has a negative energy in the rotating frame, where the Hamiltonian is time-independent (see eq. (2.22)). The two modes can be represented as in fig. 4.7 with energy levels in two parabolas, inverted with respect to each other. The first mode can always gain energy by exchanging an excitation with the second mode, which can always be lowered in energy. The two ladders of energy levels, one of them can be infinitely climbed up and the other down, lead to amplification of the oscillations in the modes and eventually to the masing instability. The downward parabola is an analog of the inverted population of a two-level system. In the latter, the energy can always be lowered by swapping excitations with the maser mode, since the system is instantly pumped back to the state of population inversion.

Below the masing threshold, the microwave mode coupled to the dissipative bath acts as a phase-insensitive parametric amplifier (Caves, 1982;

Nunnenkamp et al., 2014) for incoming signals. For $\kappa_0 + \kappa_{\text{om}} < 0$, there is a net internal gain and the susceptibility $S_{11}(\omega)$ develops a peak, such that reflection is larger than input for signals within the resonance bandwidth (in-band). The power gain of the amplifier is defined as the resonance peak height above the background, given by

$$\mathcal{G}(\omega_c) = |S_{11}(\omega_c)|^2 = \left| \frac{(2\frac{\kappa_{\text{ex}}}{\kappa} - 1) + \mathcal{C}}{1 - \mathcal{C}} \right|^2. \quad (4.10)$$

The bandwidth of the amplifier is the linewidth of the microwave resonance, given by $\kappa_{\text{eff}} = (1 - \mathcal{C})\kappa$. In order to measure the gain, bandwidth and noise properties of the amplifier, we inject, in addition to the pump tone on the upper sideband ($\Delta = +\Omega_m$), a weak signal tone (swept in frequency around the cavity resonance) and measure the reflected signal as a function of the pump tone power. With increasing pump power, a narrowing of the cavity bandwidth (fig. 4.8a) is observed, as well as an increase in the power of the reflected signal (i.e. gain). By fitting the reflected power, the gain and bandwidth as a function of cooperativity are extracted, and found to be in good agreement with the theoretical predictions given by eq. (4.10) (fig. 4.8b). The observed gain exceeds 42 dB.

4.8 Near-quantum-limited amplification

Next, we study the added noise of the dissipative amplification process. The added noise \mathcal{N} , referred to the input of the amplifier, is given by the noise output of eq. (4.9) subtracting the input noise and dividing by the gain $\mathcal{G}(\omega_c)$. On resonance, it is found to be

$$\mathcal{N}(\omega_c) = \frac{4\mathcal{C}(\kappa_{\text{ex}}/\kappa)(\bar{n}_m + \frac{1}{2}) + 4(\kappa_{\text{ex}}\kappa_0/\kappa^2)(\bar{n}_{\text{cav}} + \frac{1}{2})}{(\mathcal{C} - 1 + 2\kappa_{\text{ex}}/\kappa)^2}, \quad (4.11)$$

which, in the high gain limit ($\mathcal{C} \rightarrow 1$), simplifies to $\mathcal{N}(\omega_c) \rightarrow (\kappa_0/\kappa_{\text{ex}})(\bar{n}_{\text{cav}} + \frac{1}{2}) + (\kappa/\kappa_{\text{ex}})(\bar{n}_m + \frac{1}{2})$. This quantity can be measured by recording the improvement of the signal-to-noise ratio (SNR) of amplification in and out of the bandwidth of our device. This directly compares the noise performance of our device with the commercial HEMT amplifier, which is used as a calibrated noise source (the noise temperature of the HEMT is measured separately at ω_c and found to be 3.95 ± 0.02 K, corresponding to $\mathcal{N}_{\text{HEMT}} = 20.0 \pm 0.1$ quanta (see section 3.4.2). In fig. 4.8c, the gain of the device is compared to the noise output of the chain, normalized to the HEMT noise background.

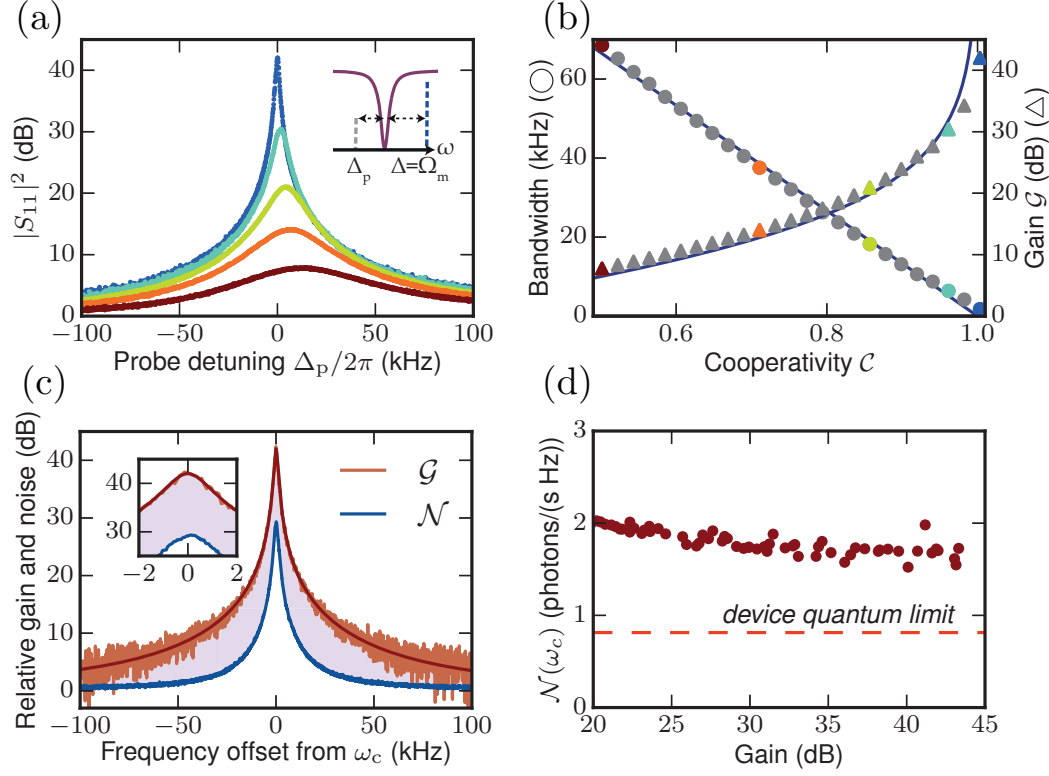


Figure 4.8: Near-quantum-limited phase-preserving amplification. (a) Linear response of the cavity, with increasing powers of the pump on the upper sideband from red to blue. (b) Power gain (triangles) and bandwidth (circles) of the amplifier extracted from a fit of the linear response, as a function of the cooperativity of the pump on the upper sideband. The colored points correspond to the curves in (a). (c) Relative gain and noise of the amplifier, sharing the same baseline. The difference from noise to gain corresponds to over 12 dB of apparent signal-to-noise ratio improvement of our device over the HEMT, from which the insertion loss between the HEMT and the device (measured separately to be 1.6 dB) must be subtracted to infer the real improvement. (d) Added noise of the amplification referred to the input, expressed in quanta. The total added noise in the high-gain limit amounts to 1.68 ± 0.02 quanta. This is only 0.87 quanta above the device quantum limit n_{DQL} , defined in eq. (4.12). Figure reproduced from Tóth, Bernier, Nunnenkamp, et al. (2017).

This calibration is corroborated by a second, independent calibration technique, which uses the scattered power in the motional sideband in conjunction with the knowledge of the intracavity photon number and g_0 . The relative gain of the signal exceeds the relative noise by over 12 dB. From this apparent SNR improvement, one must subtract the insertion loss of the components between the device and the HEMT, measured independently at 77 K to be 1.6 dB. (cf. section 3.4.2). The analysis reveals therefore that the optomechanical amplifier provides more than 10 dB of improvement over the SNR of the HEMT.

The inferred added noise on resonance is shown as a function of gain in fig. 4.8d. In the high-gain limit, it is a constant value of $\mathcal{N}(\omega_c) = 1.68 \pm 0.02$ quanta per second per unit bandwidth (with the uncertainty given by statistical fluctuations). Using eq. (4.11) and assuming $\bar{n}_{\text{cav}} = 0$, the effective occupancy of the dissipative reservoir is found to be $\bar{n}_m = 0.66$. However, the strong cooling pump increases the temperature of the cavity thermal bath to an occupancy $\bar{n}_{\text{cav}} = 1.03$, obtained by measuring the emitted thermal noise of the microwave cavity. Taking the residual cavity thermal noise into account, the estimate for the mechanical occupancy is reduced to $\bar{n}_m = 0.41$. This demonstrates that the dissipative mechanical reservoir constitutes a quantum resource.

The calibration of the added noise of the amplifier provides a convenient way to measure the occupancy of the cooled mechanical oscillator. The near-quantum limited fluctuations of the mechanical motion are amplified by a large gain and can be measured with a large SNR (see fig. 4.8c). Only the regime considered, with the mechanical oscillator serving as a reservoir for the microwave cavity, with a much larger dissipation allows this. In a sense, the amplification is not sufficient to compensate the large cooling rate of the mechanical oscillator provided by the auxiliary cavity, such that the cooled mechanical fluctuations are amplified without heating the oscillator.

We note that even in the case when all the thermal noise sources are reduced to zero ($n_{\text{eff}} = n_{\text{cav}} = 0$), the added noise of the amplifier is

$$n_{\text{DQL}} = \frac{1}{2} + \frac{\kappa_0}{\kappa_{\text{ex}}}, \quad (4.12)$$

which we call the device quantum limit and deviates from 1/2 due to the finite internal dissipation rate κ_0 . For the present system the device quantum limit amounts to 0.81 quanta for the coupling ratio of $\kappa_{\text{ex}}/\kappa = 0.76$, which is only 0.87 quanta below the added noise we measure. It is interesting to compare the present amplifier scheme, relying on a dissipative reservoir, to the microwave parametric amplifiers used in circuit QED. In the latter case,

typically both idler and signal are resonant with one or more microwave cavities (Bergeal et al., 2010; Eichler et al., 2014; Castellanos-Beltran, Irwin, et al., 2008). As the gain increases, this leads to a simultaneous increase in both the signal and idler mode population. In contrast, while the present amplifier scheme uses a parametric interaction as well, the large dissipation rate for the (mechanical) idler mode only leads to the generation of a signal photon (microwave field), suppressing the idler; the situation is akin to a Raman-type interaction found in nonlinear optics (Bloembergen, 1996).

4.9 Injection locking of the maser tone

We now demonstrate the locking of our maser with a weak injected tone. This is performed on the same sample HYB-20160524-1-12, as before, that was kept at the elevated temperature of 200 mK to increase the mechanical stability. The sample parameters have shifted slightly and it has resonance frequencies $\omega_c = 2\pi \times 4.08$ GHz and $\omega_{\text{aux}} = 2\pi \times 5.19$ GHz, and a mechanical resonance frequency $\Omega_m = 2\pi \times 6.5$ MHz.

Injection locking is a synchronization phenomenon for lasers and masers (Siegman, 1986), and has been demonstrated in many systems, including recently in a trapped-ion phonon laser (Knünz et al., 2010), a quantum cascade laser (St-Jean et al., 2014), a quantum-dots maser (Liu et al., 2015) as well as an AC Josephson junction maser (Cassidy et al., 2017). A weak tone of frequency ω_{inj} close to the maser emission frequency ω_{mas} competes for gain with it in a way that effectively couples the two oscillations and permits synchronization. The phenomenon is generally described by the Adler equation (Adler, 1946)

$$\frac{d\phi}{dt} + (\omega_{\text{inj}} - \omega_{\text{mas}}) = -\frac{1}{2}\Delta\omega_{\text{inj}} \sin(\phi) \quad (4.13)$$

which models the dynamics of the relative phase ϕ of the two oscillations. If the injected tone falls within a locking range of width

$$\Delta\omega_{\text{inj}} = 2\kappa_{\text{ex}}\sqrt{\alpha P_{\text{inj}}/P_{\text{mas}}} \quad (4.14)$$

centered around the masing frequency ω_{mas} , the two tones lock and the phase difference ϕ becomes constant. This range depends on the ratio between the injected tone power P_{inj} , attenuated by factor α at the input of the cavity, and the maser emission power P_{mas} . Outside this range, the Adler equation predicts that the maser frequency is pulled towards the injected tone

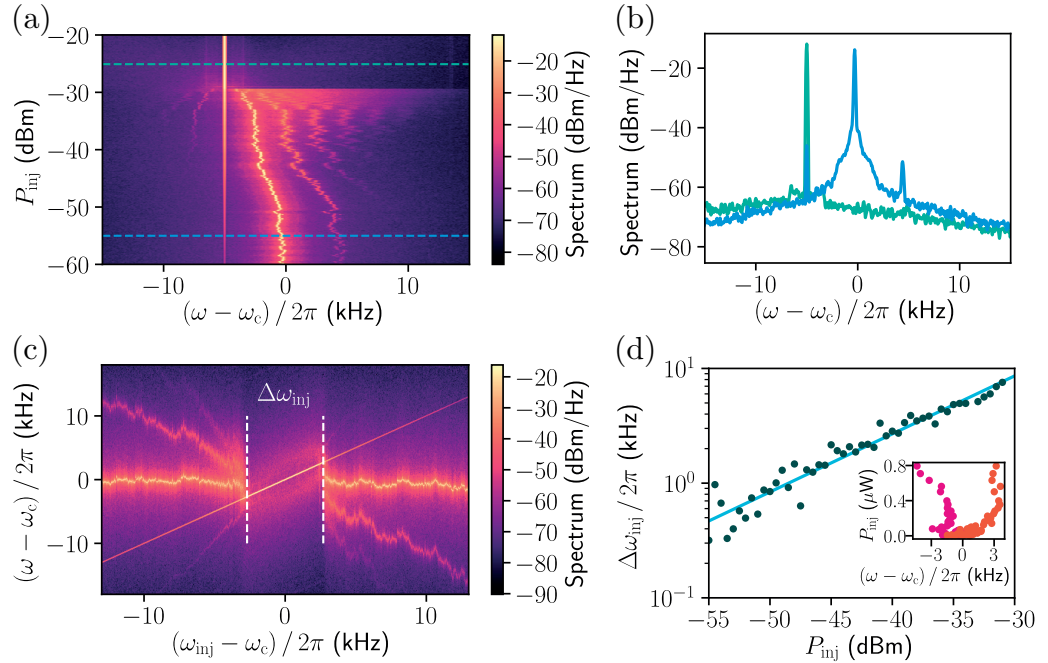


Figure 4.9: Injection locking of a maser based on dynamical backaction (a) Output spectrum of the maser, as the power P_{inj} of an injected tone detuned 5 kHz to the red is increased. The power is measured at the output of the corresponding microwave source. Above a threshold power of about -30 dBm, the maser locks to the tone, considerably suppressing the noise and eliminating the frequency jitter present in the free-running case. The intrinsic nonlinearity results in distortion sidebands from the two tones beating below threshold. (b) Spectra corresponding to cuts of A along the dashed lines, below and above the locking threshold. (c) Output spectrum of the maser as the frequency ω_{inj} of a weak tone of constant power $P_{\text{inj}} = -40$ dBm is swept across the free-running maser frequency ω_{mas} . The locking range $\Delta\omega_{\text{inj}}$, wherein the two oscillations are frequency locked, is highlighted. (d) The locking range $\Delta\omega_{\text{inj}}$ as a function of the injected tone power P_{inj} . A fit on the logarithmic scale gives a slope of 0.51, confirming the expected scaling $\Delta\omega_{\text{inj}} \propto \sqrt{P_{\text{inj}}}$. The inset depicts the actual limiting points of the locking range as a function of tone power P_{inj} , illustrating the Arnold tongue of the system. Figure adapted from Tóth, Bernier, Feofanov, et al. (2018).

and that distortion sidebands appear due to beating of the two tones and the intrinsic nonlinearity (Adler, 1946). We first study this phenomenon by placing the injected tone 5 kHz away from the maser and monitoring the output spectrum while the injected power P_{inj} is varied (fig. 4.9a). The maser emission is pulled towards the injected tone and finally locks at an injected power threshold corresponding to about -30 dBm. As the two tones become comparable in strength, distortion sidebands from the beating increase in amplitude. In the locked region, the noise surrounding the peak is considerably suppressed compared to the free-running case and the frequency jitter (originating from frequency instability of the cavity and the mechanical mode) is eliminated (fig. 4.9b). We proceed to measure the locking range $\Delta\omega_{\text{inj}}$, by fixing the injected power P_{inj} and sweeping its frequency ω_{inj} across the maser frequency (fig. 4.9c). When the frequency difference is below $\Delta\omega_{\text{inj}}$, the two tones lock. The noise around the peak is suppressed and the frequency jitter of the maser ceases. Repeating the measurement at different injected powers P_{inj} , the locking range is shown to obey the expected scaling law $\Delta\omega_{\text{inj}} \propto \sqrt{P_{\text{inj}}}$ (fig. 4.9d). Finally, the limit points of locking are shown in an inset as a function of power, drawing the so-called Arnold tongue (Pikovsky, Rosenblum, and Kurths, 2003). The asymmetric shape is due to drift of the masing frequency ω_{mas} during the measurement, which does not affect the locking range $\Delta\omega_{\text{inj}}$.

4.10 Conclusions

In summary, we have implemented and studied a new regime of circuit electromechanics by coupling an electromagnetic cavity mode to an engineered cold dissipative reservoir formed by a mechanical oscillator. The usual roles of the two modes are reversed, allowing for dynamical backaction on the microwave mode using the mechanical reservoir. We demonstrate the control of the internal losses of the cavity in the form of backaction-induced amplification, damping, and masing of the microwave field. By performing microwave amplification close to the quantum limit, we show that the mechanical reservoir functions as a useful quantum resource.

The near-quantum-limited amplification with a mechanical reservoir extends the available quantum information manipulation toolkit, adding to the existing devices based on Josephson junctions (Bergeal et al., 2010; Eichler et al., 2014; Castellanos-Beltran, Irwin, et al., 2008; Sliwa et al., 2015). While the present amplifier is not frequency-tunable, recent advances in circuit electromechanics have demonstrated such functionality (Andrews, Reed,

et al., 2015). The observed reservoir-mediated microwave damping may allow to remove residual thermal occupancy from the microwave cavity, akin to cooling schemes developed in circuit QED (Grajcar et al., 2008). Moreover, the control over internal dissipation enables all-electromechanical tuning of the coupling of the microwave resonator to the feedline, offering the potential for an electromechanical reconfigurable network (Kerckhoff, Andrews, et al., 2013). While the present scheme employs a single pump tone, dual tone pumping would lead to the preparation of squeezed states of the microwave cavity (Kronwald, Marquardt, and Clerk, 2014). Viewed more broadly, the realization of a cold mechanical reservoir for microwave light provides a central ingredient for novel electromechanical devices. Indeed, the circuit can be extended to multiple microwave resonators coupled to a shared mechanical reservoir and implement the dissipative cavity-cavity interactions that are at the heart of recent schemes to entangle microwave photons (Wang and Clerk, 2013) and, combined with coherent interactions, to perform nonreciprocal microwave transmission (Metelmann and Clerk, 2015). Such nonreciprocal devices can be of use for the rapidly expanding field of circuit QED (Wallraff et al., 2004; Devoret and Schoelkopf, 2013).

Nonreciprocity in microwave optomechanical circuits

We describe here a scheme to perform nonreciprocal frequency conversion with a multimode microwave optomechanical circuit. This chapter is adapted from the text of two previous publications (Bernier, Tóth, Koottandavida, et al., 2017; Bernier, Tóth, Feofanov, et al., 2018b). In section 5.1, we introduce nonreciprocity in the context of cavity optomechanics. In section 5.2, we develop an intuitive picture of how to achieve nonreciprocal transmission, using the gyrator as a conceptual starting block. In section 5.3, we present the scheme to implement an isolator using a multimode optomechanical microwave circuit. In section 5.4, our experimental results are detailed. In section 5.5, the optomechanical circulator is introduced as a possible extension of this working, necessitating an additional microwave cavity. Finally, in section 5.6, we conclude and give an outlook for optomechanical nonreciprocity.

5.1 Introduction

Nonreciprocal devices, such as isolators, circulators, and directional amplifiers, exhibit altered transmission characteristics if the input and output channels are interchanged. They are essential to several applications in signal processing and communication, as they protect devices from interfering signals (Pojar, 2011). At the heart of any such device lies an element break-

ing Lorentz reciprocal symmetry for electromagnetic sources (Feynman, 1988; Jalas et al., 2013). Such elements have included ferrite materials (Auld, 1959; Milano, Saunders, and Davis, 1960; Fay and Comstock, 1965), magneto-optical materials (Aplet and Carson, 1964; Shirasaki and Asama, 1982; Sato et al., 1999; Bi et al., 2011), optical nonlinearities (Manipatruni, Robinson, and Lipson, 2009; L. Fan et al., 2012; Guo et al., 2016), temporal modulation (Anderson and Newcomb, 1965; Z. Yu and S. Fan, 2009; Lira et al., 2012; Kang, Butsch, and Russell, 2011; Estep et al., 2014; Peng, Özdemir, Lei, et al., 2014), chiral atomic states (Scheucher et al., 2016), and physical rotation (Fleury et al., 2014).

Typically, a commercial nonreciprocal microwave apparatus exploits ferrite materials and magnetic fields, which leads to a propagation-direction-dependent phase shift for different field polarizations. A significant drawback of such devices is that they are ill-suited for sensitive superconducting circuits, since their strong magnetic fields are disruptive and require heavy shielding. In recent years, the major advances in quantum superconducting circuits (Devoret and Schoelkopf, 2013), that require isolation from noise emanating from readout electronics, have led to a significant interest in nonreciprocal devices operating at the microwave frequencies that dispense with magnetic fields and can be integrated on-chip.

As an alternative to ferrite-based nonreciprocal technologies, several approaches have been pursued towards nonreciprocal microwave chip-scale devices. Firstly, the modulation in time of the parametric couplings between modes of a network can simulate rotation about an axis, creating an artificial magnetic field (Anderson and Newcomb, 1965; Estep et al., 2014; Kerckhoff, Lalumière, et al., 2015; Ranzani and Aumentado, 2014) rendering the system nonreciprocal with respect to the ports. Secondly, phase matching of a parametric interaction can lead to nonreciprocity, since the signal only interacts with the pump when copropagating with it and not in the opposite direction. This causes travelling-wave amplification to be directional (Ranzani and Aumentado, 2014; White et al., 2015; Macklin et al., 2015; Hua et al., 2016).

Phase-matching-induced nonreciprocity can also occur in optomechanical systems (Aspelmeyer, Kippenberg, and Marquardt, 2014; Bowen and G. J. Milburn, 2015), where parity considerations for the interacting spatial modes apply (Hafezi and Rabl, 2012; Shen et al., 2016; Ruesink et al., 2016). Finally, interference in parametrically coupled multi-mode systems can be used. In these systems nonreciprocity arises due to interference between multiple coupling pathways along with dissipation in ancillary modes (Ranzani and Aumentado, 2015). Dissipation is a key resource there to break reciprocity, as

it forms a flow of energy always leaving the system, even as input and output are interchanged. It has therefore been viewed as a kind of reservoir engineering (Metelmann and Clerk, 2015). Following this approach, nonreciprocity has recently been demonstrated in Josephson-junctions-based microwave circuits (Sliwa et al., 2015; Lecocq, Ranzani, et al., 2017) and in a photonic-crystal-based optomechanical circuit (Fang, Luo, et al., 2017). These realisations and theoretical proposals to achieve nonreciprocity in multi-mode systems rely on a direct, coherent coupling between the electromagnetic input and output modes.

5.2 Gyration and nonreciprocity

Here we explain the origin of nonreciprocity in optomechanical systems by using the gyration-based isolator as a conceptual starting point.

5.2.1 The gyration-based isolator

Any linear quadrature-preserving two-port device can be described by its scattering matrix S , linking the incoming modes $\hat{a}_{i,\text{in}}$ to the outgoing modes $\hat{a}_{i,\text{out}}$ by

$$\begin{pmatrix} \hat{a}_{1,\text{out}} \\ \hat{a}_{2,\text{out}} \end{pmatrix} = \begin{pmatrix} S_{11} & S_{12} \\ S_{21} & S_{22} \end{pmatrix} \begin{pmatrix} \hat{a}_{1,\text{in}} \\ \hat{a}_{2,\text{in}} \end{pmatrix} + \begin{pmatrix} \hat{N}_1 \\ \hat{N}_2 \end{pmatrix}, \quad (5.1)$$

where \hat{N}_i represent added noise from the device. A starting definition for nonreciprocity is that a device is nonreciprocal when $S_{21} \neq S_{12}$. This corresponds to a change in scattering when input and output modes are interchanged.

In order to develop an intuitive picture for nonreciprocity, we introduce the gyration as a canonical nonreciprocal element. The gyration is a 2-port device which provides a nonreciprocal phase shift (Pozar, 2011), as illustrated in fig. 4.1a. In one direction, it imparts a phase shift of π , while in the other direction it leaves the signal unchanged. The scattering matrix of a lossless, matched gyration is given by $S_{\text{gyr}} = \begin{pmatrix} 0 & 1 \\ -1 & 0 \end{pmatrix}$. Recently, new implementations of microwave gyrations relying on the non-commutativity of frequency and time translations (Rosenthal et al., 2017) have been demonstrated with Josephson junctions (Abdo, Brink, and Chow, 2017; Chapman et al., 2017). The gyration is in itself is not commonly used in technological applications, but rather as a fundamental nonreciprocal building block to construct other nonreciprocal devices.

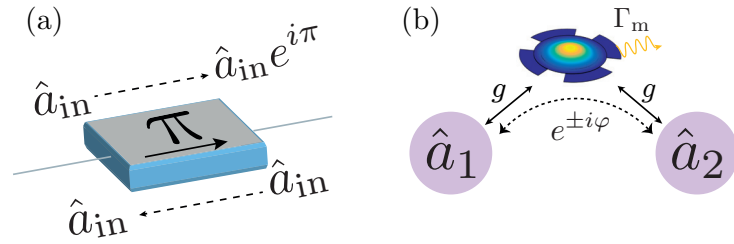


Figure 5.1: Gyrator and optomechanical coupling. (a) The gyrator is a canonical nonreciprocal component. It is a two-port device, which adds a π phase shift when a wave is traveling one way but no phase shift in the reverse direction. (b) A simple multimode optomechanical system consists of two electromagnetic modes coupled to the same mechanical oscillator. Due to the two microwave drive tones which linearize the optomechanical coupling, the conversion from \hat{a}_1 to \hat{a}_2 formally imparts a nonreciprocal phase shift, similarly to the gyrator. In the case of frequency conversion, this phase shift between tones at different frequencies is not measurable, as it depends on the reference frame. Figure reproduced from Bernier, Tóth, Feofanov, et al. (2018b).

An isolator is a useful nonreciprocal device that can be assembled from a gyrator and additional reciprocal elements (Pozar, 2011), as illustrated in fig. 5.2a. A beam splitter divides a signal in two; one part goes through a gyrator while the other propagates with no phase shift. Recombining the signals with a second beam splitter results in a 4-port device that interferes the signal nonreciprocally. For a signal injected in port 1, the recombined signal after the second beam splitter interferes destructively in port 4, but constructively in port 2. In contrast, a signal injected from port 2, reaches port 3 instead of port 1, since one arm of the signal is in this case subjected to a π shift. Overall, the device is a four-port circulator that redirects each port to the next. To obtain a two-port isolator, two of the four ports are terminated by matched loads to absorb the unwanted signal. The scattering matrix for the remaining two ports is that of an ideal isolator, $S_{is} = \begin{pmatrix} 0 & 0 \\ 1 & 0 \end{pmatrix}$.

The gyrator-based scheme helps to summarize three sufficient ingredients to realize an isolator. Firstly, an element *breaks reciprocity* by inducing a nonreciprocal phase shift. Secondly, an additional path is introduced for signals to *interfere* such that the scattering matrix becomes asymmetric in the amplitude with $|S_{21}| \neq |S_{12}|$. Finally, *dissipation* is required for an isolator, since its scattering matrix between the two ports is non-unitary and some signals must necessarily be redirected to an external degree of

freedom. The gyrator-based isolator provides a framework to understand how nonreciprocity arises in microwave optomechanical implementations.

5.2.2 Nonreciprocity in optomechanical systems

Microwave optomechanical schemes for nonreciprocity rely on scattering between coupled modes (Ranzani and Aumentado, 2014; Ranzani and Aumentado, 2015). As a first step towards optomechanical isolators, we introduce optomechanical frequency conversion (Lecocq, Clark, et al., 2016) and how it relates to the gyrator.

The simplest optomechanical scheme to couple two electromagnetic modes \hat{a}_1 and \hat{a}_2 is that both interact through a mechanical oscillator \hat{b} (fig. 4.1b). The optomechanical coupling terms $\hbar g_{0,i} \hat{a}_i^\dagger \hat{a}_i (\hat{b} + \hat{b}^\dagger)$ ($i = 1, 2$), where $g_{0,i}$ is the vacuum coupling rate of \hat{a}_i and \hat{b} , can be linearized using two applied tones, detuned by Δ_i with respect to each cavity resonance (Aspelmeyer, Kippenberg, and Marquardt, 2014). In a frame rotating at the pump frequencies, keeping only the linear terms and taking the rotating-wave approximation, the effective Hamiltonian becomes (Aspelmeyer, Kippenberg, and Marquardt, 2014)

$$H = -\hbar\Delta_1 \hat{a}_1^\dagger \hat{a}_1 - \hbar\Delta_2 \hat{a}_2^\dagger \hat{a}_2 + \hbar\Omega_m \hat{b}^\dagger \hat{b} + \hbar g_1 \left(e^{i\phi_1} \hat{a}_1 \hat{b}^\dagger + e^{-i\phi_1} \hat{a}_1^\dagger \hat{b} \right) + \hbar g_2 \left(e^{i\phi_2} \hat{a}_2 \hat{b}^\dagger + e^{-i\phi_2} \hat{a}_2^\dagger \hat{b} \right), \quad (5.2)$$

where Ω_m is the mechanical frequency, $g_i = g_{0,i} \sqrt{n_{c,i}}$ is the coupling rate enhanced by the photon number $n_{c,i}$ due to the pump field, and ϕ_i is the phase of each pump field. For the resonant case $\Delta_1 = \Delta_2 = -\Omega_m$, the frequency conversion between the two modes through mechanical motion is characterized by the scattering matrix elements (in the middle of the conversion frequency window) (Safavi-Naeini and Painter, 2011)

$$S_{21} = \frac{2\sqrt{\mathcal{C}_1 \mathcal{C}_2}}{1 + \mathcal{C}_1 + \mathcal{C}_2} e^{i(\phi_1 - \phi_2)} \quad \text{and} \quad S_{12} = S_{21}^*, \quad (5.3)$$

where κ_i is the energy decay rate of mode \hat{a}_i , and $\mathcal{C}_i = 4g_i^2/(\kappa_i \Gamma_m)$ is the cooperativity with Γ_m the energy decay rate of the mechanical oscillator (for simplicity, the cavities are assumed to be overcoupled).

While eq. (5.3) apparently fulfills the condition $S_{21} \neq S_{12}$ for nonreciprocity, the situation is more subtle when the two modes are at different frequencies in the laboratory frame. The time-dependence for the two modes can be written explicitly to understand where the issue lies. The first incoming

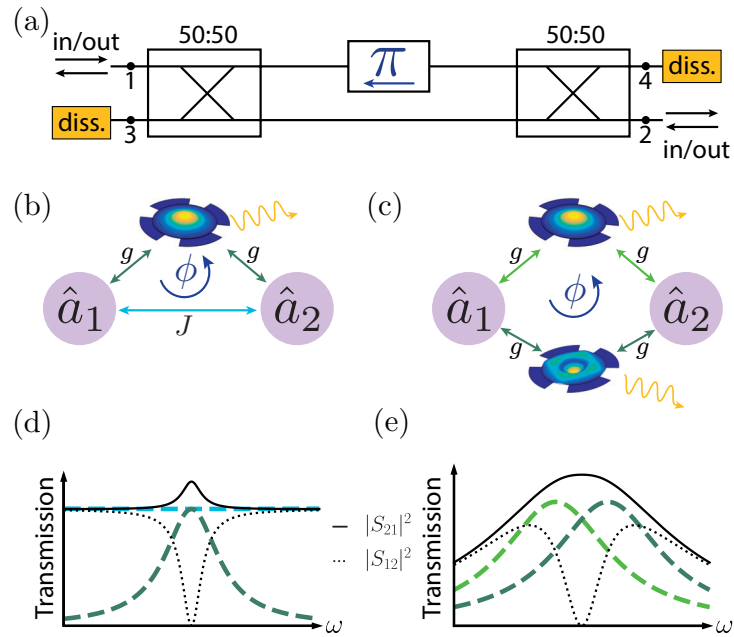


Figure 5.2: Gyration-based isolator compared to optomechanical multimode schemes. (a) An isolator can be built by combining the gyration with other reciprocal elements. By combining the gyration with two beam splitters and a transmission line, a four-port circulator is realized. Dissipation (provided by line terminations) eliminates the unwanted ports. (b) Three-mode optomechanical isolator in which two electromagnetic modes have a direct coherent J -coupling, and interact through a shared mechanical mode. (c) Four-mode optomechanical isolator, in which two electromagnetic modes interact through two different mechanical modes. (d) In the scheme (b), frequency conversion through the J coupling (light blue) and through the mechanical modes (green) interfere differently in the forward and backward direction when combined. (e) In the scheme (c), the frequency conversion through each mechanical mode (green curves) are offset in frequency to interfere in a nonreciprocal manner. Figure reproduced from Bernier, Tóth, Feofanov, et al. (2018b).

mode $\hat{a}_{1,\text{in}}(t) = e^{-i\omega_1 t} A_1$ converts to $\hat{a}_{2,\text{out}}(t) = S_{21} e^{-i\omega_2 t} A_1$ and reciprocally the other mode $\hat{a}_{2,\text{in}}(t) = e^{-i\omega_2 t} A_2$ converts to $\hat{a}_{1,\text{out}}(t) = S_{12} e^{-i\omega_1 t} A_2$, where ω_i are the mode angular frequencies and A_i are constant amplitudes. If a new origin of time t_0 is chosen, the fields transform as $\hat{a}'_i(t) = e^{-i\omega_i t_0} \hat{a}_i(t)$, equivalent to a frequency-dependent phase shift for each mode. In this new reference frame, the scattering matrix transforms as $S'_{21} = S_{21} e^{-i(\omega_2 - \omega_1)t_0}$ and $S'_{12} = S_{12} e^{+i(\omega_2 - \omega_1)t_0}$. For different frequencies $\omega_1 \neq \omega_2$, there always exists a t_0 for which the phases of S'_{21} and S'_{12} are the same. A nonreciprocal phase shift is therefore unphysical for frequency conversion, as the phase depends on the chosen reference frame. For this reason, Ranzani and Aumentado (Ranzani and Aumentado, 2015) pose the stricter requirement $|S_{12}| \neq |S_{21}|$ for nonreciprocity in coupled-modes systems. The pump tones that linearize the optomechanical coupling break reciprocity, as they are held fixed when input and output are interchanged and impose a fixed phase $\phi_1 - \phi_2$ for the coupling. Nevertheless, there is always a frame with a different origin of time in which the two pumps have the same phase and $\phi'_1 - \phi'_2 = 0$. In that frame, the symmetry between the two ports is apparently restored.

While a frame change to a new origin of time turns a phase-nonreciprocal system reciprocal for coupled-mode systems, it simultaneously turns reciprocal systems phase-nonreciprocal. With $(\omega_2 - \omega_1)t_0 = \pi/2$, the gyrotor scattering matrix transforms from $S_{\text{gyr}} = \begin{pmatrix} 0 & 1 \\ -1 & 0 \end{pmatrix}$ to $S'_{\text{gyr}} = e^{i\pi/2} \begin{pmatrix} 0 & 1 \\ 1 & 0 \end{pmatrix}$ while the transmission line scattering matrix transforms from $S_{\text{tl}} = \begin{pmatrix} 0 & 1 \\ 1 & 0 \end{pmatrix}$ to $S'_{\text{tl}} = e^{i\pi/2} \begin{pmatrix} 0 & 1 \\ -1 & 0 \end{pmatrix}$. In effect, gyrotors and transmission lines are mapped to each other. Importantly, the combination of a gyrotor and a transmission line is preserved. The isolator of fig. 5.2a is built precisely like this, combining a gyrotor and a transmission line. The frequency-converting equivalent is an isolator regardless of the chosen time frame. Note that the frame-dependent nonreciprocal phase resembles the gauge symmetry of electromagnetism that can realize the Aharonov-Bohm effect when a loop is created (Fang, Z. Yu, and S. Fan, 2012; Fang, Z. Yu, and S. Fan, 2013; Tzuang et al., 2014). To build an optomechanical isolator, one method is therefore to realize two paths between \hat{a}_1 and \hat{a}_2 , one similar to a gyrotor and the other to a transmission line, which can be done following one of two proposed schemes.

The first scheme, shown in fig. 4.3b, combines an optomechanical link between two electromagnetic modes \hat{a}_1 and \hat{a}_2 and a direct coherent coupling of strength J . The interaction term of the latter, given by $H_{\text{coh}} = \hbar J (e^{i\theta} \hat{a}_1 \hat{a}_2^\dagger + e^{-i\theta} \hat{a}_1^\dagger \hat{a}_2)$ induces by itself conversion between the two modes as

$$S_{21} = \frac{2\sqrt{\mathcal{C}_{\text{coh}}}}{1 + \mathcal{C}_{\text{coh}}} i e^{i\theta} \quad \text{and} \quad S_{12} = \frac{2\sqrt{\mathcal{C}_{\text{coh}}}}{1 + \mathcal{C}_{\text{coh}}} i e^{-i\theta} \quad (5.4)$$

where $\mathcal{C}_{\text{coh}} = 4J^2/(\kappa_1\kappa_2)$. Compared to eq. (5.3), there is an intrinsic reciprocal phase shift of $i = e^{i\pi/2}$. By choosing the phases $\phi_1 = \phi_2$ and $\theta = \pi/2$, the optomechanical link realizes a reciprocal transmission line while the coherent link breaks the symmetry and realizes a gyrator. The combination, with matching coupling rates, functions as an isolator between the modes \hat{a}_1 and \hat{a}_2 . One cannot tell which of the optomechanical or direct link breaks reciprocity, as it depends on the chosen frame. Nonetheless, there is a frame-invariant phase $\phi = \phi_1 - \phi_2 + \theta$ that globally characterizes the broken symmetry and can be seen as a synthetic magnetic flux (Peano, Brendel, et al., 2015; Fang, Luo, et al., 2017).

The second scheme to realize isolation, shown in fig. 4.3c, uses two optomechanical conversion links with two different mechanical modes. From eq. (5.3), one cannot realize the scattering matrices of a gyrator and a transmission line with the same reciprocal phase factor. Dissipation of the mechanical modes is the key to tune the overall reciprocal phase factor of conversion. By detuning the two mechanical modes in frequency, the mechanical susceptibilities induce different phases. Advantageously over the first scheme, no direct coherent coupling must be engineered and the modes \hat{a}_1 and \hat{a}_2 do not need to have the same frequency.

The first scheme (fig. 4.3b) derives from a proposal by Metelmann and Clerk (Metelmann and Clerk, 2015), who describe the optomechanical link as an effective dissipative interaction between the modes \hat{a}_1 and \hat{a}_2 . It is equivalent to a non-Hermitian Hamiltonian term $H_{\text{dis}} = -i\hbar\Gamma_{\text{dis}}(e^{i(\phi_1-\phi_2)}\hat{a}_1\hat{a}_2^\dagger + e^{-i(\phi_1-\phi_2)}\hat{a}_1^\dagger\hat{a}_2)$ with $\Gamma_{\text{dis}} = 2g_1g_2/\Gamma_{\text{m}}$. With suitable parameters, the total interaction $H_{\text{coh}} + H_{\text{dis}}$ can be made unidirectional, with for instance a term proportional to $\hat{a}_1^\dagger\hat{a}_2$ but not $\hat{a}_1\hat{a}_2^\dagger$. We note that while resonant modes are considered here, parametric interactions can implement a direct coherent J -coupling even between modes at different frequencies. The second scheme (fig. 4.3c) can be understood in the same framework, as each detuned mechanical conversion link is equivalent to an effective interaction between the modes \hat{a}_1 and \hat{a}_2 with both a coherent and a dissipative component. The total effective interaction can be made unidirectional when the total direct coherent component matches the total dissipative component and they interfere.

Both methods to achieve nonreciprocal isolation can be decomposed in terms of the three ingredients identified in the gyrator-based isolator. At the heart is the breaking of reciprocity that occurs through the time-dependent drives applied to the system that impart a complex phase to the interaction. Then a loop constituted by two arms allow the unwanted signal to be canceled in the backward direction through destructive interference while

preserving it in the forward direction. The mechanical dissipative baths are used to eliminate the backward signal. As a consequence, the nonreciprocal bandwidth (where S_{21} and S_{12} differ) is limited by the mechanical dissipation rates, as illustrated in fig. 4.3d and e. Dissipation plays a double role here, since it also gives the different reciprocal phase shift in each arms necessary to implement both a gyrator and a transmission line.

In the following, we present an experimental implementation of the second method described above, using a multimode microwave optomechanical circuit. In parallel to our work, similar systems were realized elsewhere (G. A. Peterson et al., 2017; Barzanjeh et al., 2017). The first method was realized in the optical domain (Fang, Luo, et al., 2017) using two mechanical oscillators coherently coupled to implement the optomechanical pathway.

5.3 Optomechanical isolator

We describe here a scheme to attain reconfigurable nonreciprocal transmission without a need for any direct coherent coupling between input and output modes, using purely optomechanical interactions (Aspelmeyer, Kippenberg, and Marquardt, 2014; Bowen and G. J. Milburn, 2015). This scheme neither requires cavity-cavity interactions nor phonon-phonon coupling, which are necessary for the recently demonstrated optomechanical nonreciprocity in the optical domain (Fang, Luo, et al., 2017). Two paths of transmission between the microwave modes are established, through two distinct mechanical modes. Interference between those paths with differing phases forms the basis of the nonreciprocal process (X.-W. Xu et al., 2016; Tian and Z. Li, 2016). In fact, due to the finite quality factor of the intermediary mechanical modes, both conversion paths between the electromagnetic modes are partly dissipative in nature. Nonreciprocity is in this case only possible by breaking the symmetry between the two dissipative coupling pathways. We describe the mechanism in detail below.

5.3.1 Theoretical model

We theoretically model our system to reveal how nonreciprocity arises. We consider two microwave modes (described by their annihilation operators \hat{a}_1 , \hat{a}_2) having resonance frequencies $\omega_{c,1}$, $\omega_{c,2}$ and dissipation rates κ_1 , κ_2 , which are coupled to two mechanical modes (described by the annihilation operators \hat{b}_1 , \hat{b}_2) having resonance frequencies Ω_1 , Ω_2 and dissipation rates $\Gamma_{m,1}$, $\Gamma_{m,2}$ (fig. 5.3a). The radiation-pressure-type optomechanical interaction has

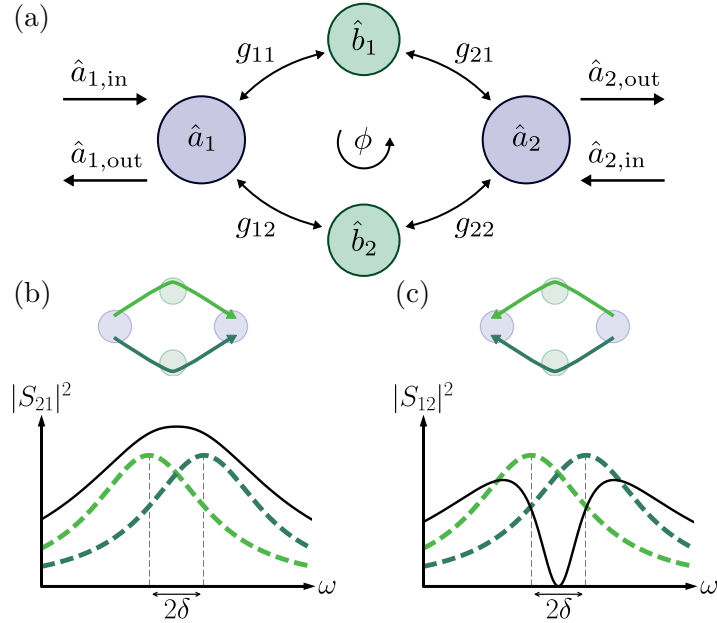


Figure 5.3: Scheme for a multimode optomechanical isolator. (a) Two microwave modes \hat{a}_1 and \hat{a}_2 are coupled via two mechanical modes \hat{b}_1 and \hat{b}_2 through optomechanical frequency conversion (as given by the coupling constants $g_{11}, g_{21}, g_{12}, g_{22}$). Nonreciprocity results from the interference between the two optomechanical (conversion) pathways g_{11}, g_{21} and g_{12}, g_{22} , in the presence of a suitably chosen phase difference ϕ between the coupling constants as well as the deliberate introduction of an asymmetry in the pathways. (b,c) The symmetry between the pathways can be broken by offsetting the optomechanical transmission windows through each mechanical mode (dashed lines in dark and light green) by a frequency difference 2δ , resulting in different $|S_{21}|$ and $|S_{12}|$ (solid lines). Each single pathway, in the absence of the other mode, is described by eq. (5.6). In the forward direction (b), the two paths interfere constructively, allowing transmission and a finite scattering matrix element S_{21} on resonance with the first microwave cavity. In contrast, in the backward direction (c), the paths interfere destructively, such that $S_{12} \approx 0$ on resonance, thereby isolating the first microwave cavity from the second. The isolation bandwidth is determined by the intrinsic dissipation rate of the mechanical modes. Figure reproduced from Bernier, Tóth, Kootandavida, et al. (2017).

the form¹ $g_{0,ij}\hat{a}_i^\dagger\hat{a}_i(\hat{b}_j + \hat{b}_j^\dagger)$ (Aspelmeyer, Kippenberg, and Marquardt, 2014; Bowen and G. J. Milburn, 2015), where $g_{0,ij}$ designates the vacuum optomechanical coupling strength of the i^{th} microwave mode to the j^{th} mechanical mode. Four microwave tones are applied, close to each of the two lower sidebands of the two microwave modes, with detunings of $\Delta_{11} = \Delta_{21} = -\Omega_1 - \delta$ and $\Delta_{12} = \Delta_{22} = -\Omega_2 + \delta$ (fig. 5.4c). We linearise the Hamiltonian, neglect counter-rotating terms, and write it in a rotating frame with respect to the mode frequencies as

$$H = -\delta\hat{b}_1^\dagger\hat{b}_1 + \delta\hat{b}_2^\dagger\hat{b}_2 + g_{11}(\hat{a}_1\hat{b}_1^\dagger + \hat{a}_1^\dagger\hat{b}_1) + g_{21}(\hat{a}_2\hat{b}_1^\dagger + \hat{a}_2^\dagger\hat{b}_1) \\ + g_{12}(\hat{a}_1\hat{b}_2^\dagger + \hat{a}_1^\dagger\hat{b}_2) + g_{22}(e^{i\phi}\hat{a}_2\hat{b}_2^\dagger + e^{-i\phi}\hat{a}_2^\dagger\hat{b}_2) \quad (5.5)$$

where \hat{a}_i and \hat{b}_j are redefined to be the quantum fluctuations around the linearised mean fields. Here $g_{ij} = g_{0,ij}\sqrt{n_{ij}}$ are the field-enhanced optomechanical coupling strengths, where n_{ij} is the contribution to the mean intracavity photon number due to the drive tone with detuning Δ_{ij} . Although in principle each coupling is complex, without loss of generality we can take all to be real except the one between \hat{a}_2 and \hat{b}_2 with a complex phase ϕ .

We start by considering frequency conversion through a single mechanical mode. Neglecting the noise terms, the field exiting the cavity \hat{a}_2 is given by $\hat{a}_{2,\text{out}} = S_{21}\hat{a}_{1,\text{in}} + S_{22}\hat{a}_{2,\text{in}}$, which defines the scattering matrix S_{ij} . For a single mechanical pathway, setting $g_{12} = g_{22} = 0$ and $\delta = 0$, the scattering matrix between input and output mode becomes

$$S_{21}(\omega) = \sqrt{\frac{\kappa_{\text{ex},1}\kappa_{\text{ex},2}}{\kappa_1\kappa_2}} \frac{\sqrt{\mathcal{C}_{11}\mathcal{C}_{21}}\Gamma_{\text{m},1}}{\frac{\Gamma_{\text{eff},1}}{2} - i\omega}, \quad (5.6)$$

where $\kappa_{\text{ex},1}$, $\kappa_{\text{ex},2}$ denote the external coupling rates of the microwave modes to the feedline, and the (multiphoton) cooperativity for each mode pair is defined as $\mathcal{C}_{ij} = 4g_{ij}^2/(\kappa_i\Gamma_{\text{m},j})$. Conversion occurs within the modified mechanical response over an increased bandwidth $\Gamma_{\text{eff},1} = \Gamma_{\text{m},1}(1 + \mathcal{C}_{11} + \mathcal{C}_{21})$. This scenario, where a mechanical oscillator mediates frequency conversion between electromagnetic modes, has recently been demonstrated (Lecoq, Clark, et al., 2016) with a microwave optomechanical circuit (Teufel, D. Li, et al., 2011), and moreover used to create a bidirectional link between a microwave and an optical mode (Andrews, R. W. Peterson, et al., 2014). Optimal conversion, limited by internal losses in the microwave cavities, reaches at resonance $|S_{21}|_{\text{max}}^2 = \frac{\kappa_{\text{ex},1}\kappa_{\text{ex},2}}{\kappa_1\kappa_2}$ in the limit of large cooperativities $\mathcal{C}_{11} = \mathcal{C}_{21} \gg 1$.

¹When written in units where $\hbar = 1$.

We next describe nonreciprocal transmission of the full system with both mechanical modes. We consider the ratio of transmission amplitudes given by

$$\frac{S_{12}(\omega)}{S_{21}(\omega)} = \frac{g_{11}\chi_1(\omega)g_{21} + g_{12}\chi_2(\omega)g_{22}e^{+i\phi}}{g_{11}\chi_1(\omega)g_{21} + g_{12}\chi_2(\omega)g_{22}e^{-i\phi}} \quad (5.7)$$

with the mechanical susceptibilities defined as $\chi_1^{-1}(\omega) = \Gamma_{m,1}/2 - i(\delta + \omega)$ and $\chi_2^{-1}(\omega) = \Gamma_{m,2}/2 + i(\delta - \omega)$. Conversion is nonreciprocal if the above expression has a magnitude that differs from 1 (Ranzani and Aumentado, 2014; Ranzani and Aumentado, 2015). If S_{21} and S_{12} differ only by a phase, a change of time frame removes the apparent asymmetry, as explained in section 5.2.2. Upon a change in the conversion direction, the phase ϕ of the coherent coupling (between the microwave and mechanical mode) is conjugated, while the complex phase associated with the response of the dissipative mechanical modes remains unchanged. Physically, scattering from $1 \rightarrow 2$ is related to scattering from $2 \rightarrow 1$ via time-reversal, which conjugates phases due to coherent evolution of the system. Dissipation is untouched by such an operation and thus remains invariant. Indeed, the mechanical dissipation is an essential ingredient for the nonreciprocity to arise in this system, but not sufficient on its own. In fact, if we align the frequency conversion windows corresponding to the two mechanical modes by setting $\delta = 0$, the system becomes reciprocal on resonance ($\omega = 0$), since there is no longer any phase difference between numerator and denominator. This situation corresponds to two symmetric pathways resulting from purely dissipative couplings; they can interfere only in a reciprocal way.

Optimal conditions

We study the conditions for isolation, when the backward transmission S_{12} vanishes while the forward transmission S_{21} is non-zero. A finite offset 2δ between the mechanical conversion windows causes an intrinsic phase shift for signals on resonance ($\omega = 0$) between the two mechanical pathways, as they fall either on the red or the blue side of each mechanical resonance. The coupling phase ϕ is then adjusted to suppress propagation in the backward direction S_{12} (fig. 5.3c), by canceling the two terms in the numerator of eq. (5.7). In general, there is always a frequency ω for which the two mechanical pathways have the same conversion amplitude, $|g_{11}\chi_1(\omega)g_{21}| = |g_{12}\chi_2(\omega)g_{22}|$, such that the phase ϕ can be tuned to cancel transmission in one direction. Specifically, for two mechanical modes with identical decay rates ($\Gamma_{m,1} = \Gamma_{m,2} = \Gamma_m$) and symmetric couplings ($g_{11}g_{21} = g_{12}g_{22}$), we find that transmission from

ports 2 to 1 vanishes on resonance if

$$\frac{\Gamma_m}{2\delta} = \tan \frac{\phi}{2}. \quad (5.8)$$

The corresponding terms of the denominator have a different relative phase, and the signal adds constructively in the forward direction (fig. 5.3b). The device thus acts as an isolator from \hat{a}_1 to \hat{a}_2 , realised without relying on the Josephson nonlinearity (Sliwa et al., 2015; Lecocq, Ranzani, et al., 2017).

We now describe the conditions to minimise insertion loss of the isolator in the forward direction. Still considering the symmetric case, the cooperativity is set to be the same for all modes ($\mathcal{C}_{ij} = \mathcal{C}$). For a given separation δ , transmission on resonance ($\omega = 0$) in the transmitting direction has the maximum

$$|S_{21}|_{\max}^2 = \frac{\kappa_{\text{ex},1}\kappa_{\text{ex},2}}{\kappa_1\kappa_2} \left(1 - \frac{1}{2\mathcal{C}}\right) \quad (5.9)$$

for a cooperativity $\mathcal{C} = 1/2 + 2\delta^2/\Gamma_m^2$. As in the case for a single mechanical pathway in eq. (5.6), for a large cooperativity the isolator can reach an insertion loss only limited by the internal losses of the microwave cavities.

The unusual and essential role of dissipation in this nonreciprocal scheme is also apparent in the analysis of the bandwidth of the isolation. Although the frequency conversion through a single mechanical mode has a bandwidth $\Gamma_{\text{eff},j}$ (see eq. (5.6)), increased from the bare mechanical dissipation rate Γ_m by the optomechanical damping of the pumps on the lower sidebands, the nonreciprocal bandwidth is set by the intrinsic mechanical damping rates. Examination of eq. (5.7) reveals that nonreciprocity originates from the interference of two mechanical susceptibilities of widths $\Gamma_{m,j}$. One can conclude that the intrinsic mechanical dissipation, which takes energy out of the system regardless of the transmission direction, is an essential ingredient for the nonreciprocal behaviour reported here, as discussed previously (Ranzani and Aumentado, 2015; Metelmann and Clerk, 2015). In contrast, optomechanical damping works symmetrically between input and output modes. By increasing the coupling strengths, using higher pump powers, the overall conversion bandwidth increases, while the nonreciprocal bandwidth stays unchanged.

5.4 Experimental results

We experimentally realise this nonreciprocal scheme using a superconducting circuit optomechanical system in which the mechanical motion is capacitively coupled to a multi-mode microwave circuit (Teufel, D. Li, et al., 2011). The

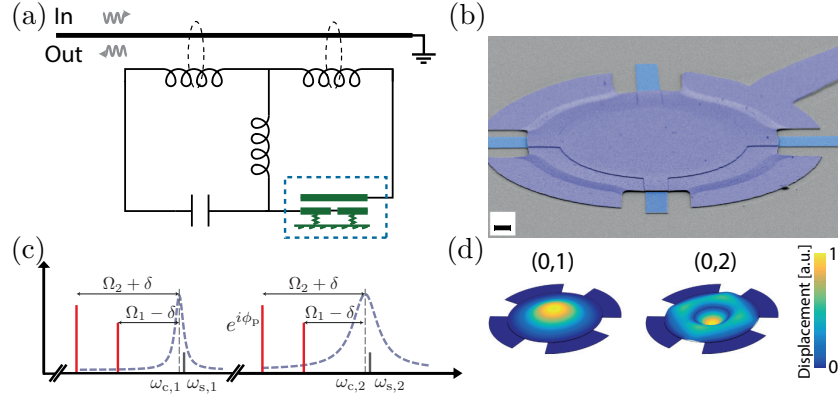


Figure 5.4: Implementation of a superconducting microwave circuit optomechanical device for nonreciprocity. (a) A superconducting circuit featuring two electromagnetic modes in the microwave domain is capacitively coupled to a mechanical element (a vacuum-gap capacitor, dashed rectangle) and inductively coupled to a microstrip feedline. The end of the feedline is grounded and the circuit is measured in reflection. (b) Scanning electron micrograph of the drum-head-type vacuum gap capacitor (dashed rectangle in (a)) with a gap distance below 50 nm, made from aluminium on a sapphire substrate. The scale bar indicates 2 μm . (c) Frequency domain schematic of the microwave pump setup to achieve nonreciprocal mode conversion. Microwave pumps (red bars) are placed at the lower motional sidebands - corresponding to the two mechanical modes - of both microwave resonances (dashed purple lines). The pumps are detuned from the exact sideband condition by $\pm\delta = 2\pi \times 18$ kHz, creating two optomechanically induced transparency windows detuned by 2δ from the microwave resonance frequencies (denoted by $\omega_{c,1}$ and $\omega_{c,1}$, vertical dashed line). The phase ϕ_p of one the pumps is tuned. The propagation of an incoming signal (with frequency $\omega_{s,1}$ or $\omega_{s,2}$, solid grey bar) in the forward and backward direction depends on this phase and nonreciprocal microwave transmission can be achieved. (d) Finite-element simulation of the displacement of the fundamental (0,1) and second order radially symmetric (0,2) mechanical modes (with respective measured resonance frequencies $\Omega_1/2\pi = 6.5$ MHz and $\Omega_2/2\pi = 10.9$ MHz), which are exploited as intermediary dissipative modes to achieve nonreciprocal microwave conversion. Figure reproduced from Bernier, Tóth, Koottandavida, et al. (2017).

sample is HYB-20160524-1-12. The circuit, schematically shown in fig. 5.4a, supports two electromagnetic modes with resonance frequencies $(\omega_{c,1}, \omega_{c,2}) = 2\pi \times (4.1, 5.2)$ GHz and energy decay rates $(\kappa_1, \kappa_2) = 2\pi \times (0.2, 3.4)$ MHz, both of them coupled to the same vacuum-gap capacitor. We utilise the fundamental and second order radially symmetric $(0, 2)$ modes of the capacitor's mechanically compliant top plate (Cicak et al., 2010) (see fig. 5.4b, d) with respective resonance frequencies $(\Omega_1, \Omega_2) = 2\pi \times (6.5, 10.9)$ MHz, intrinsic energy decay rates $(\Gamma_{m,1}, \Gamma_{m,2}) = 2\pi \times (30, 10)$ Hz and optomechanical vacuum coupling strengths $(g_{0,11}, g_{0,12}) = 2\pi \times (91, 12)$ Hz (with $g_{0,11} \approx g_{0,21}$ and $g_{0,12} \approx g_{0,22}$, as the two microwave cavities are symmetrically coupled to the mechanical modes). The device is placed at the mixing chamber of a dilution refrigerator at 200 mK and all four incoming pump tones are heavily filtered and attenuated to eliminate Johnson and phase noise. We establish a parametric coupling between the two electromagnetic and the two mechanical modes by introducing four microwave pumps with frequencies slightly detuned from the lower motional sidebands of the resonances, as shown in fig. 5.4c and as discussed above.

5.4.1 Transmission measurements

Certain calibrations are required in order to measure the scattering coefficients for a frequency conversion experiment. The diagram of the measurement chain is shown in fig. 5.5. The complication arises from the fact that there is an unknown attenuation on the input line $\alpha(\omega)$ and an overall measurement gain after the device $\mathcal{G}(\omega)$ that are both frequency dependent. We describe here the model for a measurement of frequency conversion from ω_1 to ω_2 . A tone at frequency ω_1 and power $P_{\text{in}}^{\text{src}}(\omega_1)$ is sent to the device. After an attenuation $\alpha(\omega_1)$, it is converted to ω_2 with a power coefficient $|S_{21}|^2$, then amplified by a gain $\mathcal{G}(\omega_2)$ before it is measured to have a power $P_{\text{out}}^{\text{meas}}(\omega_2)$. The scattering coefficient is given by

$$|S_{21}|^2 = \frac{1}{\alpha(\omega_1)\mathcal{G}(\omega_2)} \frac{P_{\text{out}}^{\text{meas}}(\omega_2)}{P_{\text{in}}^{\text{src}}(\omega_1)}. \quad (5.10)$$

The constants $\alpha(\omega_1)$ and $\mathcal{G}(\omega_2)$ must be calibrated through some auxiliary measurements. We rely on the calibration of the HEMT amplifier that is the dominating source of added noise (see section 3.4.2) as an absolute scale for power at the device level.

To estimate the attenuation $\alpha(\omega)$, we employ a calibration tone and compare the signal strength to the noise background. We assume that the HEMT

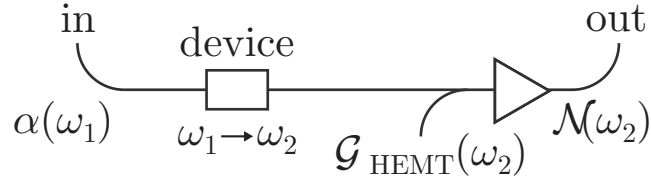


Figure 5.5: Diagram of the measurement chain for frequency conversion. The incoming signal at ω_1 is first attenuated by $\alpha(\omega_1)$. It is then converted to the frequency ω_2 by the optomechanical isolator. Finally, it is combined with the HEMT added noise $\mathcal{N}_{\text{HEMT}}(\omega_2)$ and amplified by an overall gain $\mathcal{G}(\omega_2)$ before it is measured.

added noise $\mathcal{N}_{\text{HEMT}}(\omega)$ is the dominating source of added noise in the measurement chain. That means that the SNR of a calibration tone of power $P_{\text{cal.}}^{\text{src}}(\omega)$ against the noise background is the same at the level of the device and at the end of the measurement chain. The same overall gain $\mathcal{G}(\omega)$ amplifies both the calibration tone after the device (of power $\alpha(\omega)P_{\text{cal.}}^{\text{src}}(\omega)$) and the HEMT added noise $\mathcal{N}_{\text{HEMT}}(\omega)$ that constitutes the noise background. They are given by

$$\text{SNR}_{\text{cal.}}(\omega) = \frac{P_{\text{cal.}}^{\text{meas}}(\omega)}{N^{\text{meas}}(\omega)} = \frac{\alpha(\omega)P_{\text{cal.}}^{\text{src}}(\omega)}{\mathcal{N}_{\text{HEMT}}(\omega)} \quad (5.11)$$

where $N^{\text{meas}}(\omega)$ is the measured level of the noise background. The attenuation is therefore

$$\alpha(\omega) = \frac{P_{\text{cal.}}^{\text{meas}}(\omega)}{P_{\text{cal.}}^{\text{src}}(\omega)} \frac{\mathcal{N}_{\text{HEMT}}(\omega)}{N^{\text{meas}}(\omega)} \quad (5.12)$$

where all quantities are known and measured. In practice, the calibration tone is set outside the cavity resonance, to avoid absorption by the cavity. It is assumed that the attenuation α varies little with frequency over a frequency range in the order of the cavities linewidths $\kappa_{1,2}$.

The calibration of $\mathcal{G}(\omega)$ only requires the measurement of the noise background. Since we assume that the HEMT added noise dominates, the measured background $N^{\text{meas}}(\omega)$ is the HEMT noise amplified by the overall gain $\mathcal{G}(\omega)$, such that

$$\mathcal{G}(\omega) = \frac{N^{\text{meas}}(\omega)}{\mathcal{N}_{\text{HEMT}}(\omega)}. \quad (5.13)$$

To measure $|S_{21}|^2$, we use a weak probing tone at frequency $\omega_1 + \delta$ that is measured at $\omega_2 + \delta$ with a spectrum analyzer. This gives the measured power of the converted signal $P_{\text{out}}^{\text{meas}}(\omega_2 + \delta)$ as a function of an input power $P_{\text{in}}^{\text{src}}(\omega_1 +$

δ). From eq. (5.10), and the calibration of $\alpha(\omega_1)$ and $\mathcal{G}(\omega_2)$, we deduce the scattering coefficient $|S_{21}|^2$. The frequency offset δ is spanned to cover the frequency dependence of transmission in the optomechanically mediated frequency conversion. Conversely, to measure $|S_{12}|^2$, the same procedure is done with the probing tone set at $\omega_2 + \delta$ and the converted tone measured at $\omega_1 + \delta$.

Frequency conversion in both directions, $|S_{21}(\omega)|^2$ and $|S_{12}(\omega)|^2$, are measured and compared in fig. 5.6a-c. The powers of the four pumps are chosen such that the associated individual cooperativities are given by $\mathcal{C}_{11} = 520$, $\mathcal{C}_{21} = 450$, $\mathcal{C}_{12} = 1350$ and $\mathcal{C}_{22} = 1280$. The detuning from the lower motional sidebands is set to $\delta = 2\pi \times 18$ kHz. By pumping both cavities on the lower sideband associated with the same mechanical mode, a signal injected on resonance with one of the cavities is converted in frequency to the other cavity. This process can add negligible noise when operating with a sufficiently high cooperativity, as demonstrated recently (Lecocq, Clark, et al., 2016). In the experiment, the four driving tones are all phase-locked and the phase of one tone ϕ_p is varied continuously from $-\pi$ to π . The pump phase is linked to the coupling phase ϕ by a constant offset, in our case $\phi_p \approx \phi + \pi$. Between the two transmission peaks corresponding to each mechanical mode, a region of nonreciprocity develops, depending on the relative phase ϕ_p .

The amount of nonreciprocity that occurs in this process is quantified and measured by the ratio of forward to backward conversion $|S_{21}/S_{12}|^2$. Figure 5.6d shows this quantity as a function of probe detuning and the relative pump phase. Isolation of more than 20 dB is demonstrated in each direction in a reconfigurable manner. The direction of isolation can be switched by taking $\phi_p \rightarrow -\phi_p$, as expected from eq. (5.8).

The ideal theoretical model, which takes into account $\Gamma_{m,1} \neq \Gamma_{m,2}$, predicts that the bandwidth of the region of nonreciprocity is commensurate with the arithmetic average of the bare mechanical dissipation rates, which is $\sim 2\pi \times 20$ Hz. However, given the significantly larger coupling strength of the fundamental mechanical mode compared to the second-order mode, and that $\kappa_2/\Omega_{1,2}$ is not negligible, the pump detuned by $\Omega_2 - \delta$ from the microwave mode \hat{a}_2 introduces considerable damping for the fundamental mode. This cross-damping, measured separately to be $\Gamma_{m,1}^{(\text{cross})} \approx 2\pi \times 20$ kHz at the relevant pump powers, widens the effective bandwidth of nonreciprocal behaviour by over two orders of magnitude and effectively cools the mechanical oscillator. It also acts as a loss in the frequency conversion process and thus effectively lowers the cooperativities to $(\mathcal{C}_{11}, \mathcal{C}_{21}) \approx (0.78, 0.68)$. This lowered cooperativity accounts for the overall ~ 10 dB loss in the forward direction. This limitation can be overcome in a future design by increasing the sideband

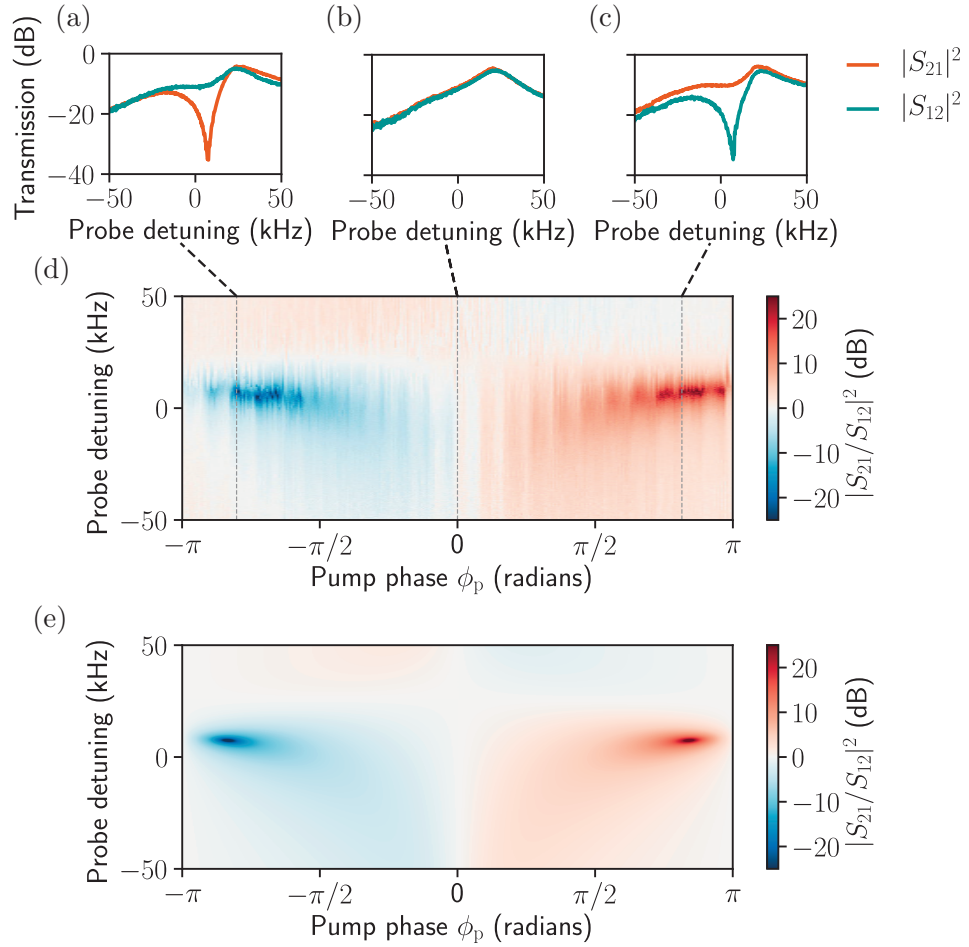


Figure 5.6: Experimental demonstration of nonreciprocity. (a-c) Power transmission between modes 1 and 2 as a function of probe detuning, shown in both directions for pump phases $\phi_p = -0.8\pi, 0, 0.8\pi$ radians (respectively (a), (b) and (c)). Isolation of more than 20 dB in the forward (c) and backward (a) directions is demonstrated, as well as reciprocal behaviour (b). (d) The ratio of transmission $|S_{21}/S_{12}|^2$, representing a measure of nonreciprocity, is shown as a function of pump phase ϕ_p and probe detuning. Two regions of nonreciprocity develop, with isolation in each direction. (e) Theoretical ratio of transmission from eq. (5.7), calculated with independently estimated experimental parameters. The theoretical model includes effectively lowered cooperativities for the mechanical mode \hat{b}_1 due to cross-damping (optomechanical damping of the lower frequency mechanical mode by the pump on the sideband of the higher frequency mechanical mode) acting as an extra loss channel. Figure adapted from Bernier, Tóth, Koottandavida, et al. (2017).

resolution with decreased κ_i or using the fundamental modes of two distinct mechanical elements with similar coupling strengths. To compare the experiment to theory we use a model that takes into account the cross-damping and an increased effective mechanical dissipation of the fundamental mode. The model is compared to the experimental data in fig. 5.6e, showing good qualitative agreement.

5.4.2 Noise measurements

From a technological standpoint, it does not suffice for an isolator to have the required transmission properties. Since its purpose is to protect the input from any noise propagating in the backward direction, the isolator's own noise emission is relevant. We therefore return to the theoretical description and derive the noise properties expected from the device, in the limit of overcoupled cavities ($\kappa_{\text{ex},i} \approx \kappa_i$).

In the forward direction on resonance, the emitted noise amounts to

$$N_{\text{fw}}(0) = 1/2 + (\bar{n}_{\text{m},1} + \bar{n}_{\text{m},2})/(4\mathcal{C}), \quad (5.14)$$

where $\bar{n}_{\text{m},j}$ is the thermal occupation of each mechanical mode. In the limit of a large cooperativity (implying a low insertion loss), the added noise becomes negligible in the forward direction.

More relevant for the purpose of using an isolator to protect sensitive quantum apparatus is the noise emitted in the backward direction, given by

$$N_{\text{bw}}(0) = 1/2 + (\bar{n}_{\text{m},1} + \bar{n}_{\text{m},2})/2. \quad (5.15)$$

Here the noise is directly commensurate with the occupation of the mechanics which can be of hundreds of quanta even at cryogenic millikelvin temperatures, due to the low mechanical frequencies. This is a direct consequence of isolation through absorption, since it prevents fluctuations from either cavity to emerge in the backward direction. In order to preserve the commutation relations of the bosonic output modes, the fluctuations have to originate from the mechanical modes. A practical low-noise design therefore requires a scheme to externally cool the mechanical modes, for instance via sideband cooling using an additional auxiliary microwave mode.

The origin of this noise asymmetry can be understood as noise interference. The thermal fluctuations of one mechanical oscillator are converted to microwave noise in each cavity through two paths, illustrated in fig. 5.7a, d: a direct (orange) and an indirect (yellow) link. Each pathway, on its own and

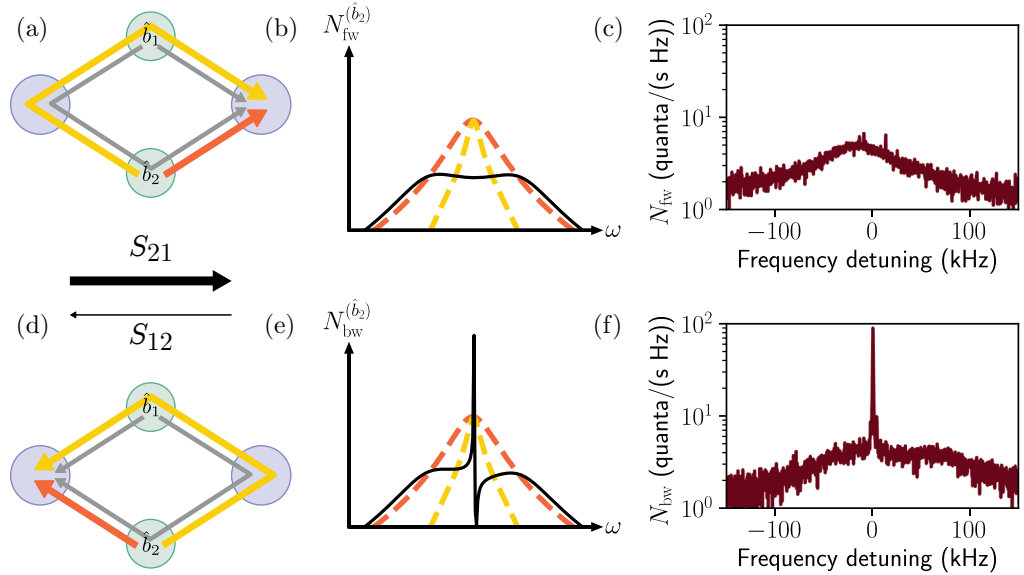


Figure 5.7: Asymmetric noise emission of the nonreciprocal circuit. The noise emission is mainly due to mechanical thermal noise, that is converted through two paths to the microwave modes. The resulting interference creates a different noise pattern in the forward (a-c) and the backward (d-f) directions when the circuit is tuned as an isolator from mode \hat{a}_1 to \hat{a}_2 . (a,d) The two possible paths for the noise are shown for each mechanical mode. For \hat{b}_2 , the direct path (orange) and the indirect path going through mode \hat{b}_1 (yellow) are highlighted (the corresponding paths for \hat{b}_1 are shown in grey). (b,e) Each path on its own would result in a wide noise spectrum that is equally divided between the two microwave cavities (dashed yellow and orange lines). When both paths are available however, the noise interferes differently in each direction (solid lines). In the backward direction (e), a sharp interference peak appears, of a much larger amplitude than the broad base. The theoretical curves (on an arbitrary logarithmic scale) are shown for the symmetric case ($\Gamma_{m,1} = \Gamma_{m,2}$) and for the single mode \hat{b}_2 . Note that for the mode \hat{b}_1 , the shape of the asymmetric peak in the backward noise would be the mirror image. (c,f) Measured output spectra of modes \hat{a}_2 (c) and \hat{a}_1 (f), calibrated to show the photon flux leaving the circuit. Because cross-damping provides extra cooling for the mode \hat{b}_1 , the thermal noise of \hat{b}_2 is expected to dominate. Figure reproduced from Bernier, Tóth, Koottandavida, et al. (2017).

with the same coupling strength, would result in symmetric noise that decreases in magnitude with increasing cooperativity. When both are present, however, the noise interferes with itself differently in each direction. In the forward direction, the noise interferes destructively (fig. 5.7b) leading to low added noise, but in the backward direction a sharp interference peak arises (fig. 5.7e) with finite noise in the nonreciprocal bandwidth even in the high-cooperativity limit. In an intuitive picture, the circuit acts as a circulator that routes noise from the output port to the mechanical thermal bath and in turn the mechanical noise to the input port, similarly to the gyrator-based isolator of fig. 5.2a.

We demonstrate experimentally the noise asymmetry by detecting the output spectra at each microwave mode while the device isolates the mode \hat{a}_1 from \hat{a}_2 by more than 25 dB (fig. 5.7c, f). The measurement is done at the elevated temperature of 200 mK to help stabilize the mechanical mode emission and increase the overall noise visibility. The cooperativities are here set to $(\mathcal{C}_{11}, \mathcal{C}_{21}, \mathcal{C}_{12}, \mathcal{C}_{22}) = (20.0, 14.2, 106, 89)$ with a cross-damping $\Gamma_{m,1}^{(\text{cross})} \approx 2\pi \times 2.6$ kHz, in order to optimise the circuit for a lower insertion loss and increase the noise visibility. As there is additional cooling from the off-resonant pump on mode \hat{b}_1 , we expect noise from \hat{b}_2 to dominate.

5.5 Optomechanical circulator

There exists a way to circumvent the mechanical noise entirely: by introducing one extra microwave mode \hat{a}_3 , we can realise a circulator, where instead of mechanical fluctuations, fluctuations from the third microwave mode emerge in the backward direction. The scheme is illustrated in fig. 5.8a. As before, the two mechanical modes are used to create two interfering pathways, now between the three microwave cavities. Since there are now two independent loops, two phases matter; we choose the phases associated to the couplings g_{11} and g_{21} and set them respectively to $\phi_1 = 2\pi/3$ and $\phi_2 = -2\pi/3$. With the mechanical detunings set to $\delta_i = \frac{\sqrt{3}}{2}(\mathcal{C} + \frac{1}{3})\Gamma_{m,i}$, the system then becomes a circulator that routes the input of port \hat{a}_1 to \hat{a}_2 , \hat{a}_2 to \hat{a}_3 and \hat{a}_3 to \hat{a}_1 . Critically and in contrast to the isolator, counter-propagating signals are not dissipated in the mechanical oscillators, but directed to another port, with two advantages. First, the bandwidth of nonreciprocity is not limited to the mechanical dissipation rate, but instead increases with \mathcal{C} until it reaches the ultimate limit given by the cavity linewidth (see fig. 5.8b, c). Second, the mechanical noise emission is symmetrically spread between the three modes, and over the wide conversion bandwidth (see fig. 5.8d, e). In

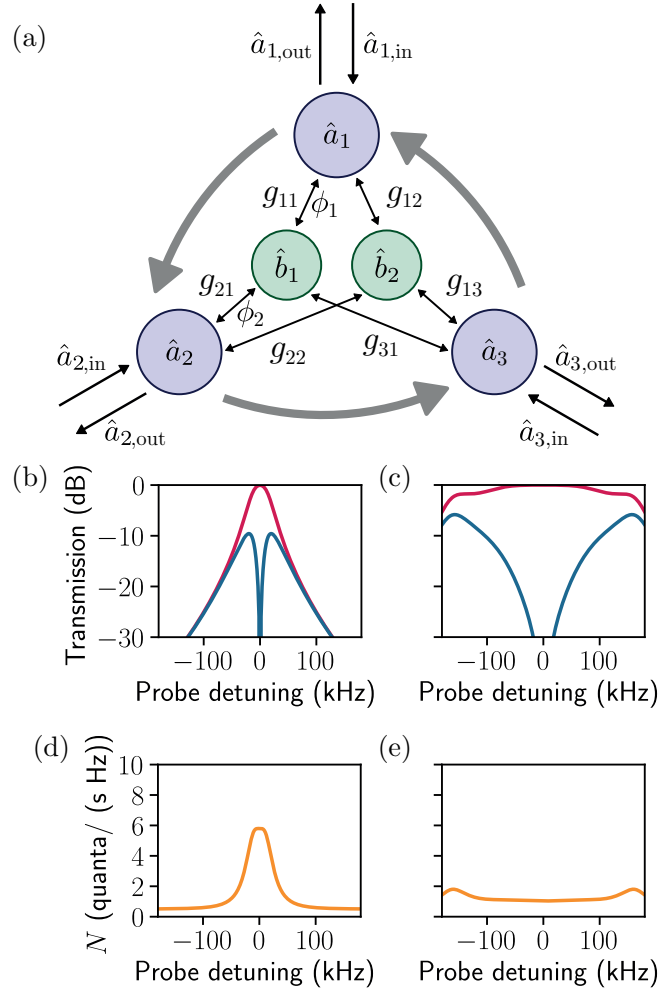


Figure 5.8: Proposal for a microwave optomechanical circulator. (a) Scheme for a circulator with three microwave cavities and two mechanical modes. The circuit involves two independent loops, with two phases ϕ_1 and ϕ_2 that can be tuned with the phases respectively associated with g_{21} and g_{11} . (b,c) Theoretical transmission in the circulating direction (counter-clockwise, in red) and the opposite direction (clockwise, in blue), for the cooperativities $\mathcal{C} = 100$ (b) and $\mathcal{C} = 1000$ (c). The isolation bandwidth scales with \mathcal{C} and is only limited by the microwave energy decay rates. Experimentally realistic parameters are chosen with overcoupled cavities of energy decay rates $\kappa_1 = \kappa_2 = \kappa_3 = 2\pi \times 200$ kHz and $\Gamma_{m,1} = \Gamma_{m,2} = 2\pi \times 100$ Hz. (d,e) Noise emission spectra for the same two cooperativities ($\mathcal{C} = 100$ (d) and $\mathcal{C} = 1000$ (e)), for the mechanical occupancies $\bar{n}_{m,1} = \bar{n}_{m,2} = 800$. Note that for the circulator the noise is symmetric for all the cavities, and that it decreases with increasing cooperativity. Figure reproduced from Bernier, Tóth, Kootandavida, et al. (2017).

the large cooperativity limit, the nonreciprocal process becomes quantum limited, irrespective of the temperature of the mechanical thermal baths.

5.6 Outlook

In conclusion, we described and experimentally demonstrated a new scheme for reconfigurable nonreciprocal transmission in the microwave domain using a superconducting optomechanical circuit. This scheme is based purely on optomechanical couplings, thus it alleviates the need for coherent microwave cavity-cavity (or direct phonon-phonon) interactions, and significantly facilitates the experimental realisation, in contrast to recently used approaches of optomechanical nonreciprocity in the optical domain (Fang, Luo, et al., 2017).

An intuitive picture built on the gyrator helps to explain the origin of nonreciprocity in the system. It arises due to interference in the two mechanical modes, which mediate the microwave cavity-cavity coupling. This interference also manifests itself in the asymmetric noise output of the circuit. Moreover, an additional microwave mode would enable quantum-limited microwave circulators on-chip with large bandwidth, limited only by the energy decay rate of the microwave modes.

The isolator scheme can be readily extended to implement quantum-limited phase-preserving and phase-sensitive directional amplifiers (Malz et al., 2018), as illustrated in fig. 5.9. Swapping two blue-detuned pump tones for two of the red-detuned pump tones in fig. 5.4c transforms the isolator into a directional phase-preserving amplifier (fig. 5.9a,b). With two additional red-detuned pump tones, the amplification becomes phase-sensitive (fig. 5.9c,d). While the added noise in the forward direction can be quantum-limited for large cooperativities, the back-propagating noise is not. As in the case of the isolator discussed in section 5.4.2, noise commensurate with the large mechanical thermal fluctuations is emitted backwards. An additional auxiliary microwave mode could be used to cool the mechanical motion and make the directional amplifiers compatible with sensitive quantum devices.

Finally, the presented scheme can be generalised to an array, and thus form a platform to study topological phases of light and sound (Peano, Brendel, et al., 2015) or topologically protected chiral amplifying states (Peano, Houde, et al., 2016) in arrays of electromechanical circuits, without requiring cavity-cavity or phonon-phonon mode hopping interactions.

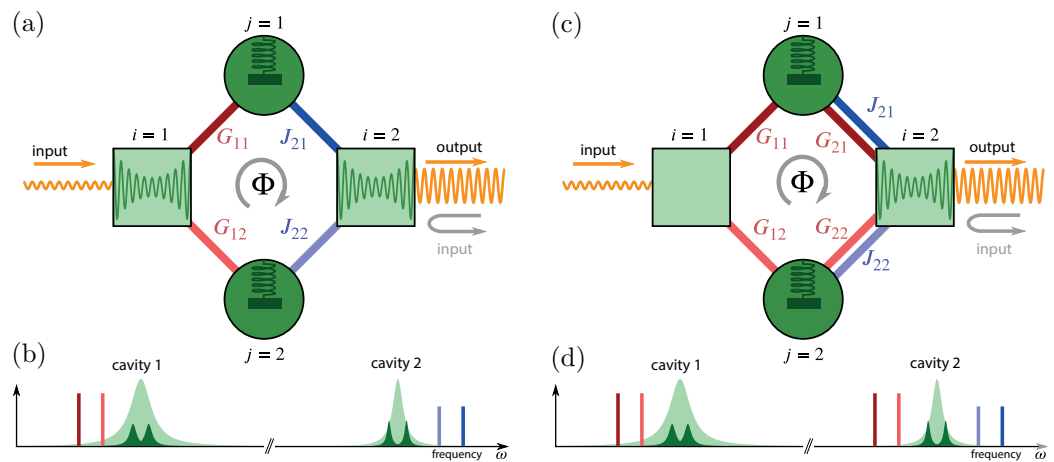


Figure 5.9: Schemes for directional amplification with an optomechanical circuit. (a,b) Using two blue-detuned and two red-detuned pump tones, the system of fig. 5.3a can be used as a phase-preserving directional amplifier. (c,d) With two additional red-detuned pump tones, the amplification is phase-sensitive. The amplification in both cases becomes quantum-limited in its added noise for large coupling rates. The noise emitted in the backwards direction is however limited by the mechanical thermal fluctuations. Figure adapted from Malz et al. (2018).

Level attraction in a microwave optomechanical circuit

We here introduce the concept of level attraction and explain how it can be studied with a microwave optomechanical circuit. This chapter is adapted from the text of a previous publication (Bernier, Tóth, Feofanov, et al., 2018a). In section 6.1, we introduce level attraction. In section 6.2, we give a theoretical exposition of the phenomenon and how it is linked to exceptional points. In section 6.3, we demonstrate level attraction experimentally in a multimode optomechanical circuit. Finally, in section 6.4, we conclude and provide an outlook.

6.1 Introduction

Level repulsion of two coupled modes with an energy crossing has applications ranging from solid state theory (Ashcroft and Mermin, 1976) to quantum chemistry (Atkins and Paula, 2009). While deceptively simple, it underpins more exotic phenomena. With the introduction of dissipation or gain, an exceptional point (Heiss, 2012) appears that is topologically non-trivial (Dembowski et al., 2001; Uzdin, A. Mailybaev, and Moiseyev, 2011; T. J. Milburn et al., 2015). The special case of two modes with equal dissipation and gain rates is an example of parity-time symmetry (Bender, 2005; Bender, Berntson, et al., 2013). The spontaneous breaking of that symmetry is marked by the exceptional point. In recent years, exceptional points gathered

significant interest and they were demonstrated in a variety of systems including active microwave circuits (Stehmann, Heiss, and Scholtz, 2004; Schindler et al., 2011; Assawaworrarit, X. Yu, and S. Fan, 2017), lasers (Brandstetter et al., 2014; Peng, Özdemir, S. Rotter, et al., 2014) and optical microresonators (Bender, Gianfreda, et al., 2013; Peng, Özdemir, Lei, et al., 2014; W. Chen et al., 2017). In particular, the topological transfer of energy between states by circling an exceptional point has been demonstrated with a microwave cavity (Dembowski et al., 2001), a microwave waveguide (Doppler et al., 2016), as well as an optomechanical system (H. Xu et al., 2016; Jing et al., 2014).

Strikingly, if one mode has negative energy, the energy levels of two interacting modes do not repel, but attract instead (Bernier, Dalla Torre, and Demler, 2014; Eleuch and I. Rotter, 2014; Seyranian, Kirillov, and A. A. Mailybaev, 2005). The Hamiltonian leads to hybridized modes of complex eigenfrequencies, one of which is unstable. As in level repulsion, an exceptional point marks the transition between the regimes of real and complex frequencies. In the process, the real components of the frequencies become identical in a way that is reminiscent of the synchronization of driven oscillators (Pikovsky, Rosenblum, and Kurths, 2003).

Negative-energy modes (equivalent to harmonic oscillators with negative mass) have been studied in schemes to evade quantum measurement backaction (Tsang and Caves, 2012; K. Zhang, Meystre, and W. Zhang, 2013; Polzik and Hammerer, 2015). Such a scheme was recently demonstrated with an atomic spin ensemble, prepared in its maximal-energy spin state in a magnetic field (Møller et al., 2017). Spin flips decrease the energy and correspond to excitations of a harmonic oscillator with a negative mass. Alternatively, the negative-energy mode can be effectively realized in a frame rotating faster than the mode itself (Woolley and Clerk, 2013; Ockeloen-Korppi et al., 2016).

In cavity optomechanics (Aspelmeyer, Kippenberg, and Marquardt, 2014), a blue-detuned pump tone induces a time-dependent interaction between the electromagnetic mode and the mechanical oscillator. In a frame rotating at the pump frequency, the Hamiltonian is time-independent, and the electromagnetic mode appears to have negative energy. While level repulsion was demonstrated in the strong coupling regime of cavity optomechanics (Gröblacher et al., 2009; Teufel, D. Li, et al., 2011; Verhagen et al., 2012), level attraction has so far not been observed.

Here we construct a general theoretical framework for level attraction and demonstrate the phenomenon in a microwave optomechanical circuit using engineered dissipation. First in section 6.2, it is shown how a coherent coupling between modes of positive and negative energy gives rise to level

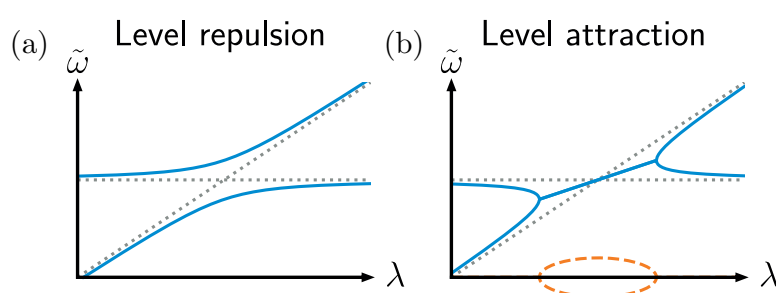


Figure 6.1: Level repulsion and attraction. Two modes, whose bare frequencies depend on a parameter λ , have a level crossing (dotted lines). A coherent coupling in general lifts the degeneracy. (a) In the more usual case, level repulsion, the coupling opens a gap between the frequencies of the hybridized eigenmodes $\tilde{\omega}$ (blue solid lines) and the eigenfrequencies bend away from each other. (b) In contrast, if one of the modes has negative energy, level attraction occurs. The real components of the eigenfrequencies $\tilde{\omega}$ (blue solid lines) bend towards each other and converge. They meet at two exceptional points, where the curves have kinks. A gap opens in the imaginary components of the frequencies (orange dashed lines). The mode with a negative imaginary component to the frequency is unstable and grows exponentially. Figure reproduced from Bernier, Tóth, Feofanov, et al. (2018a).

attraction. The role of dissipation is discussed and explains the difficulty in observing level attraction in such systems, as the dissipation rates of the two modes must be similar. The symmetry between level repulsion and attraction is explicated in section 6.2.1. And an intuitive way to classify different types of exceptional points in two-modes system is developed in section 6.2.2, with level repulsion and attraction as special cases. In section 6.3, both level attraction and repulsion are demonstrated experimentally in the same microwave optomechanical circuit, where the mechanical dissipation rate can be engineered to match the microwave one.

6.2 Theoretical exposition of level attraction

We start with a general theoretical model of a positive-energy mode coherently coupled to a negative-energy one. The two modes, of annihilation operators \hat{a} and \hat{b} and coherently coupled with strength g , are described by the Hamiltonian

$$\hat{H} = -\hbar\omega_1(\lambda)\hat{a}^\dagger\hat{a} + \hbar\omega_2(\lambda)\hat{b}^\dagger\hat{b} + \hbar g (\hat{a}\hat{b} + \hat{a}^\dagger\hat{b}^\dagger) \quad (6.1)$$

where the two positive frequencies ω_1 and ω_2 vary with respect to an external parameter λ . The linear coupling chosen here is quite general: if we assume the modes close in frequency, other linear terms $\hat{a}^\dagger\hat{b}$, $\hat{a}\hat{b}^\dagger$ can be neglected in the rotating wave approximation (valid only if the frequencies $\omega_{1,2}$ dominate over the dissipation rates for an open system, see appendix A). The coupling rate g is chosen to be real, as any complex phase can be absorbed in a redefinition of \hat{a} or \hat{b} .

In the Heisenberg picture, this leads to the equations of motion

$$\frac{d}{dt} \begin{pmatrix} \hat{a} \\ \hat{b}^\dagger \end{pmatrix} = i \begin{pmatrix} \omega_1 & -g \\ g & \omega_2 \end{pmatrix} \begin{pmatrix} \hat{a} \\ \hat{b}^\dagger \end{pmatrix} \quad (6.2)$$

where we drop the explicit λ dependence. We note that the uncoupled, bare modes evolve as $\hat{a}(t) = e^{i\omega_1 t}\hat{a}(0)$ and $\hat{b}^\dagger(t) = e^{i\omega_2 t}\hat{b}^\dagger(0)$ with a positive phase. The hybridized eigenmodes of the system are found by diagonalizing the matrix in eq. (6.2), and have eigenfrequencies

$$\tilde{\omega}_{1,2} = \frac{\omega_1 + \omega_2}{2} \pm \sqrt{\left(\frac{\omega_1 - \omega_2}{2}\right)^2 - g^2}. \quad (6.3)$$

The negative sign in front of g^2 is the only difference with the eigenfrequencies for the case of level repulsion (when \hat{a} has positive energy) but dramatically impacts on the resulting dynamics.

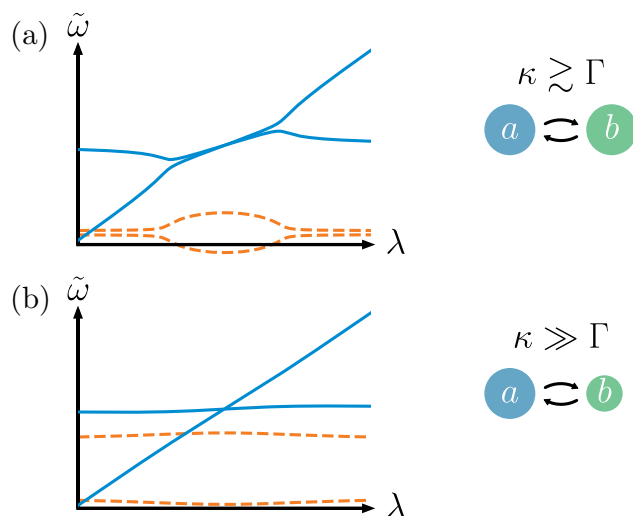


Figure 6.2: The effect of dissipation on level attraction. Two modes, \hat{a} and \hat{b} cross in frequency (the mode \hat{a} having negative energy), with respective dissipation rates κ and Γ . The real component of the frequency is the solid blue line and the imaginary component the dashed orange line. (a) While a finite average dissipation rate simply translates the imaginary components of the frequency, a difference in the two rates ($\kappa \neq \Gamma$) affects qualitatively level attraction. The kinks and the exceptional points disappear and the picture is overall smoothed out. (b) When the dissipation rates differ significantly, no trace of level attraction is visible anymore. In both cases, one of the hybridized mode becomes unstable if the imaginary component of its frequency turns negative. Figure reproduced from Bernier, Tóth, Feofanov, et al. (2018a).

In fig. 6.1, level attraction is compared to level repulsion, with two striking features. First, instead of avoiding each other, the eigenfrequencies pull towards one another. Second, when they meet at $4g^2 = (\omega_1 - \omega_2)^2$, the frequencies acquire positive and negative imaginary parts, causing exponential decay and growth. The hybridized mode with a negative imaginary component grows exponentially and is therefore unstable.

The transition between the regimes of real and complex eigenfrequencies is marked by exceptional points, which can be understood by studying the matrix of eq. (6.2). Decomposed in terms of Pauli matrices¹ and omitting the term proportional to the identity, it can be expressed as $\frac{1}{2}(\omega_1 - \omega_2)\sigma_z - ig\sigma_y$.

¹ The Pauli matrices are defined as $\sigma_x = \begin{pmatrix} 0 & 1 \\ 1 & 0 \end{pmatrix}$, $\sigma_y = \begin{pmatrix} 0 & -i \\ i & 0 \end{pmatrix}$ and $\sigma_z = \begin{pmatrix} 1 & 0 \\ 0 & -1 \end{pmatrix}$.

In contrast with level repulsion for which the interaction term would be $g\sigma_x$, the Hermitian Pauli matrix is here multiplied by an *imaginary* coefficient. If the first term has a larger amplitude, the eigenfrequencies are real, while they are complex if the second term dominates. When the two Pauli matrices have coefficients of the same amplitude, the matrix is proportional to $\sigma_z - i\sigma_y$. At this point, the two eigenvectors coalesce and a single eigenvector with a single eigenvalue subsists: it is an exceptional point (Heiss, 2012). More generally for all two-mode systems, any point for which the dynamics is determined by a matrix proportional to $\sigma_\alpha + i\sigma_\beta$, with $\alpha \neq \beta$, is an exceptional point. In the section 6.2.2, we develop this decomposition and construct an intuitive classification of the various realizations of exceptional points.

Level attraction arises whenever the coupling term consists of a Pauli matrix with an imaginary coefficient. In fact, coupled oscillators of positive and negative energy are only one way to achieve this. An alternative relies on linking the two modes with a coupling that cannot be derived from a Hamiltonian, such as a dissipative interaction through one or multiple intermediary modes (Metelmann and Clerk, 2014). The mode hybridization observed between positive-energy oscillators with dissipative (H. Xu et al., 2016; Khanbekyan et al., 2015) and non-conservative (Gloppe et al., 2014) interactions can be interpreted as level attraction.

While level attraction of two linearly coupled modes displays intriguing similarities with the synchronization of driven oscillators, important differences exist. As in synchronization, the real components of the frequencies “lock” over a frequency range that increases with the coupling rate g , forming the equivalent of an Arnold tongue (Pikovsky, Rosenblum, and Kurths, 2003). The physical process differs however. In synchronization, one starts with two oscillators that are driven nonlinearly to their limit-cycles, then a coupling is introduced that locks their frequencies and their phases (Weiss, Kronwald, and Marquardt, 2016). In level attraction by contrast, the frequencies of the two modes attract through *linear* dynamics until they become identical. The state of the two hybridized modes remain independent and their phases can be set arbitrarily.

To understand why level attraction is in practice less common than level repulsion, the role of dissipation should be studied. We open the system and include in our treatment the energy dissipation rates κ and Γ respectively for the modes \hat{a} and \hat{b} . They can be introduced as positive imaginary components of the bare frequencies in the equations of motion. The results of eq. (6.2) and (6.3) can be extended by replacing ω_1 with $\omega_1 + i\kappa/2$ and ω_2 with $\omega_2 + i\Gamma/2$. In fig. 6.2, we compare the resulting eigenfrequencies. If the dissipation rates are equal ($\kappa = \Gamma$), the level structure of fig. 6.1b is reproduced with the

imaginary components translated to a finite average. However, in the case of even slightly mismatched dissipation rates $\kappa \gtrsim \Gamma$ (fig. 6.2a), the exceptional points and the kinks in the frequencies disappear. For increasingly dissimilar rates $\kappa \gg \Gamma$ (fig. 6.2b), the level-attraction picture progressively disappears until the modes seem to cross without interacting. Therefore, only in a system where dissipation rates can be tuned to closely match each other is level attraction observable.

6.2.1 Symmetry of level repulsion and attraction

To understand better the relation between level repulsion and attraction, we explicitly derive here a minimal model for each. We show that a symmetry relation links the two cases; they are images of each other under the exchange of frequency and dissipation rates.

First, we review level repulsion. Two modes of positive energy (with annihilation operators \hat{a} and \hat{b} , and respective frequencies ω_1 and ω_2) interact, as described by the Hamiltonian

$$\hat{H}_{\text{LR}} = \hbar\omega_1\hat{a}^\dagger\hat{a} + \hbar\omega_2\hat{b}^\dagger\hat{b} + \hbar g \left(\hat{a}\hat{b}^\dagger + \hat{a}^\dagger\hat{b} \right) \quad (6.4)$$

with g the linear coupling strength. The equation of motion in the Heisenberg picture is given by

$$\frac{d}{dt} \begin{pmatrix} \hat{a} \\ \hat{b} \end{pmatrix} = -i \begin{pmatrix} \omega_1 & g \\ g & \omega_2 \end{pmatrix} \begin{pmatrix} \hat{a} \\ \hat{b} \end{pmatrix}. \quad (6.5)$$

To solve the system in terms of eigenmodes, the matrix is diagonalized. The eigenfrequencies are given by

$$\tilde{\omega}_{1,2}^{\text{LR}} = \frac{\omega_1 + \omega_2}{2} \pm \sqrt{\left(\frac{\omega_1 - \omega_2}{2}\right)^2 + g^2}. \quad (6.6)$$

The model is extended to describe modes with dissipation by adding imaginary components to the bare frequencies, substituting $\omega_1 \rightarrow \omega_1 - i\Gamma_1/2$ and $\omega_2 \rightarrow \omega_2 - i\Gamma_2/2$. Note that a negative sign is required to obtain decaying exponentials. For ease of notation, we define $\omega_0 = (\omega_1 + \omega_2)/2$, $\Gamma_0 = (\Gamma_1 + \Gamma_2)/2$, $\Delta\omega = \omega_1 - \omega_2$, and $\Delta\Gamma = \Gamma_1 - \Gamma_2$. The eigenfrequencies can now be written as

$$\tilde{\omega}_{1,2}^{\text{LR}} = \omega_0 - i\frac{\Gamma_0}{2} \pm \sqrt{\left(\frac{\Delta\omega - i\Delta\Gamma/2}{2}\right)^2 + g^2}. \quad (6.7)$$

The frequency of oscillation of the eigenmodes is given by the real component of $\tilde{\omega}_{1,2}^{\text{LR}}$ and the dissipation rate by twice its imaginary component (with a minus sign).

We now consider level attraction. One (and only one) mode has negative energy such that the system is described by the Hamiltonian

$$\hat{H}_{\text{LA}} = -\hbar\omega_1\hat{a}^\dagger\hat{a} + \hbar\omega_2\hat{b}^\dagger\hat{b} + \hbar g \left(\hat{a}\hat{b} + \hat{a}^\dagger\hat{b}^\dagger \right). \quad (6.8)$$

The equations of motion are given by

$$\begin{pmatrix} \dot{\hat{a}} \\ \dot{\hat{b}^\dagger} \end{pmatrix} = i \begin{pmatrix} \omega_1 & -g \\ g & \omega_2 \end{pmatrix} \begin{pmatrix} \hat{a} \\ \hat{b}^\dagger \end{pmatrix} \quad (6.9)$$

with eigenfrequencies

$$\tilde{\omega}_{1,2}^{\text{LA}} = \frac{\omega_1 + \omega_2}{2} \pm \sqrt{\left(\frac{\omega_1 - \omega_2}{2}\right)^2 - g^2}. \quad (6.10)$$

The only difference with eq. (6.6) is the sign in front of g^2 , which can result in a complex eigenvalue, meaning an instability for the system.

It might be unintuitive that the Hermitian Hamiltonian in eq. (6.8) leads to complex eigenfrequencies and unstable dynamics. In fact, in an infinite-dimensional Hilbert space, an operator must be compact as well as Hermitian to guarantee the existence of real eigenvalues (Le Bellac, 2012), which is not the case here. We also note that only when the eigenfrequencies are real can the eigenoperators be interpreted as Bogolyubov modes (Fetter, Walecka, and Physics, 2003). When the eigenfrequencies are complex, the required commutation relations cannot be satisfied.

In order to include dissipation, we substitute again $\omega_1 \rightarrow \omega_1 + i\Gamma_1/2$ and $\omega_2 \rightarrow \omega_2 + i\Gamma_2/2$. Note that the opposite sign for the imaginary component is required here to obtain decaying exponentials. The eigenfrequencies including dissipation become

$$\tilde{\omega}_{1,2}^{\text{LA}} = \omega_0 + i\frac{\Gamma_0}{2} \pm \sqrt{\left(\frac{\Delta\omega + i\Delta\Gamma/2}{2}\right)^2 - g^2}. \quad (6.11)$$

There is a symmetry between eq. (6.7) and eq. (6.11). They are equivalent under the transformation $\omega' = \Gamma/2$ and $\Gamma' = 2\omega$, if eq. (6.11) is multiplied by a factor $-i$:

$$\tilde{\omega}_{1,2}^{\text{LA}} = \omega'_0 - i\frac{\Gamma'_0}{2} \pm \sqrt{\left(\frac{\Delta\omega' - i\Delta\Gamma'/2}{2}\right)^2 + g^2}. \quad (6.12)$$

We conclude that level attraction and repulsion are equivalent to each other through the exchange of frequency and dissipation rates (within a factor of 2). In fig. 6.3, this symmetry is highlighted by contrasting equivalent situations for both level repulsion and level attraction Hamiltonians. In fig. 6.3a-d, the curves for the real and imaginary parts of the eigenfrequencies are interchanged when going from the left column (level repulsion) to the right (level attraction). Figure 6.3e-f can be compared with fig. 6.1, where the characteristic shape of level attraction is here seen for the dissipation rates of the level-repulsion Hamiltonian and vice versa. In general, for level repulsion, when a coupling is introduced the *frequencies repel*, while the *dissipation rates attract*. The exact opposite is true for level attraction: a coupling makes the *dissipation rates repel* and the *frequencies attract*.

6.2.2 Classification of exceptional points

We describe here how to classify exceptional points of 2×2 matrices using Pauli matrices. The classification is then used to sort recent experimental demonstrations of exceptional points.

In general, the equations of motion for a 2-modes system can be written in the form

$$i \frac{d}{dt} \begin{pmatrix} \hat{d}_1 \\ \hat{d}_2 \end{pmatrix} = M \begin{pmatrix} \hat{d}_1 \\ \hat{d}_2 \end{pmatrix} \quad (6.13)$$

where \hat{d}_1 , \hat{d}_2 are operators for the two modes and M is a 2×2 matrix. The eigenmodes of the system and their eigenfrequencies correspond to the eigenvectors and eigenvalues of M . If for some parameter values, M only has a single eigenvector and a single eigenvalue, this is called an exceptional point.

The matrix M can always be decomposed in terms of the Pauli matrices, defined as

$$\sigma_x = \begin{pmatrix} 0 & 1 \\ 1 & 0 \end{pmatrix}, \quad \sigma_y = \begin{pmatrix} 0 & -i \\ i & 0 \end{pmatrix}, \quad \text{and} \quad \sigma_z = \begin{pmatrix} 1 & 0 \\ 0 & -1 \end{pmatrix}, \quad (6.14)$$

in the form

$$M = a_0 \mathbb{1} + a_1 \sigma_x + a_2 \sigma_y + a_3 \sigma_z \quad (6.15)$$

with $\mathbb{1}$ the identity matrix and a_i complex numbers. The eigenvalues of M are now easily expressed as

$$\lambda_{1,2} = a_0 \pm \sqrt{a_1^2 + a_2^2 + a_3^2}. \quad (6.16)$$

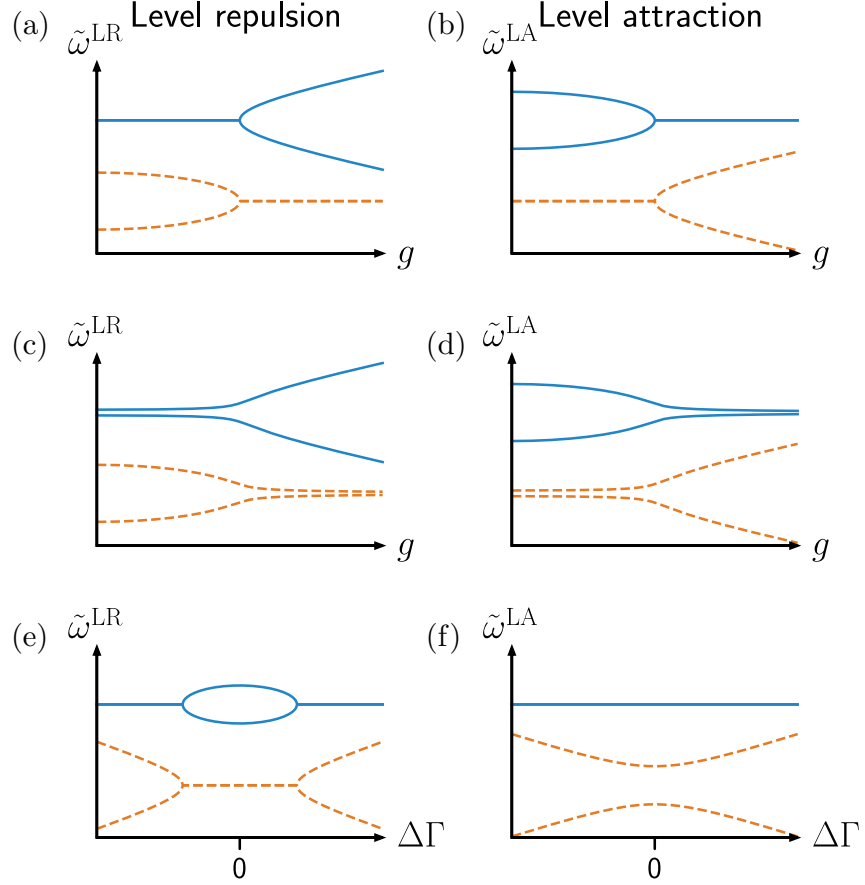


Figure 6.3: Comparison of the real (solid blue lines) and imaginary (dashed orange lines) components of the eigenfrequencies $\tilde{\omega}$ for the level-repulsion Hamiltonian \hat{H}_{LR} (left column) and the level-attraction Hamiltonian \hat{H}_{LA} (right column). (a,b) The transition through an exceptional point, as a function of the coupling strength g . For level repulsion (a), the modes are originally degenerate ($\Delta\omega = 0$), while for level attraction (b) they originally have matching dissipation rates ($\Delta\Gamma = 0$). (c,d) Same as (a,b) with a slight nondegeneracy ($\Delta\omega \neq 0$ for level repulsion (c) and $\Delta\Gamma \neq 0$ for level attraction (d)), such that the exceptional point is avoided. (e,f) The difference in dissipation rates $\Delta\Gamma$ is varied, for degenerate modes $\Delta\omega = 0$. For level repulsion (e), the imaginary component of the frequency attract and converge in a region where a gap opens in the real components of the frequency. For level attraction (f), the real component is unchanged while the dissipation rates have an avoided crossing. Figure reproduced from Bernier, Tóth, Feofanov, et al. (2018a).

Note that the first term in eq. (6.15), proportional to the identity, only shifts the eigenvalues by a constant and has no effect on the eigenvectors. Anytime that the matrix M can be written as a multiple of $\sigma_\alpha + i\sigma_\beta$ ($\alpha \neq \beta$) (omitting the identity), there is only one eigenvalue and this is an exceptional point (Steeb and Hardy, 2014). We can use this decomposition to classify examples of exceptional points.

(I) The most common case is the level repulsion of two (positive-energy) modes of degenerate frequencies due to a coherent coupling. Many experimentally demonstrated exceptional points fall in this category (Dembowski et al., 2001; Schindler et al., 2011; Bender, Gianfreda, et al., 2013; Brandstetter et al., 2014; Peng, Özdemir, Lei, et al., 2014; Peng, Özdemir, S. Rotter, et al., 2014; Doppler et al., 2016; Assaworrorarit, X. Yu, and S. Fan, 2017). The two modes are $\hat{d}_1 = \hat{a}$ and $\hat{d}_2 = \hat{b}$, in our previous notation. The matrix M can be written as

$$M = \left(\omega_0 - i \frac{\Gamma_0}{2} \right) \mathbb{1} - i \frac{\Delta\Gamma}{4} \sigma_z + g\sigma_x. \quad (6.17)$$

For a low coupling rate g , M is diagonal with a gap for dissipation rates. For a large g , the last term dominates such that the eigenmodes are eigenvectors of σ_x : g opens a gap in frequency, while the dissipation rates are evenly distributed between the modes. The transition between the regimes is marked by an exceptional point at $g = \Delta\Gamma/4$.

(II) Here, we consider the case of level attraction between modes of negative and positive energies and matching dissipation rates. The operators are $\hat{d}_1 = \hat{a}$ and $\hat{d}_2 = \hat{b}^\dagger$ in our notation. The matrix M can be written as

$$-M = \left(\omega_0 + i \frac{\Gamma_0}{2} \right) \mathbb{1} + \frac{\Delta\omega}{2} \sigma_z - ig\sigma_y. \quad (6.18)$$

For a low coupling g , there is a gap in frequency, while for a large coupling, the σ_y term opens a gap in dissipation rates and the frequencies are identical. An exceptional point marks the transition at $g = \Delta\omega/2$. Note that the coherent coupling corresponds to a term with an imaginary coefficient for a system with one mode of negative energy.

(III) Level attraction of two modes can be realized in any system in which the coupling term has an imaginary component. In particular, dissipative interactions (Metelmann and Clerk, 2014) represent an alternative way to the one presented in this article. Two modes are coupled by both interacting with a third oscillator. When the third mode is eliminated, the effective interaction between the two modes is expressed by the matrix M as

$$M = \left(\omega_0 - i \frac{\Gamma_{\text{eff}}}{2} \right) \mathbb{1} + \frac{\Delta\omega}{2} \sigma_z + ig_{\text{dis}} \sigma_x \quad (6.19)$$

where for simplification the effective dissipation rate Γ_{eff} of the two coupled modes is taken to be approximately equal. The effective interaction between the two modes has an imaginary coefficient and they have an increased effective dissipation rate Γ_{eff} due to the dissipative interaction as well. Similarly to the previous case, by increasing the coupling g_{dis} the original gap in frequency is closed and a difference in dissipation rates is created. In contrast however, Γ_{eff} grows proportionally with g_{dis} , such that the gap in dissipation rates does not result in an instability. The mode hybridization between modes of positive energy coupled with dissipative interactions can be interpreted as level attraction.

Examples of this type of exceptional points were realized experimentally. In the experiment of H. Xu et al. (2016), two mechanical oscillators are effectively coupled by both interacting with the same optical cavity. In the experiment of Khanbekyan et al. (2015), two modes of an optical resonator interact through multiple quantum dots. In the experiment of Glorpe et al. (2014), two modes of a nanowire interact through the non-conservative force of an optical field, which although not dissipative in nature, cannot be derived from a Hamiltonian in a similar way.

(IV) Finally, yet another way to implement an exceptional point was realized in the experiment of W. Chen et al. (2017). The clockwise and counterclockwise modes of a whispering-gallery-mode resonator (of degenerate frequencies and dissipation rates) interact through two Rayleigh scatterers. This results in a combination of coherent and dissipative interaction that can be described by

$$M = \left(\omega_0 - i\frac{\Gamma_0}{2} \right) \mathbb{1} + g_{\text{coh}}\sigma_x + ig_{\text{dis}}\sigma_y. \quad (6.20)$$

As the coupling g_{coh} and g_{dis} are varied, the relative phases of the bare modes that compose the hybrid eigenmodes change. When the two coupling strengths match ($g_{\text{coh}} = g_{\text{dis}}$), the two eigenmodes coalesce and there is an exceptional point. Interestingly, this corresponds to a point of maximal nonreciprocity, with one bare mode coupled to the second but not the other way around (Metelmann and Clerk, 2015).

6.3 Optomechanical level attraction

Cavity optomechanics provides an ideal setting to study level attraction and compare it to level repulsion. We now take \hat{a} to represent an electromagnetic mode and \hat{b} a mechanical oscillator, coupled through the optomechanical in-

teraction $\hbar g_0 \hat{a}^\dagger \hat{a} (\hat{b} + \hat{b}^\dagger)$, where g_0 is the vacuum optomechanical coupling (Aspelmeyer, Kippenberg, and Marquardt, 2014). With a blue-detuned pump tone applied to the system, the three-wave-mixing coupling is linearized and the Hamiltonian reduces to the form of eq. (6.1)

$$\hat{H} = -\hbar \Delta \hat{a}^\dagger \hat{a} + \hbar \Omega_m \hat{b}^\dagger \hat{b} + \hbar g (\hat{a} \hat{b} + \hat{a}^\dagger \hat{b}^\dagger), \quad (6.21)$$

where Δ is the detuning of the pump tone, Ω_m the mechanical mode frequency and $g = g_0 \sqrt{n_c}$ the linear coupling enhanced by the mean cavity photon number n_c due to the pump tone. As above, we neglect counter-rotating terms and assume the detuning Δ to be close to Ω_m . Critically, the Hamiltonian is expressed in a frame rotating at the pump frequency in order to be time-independent. Hence, for a blue detuning $\Delta > 0$, the cavity mode effectively has a *negative* energy, since the photons have a negative relative frequency with respect to the pump.

In this context, the well-known parametric instability of optomechanics (Aspelmeyer, Kippenberg, and Marquardt, 2014) can be interpreted as resulting from the physics of level attraction. The instability stems from the negative imaginary component that develops in the eigenfrequencies of the equations of motion, above the critical coupling $g_{\text{crit}} = \sqrt{\kappa \Gamma}/2$.

For level attraction to be observable, the magnitudes of κ and Γ should be close. For usual experimental parameters, however, the electromagnetic decay rate κ is much larger than the mechanical rate Γ , and no attraction can in practice be observed for the mechanical and electromagnetic modes.

6.3.1 Experimental results

In our experiment, the effective mechanical energy decay rate Γ_{eff} is artificially increased to match κ using sideband cooling with an auxiliary mode. We use a superconducting electromechanical circuit (Teufel, D. Li, et al., 2011) containing two microwave LC modes interacting with the vibrational mode of a vacuum-gap capacitor (represented schematically in fig. 6.4a and shown in fig. 6.4b). The design, which is described in section 4.2, uses two hybridized electromagnetic modes of the circuit to ensure that one has a much larger external coupling rate to the microwave feedline than the other. The more dissipative, auxiliary mode \hat{a}_{aux} is used to perform sideband cooling of the mechanical oscillator with a red-detuned pump tone. This damps the oscillator and increases its effective dissipation rate to $\Gamma_{\text{eff}} \approx \kappa$. Meanwhile, the less dissipative, primary mode \hat{a} undergoes level attraction with the damped mechanical oscillator.

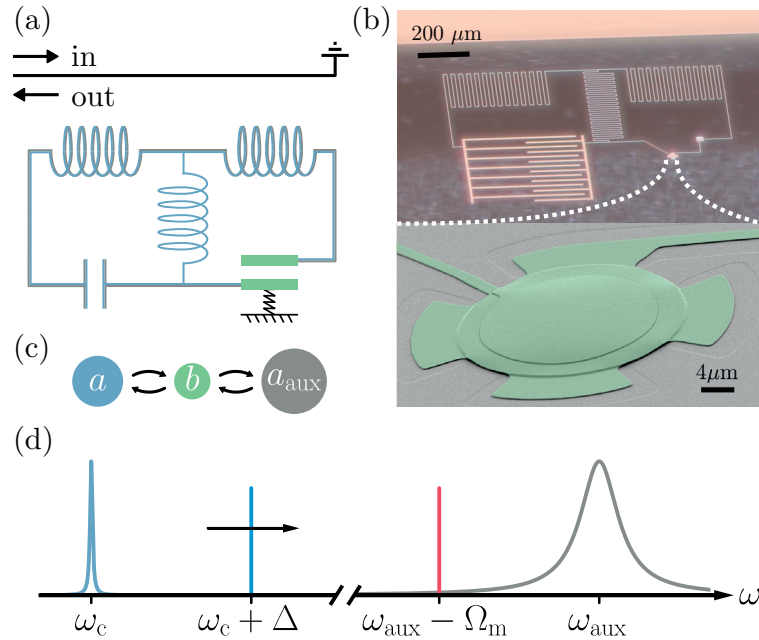


Figure 6.4: Engineering dissipation in a multimode optomechanical circuit. In order to observe level attraction, the dissipation rate Γ_m of the mechanical mode \hat{b} must be increased to match κ , the much larger dissipation rate of the primary electromagnetic mode \hat{a} . To that end, an auxiliary mode \hat{a}_{aux} is used for sideband cooling. (a) Schematic of the microwave optomechanical circuit, coupled inductively to a microwave feedline and measured in reflection. The two hybridized modes of the circuit \hat{a} and \hat{a}_{aux} interact with the motion of the top membrane of a shared capacitor, the mechanical oscillator \hat{b} (in green). (b) Photograph of the circuit and scanning-electron micrograph of the vacuum-gap capacitor. (c) Diagram of the three interacting modes. (d) Frequency domain representation of the level-attraction experiment. A microwave pump tone (vertical red line), red-detuned by the mechanical frequency Ω_m with respect to the auxiliary mode resonance ω_{aux} (grey peak) is used for sideband cooling. Level attraction of the modes \hat{a} and \hat{b} is achieved by sweeping the detuning Δ of a pump tone (vertical blue line) near the blue sideband of the primary mode resonance ω_c (blue peak). For level repulsion, the pump tone is instead swept near the red sideband. Figure reproduced from Bernier, Tóth, Feofanov, et al. (2018a).

In the experiment, the device is placed inside a dilution refrigerator and cooled to the base temperature, below 50 mK, at which the circuit is superconducting and its internal Q -factor is enhanced. The sample is HYB-20160524-1-12. The two microwave modes \hat{a} and \hat{a}_{aux} have respective resonance frequencies $\omega_c = 2\pi \times 4.11$ GHz and $\omega_{\text{aux}} = 2\pi \times 5.22$ GHz, and dissipation rates $\kappa = 2\pi \times 110$ kHz and $\kappa_{\text{aux}} = 2\pi \times 1.8$ MHz. They interact with the fundamental vibrational mode of the top plate of the vacuum-gap capacitor, that has a frequency $\Omega_m = 2\pi \times 6.3$ MHz. By placing a pump tone red-detuned by Ω_m from the auxiliary mode resonance (see fig. 6.4d), the mechanical oscillator is damped. The mechanical dissipation rate Γ_m , originally below $2\pi \times 100$ Hz, is tuned to an effective dissipation rate $\Gamma_{\text{eff}} \approx \kappa = 2\pi \times 110$ kHz.

Level repulsion and attraction of the primary microwave mode and the damped mechanical oscillator are both measured. As a pump tone is tuned to the blue or red sideband of the primary microwave mode (the former case is illustrated in fig. 6.4d), the weak probe tone of a vector network analyser is applied near the resonance of the microwave cavity to obtain its linear response. Due to the hybridization of the modes, the response carries information about both microwave and mechanical modes. For both red and blue detunings, the same pump power is set to obtain a coupling strength $g \approx 2\pi \times 200$ kHz corresponding to a mean cavity photon number $n_c \approx 4 \times 10^6$.

The known case of level repulsion is obtained with a red-detuned tone (fig. 6.5a). As the bare effective mechanical mode frequency comes near the microwave resonance, the two modes hybridize; their eigenfrequencies bend away from each other with a gap of $2g$.

With a blue-detuned tone, level attraction occurs instead. The response, shown in fig. 6.5b, displays the characteristic level structure of fig. 6.1b. The resonance frequencies of the modes attract and converge to the points where the bare frequencies of the modes differ by $\pm 2g$. In order for the level attraction to be clearly visible, the coupling rate g is set to dominate over the dissipation rates κ and Γ_{eff} . It therefore exceeds the critical coupling g_{crit} , resulting in parametric instability. One of the modes grows exponentially until the conditions of the validity of eq. (6.21) are no longer fulfilled. Namely, the fluctuating field is no more negligible compared to the mean cavity photon number n_c . The original nonlinear optomechanical interaction constrain the system to a limit-cycle with a modified cavity resonance frequency (Marquardt, Harris, and Girvin, 2006), the description of which lies beyond the scope of this article. Data is omitted for clarity in the unstable region.

In fig. 6.6a,c, two individual responses from fig. 6.5 are shown for specific detunings of the pump tone. The two resonances take the form of two dips

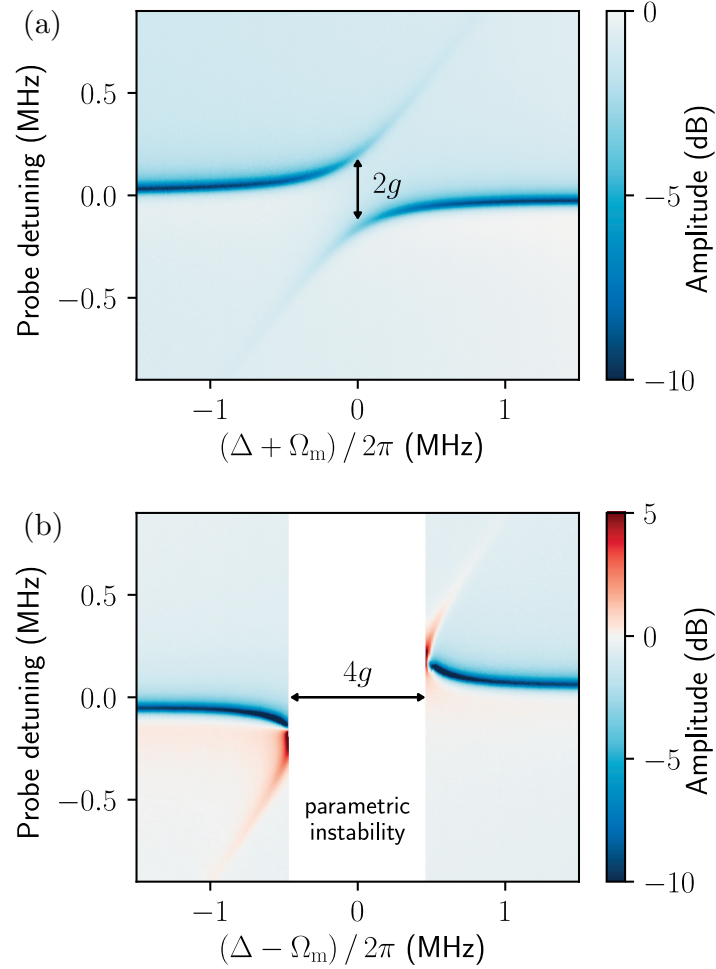


Figure 6.5: Experimental demonstration of level repulsion and attraction in a microwave optomechanical circuit. Amplitude response of the system as the detuning Δ of the pump tone is varied, when the effective dissipation rate of the mechanical mode \hat{b} matches that of the microwave mode \hat{a} . In the laboratory frame, Δ determines the effective frequency of the mechanical oscillator, that is swept across the microwave resonance. (a) When the pump tone is swept in frequency across the red sideband of the microwave mode, the two resonances bend away from each other. (b) If the pump tone is swept across the blue sideband instead, the resonances pull towards each other and converge near two exceptional points. Data is omitted for clarity where the system becomes unstable and one hybridized mode grows exponentially until the conditions of validity of eq. (6.21) are no longer fulfilled (parametric instability). Figure adapted from Bernier, Tóth, Feofanov, et al. (2018a).

in amplitude in the case of level repulsion, while the feature corresponding to the mechanical resonance takes the form of a peak in amplitude in the case of level attraction. Represented on the complex plane, the resonances form circles. In level repulsion (fig. 6.6b), the two circles are circumscribed. The radii of the circles correspond to how the two hybridized modes are coupled to the measurement channel. With a resonant pump tone $\Delta = \Omega_m$, the two modes are coupled the same and the two circles have the same radius. This is a direct analog of OMIT with a red-detuned drive as described in section 3.6.2. For level attraction (fig. 6.6d) however, the circle corresponding to the mechanical lies outside the circle of the microwave resonance.

6.4 Outlook

In summary, level attraction was experimentally demonstrated using a dual-mode electromechanical circuit. Although related to the well-studied parametric instability of optomechanics, the vastly different dissipation rates for the mechanical and electromagnetic modes prevented its observation until now. Level attraction, similarly to level repulsion in open systems, gives rise to exceptional points. In both cases, the real part of the frequencies converge and a gap opens in the imaginary part (or vice versa) precisely at the exceptional point. In future work, the exceptional points of level attraction could be harnessed to demonstrate topological phenomena by circling such a point in a two-dimensional parameter space (Dembowski et al., 2001; H. Xu et al., 2016; Doppler et al., 2016). Since the exceptional point only exists when the dissipation rates of the two modes match exactly, the tunable mechanical damping rate Γ_{eff} can be used as one parameter in such an experiment, with the tunable coupling rate g as the second.

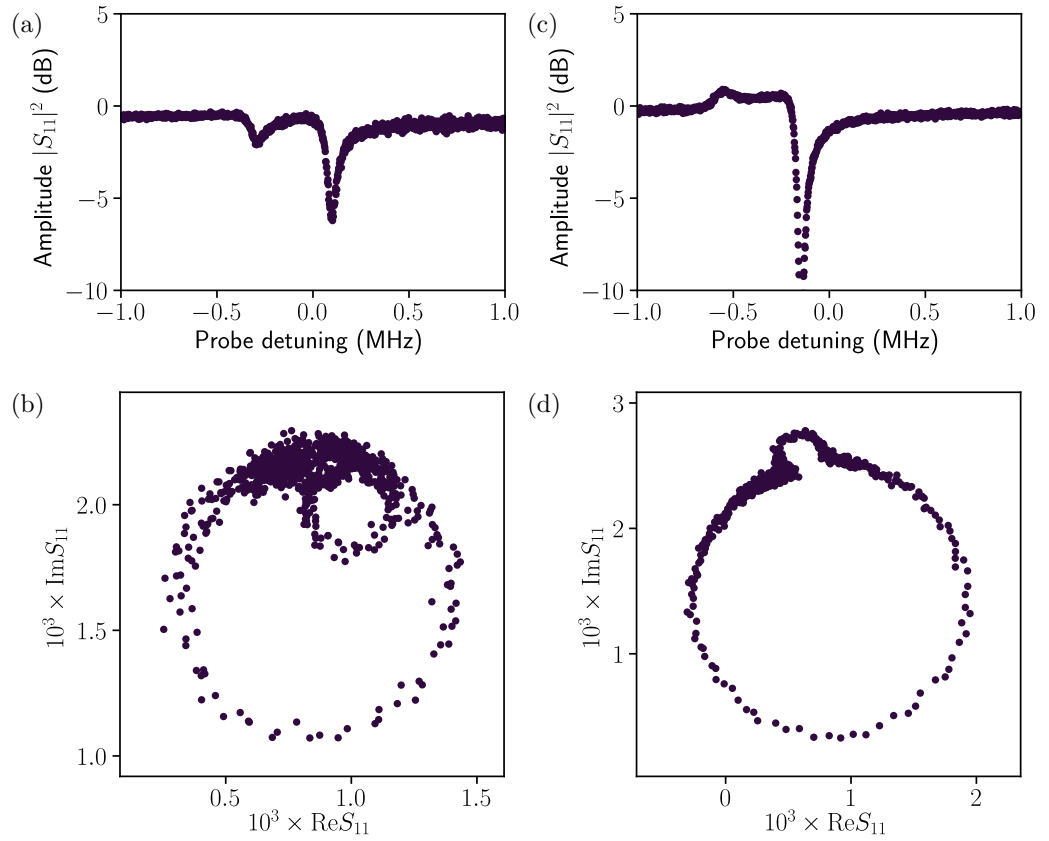


Figure 6.6: Amplitude and complex responses for level repulsion and attraction. (a,b) Level-repulsion response corresponding to the data of fig. 6.5a for a pump detuning $\Delta + \Omega_m = -2\pi \times 180$ kHz, shown in amplitude (a) and on the complex plane (b). (c,d) Level-attraction response corresponding to the data of fig. 6.5b for a pump detuning $\Delta - \Omega_m = -2\pi \times 630$ kHz, shown in amplitude (c) and on the complex plane (d).

Outlook on high-efficiency optomechanical measurements with a traveling-wave parametric amplifier

In this chapter, we introduce the use of a traveling wave parametric amplifier (TWPA), developed in a collaboration between the group of Prof. Siddiqi at UC Berkeley and the Lincoln Laboratory at the Massachusetts Institute of Technology. After an introduction in section 7.1, its installation and function are detailed in section 7.2. In section 7.3, we present a demonstration of an optomechanical measurement previously unattainable in our experiment. As an outlook, we present in section 7.4 ongoing efforts to precisely calibrate the added noise of the device and ideas for future experiments relying on high-efficiency detection.

7.1 Introduction

The amplifier plays the central role in quantum measurements at microwave frequencies. Since there exists no detector for microwave photons, gain is required for the signals to be measured classically. As such, the amplification process itself can be thought of as the quantum measurement, as argued in section 2.2.3. In appendix B, amplification is compared to the equivalent

detection process at optical frequencies. The added noise of the amplifier corresponds to an equivalent quantum efficiency

$$\eta_{\text{eq}} = \frac{1}{\mathcal{N}_{\text{added}} + \frac{1}{2}}. \quad (7.1)$$

In the case of HEMT amplifiers, the efficiency typically is $\eta_{\text{HEMT}} \approx 0.05$. It is as if 95 % of the signals of interest is discarded before measurement, resulting in a much reduced signal-to-noise ratio compared to the ideal case. Long averages are needed to resolve weak signals and certain experiments cannot be performed since the noise is too large. The great potential improvement in SNR motivates us to investigate more recent technologies that provides amplification much closer to the quantum limit in terms of added noise.

Josephson parametric amplifiers (Castellanos-Beltran and Lehnert, 2007; Bergeal et al., 2010; Hatridge et al., 2011) can provide an added noise close to the quantum limit. They rely on a microwave cavity that is enhanced by the nonlinearity provided by Josephson junctions. With a driving tone, this nonlinearity results in a reduced effective dissipation rate for the cavity and gain. The resonance at the heart of the mechanism limits the amplification to a bandwidth near the resonance frequency. While the frequency can be tuned, with a magnetic flux for instance (Castellanos-Beltran and Lehnert, 2007), there remains strong limitations in terms of the bandwidth, which is limited to the range of MHz due to the finite linewidth of the cavity. To remedy this, Macklin et al. (2015) dispense with the cavity and form a metamaterial transmission line with a long chain of Josephson junctions. By sending a driving tone copropagating with the signal on the line, the interaction through the nonlinearity results in amplification with a very low added noise and a bandwidth in the order of GHz. The device is called a Josephson traveling-wave parametric amplifier. One such device was provided to us by the Lincoln Laboratory at the Massachusetts Institute of Technology.

7.2 Installing and operating the TWPA

We present here how the typical experimental setup introduced in section 3.3 is adapted to incorporate the TWPA. The new setup is shown schematically and in photograph in fig. 7.1. The TWPA is placed on the breadboard at the base plate, right after the sample holder. By precaution, one of the two isolators is placed before it, to absorb any strong tones that might backscatter towards the optomechanical circuit. The backward gain of the TWPA should ideally be 0 dB, but if the pump tone used to drive it is reflected somewhere

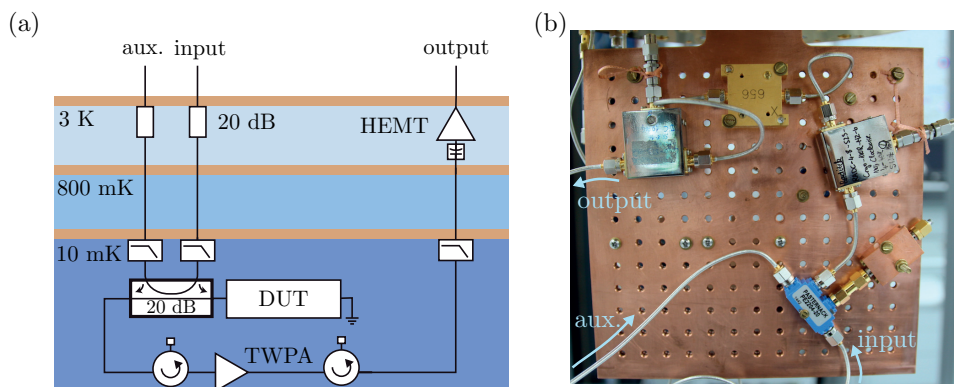


Figure 7.1: Setup for the TWPA. (a) Schematics of the modification of the setup inside the dilution refrigerator to incorporate the TWPA. (b) Photograph of the relevant components, with the ports labeled.

along the line, there can potentially be non-zero backward gain. The rest of the components that sit inside the dilution refrigerator is not affected. The auxiliary port has the added function to send in the driving tone for the TWPA, as well as to be used for tone cancellation as previously.

The large sensitivity of the TWPA has the disadvantage that even relatively weak coherent tones in the input signals can saturate the amplification process, causing distortion. The tone cancellation strategy used previously (detailed in section 3.3.4) that provides up to 30 dB of cancellation proved insufficient. Instead, an improved approach, illustrated in fig. 7.1, was implemented that can reliably cancel tones by over 70 dB, in an automated way. We use digitally controlled tunable attenuators (Vaunix LDA-602EH, with steps of 0.1 dB) and phase shifters (Vaunix LPS-802, with steps of 1 degree). With a set of one phase shifter and one attenuator, a tone can be tuned in amplitude and phase precisely enough to cancel a copy of itself by 35 dB. Two stages of tone cancellation are used to achieve about 70 dB of cancellation overall. The microwave tone used to drive the system is first split. One half is sent to the input port, after some attenuation. The other half goes through the tone cancellation circuit. It is again split in two, this time with a directional coupler. Each part goes through a stepped attenuator and a phase shifter before being recombined. The microwave tone that drives the TWPA joins the tone cancellation signal and they both are sent in the auxiliary port. The digitally controlled devices enables the tone cancellation procedure to be fully automatized through a programmed script. One disadvantage compared to the previously used devices is that they have

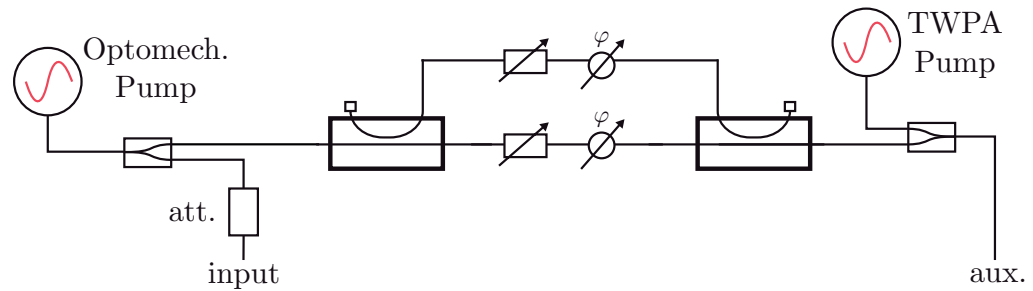


Figure 7.2: Scheme for tone cancellation. The TWPA requires efficient tone cancellation for the strong optomechanical pump tones used. Through two stages of tone cancellation with one variable attenuator and phase shifter each, tone cancellation of 70 dB is achieved. Some attenuation is required for the pump tone to match the large insertion loss of the tone cancellation circuit.

a large insertion loss (about 10 dB at a minimum for the attenuator). Some attenuation must be introduced on the input line to equilibrate the two arms. That implies a reduction to the maximal power that can be applied on chip.

The linear response of the TWPA shows a dispersive feature near 6 GHz, at which absorption occurs. When a strong microwave tone is applied to the red of this feature, any other signal co-propagating is amplified in a wide band, from about 4 to 8 GHz. The driving tone is swept both in frequency and power to find an optimal operating point, with large and regular gain over the bandwidth of interest. While the absolute gain and added noise are not immediately accessible, they can easily be compared to that of the HEMT on its own by turning the pump tone off. The comparison of the linear response gives a measure of the relative gain provided by the TWPA. By comparing the SNR of a weak calibration tone at a particular frequency in the same conditions, the effective added noise of the TWPA can be measured relatively to that of the HEMT. Although that is not a very precise calibration, this provides an idea whether the TWPA is operated in good conditions. There are parameters for the pump tone for which the gain appears high, but the added noise is large as well, defeating the purpose.

7.3 Detailed balance in sideband cooling

The TWPA offers the combined characteristics of nearly quantum-limited added noise over very large bandwidths. As a demonstration case of how

this can be an advantage for optomechanical measurements, we present here preliminary results on the measurement of both mechanical sidebands of the pump tone in a sideband-cooling experiment. The cooling power can be thought of as due to the imbalance between Stokes and anti-Stokes scattering of a pump tone applied to the system. The former adds energy to the mechanical oscillator while the latter subtracts from it. For a red-detuned pump tone, the anti-Stokes process dominates and the mechanical mode cools down. For large enough pump powers however, the system reaches stationary conditions with a detailed balance in which the two processes equilibrate. For sideband-resolved optomechanical systems, the lower sideband is very weak and hard to measure. We demonstrate the use of the TWPA by measuring both sidebands at once. In the following, we first introduce the theoretical model for the sideband cooling, and then the experimental results.

7.3.1 Theoretical model

For a pump tone at a detuning Δ , the Stokes and anti-Stokes processes have rates that respectively correspond to A^+ ($\bar{n}_m + 1$) for the red sideband and $A^- \bar{n}_m$ for the blue sideband (Aspelmeyer, Kippenberg, and Marquardt, 2014, section VII.A), where \bar{n}_m is the average phonon occupancy and the rates are given by

$$A^- = g^2 \frac{\kappa_{\text{ex}}}{(\kappa/2)^2 + (\Delta + \Omega_m)^2} \quad \text{and} \quad A^+ = g^2 \frac{\kappa_{\text{ex}}}{(\kappa/2)^2 + (\Delta - \Omega_m)^2}. \quad (7.2)$$

The situation is illustrated in fig. 7.3a. The occupancy \bar{n}_m is found by solving the stationary solution of the birth-death process and given by

$$\bar{n}_m = \frac{A^+ + \bar{n}_{m,\text{th}} \Gamma_m}{A^- - A^+ + \Gamma_m}. \quad (7.3)$$

This results in total average rates for the Sidebands

$$\Gamma_{\text{red}} = \frac{A^+ (A^- + (\bar{n}_{m,\text{th}} + 1) \Gamma_m)}{A^- - A^+ + \Gamma_m}, \quad (7.4)$$

$$\Gamma_{\text{blue}} = \frac{A^- (A^+ + \bar{n}_{m,\text{th}} \Gamma_m)}{A^- - A^+ + \Gamma_m}, \quad (7.5)$$

which are measured in quanta per second.

The sidebands are spread over a certain bandwidth in frequency domain, with a density $I_{\text{SB}}(\omega) = \Gamma_{\text{eff}} / (2\pi) / ((\omega - \omega_0)^2 + (\Gamma_{\text{eff}}/2)^2)$. This is normalized such that $\int I_{\text{SB}}(\omega) d\omega = 1$. To obtain the spectral density, measured in quanta

per second per Hz, a different normalization must be used. The spectra of the sidebands are given by $S_{\text{red/blue}}(f) = \Gamma_{\text{red/blue}} \times 2\pi \times I_{\text{SB}}(2\pi f)$ to get the correct normalization. What we are interested in is the maximum rate in the middle of the Lorentzian. Those rates are given by

$$S_{\text{red}}^{\text{max}} = \frac{4A^+ (A^- + (\bar{n}_{\text{m,th}} + 1)\Gamma_{\text{m}})}{(A^- - A^+ + \Gamma_{\text{m}})^2} = \frac{4A^+(\bar{n}_{\text{m}} + 1)}{\Gamma_{\text{eff}}}, \quad (7.6)$$

$$S_{\text{blue}}^{\text{max}} = \frac{4A^- (A^+ + \bar{n}_{\text{m,th}}\Gamma_{\text{m}})}{(A^- - A^+ + \Gamma_{\text{m}})^2} = \frac{4A^-\bar{n}_{\text{m}}}{\Gamma_{\text{eff}}}. \quad (7.7)$$

Both are measured in quanta per second per Hz. The same spectra can be computed from the Langevin equations. The noise due to the mechanical bath and from the input electromagnetic field must be combined, as the latter (giving rise to backaction noise) becomes relevant for large cooling powers. The asymmetry between the two sidebands, that are proportional to \bar{n}_{m} and $\bar{n}_{\text{m}} + 1$ can be traced to the interference of the electromagnetic vacuum noise (Sudhir et al., 2017; Sudhir, 2018).

The sideband spectrum signals are to be compared to the noise background. It is constituted of vacuum fluctuations (0.5 quanta per second per Hz) plus the added noise from the TWPA (a minimum of 0.5 quanta per second per Hz). This means the SNR is given by

$$\text{SNR}_{\text{red}} = \frac{S_{\text{red}}^{\text{max}}}{\frac{1}{2} + \mathcal{N}_{\text{added}}}, \quad \text{SNR}_{\text{blue}} = \frac{S_{\text{blue}}^{\text{max}}}{\frac{1}{2} + \mathcal{N}_{\text{added}}}. \quad (7.8)$$

The derived results imply a priori that the effective mechanical occupancy \bar{n}_{m} can be extracted from the ratio of SNR of the two sidebands $\text{SNR}_{\text{red}}/\text{SNR}_{\text{blue}}$ if the ratio A^+/A^- is known, without any knowledge of the TWPA added noise $\mathcal{N}_{\text{added}}$ required. Then using the knowledge of \bar{n}_{m} , the added noise $\mathcal{N}_{\text{added}}$ can be retrospectively deduced from the absolute SNR. This relies on the assumption that both sidebands are amplified in the same way through the TWPA. As we shall see, it is not verified in practice and the measurement cannot be made in a fully self-calibrated manner.

7.3.2 Preliminary experimental results

The experiment is performed by applying a pump tone detuned to the red of the cavity resonance of an optomechanical circuit. The two sidebands, amplified by the TWPA, are measured with a spectrum analyzer for various pump powers. At each power, the tone cancellation parameters are optimized, to cancel the pump tone by about 70 dB before the TWPA.

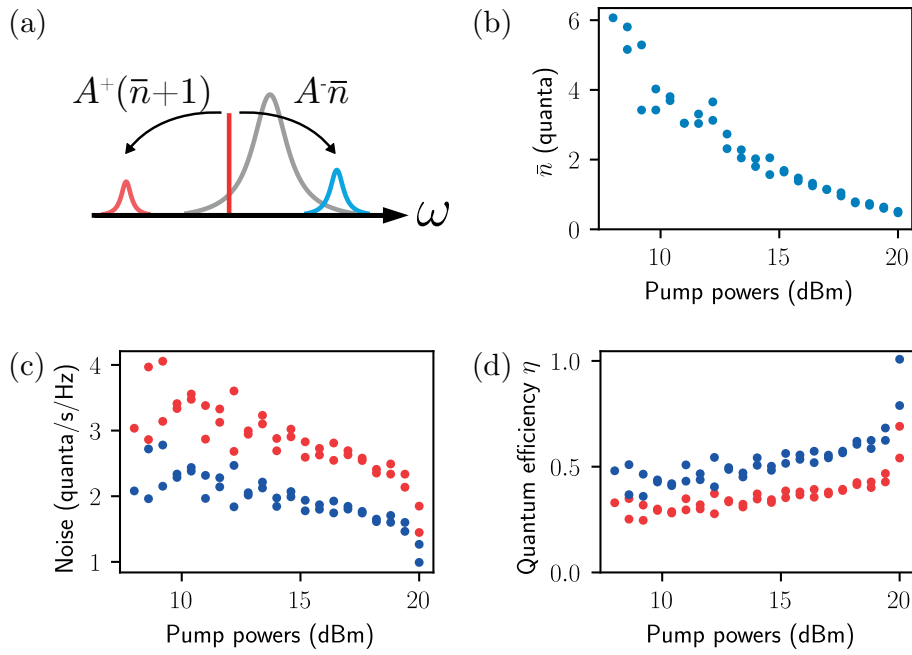


Figure 7.3: Sideband asymmetry experiment with the TWPA. (a) Schematic of the experiment in the frequency domain. A red-detuned pump tone is applied to the cavity to perform sideband cooling. The two resulting mechanical sidebands are measured. (b) Mechanical occupancy \bar{n}_m , deduced from the asymmetry of the two sidebands. (c) Calibrated absolute power of the noise background for the red (red dots) and blue (blue dots) sidebands. Knowing \bar{n}_m , the total noise background, including the added noise $\mathcal{N}_{\text{added}}$ is deduced from the absolute SNR of each sideband. (d) Quantum efficiency of the TWPA for each sideband, deduced from the added noise $\mathcal{N}_{\text{added}}$.

The original aim was for a fully self-calibrated experiment, relying on the assumption that the added noise of the TWPA is the same at the frequencies of both sidebands. However, we find this not to be the case. For low cooling powers (corresponding to a large mechanical occupancy \bar{n}_m), the ratio of SNR of the two sidebands $\text{SNR}_{\text{blue}}/\text{SNR}_{\text{red}}$ should be given by A^-/A^+ . The latter depends only on the detuning Δ , the dissipation rate κ and the mechanical frequency Ω_m , and can be computed independently. The measured ratio $\text{SNR}_{\text{blue}}/\text{SNR}_{\text{red}}$ exceeds the computed ratio A^-/A^+ (which would imply a negative mechanical occupancy in the model). We suppose that it is due to a difference in added noise at the frequencies of the two sidebands, that increases the measured ratio compared to the model. By supposing a difference in added noise of 1.6 dB, the experimental data correspond to what is expected. We present those here as preliminary results. Further calibrations are necessary to confirm that such a difference in added noise exists and is indeed what causes the discrepancy.

The results are shown in fig. 7.3. The sample is HYB-20150924-4-17, using the microwave resonator at 5.3 GHz. We find that the mechanical oscillator is cooled to $\bar{n}_m \approx 0.5$ quanta, from the measured ratio $\text{SNR}_{\text{blue}}/\text{SNR}_{\text{red}}$ (see fig. 7.3b). Then, the mechanical occupancy is used in turn to transform the SNR into a measure of the background noise with an absolute scale (see fig. 7.3c). We assume that the apparent drop in the noise for larger cooling powers is due to classical heating from the pump tone noise that is not taken into account in the model and increases the SNR ratio. The background noise of approximately 2 quanta correspond to an added noise of 1.5 quanta and a quantum efficiency of 0.5 (see fig. 7.3d).

An example of the two measured sidebands is shown in fig. 7.4. The usefulness of the TWPA for such a measurement is demonstrated by comparing the result when switching the TWPA pump tone off. The SNR of the sidebands, in particular the red-detuned one, is reduced dramatically when only the HEMT amplifier is used to amplify them.

7.4 Precise noise calibration

The TWPA promises tremendous improvement in measurement efficiency, boosting SNR, reducing measurement time and allowing very weak signals to be detected. Nevertheless, to unleash its full potential, a scheme for the precise calibration of the added noise must be implemented. The method used to calibrate the HEMT amplifiers, introduced in section 3.4.2, cannot be used, since it relies on changing the temperature of the whole mixing-

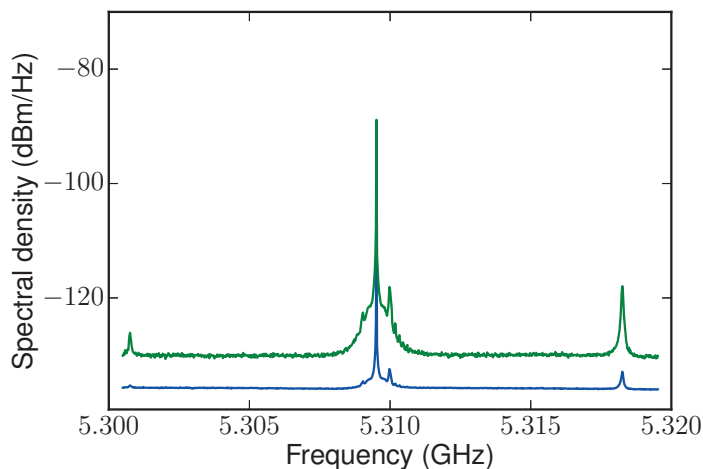


Figure 7.4: Comparison of the sideband measurement with the TWPA turned on and off. The two sidebands of a pump detuned to the red of a microwave cavity are measured while the pump tone that drives the TWPA is on (green) and off (blue). In the latter case, the SNR is limited by the added noise of the HEMT amplifier. Figure courtesy of Alexey Feofanov.

chamber plate and that would affect the performance of the TWPA. In the following, we introduce the ongoing effort to calibrate the TWPA with a locally heated matched load.

As explained in section 3.4.2, at the heart of any added-noise calibration lies a calibrated noise reference, that provides an absolute power scale compared to which the amplifier performance can be gauged. A cryogenic matched load (XMA 2001-6112-02) at a known temperature is used for this purpose. The temperature of the load is tuned with a heater and measured with a thermometer. The required equipment configuration is illustrated in fig. 7.5. A holder made of OFHC copper was designed and fabricated by the workshop of the institute of physics at EPFL (shown in fig. 7.5b, the files are available online (Bernier, 2018)). The thermometer (Lakeshore Cernox CU-HT) is clamped to it with a bolt that is screwed in a threaded hole. The heater (Lakeshore HTR-50) is inserted in a cylindrical hole of the holder and fixed with varnish. The holder surrounds the cylindrical matched load and can be tightened around it with a bolt to guarantee good thermal contact. New DC lines are installed inside the dilution refrigerator. A twisted pair connects the heater to a control box (Lakeshore 370 AC resistance bridge), and is used to send a current and increase the temperature. The resistance of the thermometer is measured with a 4-wire method, using the same control

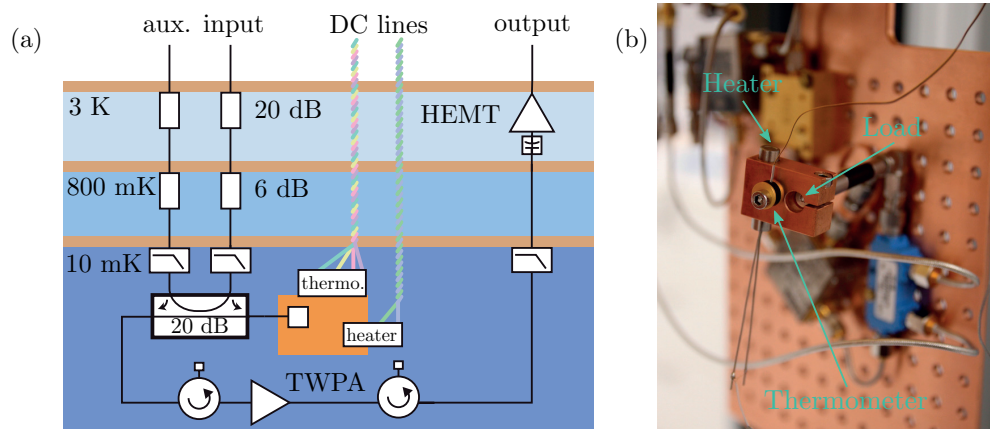


Figure 7.5: Setup for the calibration of the TWPA. (a) Schematic of the setup. The matched load replaces the sample holder on the base plate. It is fixed in an OFHC copper holder, with a thermometer and a heater. DC lines are required to supply the current for the heater and measure the resistance of the thermometer. (b) Photograph of the load in the holder, installed in the dilution refrigerator (photograph courtesy of Nick Sauerwein).

box.

In a first preliminary measurement, the thermometer is fixed to the base plate. Using data acquired during the cooldown and warmup of the dilution refrigerator, the resistance of the thermometer is calibrated against the existing mixing-chamber thermometer.

In the main measurement, the load (fixed in the OFHC-copper holder) replaces the sample holder on the breadboard of the base plate. The added noise can then be calibrated exactly at the reference plane of the chip, taking into account any insertion loss between the sample holder and the TWPA, as well as any added noise of the rest of the measurement line, as explained in section 3.4.2. The aim is to measure the added noise of the TWPA in this situation and use this calibration for subsequent experiments.

Unlike the HEMT amplifiers, the performance of the TWPA is not constant. It depends critically on the pump tone that drives the amplification process. We do not suppose that the gain and added noise are always the same at the same nominal power and frequency of the pump tone. Any slight variation along the line, any reflections due to an impedance mismatch will change the power slightly and affect the result. Therefore, we need a way to translate the calibration result to a later time when the added noise might have changed. For this purpose, we plan to use a calibration tone that propagates alongside the TWPA pump tone. The SNR of such a tone gives a

local relative measure of the added noise. The calibration with the heater anchors it on an absolute scale. For a given configuration of the TWPA, both the added noise $\mathcal{N}_{\text{added}}[\omega]$ and the SNR of the calibration tone $\text{SNR}_{\text{cal.}}[\omega]$ are recorded as a function of frequency ω . In an actual experiment, where a chip supplants the heated load, the SNR of a calibration is measured at equal power and frequency. If the path of the calibration tone is in all points identical, any modification of the SNR can be attributed to a change in added noise of the TWPA. The correct added noise can then be deduced from the calibration.

The precise calibration of the TWPA, still an ongoing effort, will refine this powerful tool for high efficiency measurements. Without an absolute scale given by the added noise of the TWPA, it is difficult to extract any information from the measured signals, even if the SNR is improved compared to the HEMT. The sideband asymmetry measurements of section 7.3 can be revisited to confirm the results and analyze the low mechanical occupancy achieved with sideband cooling more carefully. As a further step, there are plans to measure the ponderomotive squeezing (Purdy et al., 2013) in the microwave domain. That requires an accurate knowledge of the level of quantum noise to ensure that the squeezing is indeed of the vacuum fluctuations. In general, this new measurement technique constitutes a colossal improvement in the quantum efficiency previously achieved in our experiments and will improve measurement throughout microwave circuit optomechanics.

Conclusions and outlook

We first summarize the results of this thesis in section 8.1, and proceed to describe future possible directions for the work in section 8.2.

8.1 Summary of the results

Microwave optomechanical circuits constitute a powerful framework in which to study the linear interactions of harmonic oscillators, down to their quantum fluctuations. The linearization of the optomechanical coupling with a driving tone effectively renders the coupling rate and the relative frequencies of the two modes (in the rotating frame) tunable (see section 2.1.4). In chapter 4, we have shown how the relative dissipation rates can be controlled as well, giving access to the full parameter space of two coupled modes. We demonstrate this capability by reversing the usual hierarchy of dissipation rates of optomechanical systems, with a mechanical dissipation rate that dominates over the electromagnetic one. The mechanical oscillator thus plays the role of a reservoir, allowing the microwave cavity properties to be altered. The microwave mode can be turned into a maser and amplify signals with nearly quantum-limited added noise, demonstrating that the mechanical oscillator acts as a useful quantum resource.

The next step in our study is to ask the fundamental question of how the relation between two oscillators can be made nonreciprocal. How can the symmetry be broken such that one oscillator receives information from the second but not the other way around? In chapter 5, we demonstrate such a

unidirectional interaction between two microwave cavity modes interacting through two intermediary mechanical modes. The employed method relies on two key requirements that are naturally provided through the optomechanical interaction. First, the symmetry is broken by applying a complex phase to the interaction, which corresponds to the phase of the driving tone that linearizes the coupling between the electromagnetic and the mechanical mode. Second, the dissipative nature of the mechanical oscillators, which act as links between the two microwave modes, is required to absorb the information in one direction.

The study of linear interactions between two harmonic modes culminates in chapter 6 with a classification of the types of possible coupling situations, through the lens of the different ways an exceptional point can be realized. In particular, the well-known case of level repulsion is contrasted with level attraction. Both are demonstrated in the same microwave optomechanical circuit, arising respectively when the driving tone linearizing the optomechanical interaction is red and blue detuned. The dissipation engineering technique introduced in chapter 4 is essential, as the dissipation rates of the two modes must be made equal for level attraction to occur.

Finally, ongoing efforts for a new measurement scheme are presented in chapter 7. The travelling-wave parametric amplifier can provide a greatly improved quantum efficiency in measurements over a wide bandwidth.

8.2 Outstanding challenges and outlook

The different main results of this thesis represent research direction that could be further explored in the future. The mechanical reservoir demonstrated in chapter 4 can be used for more than amplification and masing. For instance, by using two pump tones to couple the microwave mode to it, it can be used to engineer a squeezed ground state for the microwaves (Kronwald, Marquardt, and Clerk, 2013). The demonstrated optomechanical isolator of chapter 5 can readily be turned into a directional amplifier (Malz et al., 2018), and with the addition of a third microwave mode into a circulator (Bernier, Tóth, Koottandavida, et al., 2017; Barzanjeh et al., 2017). The topological properties of the exceptional points of the level attraction demonstrated in chapter 6 could be demonstrated by encircling one in parameter space (H. Xu et al., 2016; Jing et al., 2014). The high-efficiency measurements in a large bandwidth with a TWPA shown in chapter 7 could be used to measure ponderomotive squeezing (Purdy et al., 2013) and to cool the mechanical oscillator to its ground state using feedback (Wilson et al., 2015; Rossi et al.,

2018). In the longer term however, another direction might prove especially fruitful for this optomechanical platform.

The optomechanical interaction can be realized in a variety of systems and one might ponder on the particular merits of microwave optomechanical circuits. In the author's opinion, the implementation as a circuit precisely constitutes its main quality. Any circuit shape is as easy (or complicated) to fabricate as any other. The complexity of function is only limited by the design. That makes microwave circuits especially versatile. They can be hybridized with other systems, for instance integrating superconducting qubits on the same device (O'Connell et al., 2010; Lecocq, Teufel, et al., 2015; Pirkkalainen, Cho, et al., 2015). The direction followed in the work of this thesis has been the integration of multiple optomechanical systems together: multimode cavity optomechanics with up to two electromagnetic and two mechanical modes.

There are challenges to extend the number of modes further, though. First, it has proven difficult to design a circuit with more microwave modes in a simple way (Stevens, 2017). New microwave engineering ideas are needed for scalable designs that can accommodate an arbitrary number of modes. The second challenge concerns the structure of the mechanical element itself. The suspended capacitor has not had any substantial change in its design since its first demonstration in 2011 (Teufel, Donner, et al., 2011). It suffers from a few weaknesses that should be remedied in the future. The precise shape of its bulging membrane, clamped to the substrate on the sides, varies substantially from one capacitor to the next. That hinders the design of microwave resonances since the average gap should be precisely known at cryogenic temperatures to know the resulting capacitance. The mechanical properties of the membrane vary as well as they depend on local stress which cannot be finely controlled.

One idea is to give the vibrating membrane a level geometry with a flat surface. It could be clamped to each side of a "trench" dug out in the substrate, with the second capacitor plate at the bottom, as illustrated in fig. 8.1. The gap that determines the capacitance would then be precisely known and the stress in the film could be more homogeneous and engineered for better mechanical performance. From there, the film could be patterned to improve the quality factor using the techniques of soft clamping and strain engineering (Tsaturyan et al., 2017; Ghadimi et al., 2018).

With the capability to make reliable multimode optomechanical circuits, a first step would be to implement a circuit with three microwave modes interacting with two mechanical modes and realize a circulator (see section 5.5). For more general systems with n microwave modes and m mechanical modes,

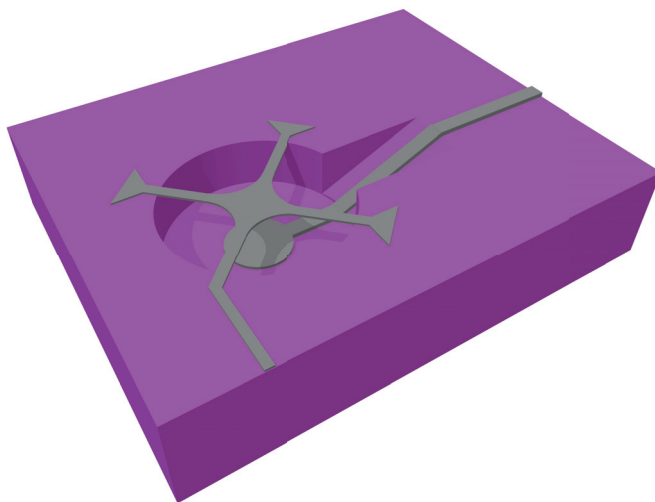


Figure 8.1: Proposal for a new geometry for the capacitor. A “trench” is dug in the substrate (in purple) over which the vibrating capacitor membrane is stretched (in gray). Figure courtesy of Amir Youssefi.

an optomechanical lattice can be built. This would form a complex nonlinear medium for which topological phases have been predicted (Peano, Brendel, et al., 2015; Peano, Houde, et al., 2016).

The rotating wave approximation

The importance of the rotating wave approximation (RWA) in optomechanics (as well as more generally in quantum optics) justifies to carefully examine under what conditions it is valid. We start from the time-independent Hamiltonian of eq. (2.22). Only the case $\Delta \approx -\Omega_m$ is examined for simplicity. The twin case $\Delta \approx \Omega_m$ follows an almost identical argument.

In the rotating frame, a cavity mode $\delta\hat{a}$ interacts with the mechanical oscillator $\delta\hat{b}$ with an almost-resonant drive of detuning $\Delta = -\Omega_m - \delta$, with the Hamiltonian

$$H = \hbar(\Omega_m + \delta)\delta\hat{a}^\dagger\delta\hat{a} + \hbar\Omega_m\delta\hat{b}^\dagger\delta\hat{b} + \hbar g(\delta\hat{b} + \delta\hat{b}^\dagger)(\delta\hat{a} + \delta\hat{a}^\dagger). \quad (\text{A.1})$$

In a new rotating frame with respect to the rest Hamiltonian $H_0 = \hbar(\Omega_m + \delta)\delta\hat{a}^\dagger\delta\hat{a} + \hbar\Omega_m\delta\hat{b}^\dagger\delta\hat{b}$, only the time-dependent interaction remains in the interaction picture with

$$\begin{aligned} H' &= \hbar g(\delta\hat{b}e^{-i\Omega_m t} + \delta\hat{b}^\dagger e^{i\Omega_m t})(\delta\hat{a}e^{-i(\Omega_m + \delta)t} + \delta\hat{a}^\dagger e^{i(\Omega_m + \delta)t}) \\ &= \hbar g(\delta\hat{a}\delta\hat{b}^\dagger e^{-i\delta t} + \delta\hat{a}^\dagger\delta\hat{b}e^{i\delta t} + \delta\hat{a}\delta\hat{b}e^{-i(2\Omega_m + \delta)t} + \delta\hat{a}^\dagger\delta\hat{b}^\dagger e^{i(2\Omega_m + \delta)t}) \end{aligned} \quad (\text{A.2})$$

The effect of the first two slowly oscillating terms should be compared to the last two that have fast oscillations. Let Δt be a time short compared to $1/\delta$, but large compared to $1/(2\Omega_m + \delta)$. During that time, the state evolves due to the slow terms with a change of the order $g\Delta t$. In the same time, the fast terms oscillate many times in a way that cancels their effect; their contribution is limited to the fraction of the last period not compensated by

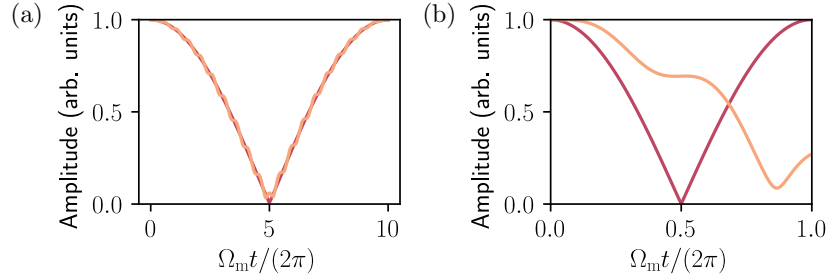


Figure A.1: Comparison of cases when the RWA is valid or not. The case without dissipation is considered with two modes evolving according to eq. (A.1), with a detuning $\delta = \Omega_m/1000$. The average population of one mode for the classical evolution is shown in the exact solution (orange solid line) and in the RWA (purple solid line). (a) Evolution for a coupling rate $g = 0.05 \Omega_m$. The RWA is valid and the two lines agree on average. (b) Evolution for a coupling rate $g = 0.25 \Omega_m$. The RWA is not valid anymore and the oscillations due to the counter-rotating terms have a contribution that does not cancel out on average.

previous cycles, with a change of the order of $g/(2\Omega_m + \delta)$. The fast terms can therefore be neglected if $\delta \ll 2\Omega_m$.

We note that although the comparison between the fast and slow terms does not involve g , the argument relies on the fact Δt is a short time scale such that $g \Delta t \ll 1$. This implies the supplementary condition of a small coupling rate $g \ll 2\Omega_m$. If this last condition does not hold, then even though the fast terms effects cancel out on average, they can still contribute significantly to the state evolution and the approximation to neglect them is not justified. In fig. A.1, the two case are compared.

The condition $\delta \ll 2\Omega_m$ would be sufficient for the RWA if the Hamiltonian eq. (A.1) were all that dictates the time evolution. In fact, the interaction with the environment plays a role and the dissipation rates κ , Γ_m must be taken into account. We write the Langevin equations (forgetting here the input modes to concentrate on the internal dynamics) as

$$\dot{\delta\hat{a}}' = -ig\delta\hat{b}'e^{(i\delta-\Gamma_m/2)t} - ig\delta\hat{b}'^\dagger e^{(i(2\Omega_m+\delta)-\Gamma_m/2)t}, \quad (\text{A.3})$$

$$\dot{\delta\hat{b}}' = -ig\delta\hat{a}'e^{(-i\delta-\kappa/2)t} - ig\delta\hat{a}'^\dagger e^{(-i(2\Omega_m+\delta)-\kappa/2)t}, \quad (\text{A.4})$$

where we have used the change of variables $\delta\hat{a}' = e^{(\kappa/2)t}\delta\hat{a}$, $\delta\hat{b}' = e^{(\Gamma_m/2)t}\delta\hat{b}$ to place dissipation and oscillation dynamics on the same footing. The condition $\delta \ll 2\Omega_m$ is no longer in itself sufficient to neglect the rapidly oscillating

terms. If the dissipation rate κ is large, the fast and slow terms both decay similarly in a short timescale, preventing any cancellation due to the oscillations. To recover the previous condition, we assume $\kappa \ll 4\Omega_m$, a condition known as the sideband resolution, when the mechanical sidebands with respect to cavity resonance fall well outside of the cavity linewidth. The condition $\Gamma_m \ll 4\Omega_m$, similarly required, is generally true as it is equivalent to a large quality factor for the mechanical oscillator.

In summary, we have shown three conditions under which the RWA is valid. First, there is the condition of sideband resolution $\kappa \ll 4\Omega_m$; second, the condition of resonant drive $||\Delta| - \Omega_m| \ll 2\Omega_m$; third, the derivation is only valid for a small enough coupling rate, when $g \ll 2\Omega_m$.

Quantum heterodyne detection as an amplification process

Although the fields of circuit QED and quantum optics study similar phenomena, in practice there is often a dissonance in the language used to describe the experiments, that creates unnecessary confusion. A major source of the schism lies in the measurement processes that use different mechanisms, since there exist no sensitive photodetectors working at microwave frequencies. Nevertheless, there is a strong formal analogy between the use of a low-noise microwave amplifier and the detection schemes used at optical frequencies. In this appendix, we present an overview of the heterodyne detection that is commonly used in quantum optics and how it relates to the quantum measurements of continuous signals in general. We then present the similarities with the phase-preserving amplifier introduced in section 2.2.3 and try to bridge the gap in the language used to describe the two. We follow the treatment of the subject by Sudhir (2018).

In appendix B.1, the formal requirement for a quantum continuous measurement are presented in order to link it to the definition of the quantum spectral density. In appendix B.2, the spectral density of the signal is derived for the direct photodetection of an optical field with a strong mean-field component. In appendix B.3, the spectral density for the heterodyne detection is derived. In appendix B.4, we compare the case of heterodyne detection in quantum optics to the scattering amplifier used in circuit QED and show how they are equivalent.

B.1 Quantum measurements and spectral densities

A key question in the quantum measurement of continuous signals is how the classical random signal that is the outcome of measurement relates to the quantum observable, or how the classical spectral density relates to the different definitions of the quantum spectral density (eqs. (2.53) and (2.54)).

We consider a Hermitian time-dependent observable $\hat{X}(t)$ to be measured. Subtracting the average value, the quantum fluctuations of $\hat{X}(t)$ are $\delta\hat{X}(t) = \hat{X}(t) - \langle\hat{X}(t)\rangle$. The process is assumed to be stationary, with the quantum probabilities associated with $\delta\hat{X}(t)$ independent of time. We restrict ourselves to a class of operators called continuous observables defined by Sudhir (2018, section 2.1.2) to obey

$$\left[\delta\hat{X}(t), \delta\hat{X}(t')\right] = 0. \quad (\text{B.1})$$

Thanks to this absence of memory, the measurement of $\delta\hat{X}$ at time t has no influence on the result of a second measurement at time t' . All the observables $\delta\hat{X}(t)$ indexed by t form a set of commuting observables that can be thought to obey a many-variable probability distribution, mimicking a classical stochastic process.

A new alternative set of observables is given by the windowed Fourier transforms of $\delta\hat{X}(t)$,

$$\delta\hat{X}_T[\omega] = \frac{1}{\sqrt{T}} \int_{-T/2}^{T/2} e^{i\omega t} \delta\hat{X}(t) \quad (\text{B.2})$$

now indexed by ω . Note that although the operators are not Hermitian, they can be written in the form $\delta\hat{X}_T[\omega] = \hat{A} + i\hat{B}$ with \hat{A} and \hat{B} commuting Hermitian operators. Due to eq. (B.1), they also form a set of commuting observables that can be measured independently without disturbing each other. The variance in their measurement is given by

$$\text{Var}(\delta\hat{X}[\omega]) = \text{Var}\hat{A} + \text{Var}\hat{B} = \left\langle \frac{1}{2} \left\{ \delta\hat{X}_T[\omega], (\delta\hat{X}_T[\omega])^\dagger \right\} \right\rangle \xrightarrow{T \rightarrow \infty} \bar{\mathcal{S}}_{\delta\hat{X}\delta\hat{X}}[\omega]. \quad (\text{B.3})$$

The quantum symmetrized spectrum density is precisely the variance of the observables $\delta\hat{X}_T[\omega]$. This makes the connection to the classical signal corresponding to the measurement straightforward. The fluctuations in the random classical signal are given by the the quantum variance (B.3) such

that the classical spectral density is given by the quantum spectral density $\bar{\mathcal{S}}_{\delta\hat{X}\delta\hat{X}}[\omega]$. Note that there is some arbitrariness in picking the symmetrized spectrum here, as it is equal to the unsymmetrized definition since all operators commute with each other.

B.2 Direct photodetection: measuring the amplitude quadrature

Before diving into the full details of the heterodyne detection, we first consider the direct photo-detection of a travelling wave containing a large classical amplitude, with $\hat{a}(t) = \bar{a}e^{-i\omega_s t} + \delta\hat{a}(t)$. The first step is to go to a rotating frame in order to keep only the slow changes in the field, $\delta\hat{a}'(t) = e^{i\omega_s t}\delta\hat{a}(t)$ to get $\hat{a}(t) = (\bar{a} + \delta\hat{a}'(t))e^{-i\omega_s t}$ (the prime is henceforth dropped for ease of notation). The detector measures the flux of photons

$$\hat{n}(t) = \delta\hat{a}^\dagger(t)\delta\hat{a}(t) = \bar{a}^2 + \bar{a}(\delta\hat{a}(t) + \delta\hat{a}^\dagger(t)) + \delta\hat{a}^\dagger(t)\delta\hat{a}(t) \quad (\text{B.4})$$

where the mean-field amplitude \bar{a} is assumed to be real. For a large amplitude \bar{a} , only the terms linear in $\delta\hat{a}$, $\delta\hat{a}^\dagger$ are kept and the third term is neglected¹. The photon flux gives a measure of the amplitude quadrature of the field $\delta\hat{p} = \frac{1}{2}(\delta\hat{a} + \delta\hat{a}^\dagger)$. The photon flux fluctuations $\delta\hat{n} = \hat{n} - \langle\hat{n}\rangle$ obeys

$$[\delta\hat{n}(t), \delta\hat{n}(t')] = 2\bar{a}[\delta\hat{p}(t), \delta\hat{p}(t')] = \bar{a}([\delta\hat{a}(t), \delta\hat{a}^\dagger(t')] + [\delta\hat{a}^\dagger(t), \delta\hat{a}(t')]) = 0 \quad (\text{B.5})$$

and constitutes a continuous observable. The photocurrent $I(t)$, the classical signal that corresponds to the measured photon flux, has the spectral density

$$\mathcal{S}_{II}[\omega] = 2\bar{a}^2\mathcal{S}_{\delta\hat{p}\delta\hat{p}}[\omega] \quad (\text{B.6})$$

(the proportionality constant between the photon flux and the photocurrent is taken to be 1 here for simplicity). The quantum fluctuations of $\delta\hat{p}$ are amplified by the amplitude \bar{a} to form a classical signal $I(t)$.

While the treatment above takes the photo-detector to be ideal, a realistic photo-detector loses part of the signal, which then cannot be measured. We

¹ While formally we have that $\langle\delta\hat{a}^\dagger(t)\delta\hat{a}(t)\rangle = \delta(0) \rightarrow \infty$ from eq. (2.46), this is only due to the formalism used to describe the white noise spectrum. In reality, the zero-time correlation due to the quantum fluctuations must be finite and the short-time correlations spread over a time very short compared to the bandwidth of the detector, as mentioned in section 2.2.1. Neglecting the term $\delta\hat{a}^\dagger(t)\delta\hat{a}(t)$ is thus justified and avoids having to deal with the infinities.

model it as an unequal beam-splitter (characterized by the real parameter η) that combines the signal \hat{a} with that of another port \hat{a}_0 (assumed to be in the vacuum state) in a new field

$$\hat{a}_{\text{det}}(t) = \sqrt{\eta}(\bar{a} + \delta\hat{a}(t)) + \sqrt{1-\eta}\hat{a}_0 \quad (\text{B.7})$$

that is detected by an ideal photo-detector. The photon flux reaching the detector is now

$$\hat{n}_{\text{det}}(t) = \eta\bar{a}^2 + \eta\bar{a}(\delta\hat{a}(t) + \delta\hat{a}^\dagger(t)) + 2\sqrt{\eta(1-\eta)}\bar{a}(\hat{a}_0(t) + \hat{a}_0^\dagger(t)) \quad (\text{B.8})$$

that combines the amplitude quadratures of both input $\delta\hat{p}$ and vacuum port $\delta\hat{p}_0$. In that case, the photocurrent spectrum is

$$\mathcal{S}_{II}[\omega] = \mathcal{S}_{\delta\hat{n}_{\text{det}}\delta\hat{n}_{\text{det}}}[\omega] = 2\eta^2\bar{a}^2\mathcal{S}_{\delta\hat{p}\delta\hat{p}}[\omega] + 2\eta(1-\eta)\bar{a}^2\mathcal{S}_{\hat{p}_0\hat{p}_0}[\omega]. \quad (\text{B.9})$$

If the quantum fluctuations of the field $\delta\hat{a}$ are decomposed into signal and vacuum fluctuations $\delta\hat{p} = \delta\hat{p}_s + \delta\hat{p}_{\text{vac}}$, the result can be re-expressed as

$$\begin{aligned} \mathcal{S}_{II}[\omega] &= 2\eta^2\bar{a}^2\mathcal{S}_{\delta\hat{p}\delta\hat{p}}^s[\omega] + 2\eta\bar{a}^2(\eta\mathcal{S}_{\delta\hat{p}\delta\hat{p}}^{\text{vac}}[\omega] + (1-\eta)\mathcal{S}_{\hat{p}\hat{p}}^0[\omega]) \\ &= 2\eta\bar{a}^2\left(\eta\mathcal{S}_{\delta\hat{p}\delta\hat{p}}^s[\omega] + \frac{1}{2}\right). \end{aligned} \quad (\text{B.10})$$

The vacuum port replaces the part of the vacuum noise of the signal that is removed by the finite efficiency η , such that it is as if the loss affects the signal only and not the quantum noise. In the ideal case $\eta = 1$, no extra noise must be added to the system. The process (analog to a homodyne detection) corresponds to the case of phase-sensitive amplification, which can amplify a single quadrature without any noise.

In practice, there are other sources of classical noise in the detection process that give a contribution to $\mathcal{S}_{II}[\omega]$. By increasing the amplitude \bar{a} , they can be made negligible compared to the (amplified) vacuum fluctuations and the detection is said to be “shot-noise limited”.

In the rotating frame, only the slow changes of the field $\delta\hat{a}(t)$ are taken into account, by canceling the rapid oscillations at frequency ω_s . This means that the spectrum at frequency ω in the measured signal $I(t)$, which is proportional to the spectrum of the slow-varying field, actually corresponds to changes of the optical field at the frequency $\omega_s + \omega$ in the laboratory frame. There is process of “mixing down” in which the signal at optical frequencies are brought down to much lower frequencies by combining it with a local oscillator (here given by the signal itself).

B.3 Optical heterodyne detection

We are now ready to investigate the heterodyne detection of an optical field. The signal of interest that carries information near a carrier frequency ω_s is combined with a strong local oscillator at frequency $\omega_s + \Delta$ through a balanced beam-splitter. The fields in the two output arms of the beam-splitter are given by

$$\hat{a}_{\text{det},i}(t) = \frac{1}{\sqrt{2}} (\bar{a} + \delta\hat{a}(t)) e^{-i\omega_s t} + \frac{\nu}{\sqrt{2}} (\bar{a}_{\text{LO}} + \delta\hat{a}_{\text{LO}}(t)) e^{-i(\omega_s + \Delta)t} \quad (\text{B.11})$$

where $\nu = 1$ for the port labeled with $i = 1$ and $\nu = -1$ for the port labeled with $i = 2$. The corresponding photon fluxes are

$$\begin{aligned} \hat{n}_{\text{det},i}(t) &= \frac{1}{2} \bar{a}^2 + \frac{\nu^2}{2} \bar{a}_{\text{LO}}^2 + \frac{1}{2} \bar{a} (\delta\hat{a}(t) + \delta\hat{a}^\dagger(t)) + \frac{\nu^2}{2} \bar{a}_{\text{LO}} (\delta\hat{a}_{\text{LO}}(t) + \delta\hat{a}_{\text{LO}}^\dagger(t)) \\ &\quad + \frac{\nu}{2} \bar{a} (\delta\hat{a}_{\text{LO}}(t) e^{-i\Delta t} + \delta\hat{a}_{\text{LO}}^\dagger(t) e^{i\Delta t}) + \frac{\nu}{2} \bar{a}_{\text{LO}} (\delta\hat{a}(t) e^{i\Delta t} + \delta\hat{a}^\dagger(t) e^{-i\Delta t}). \end{aligned} \quad (\text{B.12})$$

Of interest is only the last term, that measures the fluctuations of the signal $\delta\hat{a}$ amplified by the local oscillator amplitude \bar{a}_{LO} . Balanced heterodyne detection gets rid of most other terms. It consists in measuring both outputs with two detectors and subtracting the two resulting photocurrents, to obtain

$$\begin{aligned} I_{\text{het}}(t) &= \hat{n}_{\text{det},1}(t) - \hat{n}_{\text{det},2}(t) \\ &= \bar{a} (\delta\hat{a}_{\text{LO}}(t) e^{-i\Delta t} + \delta\hat{a}_{\text{LO}}^\dagger(t) e^{i\Delta t}) + \bar{a}_{\text{LO}} (\delta\hat{a}(t) e^{i\Delta t} + \delta\hat{a}^\dagger(t) e^{-i\Delta t}). \end{aligned} \quad (\text{B.13})$$

For a sufficiently strong local oscillator $\bar{a}_{\text{LO}} \gg \bar{a}$, the first term can be neglected². The heterodyne photocurrent I_{het} measures a rotating quadrature $\delta\hat{q}^{\theta(t)} = (\delta\hat{a}e^{i\theta(t)} + \delta\hat{a}^\dagger e^{-i\theta(t)})/\sqrt{2}$ with $\theta(t) = \Delta t$. The quadrature rotates in phase space and alternates between the phase and amplitude quadratures at a rate given by the detuning Δ . The operator obeys

$$\left[\delta\hat{q}^{\theta(t)}(t), \delta\hat{q}^{\theta(t')}(t') \right] = i\delta(t - t') \sin(\Delta(t - t')) = 0 \quad (\text{B.14})$$

ensuring that it is a continuous observable, despite the fact that amplitude and phase quadrature do not in general commute with each other.

² This also assumes that the classical noise associated with the local oscillator in $\delta\hat{a}_{\text{LO}}$ on top of the vacuum fluctuations is not too strong.

The correlations of the heterodyne photocurrents are

$$\begin{aligned} \frac{1}{\bar{a}_{\text{LO}}^2} \langle I_{\text{het}}(t) I_{\text{het}}(t') \rangle &= \langle \delta \hat{a}^\dagger(t) \delta \hat{a}(t') \rangle e^{-i\Delta(t-t')} + \langle \delta \hat{a}(t) \delta \hat{a}^\dagger(t') \rangle e^{i\Delta(t-t')} \\ &\quad + \langle \delta \hat{a}(t) \delta \hat{a}(t') \rangle e^{i\Delta(t+t')} + \langle \delta \hat{a}^\dagger(t) \delta \hat{a}^\dagger(t') \rangle e^{-i\Delta(t+t')}. \end{aligned} \quad (\text{B.15})$$

The last two terms are not stationary; they depend on $t + t'$ rather than $t - t'$. They are cyclostationary noise: a stationary process that is periodically oscillating in time, here with a phase oscillating at a frequency 2Δ . Fortunately, in most practical cases, the frequency 2Δ is large compared to the frequency of the signal of interest. They can then be neglected and the process becomes stationary again (in the relevant bandwidth). It is then possible to define the spectral density of the photocurrent as

$$\begin{aligned} \mathcal{S}_{II}^{\text{het}}[\omega] &= \bar{a}_{\text{LO}}^2 \int_{-\infty}^{\infty} dt \left(\langle \delta \hat{a}^\dagger(t) \delta \hat{a}(0) \rangle e^{-i(\omega-\Delta)t} + \langle \delta \hat{a}(t) \delta \hat{a}^\dagger(0) \rangle e^{-i(\omega+\Delta)t} \right) \\ &= \bar{a}_{\text{LO}}^2 \left(\mathcal{S}_{\delta \hat{a}^\dagger \delta \hat{a}}[\omega - \Delta] + \mathcal{S}_{\delta \hat{a} \delta \hat{a}^\dagger}[\omega + \Delta] \right). \end{aligned} \quad (\text{B.16})$$

The classical photocurrent spectrum is proportional to the unsymmetrized quantum spectrum $\mathcal{S}_{\delta \hat{a}^\dagger \delta \hat{a}}$, shifted in frequency. The quantum information, that was encoded in the asymmetry between positive and negative frequencies in $\mathcal{S}_{\delta \hat{a}^\dagger \delta \hat{a}}[\pm\omega]$ is transcribed classically at the positive frequencies $\mathcal{S}_{II}[\Delta \pm \omega]$ (for $|\omega| < |\Delta|$). For the spectrum to be overall classical and symmetric for negative frequencies, the conjugated term $\mathcal{S}_{\delta \hat{a} \delta \hat{a}^\dagger}$ that presents the same information at negative frequencies is necessary. This conjugated term has the effect to increase the noise background at positive frequencies.

A classical interpretation of the heterodyne scheme may help shed some more light for the interpretation of the conjugated term. The local oscillator beats at a frequency Δ with the signal around ω_s , but equally with whichever field lies symmetrically on the other side, at $\omega_s + 2\Delta$ (see fig. B.1). The term $\mathcal{S}_{\delta \hat{a} \delta \hat{a}^\dagger}[\omega + \Delta]$, detuned by 2Δ with respect to $\mathcal{S}_{\delta \hat{a}^\dagger \delta \hat{a}}[\omega - \Delta]$, represents precisely that alternative input port. Classically, that port can have zero field such that the contribution of $\mathcal{S}_{\delta \hat{a} \delta \hat{a}^\dagger}[\omega + \Delta]$ at positive frequencies vanishes. Quantum mechanically however, there exists a minimum amount of disturbance due to vacuum fluctuations. The spectrum $\mathcal{S}_{\delta \hat{a} \delta \hat{a}^\dagger}[\omega + \Delta]$ (evaluated at positive frequencies) can then be interpreted as representing the vacuum fluctuations of the input field at the symmetric heterodyne port at $\omega_s + 2\Delta$. This gives a white noise of 1 as the minimum contribution from the vacuum fluctuations and limits the performance of the heterodyne measurement. Precisely

B.4 Comparison between heterodyne detection and phase-preserving amplification

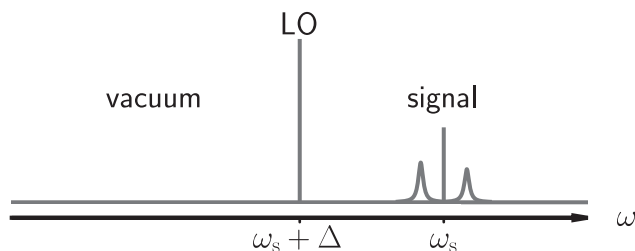


Figure B.1: Scheme for heterodyne detection. The signal at ω_s beats with the local oscillator at $\omega_s + \Delta$. The vacuum noise on the other side beats as well with the LO and can be understood as the source of the increased noise background in the heterodyne signal.

the same was observed in the case of the linear amplifier in section 2.2.3: the minimum added noise is the amount necessary to symmetrize the white noise due to vacuum fluctuations between $\mathcal{S}_{\delta\hat{a}^\dagger\delta\hat{a}}$ and $\mathcal{S}_{\delta\hat{a}\delta\hat{a}^\dagger}$.

For a realistic detection process with a finite quantum efficiency η , the same steps can be taken as from eq. (B.6) to eq. (B.9). The photocurrent becomes

$$\mathcal{S}_{II}^{\text{het}}[\omega] = \eta \bar{a}_{\text{LO}}^2 \left(\eta \left(\mathcal{S}_{\delta\hat{a}^\dagger\delta\hat{a}}[\omega - \Delta] + \mathcal{S}_{\delta\hat{a}\delta\hat{a}^\dagger}[\omega + \Delta] \right) + (1 - \eta) \right) \quad (\text{B.17})$$

where the vacuum port fluctuations have been introduced. If we assume that only the vacuum fluctuations of the conjugated term $\mathcal{S}_{\delta\hat{a}\delta\hat{a}^\dagger}[\omega + \Delta]$ play a role for positive frequencies, the expression finally simplifies to

$$\mathcal{S}_{II}^{\text{het}}[\omega] = \eta \bar{a}_{\text{LO}}^2 (\eta \mathcal{S}_{\delta\hat{a}^\dagger\delta\hat{a}}[\omega - \Delta] + 1). \quad (\text{B.18})$$

Compared to eq. (B.10), the white noise background has gone from $1/2$ to 1 . This is because a single quadrature (amplitude) was measured in the case of direct photodetection, while heterodyne detection measures both quadratures at once, with the penalty of a lower signal-to-noise ratio.

B.4 Comparison between heterodyne detection and phase-preserving amplification

Strong similarities exist between the heterodyne detection and the phase-preserving amplifier considered in section 2.2.3. We rewrite eq. (B.18) as

$$\frac{1}{\eta^2 \bar{a}_{\text{LO}}^2} \mathcal{S}_{II}^{\text{het}}[\omega] = \mathcal{S}_{\delta \hat{a}^\dagger \delta \hat{a}}[\omega - \Delta] + \frac{1}{\eta} \quad (\text{B.19})$$

for positive frequencies. Comparing it to eq. (2.67), we can identify $\mathcal{G} = \eta^2 \bar{a}_{\text{LO}}^2$ and $n_{\text{fluct}} + 1 = 1/\eta$. The heterodyne detection can be interpreted as linear amplification with a power gain \bar{a}_{LO}^2 (reduced by inefficiencies) and an added noise

$$\mathcal{N}_{\text{added}} = \frac{1}{\eta} - \frac{1}{2}. \quad (\text{B.20})$$

Fully quantum efficient detection corresponds to $n_{\text{fluct}} = 0$ and hence to an added noise (as defined for the symmetrized spectrum) of $\mathcal{N}_{\text{added}} = 1/2$.

In heterodyne detection, the nonlinearity of the photodetector (that measures the field intensity rather than its amplitude) is required to mix the signal and local oscillator. By contrast, the amplifier amplifies a combination of signal and idler modes independently of the measurement. Despite the differences, precisely the same constraints in terms of added noise apply to them, since they both amplify the two quadratures of the field at the same time.

There is an equivalence between the notion of thermal added noise in amplification and quantum inefficiency in heterodyne detection. At optical frequencies, the fields can be assumed to be in the vacuum state even at room temperature. For this reason, the added noise is always assumed to be given by vacuum fluctuations. A non-ideal quantum efficiency for the detector loses signal while keeping the noise to the level of vacuum fluctuations, effectively resulting in higher added noise in exactly the same way as a finite thermal occupancy implies for microwave amplification. The difference is in a way down to model preferences. In either case, the same fundamental quantum limits must be respected. One could have as well assumed the vacuum port to have a finite effective temperature in modeling the heterodyne detection, or introduced a quantum efficiency for the microwave amplifiers. They are equivalent in the end.

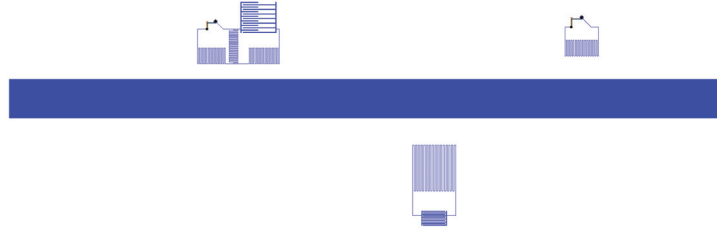
Similarly, although we do not go through the details here, homodyne detection of a single quadrature corresponds to the phase-sensitive amplifier. Since only one quadrature is amplified, no minimum amount of added noise is required by quantum mechanics, as the noise from the idler port can effectively be directed to the unmeasured quadrature.

Samples used in the experiment

We give a list here of the different fabricated chips that were used in the experiments within this thesis. The layout is given, as well as measured parameters. Because the latter can change over time (especially after warm-up and cool-down cycles), only representative values are shown. For that reason, the parameters given in the chapters corresponding to the experiments can differ slightly. On a single chip, there are typically multiple microwave resonators, with and without associated mechanical modes. For the hybrid circuit where two microwave modes interact with a common mechanical mode, the two values of g_0 are given separately only when they differ significantly.

Table C.1: HYB-20150924-4-24

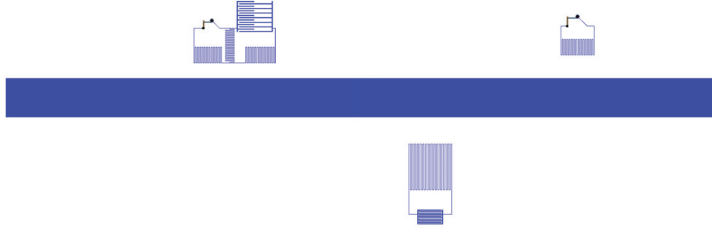
HYB-20150924-4-24 C=217um



24

Planar resonator			
Microwave properties			
$\omega_c/2\pi$	$\kappa/2\pi$	$\kappa_{\text{ex}}/2\pi$	$\kappa_0/2\pi$
3.05 GHz	97 kHz	17 kHz	79 kHz
Single optomechanical resonator			
Microwave properties			
$\omega_c/2\pi$	$\kappa/2\pi$	$\kappa_{\text{ex}}/2\pi$	$\kappa_0/2\pi$
5.59 GHz	104 kHz	11 kHz	94 kHz
Mechanical properties			
$\Omega_m/2\pi$	$\Gamma_m/2\pi$	$g_0/2\pi$	
4.5 MHz	60 Hz	53 Hz	
Hybrid optomechanical resonators			
Microwave properties			
$\omega_c/2\pi$	$\kappa/2\pi$	$\kappa_{\text{ex}}/2\pi$	$\kappa_0/2\pi$
4.26 GHz	118 kHz	42 kHz	76 kHz
5.48 GHz	4.48 MHz	4.23 MHz	245 kHz
Mechanical properties			
$\Omega_m/2\pi$	$\Gamma_m/2\pi$	$g_0/2\pi$	
5.33 MHz	30 Hz	60 Hz	

Table C.2: HYB-20160524-1-12
 HYB-20160524-1-12 C=214um

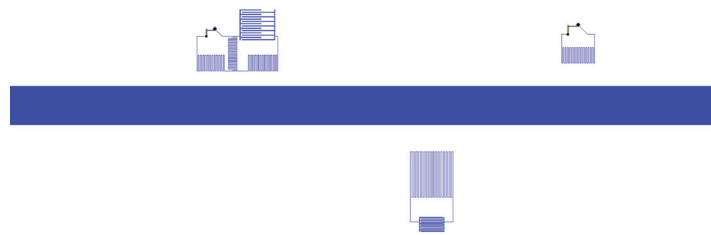


12

Planar resonator			
Microwave properties			
$\omega_c/2\pi$	$\kappa/2\pi$	$\kappa_{\text{ex}}/2\pi$	$\kappa_0/2\pi$
3.05 GHz	97 kHz	17 kHz	79 kHz
Single optomechanical resonator			
Microwave properties			
$\omega_c/2\pi$	$\kappa/2\pi$	$\kappa_{\text{ex}}/2\pi$	$\kappa_0/2\pi$
5.59 GHz	104 kHz	11 kHz	94 kHz
Mechanical properties			
$\Omega_m/2\pi$	$\Gamma_m/2\pi$	$g_0/2\pi$	
4.5 MHz	60 Hz	53 Hz	
Hybrid optomechanical resonators			
Microwave properties			
$\omega_c/2\pi$	$\kappa/2\pi$	$\kappa_{\text{ex}}/2\pi$	$\kappa_0/2\pi$
4.13 GHz	197 kHz	150 kHz	47 kHz
5.24 GHz	3.32 MHz	3.07 MHz	250 kHz
Mechanical properties			
$\Omega_m/2\pi$	$\Gamma_m/2\pi$	$g_0/2\pi$	
6.35 MHz	100 Hz	106, 79 Hz	
10.9 MHz	10 Hz	12 Hz	

Table C.3: HYB-20150924-4-17

HYB-20150924-4-17 C=273um



17

Planar resonator		
Microwave properties		
$\omega_c/2\pi$	$\kappa/2\pi$	
3.05 GHz	204 kHz	
Hybrid optomechanical resonators		
Microwave properties		
$\omega_c/2\pi$	$\kappa/2\pi$	
3.95 GHz	331 kHz	
5.33 GHz	5.3 MHz	
Mechanical properties		
$\Omega_m/2\pi$	$\Gamma_m/2\pi$	$g_0/2\pi$
8.82 MHz	200 Hz	109 Hz

Table C.4: AY_old_moreH-20180516-1-21
 AY_old_moreH-20180516-1-21



21

Planar resonator		
Microwave properties		
$\omega_c/2\pi$	$\kappa/2\pi$	
3.14 GHz	285 kHz	
Hybrid optomechanical resonator		
Microwave properties		
$\omega_c/2\pi$	$\kappa/2\pi$	
4.48 GHz	927 kHz	
6.433 GHz	331 kHz	
Mechanical properties		
$\Omega_m/2\pi$	$\Gamma_m/2\pi$	$g_0/2\pi$
6.15 MHz	20 Hz	0, 194 Hz
Single optomechanical resonator		
Microwave properties		
$\omega_c/2\pi$	$\kappa/2\pi$	
7.64 GHz	200 kHz	
Mechanical properties		
$\Omega_m/2\pi$	$\Gamma_m/2\pi$	$g_0/2\pi$
5.62 MHz		

Bibliography

- Abdo, B., M. Brink, and J. M. Chow (2017). “Gyrator Operation Using Josephson Mixers”. In: *Physical Review Applied* 8 (3), p. 034009.
- Adler, R. (1946). “A Study of Locking Phenomena in Oscillators”. In: *Proceedings of the IRE* 34 (6), pp. 351–357.
- Anderson, B. D. O. and R. W. Newcomb (1965). “On reciprocity and time-variable networks”. In: *Proceedings of the IEEE* 53 (10), pp. 1674–1674.
- Andrews, R. W., R. W. Peterson, et al. (2014). “Bidirectional and efficient conversion between microwave and optical light”. In: *Nature Physics* 10 (4), pp. 321–326.
- Andrews, R. W., A. P. Reed, et al. (2015). “Quantum-enabled temporal and spectral mode conversion of microwave signals”. In: *Nature Communications* 6, p. 10021.
- Aplet, L. J. and J. W. Carson (1964). “A Faraday Effect Optical Isolator”. In: *Applied Optics* 3 (4), pp. 544–545.
- Arcizet, O. et al. (2006). “Radiation-Pressure Cooling and Optomechanical Instability of a Micromirror”. In: *Nature* 444 (7115), pp. 71–74.
- Ashcroft, N. and N. Mermin (1976). *Solid State Physics*. New York: Brooks Cole.
- Aspelmeyer, M., T. J. Kippenberg, and F. Marquardt (2014). “Cavity optomechanics”. In: *Reviews of Modern Physics* 86 (4), pp. 1391–1452.
- Assaworrorarit, S., X. Yu, and S. Fan (2017). “Robust Wireless Power Transfer Using a Nonlinear Parity-Time-Symmetric Circuit”. In: *Nature* 546 (7658), pp. 387–390.
- Astafiev, O. et al. (2007). “Single artificial-atom lasing”. In: *Nature* 449 (7162), pp. 588–590.
- Atkins, P. and J. de Paula (2009). *Atkins’ Physical Chemistry*. 9 edition. Oxford ; New York: OUP Oxford.

- Auld, B. A. (1959). “The Synthesis of Symmetrical Waveguide Circulators”. In: *IRE Transactions on Microwave Theory and Techniques* 7 (2), pp. 238–246.
- Barends, R. et al. (2011). “Minimizing Quasiparticle Generation from Stray Infrared Light in Superconducting Quantum Circuits”. In: *Applied Physics Letters* 99 (11), p. 113507.
- Barreiro, J. T. et al. (2011). “An open-system quantum simulator with trapped ions”. In: *Nature* 470 (7335), pp. 486–491.
- Barzanjeh, S. et al. (2017). “Mechanical on-chip microwave circulator”. In: *Nature Communications* 8 (1), p. 953.
- Bender, C. M. (2005). “Introduction to \mathcal{PT} -Symmetric Quantum Theory”. In: *Contemporary Physics* 46 (4), pp. 277–292.
- Bender, C. M., B. K. Berntson, et al. (2013). “Observation of PT Phase Transition in a Simple Mechanical System”. In: *American Journal of Physics* 81 (3), pp. 173–179.
- Bender, C. M., M. Gianfreda, et al. (2013). “Twofold Transition in \mathcal{PT} -Symmetric Coupled Oscillators”. In: *Physical Review A* 88 (6), p. 062111.
- Bergeal, N. et al. (2010). “Phase-preserving amplification near the quantum limit with a Josephson ring modulator”. In: *Nature* 465 (7294), pp. 64–68.
- Bernier, N. R. (2018). *Data and Code for “Multimode Microwave Circuit Optomechanics as a Platform to Study Coupled Quantum Harmonic Oscillators”*. DOI: 10.5281/zenodo.1457216.
- Bernier, N. R., L. D. Tóth, A. K. Feofanov, et al. (2018a). “Level Attraction in a Microwave Optomechanical Circuit”. In: *Physical Review A* 98 (2), p. 023841.
- Bernier, N. R., L. D. Tóth, A. K. Feofanov, et al. (2018b). “Nonreciprocity in Microwave Optomechanical Circuits”. In: *IEEE Antennas and Wireless Propagation Letters* 17 (11), pp. 1983–1987.
- Bernier, N. R., L. D. Tóth, A. Koottandavida, et al. (2017). “Nonreciprocal Reconfigurable Microwave Optomechanical Circuit”. In: *Nature Communications* 8 (1), p. 604.
- Bernier, N. R., E. G. Dalla Torre, and E. Demler (2014). “Unstable Avoided Crossing in Coupled Spinor Condensates”. In: *Physical Review Letters* 113 (6), p. 065303.
- Bertet, P., C. J. P. M. Harmans, and J. E. Mooij (2006). “Parametric Coupling for Superconducting Qubits”. In: *Physical Review B* 73 (6), p. 064512.
- Bi, L. et al. (2011). “On-chip optical isolation in monolithically integrated non-reciprocal optical resonators”. In: *Nature Photonics* 5 (12), pp. 758–762.
- Bloembergen, N. (1996). *Nonlinear Optics*. 4th. World Scientific Pub Co Inc.

- Bowen, W. P. and G. J. Milburn (2015). *Quantum Optomechanics*. CRC Press.
- Braginski, V. B. and A. B. Manukin (1967). “Ponderomotive Effects of Electromagnetic Radiation”. In: *Sov. Phys. JETP* 25, pp. 653–655.
- Braginsky, V. B., S. E. Strigin, and S. P. Vyatchanin (2001). “Parametric Oscillatory Instability in Fabry–Perot Interferometer”. In: *Physics Letters A* 287 (5–6), pp. 331–338.
- Braginsky, V. B. and S. P. Vyatchanin (2002). “Low Quantum Noise Tranquillizer for Fabry–Perot Interferometer”. In: *Physics Letters A* 293 (5–6), pp. 228–234.
- Braginsky, V. and A. Manukin (1977). *Measurement of weak forces in Physics experiments*. Univ. of Chicago Press.
- Braginsky, V., A. Manukin, and M. Y. Tikhonov (1970). “Investigation of Dissipative Ponderomotive Effects of Electromagnetic Radiation”. In: *Sov. Phys. JETP* 31 (5), p. 829.
- Brandstetter, M. et al. (2014). “Reversing the Pump Dependence of a Laser at an Exceptional Point”. In: *Nature Communications* 5, ncomms5034.
- Bromberg, J. L. (2008). “The Birth of the Laser”. In: *Physics Today* 41 (10), p. 26.
- Bruno, A. et al. (2015). “Reducing Intrinsic Loss in Superconducting Resonators by Surface Treatment and Deep Etching of Silicon Substrates”. In: *Applied Physics Letters* 106 (18), p. 182601.
- Caldeira, A. O. and A. J. Leggett (1981). “Influence of Dissipation on Quantum Tunneling in Macroscopic Systems”. In: *Phys. Rev. Lett.* 46 (4), pp. 211–214.
- Callen, H. B. and T. A. Welton (1951). “Irreversibility and Generalized Noise”. In: *Physical Review* 83 (1), pp. 34–40.
- Cardwell, D. A. and D. S. Ginley (2003). *Handbook of Superconducting Materials*. CRC Press.
- Cassidy, M. C. et al. (2017). “Demonstration of an Ac Josephson Junction Laser”. In: *Science* 355 (6328), pp. 939–942.
- Castellanos-Beltran, M. A., K. D. Irwin, et al. (2008). “Amplification and squeezing of quantum noise with a tunable Josephson metamaterial”. In: *Nat Phys* 4 (12), pp. 929–931.
- Castellanos-Beltran, M. A. and K. W. Lehnert (2007). “Widely Tunable Parametric Amplifier Based on a Superconducting Quantum Interference Device Array Resonator”. In: *Applied Physics Letters* 91 (8), p. 083509.
- Caves, C. M. (1982). “Quantum limits on noise in linear amplifiers”. In: *Physical Review D* 26 (8), pp. 1817–1839.
- Chan, J. et al. (2011). “Laser cooling of a nanomechanical oscillator into its quantum ground state”. In: *Nature* 478 (7367), pp. 89–92.

- Chapman, B. J. et al. (2017). “Widely Tunable On-Chip Microwave Circulator for Superconducting Quantum Circuits”. In: *Physical Review X* 7 (4), p. 041043.
- Chen, W. et al. (2017). “Exceptional Points Enhance Sensing in an Optical Microcavity”. In: *Nature* 548 (7666), pp. 192–196.
- Cicak, K. et al. (2010). “Low-loss superconducting resonant circuits using vacuum-gap-based microwave components”. In: *Applied Physics Letters* 96 (9), p. 093502.
- Clerk, A. A. et al. (2010). “Introduction to quantum noise, measurement, and amplification”. In: *Reviews of Modern Physics* 82 (2), pp. 1155–1208.
- Córcoles, A. D. et al. (2011). “Protecting Superconducting Qubits from Radiation”. In: *Applied Physics Letters* 99 (18), p. 181906.
- Dembowski, C. et al. (2001). “Experimental Observation of the Topological Structure of Exceptional Points”. In: *Physical Review Letters* 86 (5), pp. 787–790.
- Deng, C., M. Otto, and A. Lupascu (2013). “An Analysis Method for Transmission Measurements of Superconducting Resonators with Applications to Quantum-Regime Dielectric-Loss Measurements”. In: *Journal of Applied Physics* 114 (5), p. 054504.
- Devoret, M. H. and R. J. Schoelkopf (2013). “Superconducting Circuits for Quantum Information: An Outlook”. In: *Science* 339 (6124), pp. 1169–1174.
- Dobrindt, J. M., I. Wilson-Rae, and T. J. Kippenberg (2008). “Parametric Normal-Mode Splitting in Cavity Optomechanics”. In: *Phys. Rev. Lett.* 101 (26), p. 263602.
- Doppler, J. et al. (2016). “Dynamically Encircling an Exceptional Point for Asymmetric Mode Switching”. In: *Nature* 537 (7618), pp. 76–79.
- Eichler, C. et al. (2014). “Quantum-Limited Amplification and Entanglement in Coupled Nonlinear Resonators”. In: *Phys. Rev. Lett.* 113 (11), p. 110502.
- Eleuch, H. and I. Rotter (2014). “Exceptional points in open and PT-symmetric systems”. In: *Acta Polytechnica* 54 (2), pp. 106–112.
- Estep, N. A. et al. (2014). “Magnetic-free non-reciprocity and isolation based on parametrically modulated coupled-resonator loops”. In: *Nature Physics* 10 (12), pp. 923–927.
- Evans, M. et al. (2015). “Observation of Parametric Instability in Advanced LIGO”. In: *Physical Review Letters* 114 (16), p. 161102.
- Fan, L. et al. (2012). “An All-Silicon Passive Optical Diode”. In: *Science* 335 (6067), pp. 447–450.

- Fang, K., J. Luo, et al. (2017). “Generalized non-reciprocity in an optomechanical circuit via synthetic magnetism and reservoir engineering”. In: *Nat Phys* 13 (5), pp. 465–471.
- Fang, K., Z. Yu, and S. Fan (2012). “Photonic Aharonov-Bohm Effect Based on Dynamic Modulation”. In: *Physical Review Letters* 108 (15), p. 153901.
- Fang, K., Z. Yu, and S. Fan (2013). “Experimental Demonstration of a Photonic Aharonov-Bohm Effect at Radio Frequencies”. In: *Physical Review B* 87 (6), p. 060301.
- Fano, U. (1961). “Effects of Configuration Interaction on Intensities and Phase Shifts”. In: *Physical Review* 124 (6), pp. 1866–1878.
- Fay, C. E. and R. L. Comstock (1965). “Operation of the Ferrite Junction Circulator”. In: *IEEE Transactions on Microwave Theory and Techniques* 13 (1), pp. 15–27.
- Fetter, A. L., J. D. Walecka, and Physics (2003). *Quantum Theory of Many-Particle Systems*. Mineola, N.Y: Dover Publications.
- Feynman, R. P. (1988). *QED: The Strange Theory of Light and Matter*. New Ed. Princeton University Press.
- Fleury, R. et al. (2014). “Sound Isolation and Giant Linear Nonreciprocity in a Compact Acoustic Circulator”. In: *Science* 343 (6170), pp. 516–519.
- Gardiner, C. W. and M. J. Collett (1985). “Input and output in damped quantum systems: Quantum stochastic differential equations and the master equation”. In: *Physical Review A* 31 (6), pp. 3761–3774.
- Ghadimi, A. H. et al. (2018). “Elastic Strain Engineering for Ultralow Mechanical Dissipation”. In: *Science*, eaar6939.
- Gigan, S. et al. (2006). “Self-Cooling of a Micromirror by Radiation Pressure”. In: *Nature* 444 (7115), pp. 67–70.
- Gloppe, A. et al. (2014). “Bidimensional Nano-Optomechanics and Topological Backaction in a Non-Conservative Radiation Force Field”. In: *Nature Nanotechnology* 9 (11), pp. 920–926.
- Grajcar, M. et al. (2008). “Sisyphus cooling and amplification by a superconducting qubit”. In: *Nat Phys* 4 (8), pp. 612–616.
- Gröblacher, S. et al. (2009). “Observation of Strong Coupling between a Micromechanical Resonator and an Optical Cavity Field”. In: *Nature* 460 (7256), pp. 724–727.
- Grudinin, I. S. et al. (2010). “Phonon Laser Action in a Tunable Two-Level System”. In: *Phys. Rev. Lett.* 104 (8), p. 083901.
- Guo, X. et al. (2016). “On-Chip Strong Coupling and Efficient Frequency Conversion between Telecom and Visible Optical Modes”. In: *Physical Review Letters* 117 (12), p. 123902.
- Hafezi, M. and P. Rabl (2012). “Optomechanically induced non-reciprocity in microring resonators”. In: *Optics Express* 20 (7), pp. 7672–7684.

- Hatridge, M. et al. (2011). “Dispersive Magnetometry with a Quantum Limited SQUID Parametric Amplifier”. In: *Physical Review B* 83 (13), p. 134501.
- Haus, H. A. (1983). *Waves and Fields in Optoelectronics*. Englewood Cliffs, NJ: Prentice Hall.
- Heiss, W. D. (2012). “The Physics of Exceptional Points”. In: *Journal of Physics A: Mathematical and Theoretical* 45 (44), p. 444016.
- Hua, S. et al. (2016). “Demonstration of a Chip-Based Optical Isolator with Parametric Amplification”. In: *Nature Communications* 7, p. 13657.
- Jalas, D. et al. (2013). “What is — and what is not — an optical isolator”. In: *Nature Photonics* 7 (8), pp. 579–582.
- Jayich, A. M. et al. (2008). “Dispersive Optomechanics: A Membrane inside a Cavity”. In: *New Journal of Physics* 10 (9), p. 095008.
- St-Jean, M. R. et al. (2014). “Injection Locking of Mid-Infrared Quantum Cascade Laser at 14 GHz, by Direct Microwave Modulation”. In: *Laser & Photonics Reviews* 8 (3), pp. 443–449.
- Jing, H. et al. (2014). “ \mathcal{PT} -Symmetric Phonon Laser”. In: *Physical Review Letters* 113 (5), p. 053604.
- Kang, M. S., A. Butsch, and P. S. J. Russell (2011). “Reconfigurable light-driven opto-acoustic isolators in photonic crystal fibre”. In: *Nature Photonics* 5 (9), pp. 549–553.
- Kells, W. and E. D’Ambrosio (2002). “Considerations on Parametric Instability in Fabry–Perot Interferometer”. In: *Physics Letters A* 299 (4), pp. 326–330.
- Kerckhoff, J., R. W. Andrews, et al. (2013). “Tunable Coupling to a Mechanical Oscillator Circuit Using a Coherent Feedback Network”. In: *Phys. Rev. X* 3 (2), p. 021013.
- Kerckhoff, J., K. Lalumière, et al. (2015). “On-Chip Superconducting Microwave Circulator from Synthetic Rotation”. In: *Physical Review Applied* 4 (3), p. 034002.
- Khalil, M. S. et al. (2012). “An analysis method for asymmetric resonator transmission applied to superconducting devices”. In: *Journal of Applied Physics* 111 (5), p. 054510.
- Khanbekyan, M. et al. (2015). “Unconventional Collective Normal-Mode Coupling in Quantum-Dot-Based Bimodal Microlasers”. In: *Physical Review A* 91 (4), p. 043840.
- Kienzler, D. et al. (2015). “Quantum harmonic oscillator state synthesis by reservoir engineering”. In: *Science* 347 (6217), pp. 53–56.
- Kippenberg, T. J., R. Holzwarth, and S. A. Diddams (2011). “Microresonator-Based Optical Frequency Combs”. In: *Science* 332 (6029), pp. 555–559.

- Kippenberg, T. J., H. Rokhsari, et al. (2005). “Analysis of Radiation-Pressure Induced Mechanical Oscillation of an Optical Microcavity”. In: *Physical Review Letters* 95 (3), p. 033901.
- Knünz, S. et al. (2010). “Injection Locking of a Trapped-Ion Phonon Laser”. In: *Physical Review Letters* 105 (1), p. 013004.
- Koestler, A. (1959). *The Sleepwalkers: A History of Man’s Changing Vision of the Universe*. London: Hutchinson.
- Krauter, H. et al. (2011). “Entanglement Generated by Dissipation and Steady State Entanglement of Two Macroscopic Objects”. In: *Phys. Rev. Lett.* 107 (8), p. 080503.
- Kronwald, A., F. Marquardt, and A. A. Clerk (2013). “Arbitrarily large steady-state bosonic squeezing via dissipation”. In: *Physical Review A* 88 (6), p. 063833.
- Kronwald, A., F. Marquardt, and A. A. Clerk (2014). “Dissipative optomechanical squeezing of light”. In: *New Journal of Physics* 16 (6), p. 063058.
- Kruk, P. et al. (2005). “Frequency Reference for Laser Spectroscopy with the Stabilized 4-m-Long Fabry–Perot Cavity”. In: *Review of Scientific Instruments* 76 (3), p. 033109.
- Lam, C. S. (2008). “A Review of the Recent Development of MEMS and Crystal Oscillators and Their Impacts on the Frequency Control Products Industry”. In: *2008 IEEE Ultrasonics Symposium*, pp. 694–704.
- Le Bellac, M. (2012). *Quantum Physics*. Trans. by P. de Forcrand-Millard. New York: Cambridge University Press.
- Lecocq, F., J. B. Clark, et al. (2015). “Quantum Nondemolition Measurement of a Nonclassical State of a Massive Object”. In: *Physical Review X* 5 (4), p. 041037.
- Lecocq, F., J. B. Clark, et al. (2016). “Mechanically Mediated Microwave Frequency Conversion in the Quantum Regime”. In: *Physical Review Letters* 116 (4), p. 043601.
- Lecocq, F., L. Ranzani, et al. (2017). “Nonreciprocal Microwave Signal Processing with a Field-Programmable Josephson Amplifier”. In: *Phys. Rev. Applied* 7 (2), p. 024028.
- Lecocq, F., J. D. Teufel, et al. (2015). “Resolving the vacuum fluctuations of an optomechanical system using an artificial atom”. In: *Nat Phys* 11 (8), pp. 635–639.
- Leghtas, Z. et al. (2015). “Confining the state of light to a quantum manifold by engineered two-photon loss”. In: *Science* 347 (6224), pp. 853–857.
- Lin, Y. et al. (2013). “Dissipative production of a maximally entangled steady state of two quantum bits”. In: *Nature* 504 (7480), pp. 415–418.

- Lira, H. et al. (2012). “Electrically Driven Nonreciprocity Induced by Interband Photonic Transition on a Silicon Chip”. In: *Physical Review Letters* 109 (3), p. 033901.
- Liu, Y.-Y. et al. (2015). “Injection locking of a semiconductor double-quantum-dot micromaser”. In: *Physical Review A* 92 (5), p. 053802.
- Macklin, C. et al. (2015). “A near-quantum-limited Josephson traveling-wave parametric amplifier”. In: *Science* 350 (6258), pp. 307–310.
- Malz, D. et al. (2018). “Quantum-Limited Directional Amplifiers with Optomechanics”. In: *Physical Review Letters* 120 (2), p. 023601.
- Manipatruni, S., J. T. Robinson, and M. Lipson (2009). “Optical Nonreciprocity in Optomechanical Structures”. In: *Physical Review Letters* 102 (21), p. 213903.
- Marquardt, F., J. P. Chen, et al. (2007). “Quantum Theory of Cavity-Assisted Sideband Cooling of Mechanical Motion”. In: *Physical Review Letters* 99 (9).
- Marquardt, F., J. G. E. Harris, and S. M. Girvin (2006). “Dynamical Multistability Induced by Radiation Pressure in High-Finesse Micromechanical Optical Cavities”. In: *Physical Review Letters* 96 (10), p. 103901.
- Megrant, A. et al. (2012). “Planar superconducting resonators with internal quality factors above one million”. In: *Applied Physics Letters* 100 (11), p. 113510.
- Metelmann, A. and A. A. Clerk (2014). “Quantum-Limited Amplification via Reservoir Engineering”. In: *Physical Review Letters* 112 (13), p. 133904.
- Metelmann, A. and A. A. Clerk (2015). “Nonreciprocal Photon Transmission and Amplification via Reservoir Engineering”. In: *Physical Review X* 5 (2), p. 021025.
- Milano, U., J. H. Saunders, and L. Davis (1960). “A Y-Junction Strip-Line Circulator”. In: *IRE Transactions on Microwave Theory and Techniques* 8 (3), pp. 346–351.
- Milburn, T. J. et al. (2015). “General Description of Quasiadiabatic Dynamical Phenomena near Exceptional Points”. In: *Physical Review A* 92 (5), p. 052124.
- Møller, C. B. et al. (2017). “Quantum Back-Action-Evading Measurement of Motion in a Negative Mass Reference Frame”. In: *Nature* 547 (7662), pp. 191–195.
- Mumford, W. W. (1960). “Some Notes on the History of Parametric Transducers”. In: *Proceedings of the IRE* 48 (5), pp. 848–853.
- Murch, K. W. et al. (2012). “Cavity-Assisted Quantum Bath Engineering”. In: *Physical Review Letters* 109 (18), p. 183602.

- Nielsen, W. H. P. et al. (2017). “Multimode optomechanical system in the quantum regime”. In: *Proceedings of the National Academy of Sciences* 114 (1), pp. 62–66.
- Nunnenkamp, A. et al. (2014). “Quantum-Limited Amplification and Parametric Instability in the Reversed Dissipation Regime of Cavity Optomechanics”. In: *Physical Review Letters* 113 (2), p. 023604.
- Ockeloen-Korppi, C. F. et al. (2016). “Quantum Backaction Evading Measurement of Collective Mechanical Modes”. In: *Physical Review Letters* 117 (14), p. 140401.
- O’Connell, A. D. et al. (2010). “Quantum Ground State and Single-Phonon Control of a Mechanical Resonator”. In: *Nature* 464 (7289), pp. 697–703.
- Palomaki, T. A. et al. (2013). “Entangling Mechanical Motion with Microwave Fields”. In: *Science* 342 (6159), pp. 710–713.
- Paraiso, T. K. et al. (2015). “Position-Squared Coupling in a Tunable Photonic Crystal Optomechanical Cavity”. In: *Physical Review X* 5 (4), p. 041024.
- Peano, V., C. Brendel, et al. (2015). “Topological Phases of Sound and Light”. In: *Physical Review X* 5 (3), p. 031011.
- Peano, V., M. Houde, et al. (2016). “Topological Quantum Fluctuations and Traveling Wave Amplifiers”. In: *Physical Review X* 6 (4), p. 041026.
- Peng, B., Ş. K. Özdemir, S. Rotter, et al. (2014). “Loss-Induced Suppression and Revival of Lasing”. In: *Science* 346 (6207), pp. 328–332.
- Peng, B., Ş. K. Özdemir, F. Lei, et al. (2014). “Parity-time-symmetric whispering-gallery microcavities”. In: *Nature Physics* 10 (5), pp. 394–398.
- Peterson, G. A. et al. (2017). “Demonstration of Efficient Nonreciprocity in a Microwave Optomechanical Circuit”. In: *Physical Review X* 7 (3), p. 031001.
- Pikovsky, A., M. Rosenblum, and J. Kurths (2003). *Synchronization: A Universal Concept in Nonlinear Sciences*. Cambridge University Press.
- Pirkkalainen, J.-M., S. Cho, et al. (2015). “Cavity Optomechanics Mediated by a Quantum Two-Level System”. In: *Nature Communications* 6, p. 6981.
- Pirkkalainen, J.-M., E. Damskägg, et al. (2015). “Squeezing of Quantum Noise of Motion in a Micromechanical Resonator”. In: *Physical Review Letters* 115 (24), p. 243601.
- Polzik, E. S. and K. Hammerer (2015). “Trajectories without Quantum Uncertainties”. In: *Annalen der Physik* 527 (1-2), A15–A20.
- Poyatos, J. F., J. I. Cirac, and P. Zoller (1996). “Quantum Reservoir Engineering with Laser Cooled Trapped Ions”. In: *Physical Review Letters* 77 (23), pp. 4728–4731.
- Pozar, D. M. (2011). *Microwave Engineering*. Wiley.

- Probst, S. et al. (2015). “Efficient and robust analysis of complex scattering data under noise in microwave resonators”. In: *Review of Scientific Instruments* 86 (2), p. 024706.
- Purdy, T. P. et al. (2013). “Strong Optomechanical Squeezing of Light”. In: *Physical Review X* 3 (3), p. 031012.
- Ranzani, L. and J. Aumentado (2014). “A geometric description of nonreciprocity in coupled two-mode systems”. In: *New Journal of Physics* 16 (10), p. 103027.
- Ranzani, L. and J. Aumentado (2015). “Graph-based analysis of nonreciprocity in coupled-mode systems”. In: *New Journal of Physics* 17 (2), p. 023024.
- Rautio, J. C. (1986). “A Time-Harmonic Electromagnetic Analysis of Shielded Microstrip Circuits”. PhD thesis. Syracuse University.
- Rautio, J. C. and R. F. Harrington (1987). “An Electromagnetic Time-Harmonic Analysis of Shielded Microstrip Circuits”. In: *IEEE Transactions on Microwave Theory and Techniques* 35 (8), pp. 726–730.
- Riedinger, R. et al. (2016). “Non-classical correlations between single photons and phonons from a mechanical oscillator”. In: *Nature* 530 (7590), pp. 313–316.
- Romanenko, A. and D. I. Schuster (2017). “Understanding Quality Factor Degradation in Superconducting Niobium Cavities at Low Microwave Field Amplitudes”. In: *Physical Review Letters* 119 (26), p. 264801.
- Rosenthal, E. I. et al. (2017). “Breaking Lorentz Reciprocity with Frequency Conversion and Delay”. In: *Physical Review Letters* 119 (14), p. 147703.
- Rossi, M. et al. (2018). “Measurement-Based Quantum Control of Mechanical Motion”. In: *Nature* 563 (7729), p. 53.
- Ruesink, F. et al. (2016). “Nonreciprocity and Magnetic-Free Isolation Based on Optomechanical Interactions”. In: *Nature Communications* 7, p. 13662.
- Safavi-Naeini, A. H., S. Gröblacher, et al. (2013). “Squeezed light from a silicon micromechanical resonator”. In: *Nature* 500 (7461), pp. 185–189.
- Safavi-Naeini, A. H. and O. Painter (2011). “Proposal for an Optomechanical Traveling Wave Phonon–photon Translator”. In: *New Journal of Physics* 13 (1), p. 013017.
- Sankey, J. C. et al. (2010). “Strong and Tunable Nonlinear Optomechanical Coupling in a Low-Loss System”. In: *Nature Physics* 6 (9), pp. 707–712.
- Sato, T. et al. (1999). “Lens-free in-line optical isolators”. In: *Optics Letters* 24 (19), pp. 1337–1339.
- Scheucher, M. et al. (2016). “Quantum optical circulator controlled by a single chirally coupled atom”. In: *Science* 354 (6319), pp. 1577–1580.
- Schindler, J. et al. (2011). “Experimental Study of Active *LRC* Circuits with *PT* Symmetries”. In: *Physical Review A* 84 (4), p. 040101.

- Schliesser, A., P. Del’Haye, et al. (2006). “Radiation Pressure Cooling of a Micromechanical Oscillator Using Dynamical Backaction”. In: *Physical Review Letters* 97 (24), p. 243905.
- Schliesser, A., R. Rivière, et al. (2008). “Resolved-Sideband Cooling of a Micromechanical Oscillator”. In: *Nature Physics* 4 (5), pp. 415–419.
- Seyranian, A. P., O. N. Kirillov, and A. A. Mailybaev (2005). “Coupling of Eigenvalues of Complex Matrices at Diabolic and Exceptional Points”. In: *Journal of Physics A: Mathematical and General* 38 (8), p. 1723.
- Shankar, S. et al. (2013). “Autonomously stabilized entanglement between two superconducting quantum bits”. In: *Nature* 504 (7480), pp. 419–422.
- Shen, Z. et al. (2016). “Experimental realization of optomechanically induced non-reciprocity”. In: *Nature Photonics* 10 (10), pp. 657–661.
- Shirasaki, M. and K. Asama (1982). “Compact optical isolator for fibers using birefringent wedges”. In: *Applied Optics* 21 (23), pp. 4296–4299.
- Siegman, A. E. (1986). *Lasers*. Mill Valley, Calif: Univ. Science Books.
- Sliwa, K. M. et al. (2015). “Reconfigurable Josephson Circulator/Directional Amplifier”. In: *Physical Review X* 5 (4), p. 041020.
- Steeb, W.-H. and Y. Hardy (2014). “Exceptional Points, Non-Normal Matrices, Hierarchy of Spin Matrices and an Eigenvalue Problem”. In: *International Journal of Modern Physics C* 25 (11), p. 1450059.
- Stehmann, T., W. D. Heiss, and F. G. Scholtz (2004). “Observation of Exceptional Points in Electronic Circuits”. In: *Journal of Physics A: Mathematical and General* 37 (31), p. 7813.
- Stevens, J. (2017). “Theory and Design of Multimode Electromechanical Circuits”. MA thesis. École Polytechnique Fédérale de Lausanne (EPFL).
- Sudhir, V. (2018). *Quantum Limits on Measurement and Control of a Mechanical Oscillator*. Springer Theses. Cham: Springer International Publishing.
- Sudhir, V. et al. (2017). “Appearance and Disappearance of Quantum Correlations in Measurement-Based Feedback Control of a Mechanical Oscillator”. In: *Physical Review X* 7 (1), p. 011001.
- Suh, J. et al. (2014). “Mechanically detecting and avoiding the quantum fluctuations of a microwave field”. In: *Science* 344 (6189), pp. 1262–1265.
- Teufel, J. D., T. Donner, et al. (2011). “Sideband cooling of micromechanical motion to the quantum ground state”. In: *Nature* 475 (7356), pp. 359–363.
- Teufel, J. D., J. W. Harlow, et al. (2008). “Dynamical Backaction of Microwave Fields on a Nanomechanical Oscillator”. In: *Phys. Rev. Lett.* 101 (19), p. 197203.
- Teufel, J. D., D. Li, et al. (2011). “Circuit cavity electromechanics in the strong-coupling regime”. In: *Nature* 471 (7337), pp. 204–208.

- Thompson, J. D. et al. (2008). “Strong Dispersive Coupling of a High-Finesse Cavity to a Micromechanical Membrane”. In: *Nature* 452 (7183), pp. 72–75.
- Tian, L., M. S. Allman, and R. W. Simmonds (2008). “Parametric Coupling between Macroscopic Quantum Resonators”. In: *New Journal of Physics* 10 (11), p. 115001.
- Tian, L. and Z. Li (2016). “Nonreciprocal State Conversion between Microwave and Optical Photons”. In: *arXiv:1610.09556 [cond-mat, physics:quant-ph]*. arXiv: 1610.09556.
- Tóth, L. D., N. R. Bernier, A. K. Feofanov, et al. (2018). “A Maser Based on Dynamical Backaction on Microwave Light”. In: *Physics Letters A. Special Issue in memory of Professor V.B. Braginsky* 382 (33), pp. 2233–2237.
- Tóth, L. D., N. R. Bernier, A. Nunnenkamp, et al. (2017). “A Dissipative Quantum Reservoir for Microwave Light Using a Mechanical Oscillator”. In: *Nature Physics* 13 (8), pp. 787–793.
- Tóth, L. D. (2018). “Dissipation as a Resource in Circuit Quantum Electromechanics”. PhD thesis. École Polytechnique Fédérale de Lausanne (EPFL).
- Tsang, M. and C. M. Caves (2012). “Evading Quantum Mechanics”. In: *Physical Review X* 2 (3).
- Tsaturyan, Y. et al. (2017). “Ultracoherent Nanomechanical Resonators via Soft Clamping and Dissipation Dilution”. In: *Nature Nanotechnology* 12 (8), pp. 776–783.
- Tzuang, L. D. et al. (2014). “Non-reciprocal phase shift induced by an effective magnetic flux for light”. In: *Nature Photonics* 8 (9), pp. 701–705.
- Uzdin, R., A. Mailybaev, and N. Moiseyev (2011). “On the Observability and Asymmetry of Adiabatic State Flips Generated by Exceptional Points”. In: *Journal of Physics A: Mathematical and Theoretical* 44 (43), p. 435302.
- Verhagen, E. et al. (2012). “Quantum-Coherent Coupling of a Mechanical Oscillator to an Optical Cavity Mode”. In: *Nature* 482 (7383), pp. 63–67.
- Wallraff, A. et al. (2004). “Strong coupling of a single photon to a superconducting qubit using circuit quantum electrodynamics”. In: *Nature* 431 (7005), pp. 162–167.
- Walther, H. et al. (2006). “Cavity Quantum Electrodynamics”. In: *Reports on Progress in Physics* 69 (5), p. 1325.
- Wang, Y.-D. and A. A. Clerk (2013). “Reservoir-Engineered Entanglement in Optomechanical Systems”. In: *Physical Review Letters* 110 (25), p. 253601.
- Weiss, T., A. Kronwald, and F. Marquardt (2016). “Noise-Induced Transitions in Optomechanical Synchronization”. In: *New Journal of Physics* 18 (1), p. 013043.

- White, T. C. et al. (2015). “Traveling Wave Parametric Amplifier with Josephson Junctions Using Minimal Resonator Phase Matching”. In: *Applied Physics Letters* 106 (24), p. 242601.
- Wilson, D. J. et al. (2015). “Measurement-based control of a mechanical oscillator at its thermal decoherence rate”. In: *Nature* 524 (7565), pp. 325–329.
- Wilson-Rae, I. et al. (2007). “Theory of Ground State Cooling of a Mechanical Oscillator Using Dynamical Backaction”. In: *Physical Review Letters* 99 (9).
- Wollman, E. E. et al. (2015). “Quantum squeezing of motion in a mechanical resonator”. In: *Science* 349 (6251), pp. 952–955.
- Woolley, M. J. and A. A. Clerk (2013). “Two-Mode Back-Action-Evading Measurements in Cavity Optomechanics”. In: *Physical Review A* 87 (6), p. 063846.
- Woolley, M. J. and A. A. Clerk (2014). “Two-mode squeezed states in cavity optomechanics via engineering of a single reservoir”. In: *Physical Review A* 89 (6), p. 063805.
- Xu, H. et al. (2016). “Topological Energy Transfer in an Optomechanical System with Exceptional Points”. In: *Nature* 537 (7618), pp. 80–83.
- Xu, X.-W. et al. (2016). “Nonreciprocal conversion between microwave and optical photons in electro-optomechanical systems”. In: *Physical Review A* 93 (2), p. 023827.
- Yu, Z. and S. Fan (2009). “Complete optical isolation created by indirect interband photonic transitions”. In: *Nature Photonics* 3 (2), pp. 91–94.
- Zhang, K., P. Meystre, and W. Zhang (2013). “Back-Action-Free Quantum Optomechanics with Negative-Mass Bose-Einstein Condensates”. In: *Physical Review A* 88 (4), p. 043632.

Nathan Bernier
Chemin de Passerose 6
1006 Lausanne
Switzerland

Phone: (+41) 79 580 87 49 (CH)
Email: nathan.bernier@alumni.epfl.ch
Date of birth: May 10 1990



Education

- 2014 – 2018** **ÉCOLE POLYTECHNIQUE FÉDÉRALE DE LAUSANNE**, Switzerland.
PhD in physics.
▷ Experimental research on microwave superconducting circuits involving mechanical elements.
- 2011 – 2013** **ÉCOLE POLYTECHNIQUE FÉDÉRALE DE LAUSANNE**, Switzerland.
M. Sc. in physics.
▷ 5.73/6.00 GPA.
▷ Master thesis project on the theory of cold atoms at **HARVARD UNIVERSITY**.
- 2008 – 2011** **ÉCOLE POLYTECHNIQUE FÉDÉRALE DE LAUSANNE**, Switzerland.
B. Sc. in physics.
▷ Exchange year spent at **CARNEGIE MELLON UNIVERSITY** (4.00/4.00 GPA).
▷ Best GPA (5.69/6.00) in graduating class (71 students).

Skills and Languages

- Languages English (fluent), French (mother tongue), German (intermediate).
- Programming : Python, C++, Mathematica, git, L^AT_EX.
- Laboratory : Ultra-low temperature measurements, design of superconducting microwave circuits.
- Simulation : Experience with various finite-elements tools and Sonnet software for the design of microwave circuits.

Professional Experience

- 2017 – 2018**
(2 semesters) **ÉCOLE POLYTECHNIQUE FÉDÉRALE DE LAUSANNE**, Switzerland.
Teaching assistant for Quantum Optics.
▷ Sole assistant responsible for the class, coaching the students to participate in the **IBM Q Experience** competition.
- 2015 – 2018**
(3 semesters) **ÉCOLE POLYTECHNIQUE FÉDÉRALE DE LAUSANNE**, Switzerland.
Teaching assistant for Statistical Physics III.
- 2014 – 2017**
(3 semesters) **ÉCOLE POLYTECHNIQUE FÉDÉRALE DE LAUSANNE**, Switzerland.
Teaching assistant for General Physics II.
- 2011 – 2014**
(4 × 16 days) **MONTREUX JAZZ FESTIVAL**, Switzerland.
Clerk at staff management office.
▷ Responsible for the distribution of wages and food vouchers.
- 2014**
(1 semester) **BOSTON UNIVERSITY**, Boston, USA.
Teaching assistant.
▷ Helping design a new course and lab on the Science of Food.

2013 – 2014 (2 semesters)	BOSTON UNIVERSITY, Boston, USA. Teaching assistant for General Physics. ▷ In charge of multiple laboratory sections.
2012 (1 semester)	ÉCOLE POLYTECHNIQUE FÉDÉRALE DE LAUSANNE, Switzerland. Teaching assistant (Analytical Mechanics).
2010 (1 semester)	ÉCOLE POLYTECHNIQUE FÉDÉRALE DE LAUSANNE, Switzerland. Teaching assistant for Introduction to Computer Science (C++).

Publications

- Bernier *et al.*, Level attraction in a microwave optomechanical circuit.
Physical Review A, **98**, 023841 (2018).
- Bernier *et al.*, Nonreciprocity in microwave optomechanical circuits.
To appear in IEEE Antennas and Wireless Propagation Letters.
- Malz *et al.*, Quantum-limited directional amplifiers with optomechanics.
Physical Review Letters **120**, 023601 (2018).
- Bernier *et al.*, Nonreciprocal reconfigurable microwave optomechanical circuit.
Nature Communications **8**, 604 (2017).
- Tóth *et al.*, A maser based on dynamical backaction on microwave light.
Physics Letters A **382**, 2233 (2017).
- Tóth *et al.*, A dissipative quantum reservoir for microwave light using a mechanical oscillator.
Nature Physics **13**, 787-793 (2017).
- Javerzac-Galy *et al.*, On-chip microwave-to-optical quantum coherent converter based on a superconducting resonator coupled to an electro-optic microresonator.
Physical Review A **94**, 053815 (2016).
- Bernier *et al.*, Unstable Avoided Crossing in Coupled Spinor Condensates.
Physical Review Letters **113**, 065303 (2014).

Prizes and Fellowships

- EPFL Excellence Fellowship in 2011 and 2012.
- Gold medal (5th) at the Swiss Physics Olympiads in 2008.

Activities

- Technician for student radio *Fréquence Banane* for 2 years.
- Guitar player in CMU student klezmer band for one year.
- Part of the science-oriented improvisational-theater group *the Catalyst* for 2 years.
- Lindy hop and other swing partner dancing.

